



Max-Planck-Institut für Meteorologie
Max Planck Institute for Meteorology

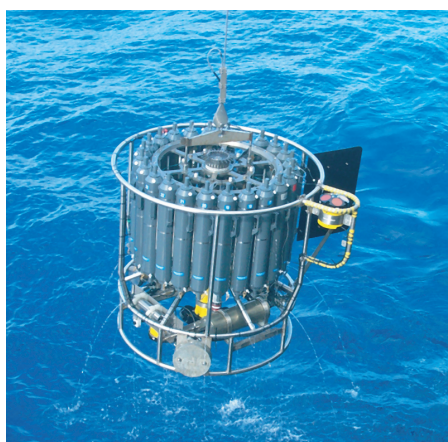


MAX-PLANCK-GESELLSCHAFT

Aggregated Carbon Cycle,
Atmospheric Chemistry,
and Climate Model (ACC2)

– Description of the forward and inverse modes –

Katsumasa Tanaka, Elmar Kriegler



Berichte zur Erdsystemforschung $\frac{40}{2007}$

Reports on Earth System Science

Hinweis

Die Berichte zur Erdsystemforschung werden vom Max-Planck-Institut für Meteorologie in Hamburg in unregelmäßiger Abfolge herausgegeben.

Sie enthalten wissenschaftliche und technische Beiträge, inklusive Dissertationen.

Die Beiträge geben nicht notwendigerweise die Auffassung des Instituts wieder.

Die "Berichte zur Erdsystemforschung" führen die vorherigen Reihen "Reports" und "Examensarbeiten" weiter.



Notice

The Reports on Earth System Science are published by the Max Planck Institute for Meteorology in Hamburg. They appear in irregular intervals.

They contain scientific and technical contributions, including Ph. D. theses.

The Reports do not necessarily reflect the opinion of the Institute.

The "Reports on Earth System Science" continue the former "Reports" and "Examensarbeiten" of the Max Planck Institute.

Anschrift / Address

Max-Planck-Institut für Meteorologie
Bundesstrasse 53
20146 Hamburg
Deutschland

Tel.: +49-(0)40-4 11 73-0
Fax: +49-(0)40-4 11 73-298
Web: www.mpimet.mpg.de

Layout:

Bettina Diallo, PR & Grafik

Titelfotos:

vorne:

Christian Klepp - Jochem Marotzke - Christian Klepp

hinten:

Clotilde Dubois - Christian Klepp - Katsumasa Tanaka

Aggregated Carbon Cycle,
Atmospheric Chemistry,
and Climate Model (ACC2)

– Description of the forward and inverse modes –

Katsumasa Tanaka, Elmar Kriegler

Hamburg 2007

Katsumasa Tanaka ^{1,2,3,4,*}

Elmar Kriegler ^{5,6,#}

Thomas Bruckner ⁷

Georg Hooss ⁸

Wolfgang Knorr ⁹

Thomas Raddatz ¹

1 Max Planck Institute for Meteorology, Hamburg, Germany

2 International Max Planck Research School on Earth System Modelling, Hamburg, Germany

3 Research Unit Sustainability and Global Change, University of Hamburg, Germany

4 Max Planck Institute for Biogeochemistry, Jena, Germany

5 Engineering and Public Policy, Carnegie Mellon University, Pittsburgh, Pennsylvania, USA

6 Potsdam Institute for Climate Impact Research (PIK), Germany

7 Institute for Energy Engineering, Technical University of Berlin, Germany

8 Schöpfung und Wandel, Lübeck, Germany

9 Quantifying and Understanding the Earth System (QUEST), University of Bristol, UK

* Correspondence author:

Katsumasa Tanaka

Max Planck Institute for Meteorology

Bundesstrasse 53, Hamburg, 20146, Germany

Email: katsumasa.tanaka@zmaw.de

Phone: +49 (40) 41173-387

Fax : +49 (40) 41173-298

Correspondence author for DOECLIM (Section 2.3):

Elmar Kriegler

Department of Engineering and Public Policy, Carnegie Mellon University

Pittsburgh, PA 15213, USA

Email: elmar@cmu.edu

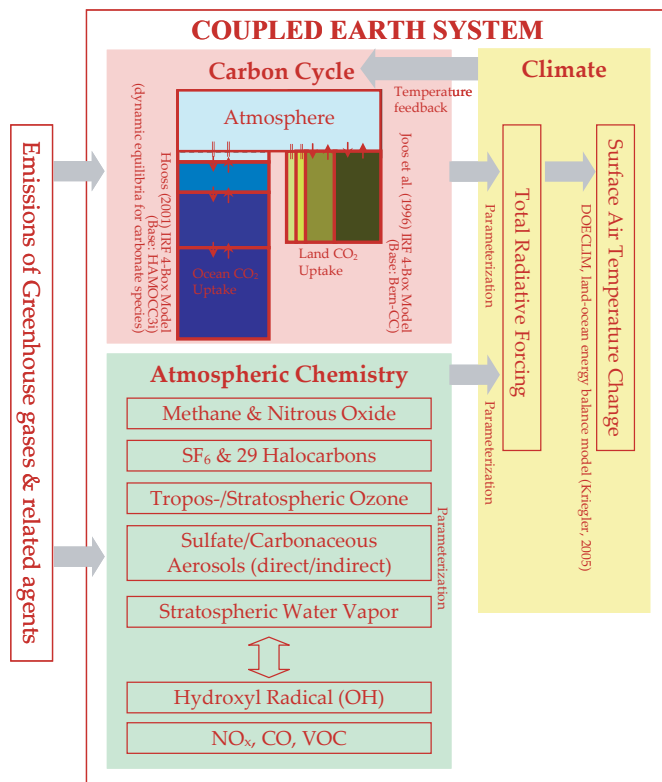
Phone: +1 (412) 268-5486

Fax: +1 (412) 268-3757

Aggregated Carbon Cycle, Atmospheric Chemistry, and Climate Model (ACC2)

– Description of the forward and inverse modes –

Aggregated Carbon Cycle, Atmospheric Chemistry, and Climate Model (ACC2)



Characteristics

- Global-annual-mean computation
- Inverse calculation for coupled Earth system
- Future projections using multi-emission scenarios

Base Models

- NICCS (Hooss, 2001)
- ICLIPS Climate Model (Bruckner et al., 2003)
- DOECLIM (Kriegler, 2005)

Coefficients and Functional Relationships

- IPCC (2001) Climate Change 2001
- WMO (2003) Ozone Depletion 2002
- IPCC (2005) Safeguarding the Ozone Layer
- IPCC (2007) Climate Change 2007: SPM

Programming Language (optimization solver)

- GAMS (CONOPT3)

Applications

- Uncertainty analysis for coupled Earth system (Tanaka et al., 2007)
- Global Warming Potential (GWP) evaluations (Tanaka et al., 2006b)
- Integrated Assessment

Katsumasa Tanaka, Elmar Kriegler

Hamburg 2007

Table of Contents

TABLE OF CONTENTS	1
ABSTRACT	3
1 INTRODUCTION	5
2 FORWARD MODELLING	9
2.1. CARBON CYCLE COMPONENT	9
2.1.1. Overview	9
2.1.2. Ocean CO ₂ Uptake	13
2.1.3. Land CO ₂ Uptake	27
2.1.4. Coupling of the Atmosphere-Ocean and Land Box Models.....	32
2.1.5. CO ₂ Radiative Forcing	33
2.2. ATMOSPHERIC CHEMISTRY COMPONENT	34
2.2.1. Overview	34
2.2.2. CH ₄	37
2.2.3. N ₂ O.....	40
2.2.4. OH	41
2.2.5. Halocarbons.....	43
2.2.6. SF ₆	46
2.2.7. Pollutants NO _x , CO, and VOC	47
2.2.8. Tropospheric O ₃	48
2.2.9. Stratospheric O ₃	49
2.2.10. EESC	50
2.2.11. Stratospheric H ₂ O.....	51
2.2.12. Aerosols.....	52
2.3. CLIMATE COMPONENT – DOECLIM	54
2.3.1. Atmosphere – Land – Surface Ocean Model.....	56
2.3.2. Interior Ocean Model	59
2.3.3. Model Calibration.....	62
2.3.4. Numerical implementation of DOECLIM.....	66
2.3.5. Coupling DOECLIM to the Other Components of ACC2.....	70
3 INVERSE MODELLING	85
3.1 BACKGROUND AND MOTIVATIONS	85
3.2 INVERSE ESTIMATION THEORIES	87
3.2.1 Generalization of Inverse Estimation Theories	87

3.2.2	Tarantola’s Inverse Estimation Theory	88
3.3	DATA IN ACC2 INVERSE CALCULATION	98
3.4	PARAMETERS IN ACC2 INVERSE CALCULATION.....	100
3.5	FACTORS INFLUENCING THE INTERANNUAL VARIABILITY.....	104
3.5.1	ENSO	104
3.5.2	Volcanic Eruptions.....	107
4	RESULTS AND CONCLUSIONS	117
4.1	RESULTS FOR PAST MODE SIMULATION.....	117
4.2	RESULTS FOR FUTURE MODE SIMULATION	119
4.3	CONCLUDING REMARKS AND FUTURE PERSPECTIVES	121
	ACKNOWLEDGMENTS	145
	REFERENCES.....	147
APPENDIX A	TECHNICALITIES.....	167
A.1	PROGRAMMING LANGUAGE AND SOLVERS.....	167
A.2	NUMERICAL INTEGRATION	170
A.3	MODEL OPERATIONS AND FILE STRUCTURE	171
A.4	PRACTICAL TIPS ON RUNNING ACC2.....	174
APPENDIX B	DETAILS OF INVERSION RESULTS.....	177
APPENDIX C	ACRONYMS AND ABBREVIATIONS.....	187

ABSTRACT

The Aggregated Carbon Cycle, Atmospheric Chemistry, and Climate model (ACC2) describes major physical-biogeochemical processes in the Earth system on a global-annual-mean basis. The starting point of the development of ACC2 is the ICLIPS Climate Model (ICM) (Bruckner et al., 2003). The novel aspect of ACC2 is the implementation of an inversion scheme, complementary to the inversion approach deriving probability densities for several climate properties (e.g. Forest et al., 2002; Gregory et al., 2002; Knutti et al., 2002; Hegerl et al., 2006). We account for a large number of uncertainties in the Earth system independently and optimize them by considering the interactions between different Earth system components. As a result, our inversion produces an Earth system evolution between the year 1750 and 2000 and generates the best guess of uncertain parameters. Such uncertainty estimates obtained for the historical period are consistently used for future projections. Further scientific applications for the ACC2 inversion include Global Warming Potential (GWP) evaluations based on the historical Earth system evolution (Tanaka et al, 2006b), climate sensitivity estimation accounting for the carbon cycle response to the temperature change (Tanaka et al., 2007), and model coupling for Integrated Assessment.

1 INTRODUCTION

A wealth of geophysical and biogeochemical observation databases indicate that the history of the Earth system has been radically changed by the onset of the anthropogenic CO₂ emission due to fossil fuel combustion in the 18th century, marking the beginning of the Anthropocene (Crutzen and Stoemer, 2000). There is a virtual agreement among scientists that present day human activities substantially influence various processes in the carbon cycle, atmospheric chemistry, and climate systems (Intergovernmental Panel on Climate Change (IPCC), 2007). These Earth system components are responding in a complex manner as they are strongly interdependent. Concerns over the fate of the Earth system are mounting and the scientific exploration of future climate projections is ever more important.

Recent years we developed the Aggregated Carbon Cycle, Atmospheric Chemistry, and Climate model (ACC2) describing major physical-biogeochemical processes in the Earth system on a global-annual-mean basis. ACC2 is a tool to advance understanding on the first-order interactions of Earth system processes and of the associated uncertainty estimates.

The development of ACC2 was motivated by its applications to multi-disciplinary investigation of the future natural and human Earth system co-evolution. This type of approach is called ‘Integrated Assessment (IA),’ in which several models ranging from climate and terrestrial biosphere models to land use and economy models are coupled (Hooss, 2004). ACC2 was implemented in IA models such as the Model of INvestment and Technological Development (MIND) (Edenhofer et al., 2005) and the ECOnomy-BIOsphere-ClimatE (ECOBICE) supermodel (Kempfert and Knorr, 2006).

The IA modelling approach relies on multiple long-term scenarios of future GreenHouse Gas (GHG) emissions (e.g. Special Report on Emissions Scenarios (SRES) (Nakićenović et al., 2000)), calling for computationally efficient models. The computational loads of the state-of-the-art General Circulation Models (GCMs) are prohibitively expensive for multi-scenario long-term runs. Only a tiny fraction of information obtained from GCM runs is meaningfully utilized by IA studies. In view of the need for dynamic yet concise representation of climate change, a reduced carbon cycle and climate model was developed in the framework of Structural Integrated Assessment Model (SIAM) (Hasselmann et al., 1997). It is based on the Impulse Response Function (IRF) approach, where the temporal evolution of a state variable (e.g. global-mean atmospheric CO₂ concentration) is extracted by perturbing the control run of a complex model. Hooss (2001) extended the applicability of the IRF-based carbon cycle model by describing the carbonate chemistry dynamically and established the Nonlinear Impulse-response representation of the coupled Carbon cycle-Climate

System model (NICCS). NICCS was utilized within the framework of the Multi-Actor Dynamic Integrated Assessment Model (MADIAM) (Weber et al., 2005). The IRF approach is a core methodology for NICCS and carried on in ACC2. Fixed spatial patterns (T21 resolution: 32 latitudinal and 64 longitudinal circles) of temperature change, cloud cover, precipitation, and sea level rise together with annual-global-mean characteristics are extracted from a 850-year quadruple CO₂ experiment of the coupled Atmosphere Ocean GCM (AOGCM) European Centre Hamburg Model 3-Large Scale Geostrophic ocean model (ECHAM3-LSG) by the Empirical Orthogonal Function (EOF) approach. In NICCS, the fixed spatial patterns are superimposed on the global-mean projections that are computed separately.

The actual starting point of the ACC2 development was the Integrated Assessment of Climate Protection Strategies (ICLIPS) Climate Model (ICM) version 1.1 (Bruckner et al., 2003), which was used for the ICLIPS IA project (Toth, 2003). ICM deals with multi-gases (CO₂, CH₄, N₂O, halocarbons, SF₆, and SO₂) in contrast to NICCS dealing with only CO₂. The functional relationships and constants in ICM have been reviewed on the basis of IPCC (1996). ICM adopts the separation of the spinup mode (running from year 1750 to 1990) and the forward mode (running from 1990 onward) with a time step of 5 years to further reduce the computational burden for future multi-scenario analyses. ICM is programmed in General Algebraic Modeling System (GAMS) while NICCS is programmed in Fortran 77. The optimization solver CONOPT2 provided with GAMS is utilized for coupling with economy models and calculating the emission corridors, within which permissible CO₂ emission pathways to satisfy certain climatic constraints are contained (Bruckner et al., 2003).

ICM has been progressively expanded to ACC2. ACC2 version 1.0 has been released in May 2005 (Tanaka et al, 2005), version 2.1 in March 2006 (Kriegler et al., 2006; Tanaka et al., 2006a), version 2.2 in September 2006 (Tanaka et al., 2006b), and version 3.0 in March 2007 (this document). Major improvements of ACC2 version 2.3 over ICM are fivefold as follows:

- 1) Update of the physical and biogeochemical functional relationships and constants in accordance with IPCC (2001), Joos et al. (2001), WMO (2003), IPCC (2005), and other recent literature¹,
- 2) Implementation of the parameterization of atmospheric chemistry involving a set of radiative forcing agents (CO₂, CH₄, N₂O, SF₆, 29 species of halocarbons, tropospheric and stratospheric O₃, sulfate aerosols (direct effect), carbonaceous aerosols (direct effect), all aerosols (indirect effect), stratospheric H₂O, hydroxyl radical (OH), and pollutants (NO_x, CO, and VOC)) on the basis of IPCC (2001) and Joos et al. (2001) (Table 2.1),
- 3) Coupling with the Diffusion Ocean Energy balance CLIMate model (DOECLIM) (Kriegler,

¹ It is necessary to reflect the latest findings summarized in IPCC (2007) to ACC2. At the time of writing this document, only the Summary for PolicyMakers (SPM) is available for public. As far as we can see in SPM, no major changes are necessary in the ACC2 model code (e.g. compare IPCC (2001, SPM, Figure 3) and IPCC (2007, SPM, Figure 2)).

- 2005), a land-ocean Energy Balance Model (EBM) to calculate the surface air temperature from the radiative forcing, as opposed to a physical interpretation of the IRF (Kriegler, unpublished) used in ICM version 1.1 and the original IRF (Hooss, 2001) used in ICM version 1.0,
- 4) Addition of the climate-carbon cycle feedback: the temperature dependency of the thermodynamic equilibria for marine carbonate species (Millero, 1995; Millero et al., 2006) and of the heterotrophic respiration using a Q10 factor, and
 - 5) Development of an inverse calculation scheme to estimate uncertain properties in the Earth system at a global-annual-mean model.

The crucial new aspect of the ACC2 methodology is the inverse calculation scheme, where the values of the uncertain parameters in the coupled carbon cycle, atmospheric chemistry, and climate system are estimated by using various measurements between the year 1750 and 2000 (Table 3.1), other independent information on such parameters (Table 3.2), and physical-biogeochemical functional relationships. Currently an inversion for the Earth system is not operational for more complex models because of the requirement for prohibitively expensive computation. In ACC2, the uncertainty analysis is utilized to re-calibrate the model as detailed processes and other radiative agents are implemented.

The theoretical underpinning of the ACC2 inversion is the probabilistic inverse estimation theory (Tarantola, 2005), which formulates an inversion as an information synthesis (Figure 3.1). The assumptions in the ACC2 inversion approach are extensively discussed under the Tarantola's theory in Section 3.2.2. Our inversion scheme theoretically computes the maximum of the joint posterior probability density of the parameters, which is equivalent to the minimum of the cost function (equation (3.2.14)). The cost function is the sum of the squared misfits for the parameters and the data weighted by respective prior uncertainty ranges. Our inversion produces an Earth system evolution between the year 1750 and 2000 and generates the best guess of uncertain parameters. The parameter estimates and model state for the year 2000 obtained from the inversion serve as a basis for future projections (Section 4.2). Such a consistent treatment of the uncertainties from the past to the future was not done in IPCC (2001).

Several inversion studies (e.g. Forest et al., 2002; Gregory et al., 2002; Knutti et al., 2002; Hegerl et al., 2006) estimated the probability densities of uncertain climate properties. It is advantageous that the probability densities present the extent of the knowledge on uncertainties. Nevertheless, our one-point estimates of the uncertainties obtained from the ACC2 optimization approach provide a distinct value. First, our approach deals with the uncertainties in the Earth system simultaneously. Previous inversion studies neglected the fact that the interactions among different Earth system compartments provide constraints for uncertainty estimation. Second, it would not be possible to pick the peaks of the posterior probability densities for parameters together as single estimates (e.g. aerosol forcing, ocean vertical diffusivity, and climate sensitivity) because of the

interdependencies of uncertainty estimates. Our one-point estimates allow straightforward interpretation and appeal to different scientific applications (e.g. Tanaka et al., 2006b; Tanaka et al., 2007). Third, the number of the uncertainties considered in probability density studies is limited to several due to the computational requirement. Our optimization approach can account for a large number of uncertainties including each point of parameters and data in time series independently although a huge number of interdependencies in the uncertainty estimates are extremely complex to analyze and produce bias to the inversion solution. Regional information cannot enter our inversion as we are at the bound of the current optimization capability. Based on the arguments above, the ACC2 inversion approach is complementary to the probability density approach.

The model operation is separated into the past mode (year 1750 – 2000) and the future mode (year 2000 onward). In the past mode, an inverse calculation is performed to estimate the uncertain parameters and model state for the year 2000, both of which are transferred to the future mode and used for the future projections. ACC2 is programmed in GAMS (Distribution 22.4) and the optimization is solved using solver CONOPT3 provided with GAMS (Section A.1). The optimization for the coupled Earth system is technically feasible because we restrict ourselves to global-annual-mean information. The numerical integration in ACC2 uses a variant of Heun's Predictor-Corrector method (Section A.2) with the time step of 1 year. The DOECLIM component uses an implicit two-stage Runge-Kutta method with maximum order 4 (Hammer and Hollingsworth method) (Section 2.3.4). The ACC2 model code contains a *switchboard* (Section A.3), an interface where one can control the parameters and data to be put into the inverse calculation and analyze the influence of particular information to the inversion results. In the switchboard one can also turn on and off the temperature feedback to the carbon cycle for sensitivity analysis (Tanaka et al., 2007).

This document aims at providing a complete description of the forward and inverse calculations of ACC2 at the level required for using the model. Discussions on relevant issues are also introduced where necessary. Assumptions in the model and their implications are explicitly stated. Some further details are directly written in the ACC2 model code. The cited references do not intend to serve as a comprehensive list of earlier works. We frequently cite IPCC (2001) and WMO (2003), which are the summary of the scientific findings in the respective fields and where further references can be found. Acronyms and abbreviations are listed in Appendix C. The main textbooks referred for the model documentation are Libes (1992), Schlesinger (1997), Zeebe and Wolf-Gladrow (2001), Mackenzie (2002), Fasham (2003), Mackenzie and Lerman (2006) and Millero (2006) for carbon cycle; Brasseur et al. (1999), Jacob (1999), Brasseur et al. (2003), and Seinfeld and Pandis (2006) for atmospheric chemistry; Wunsch (1996), Enting (2002a), and Tarantola (2005) for inverse estimation.

2 FORWARD MODELLING

2.1. CARBON CYCLE COMPONENT

2.1.1. Overview

CO₂ is the most important GHG regulating the Earth climate on the various time scales of the industrial period (IPCC, 2001), the glacial-interglacial cycle (Petit et al., 1999), and the Hothouse-Icehouse cycle (Fisher, 1984). Because of its substantial atmospheric abundance and particular molecular structure, CO₂ primarily interferes with the long-wave radiation emitted from the Earth surface and traps heat energy within the lower atmosphere. The very origin of carbon on the Earth dates back to the fusion reactions involving ⁴He and ⁸Be in the Earth interior during the planetary formation (Burbidge et al., 1957). At present, more than 99% of carbon on the Earth exists in sedimentary rocks in a form of organic carbon or carbonate minerals (Li, 2000, Table VIII-2; Mackenzie, 2002, Table 6.2), by far outnumbering the amounts stored in the ocean, the atmosphere, and the biosphere.²

On the time scale of ACC2 (typically between the year 1750 and 2100), the atmospheric abundance of CO₂ is largely controlled by the magnitudes of the CO₂ uptake from the ocean and the terrestrial biosphere and by the amounts of the anthropogenic CO₂ emission. These processes perturb an equilibrated state of the carbon cycle system assumed prior to 1750. Such an equilibrium-based approach conforms to the approach of GCMs that are tuned to produce zero net CO₂ exchange between the ocean and the atmosphere and between the land and the atmosphere in their control runs. Such an approach can also be taken as a ‘first-cut’ in view of the difficulty in modelling the riverine carbon transport in the temporal and spatial resolution of GCMs. However, the equilibrium assumption is not compatible with the accurate portray of the system even on shorter time scales

² On the geological time scale, the atmospheric CO₂ concentration is primarily controlled by the intensity of volcanism related to the plate tectonic activity; such geological processes are so drastic that the atmospheric CO₂ concentration reached as high as 5,000 ppm approximately 500 million years ago, according to geochemical evidences (Berner, 1991; Berner, 1997). The atmospheric CO₂ is removed by the weathering of limestone and calcium silicate, leaching dissolved carbon to the ocean. The dissolved carbon in the ocean is utilized to form body of life. A tiny fraction of dead body, detritus, and calcium carbonate is buried deeply in the ocean sediments. It is converted to oil and gas at elevated temperature and pressure on a time scale of million years; it is eventually returned to the mantle through subduction zones on a time scale of hundreds million years. Although such massive processes over the geological time horizon need to be remembered, the rates of these processes appear extremely slow on the annual to century time scale of ACC2 and are thus neglected here.

(Fred Mackenzie, personal communication, November 1, 2005) and is difficult to be justified in view of the constantly changing Earth system shown in various reconstructions. Thus, the particular preindustrial state assumed here is termed ‘quasi-steady state’ as coined in Ver et al. (1999).

In ACC2, the anthropogenic CO₂ emission is represented by the following two categories: the emission due to fossil fuel combustion and the emission due to land use change. The fossil fuel CO₂ emission originates from the combustion of all types of fossil fuel productions and consumptions, cement production, and gas flaring. The magnitude of the fossil fuel CO₂ emission became prominent at the onset of the Industrial Revolution, when energy-intensive machinery started to emerge. The global fossil fuel CO₂ emission is estimated to be about 7.3 GtC/year in 2003 (Marland et al., 2006). In all the 40 future emission scenarios of SRES, the fossil fuel CO₂ emission will continue to be dominant for the next one hundred years. The land use CO₂ emission means the net change in the carbon storage in terrestrial ecosystems due to human activities such as deforestation, afforestation (or reforestation), and the conversion of natural ecosystems to cultivated lands and pastures. The change in the terrestrial carbon storage due to the environmental factors is not included in the land use CO₂ emission and rather explained as the land CO₂ uptake as described later. In other words, the ecological processes of deforestation and afforestation are accounted for in the land use CO₂ emission and the physiological processes of photosynthesis and respiration for the land CO₂ uptake. The magnitude of the land use CO₂ emission has been considerable even earlier than the rise of the fossil fuel CO₂ emission. There is a hypothesis under debate that the Holocene CO₂ rise started 8,000 years ago is indeed driven by the land use CO₂ emission caused by the forest clearance in Eurasia (Ruddiman, 2003). Currently the land use CO₂ emission is the second largest human-driven CO₂ emission (2.1 GtC/year in 2000 according to Houghton and Hackler (2002)). However, the land use CO₂ emission is projected to approach zero or turn negative by 2100 in all six future emission scenarios of SRES, indicating an assumption on forest as a strong carbon sink. It should be noted that there is a speculation that the CO₂ emission due to soil erosion is substantial in magnitude (Lal, 2005). However, the soil erosion CO₂ emission is not included in ACC2 because its magnitude, even its sign, is not well-known due to the competing evidences from sedimentologists and soil scientists.

The CO₂ emission has been changing the atmospheric CO₂ composition, influencing the rates of the ocean and land CO₂ uptake. The disparity in the CO₂ partial pressure at the air-sea interface controls the rate of the oceanic CO₂ exchange. The atmospheric CO₂ concentration change directly affects the rate of photosynthesis of the terrestrial plants and indirectly controls the rate of heterotrophic respiration via the temperature change. The change in the water cycle and the nutrient availability are important factors controlling the terrestrial processes; however, these are not explicitly modelled in ACC2. The changes of ocean and land CO₂ uptake rates from the respective preindustrial levels are modelled using box model approaches as follows.

The ocean CO₂ uptake is described by an atmosphere-ocean box model. The parameters of the box model here are “back-calculated” from the output of a complex model by the IRF approach (Maier-Reimer and Hasselmann, 1987). The ocean uptake IRF (Hooss, 2001) is a mathematical substitute mimicking the ocean CO₂ uptake simulated by Hamburg Model of the Ocean Carbon Cycle (HAMOCC) 3i in response to an injection of a small amount of CO₂ into the atmosphere in the controlled state. The IRF can be interpreted as the solution of a system of differential equations that govern a four-layer atmosphere-ocean box model, allowing the estimation of the box model parameters.

The direct application of the box model obtained from the procedure above is valid only within the linear or quasi-linear range of the calibration; the validity of the atmosphere-ocean box model is limited to the cases with less than twice of the preindustrial CO₂ concentration (Hooss, 2001). The emerging nonlinear property with the departure from the calibration range stems from the fact that the atmospheric CO₂ concentration change influences the thermodynamic equilibria for the marine carbonate species such as CO₂(aq), HCO₃⁻, and CO₃²⁻ (Pilson, 1998; Millero, 2006). As a result, the ocean takes up less CO₂ with increasing atmospheric CO₂ concentration. Such a linear limitation can be overcome by furnishing the box model equations with the thermodynamic equilibrium relationships. The modified box model is then good for applications even for cases with the quadruple of the preindustrial CO₂ level (Hooss, 2001). Furthermore, we adopted the relationships of the thermodynamic constants with in-situ temperature (Millero, 1995; Millero et al., 2006; other references therein), accounting for the temperature feedback to the ocean CO₂ uptake.

The formulation of the land box model is fairly straightforward relative to the oceanic counterpart. Under the quasi-steady state assumption, the Net Primary Production (NPP), defined as the difference between the rate of Gross Primary Production (GPP) and the rate of autotrophic respiration, is assumed to be constant and balanced with the heterotrophic respiration prior to 1750. The perturbation of NPP and the change in the heterotrophic respiration is described by the four-reservoir land box model. The departure of the atmospheric CO₂ concentration from the preindustrial level leads to the change in NPP, a process called CO₂ fertilization (or CO₂ fertilization effect), which is logarithmically parameterized with the beta factor (Gifford, 1980; Friedlingstein et al., 1995). CO₂ fertilization is caused by the fact that the higher partial pressure of CO₂ is exerted on stomata (microscopic leaf openings) distributed over plant leaves, which control the rate of photosynthesis.

The fertilized biomass is released back to the atmosphere by respiration, decay, and decomposition, which is parameterized by first-order kinetic equations. The parameters in the land box model are determined by comparing the *derivatives* of the box model solution with the IRF of Joos et al. (1996). Joos' IRF is a sum of exponential functions representing the heterotrophic

respiration flux (not the reservoir size) simulated by the Bern Carbon Cycle model (Bern-CC) in response to the additional sequestration of carbon. The temperature dependency of the heterotrophic respiration is parameterized using a Q10 factor, by which the rate of terrestrial respiration increases with a temperature increase of 10°C. The temperature dependency of the heterotrophic respiration is applied not only to the fertilized carbon but also to the preindustrial (or background) carbon. The land box model is coupled to the atmosphere-ocean box model.

In the average state of the preindustrial Earth system, there is a net CO₂ outgassing flux from the ocean (-0.48 ± 0.002 GtC/year) (Fred Mackenzie, personal communication, October 26, 2005) because of the combined effect of CaCO₃ deposition and organic metabolism (Smith and Mackenzie, 1987). This is counteracted by a net CO₂ uptake flux to the terrestrial biosphere (0.36 to 0.6 GtC/year) (Fred Mackenzie, personal communication, October 26, 2005). In ACC2, constant fluxes of preindustrial ocean CO₂ outgassing and preindustrial land CO₂ uptake are separately introduced. The magnitudes of these preindustrial fluxes are estimated in the inverse calculation. The addition of the preindustrial CO₂ fluxes partially resolves the drawback of the quasi-steady state assumption discussed earlier. These preindustrial fluxes are treated as if they were emissions in a sense that they increase the atmospheric CO₂ content without decreasing the ocean and land carbon pools. Such a treatment does not lead to a serious error for the carbon budget on a time scale of the simulation because preindustrial fluxes are almost negligible relative to the gigantic carbon storages in the ocean (38,000 GtC (IPCC, 2001, Figure 3.1)) and over land (2,000 GtC (IPCC, 2001, Figure 3.1)).

The preceding discussion summarizes the carbon cycle modelling in ACC2. Detailed and technical explanations on the ocean and land CO₂ uptake follow. The explanation of the ocean CO₂ uptake is in particular devoted to the following two complications. First, the differential equations of the ocean box model are decoupled by being expressed in the eigen-system so that the decoupled differential equations are comparable with the IRF. In contrast, the conversion to the eigen-system was not needed for the land box model due to its reservoir configuration that all the four reservoirs are directly connected to the atmosphere without any flow between the reservoirs. Second, the thermodynamic equilibria among the marine carbonate species are described to adjust the ocean CO₂ uptake with increasing atmospheric CO₂ concentration. Our approach is simple relative to other approaches centering on the carbonate system (e.g. Andersson et al., 2006). Justification of our approach requires argumentation from a wider perspective of the ocean carbon cycle (subsection on limitations on ocean CO₂ uptake in ACC2).

2.1.2. Ocean CO₂ Uptake

- Atmosphere-Ocean Box Model

The ocean CO₂ uptake is represented by a four-layer box model. The uppermost layer represents a composite layer consisting of the atmosphere and the ocean mixed layer, while the three subsequent layers represent the ocean's inorganic carbon storage capacity. The mixed layer is characterized as being isothermally uniform due to the wind mixing and insolation, usually up to a depth of 50 to 150 m (Tomczak and Godfrey, 1994, p.56). The composite layer approach is justified because the model's numerical time step (= 1 year) is larger than the equilibrium time of the atmosphere-mixed layer system with respect to CO₂ (about 240 days in Zeebe and Wolf-Gladrow (2001, pp. 80–81)). Note that only inorganic carbon is modelled in this atmosphere-ocean box model.

When the CO₂ emission is exogenously added to the atmosphere in an equilibrated system, the perturbed amounts of carbon in the reservoirs over time are described in the following dynamic equation.

$$\dot{\mathbf{c}}_{atm-ocn} + \mathbf{D}\mathbf{c}_{atm-ocn} = \mathbf{e}, \quad (2.1.1)$$

$$\text{with } \mathbf{c}_{atm-ocn} = \begin{bmatrix} c_{cmp,1}(t) \\ c_{ocn,2}(t) \\ c_{ocn,3}(t) \\ c_{ocn,4}(t) \end{bmatrix}, \quad \mathbf{e} = \begin{bmatrix} e_1(t) \\ 0 \\ 0 \\ 0 \end{bmatrix}, \quad (2.1.2)$$

$$\text{and } \mathbf{D} = \begin{bmatrix} \eta_{1,2}/h_1 & -\eta_{1,2}/h_2 & 0 & 0 \\ -\eta_{1,2}/h_1 & (\eta_{1,2} + \eta_{2,3})/h_2 & -\eta_{2,3}/h_3 & 0 \\ 0 & -\eta_{2,3}/h_2 & (\eta_{2,3} + \eta_{3,4})/h_3 & -\eta_{3,4}/h_4 \\ 0 & 0 & -\eta_{3,4}/h_3 & \eta_{3,4}/h_4 \end{bmatrix}. \quad (2.1.3)$$

$c_{x,i}(t)$ denotes the amount of perturbed inorganic carbon stored in reservoir i ($i=1,2,\dots,4$) at time t . Note that $c_{x,i}(t)$ does not include the preindustrial (or background) inorganic carbon, which was present prior to the perturbation. The reservoir designation is assigned from top to bottom. $e_1(t)$ denotes the time-dependent anthropogenic CO₂ emission in the atmosphere. The inventory of the perturbed carbon is controlled through Newtonian fluxes across the boundaries. $\eta_{i,i+1}$ denotes the Newtonian transfer coefficient between reservoir i and reservoir $i+1$. h_i denotes the water-column depth of reservoir i ; in particular, h_1 is a fictitious depth of the composite layer including the water-column-equivalent depth for the atmosphere in terms of the carbon content. By expressing the dynamic equation in the eigen-system, the four-dimensional dynamic equation is 'disentangled' to a set of decoupled differential equations as follows:

$$\sum_{k=1}^4 \dot{x}_k(t)\mathbf{g}_k + \mathbf{D}\sum_{k=1}^4 x_k(t)\mathbf{g}_k = \sum_{k=1}^4 r_k(t)\mathbf{g}_k, \quad (2.1.4)$$

$$\Leftrightarrow \sum_{k=1}^4 \dot{x}_k(t) \mathbf{g}_k + \sum_{k=1}^4 \lambda_k x_k(t) \mathbf{g}_k = \sum_{k=1}^4 r_k(t) \mathbf{g}_k \quad (2.1.5)$$

$$\text{with } \mathbf{c}(t) = \sum_{k=1}^4 x_k(t) \mathbf{g}_k \quad \text{and} \quad \mathbf{e}(t) = \sum_{k=1}^4 r_k(t) \mathbf{g}_k . \quad (2.1.6)$$

\mathbf{g}_k and λ_k are the k th eigenvector of matrix \mathbf{D} and the corresponding eigenvalue, respectively.

We now consider a case with a pulse emission at time 0, that is $\mathbf{e}_\delta(t) = \delta(t) \cdot \begin{bmatrix} e_{\delta,init,1} \\ 0 \\ 0 \\ 0 \end{bmatrix}$,

where $\delta(t)$ and $e_{\delta,init,1}$ denote the Dirac's delta function and the initial magnitude of the pulse emission, respectively. The differential equation $\dot{x}_{\delta,k}(t) + \lambda_k x_{\delta,k}(t) = r_{\delta,k}(t)$, $k = 1, 2, \dots, 4$, a special case of equation (2.1.5), has the following solution: $x_{\delta,k}(t) = r_{\delta,init,k} \exp(-\lambda_k t)$, where

$$\mathbf{r}_\delta(t) = \delta(t) \cdot \begin{bmatrix} r_{\delta,init,1} \\ r_{\delta,init,2} \\ r_{\delta,init,3} \\ r_{\delta,init,4} \end{bmatrix} .^3 \text{ Now, using equation (2.1.6), the solution for the composite layer is given as}$$

$$c_{\delta,cmp,1}(t) = \sum_{k=1}^4 x_{\delta,k}(t) g_{k,1} = \sum_{k=1}^4 r_{\delta,init,k} \exp(-\lambda_k t) g_{k,1} . \quad (2.1.7)$$

In the following, the parameters in the box model are conversely obtained from the IRF, opposite to the conventional way of establishing a box model (Garrels et al., 1975).

- IRF for Ocean CO₂ Uptake

Hooss (personal communication) found that, after a pulse injection in the amount of 1% of the preindustrial CO₂ concentration, a sum of four exponential functions with different lifetimes is the best least-square model that fits the temporal attenuation curve representing the amount of CO₂

³ More generally, a perturbation driven by *continuous* emissions is expressed by the convolution of the IRF: $\int_{-\infty}^t e(t') IRF_{ocn}(t-t') dt'$, where $e(\cdot)$ denotes the time series of CO₂ emissions. The IRF convolution can be interpreted as the Green's function solution of the following system of n decoupled first-order differential equations:

$$\dot{x}_k = -\frac{x_k}{\tau_{ocn,k}} + A_{ocn,k} e(t), \quad k = 1, 2, \dots, 4 . \quad (2.1.8)$$

The solutions for the individual differential equations are summed up to

$$\sum_{k=1}^4 x_k(t) = \int_{-\infty}^t e(t') \cdot IRF_{ocn}(t-t') dt' \quad (2.1.9)$$

and each of the individual solutions is

$$x_k(t) = \int_{-\infty}^t e(t') \cdot A_{ocn,k} \exp\left(\frac{-t}{\tau_{ocn,k}}\right) dt' . \quad (2.1.10)$$

remained in the atmosphere as it is absorbed to the ocean (based on HAMOCC 3i) (Figure 2.1). The normalized IRF for ocean CO₂ uptake (R01 experiment⁴ in Hooss (2001, Figure 3.1)) is given as follows:

$$IRF_{ocn}(t) = \sum_{i=0}^4 A_{ocn,i} \exp\left(\frac{-t}{\tau_{ocn,i}}\right), \quad (2.1.11)$$

$$\text{with } \sum_{i=0}^4 A_{ocn,i} = 1, \quad \begin{bmatrix} A_{ocn,0} \\ A_{ocn,1} \\ A_{ocn,2} \\ A_{ocn,3} \\ A_{ocn,4} \end{bmatrix} = \begin{bmatrix} 0.095 \\ 0.209 \\ 0.253 \\ 0.311 \\ 0.132 \end{bmatrix}, \text{ and } \begin{bmatrix} \tau_{ocn,0} \\ \tau_{ocn,1} \\ \tau_{ocn,2} \\ \tau_{ocn,3} \\ \tau_{ocn,4} \end{bmatrix} = \begin{bmatrix} 1.271 \\ 12.17 \\ 59.52 \\ 236.5 \\ \infty \end{bmatrix}, \quad (2.1.12)$$

where t is time in year. $\tau_{ocn,i}$ is the time constant for each of the four dominant decaying modes. $\tau_{ocn,0}$ can be interpreted as the time constant for the ocean mixed layer. $A_{ocn,4}$ indicates the asymptotic fraction of the initial perturbation i.e. what eventually remains in the atmosphere.

- Parameter Estimation of Atmosphere-Ocean Box Model

In order to estimate the box model parameters, we associate the box model solutions with the IRF under the simplified case of a pulse emission. One of the box model solutions (equation (2.1.7)) represents the temporal decay of the perturbation in the composite layer whereas the IRF describes the perturbation decay only in the atmosphere. The IRF can be modified to be comparable directly with the composite layer solution by making use of the equilibrium condition for the atmosphere-mixed layer carbon transfer. $A_{ocn,0}$ (equation (2.1.12)) can be interpreted as the fraction of perturbed carbon immediately absorbed into the mixed layer after the pulse emission. Thus, the ratio of the carbon content in the atmosphere to that in the mixed layer is maintained at $\frac{A_{ocn,0}}{1 - A_{ocn,0}}$ as long as the pulse emission is sufficiently small. The corresponding lifetime $\tau_{ocn,0}$ in equation (2.1.12) confirms that the atmosphere-mixed layer equilibrium assumption is justified for the 5-year-mean NICCS and ICM. It can be also justified for the annual-mean ACC2 as long as one does not particularly look into the short-term ocean response to interannual atmospheric CO₂ variations.

Thus, the IRF (equation (2.1.11)) can be modified to express the perturbed carbon in the composite layer as follows:

$$e_{\delta,init,1} \cdot \frac{1}{1 - A_{ocn,0}} \sum_{j=1}^4 A_{ocn,j} \exp\left(\frac{-t}{\tau_{ocn,j}}\right), \quad (2.1.13)$$

⁴ The sediment interaction is not included in the R01 experiment (Georg Hooss, personal communication).

where the scaling term $\frac{1}{1 - A_{ocn,0}}$ is simply obtained from $\frac{(1 - A_{ocn,0}) + A_{ocn,0}}{1 - A_{ocn,0}}$ and the highest turnover term corresponding to $A_{ocn,0}$ has been dropped. By comparing the modified IRF (equation (2.1.13)) with the box model solution for the composite layer (equations (2.1.7)), the following relationships can be derived:

$$\lambda_j = \frac{1}{\tau_{ocn,j}}, \text{ with } j = 1, \dots, 4, \quad (2.1.14)$$

$$r_{\delta,init,j} \cdot g_{1,j} = e_{\delta,init,1} \cdot \frac{A_{ocn,j}}{1 - A_{ocn,0}}. \quad (2.1.15)$$

Equation (2.1.14) indicates $\lambda_4 = 0$.

At this point, only the relative relationships among the unknowns can be obtained. To complete the analogy between the box model solutions and the IRF, we must fix one more unknown, namely the depth of the mixed layer as follows. CO₂ dissolved in the ocean exists in different chemical forms (CO₂(aq), H₂CO₃, HCO₃⁻, and CO₃²⁻), the sum of which is collectively termed the Dissolved Inorganic Carbon (DIC). The fractional change in the atmospheric CO₂ partial pressure can be related to the fractional change in the DIC concentration in the mixed layer by using the Revelle factor, ξ , as follows:

$$\frac{c_{atm}(t)}{\bar{c}_{atm}^{pre}} = \xi \cdot \frac{[DIC(t)]_{mix} - [\overline{DIC}]_{mix}^{pre}}{[DIC]_{mix}^{pre}}. \quad (2.1.16)$$

The denominators express the preindustrial (or background) amounts while the numerators express the perturbed amounts. \bar{c}_{atm}^{pre} and $c_{atm}(t)$ denote the preindustrial (594 GtC in equation (37) of Hooss et al. (1999)) and perturbed fractions of the atmospheric carbon load, respectively. $[\overline{DIC}]_{mix}^{pre}$ and $[DIC(t)]_{mix}$ denote the DIC concentrations during the preindustrial period (2.0809 mol/m³ in equation (37) of Hooss et al. (1999)) and at time t , respectively. Note that $[DIC(t)]_{mix}$ is the total DIC including its preindustrial fraction. Here the Revelle factor is assumed to be a preindustrial constant value (= 9.25401 in equation (37) of Hooss et al. (1999)). This assumption is valid under a small perturbation (subsection on carbonate chemistry). $[DIC(t)]_{mix}$ is expressed as

$$[DIC(t)]_{mix} - [\overline{DIC}]_{mix}^{pre} = \frac{c_{mix}(t)}{Area_{ocn} \cdot h_{mix}}, \quad (2.1.17)$$

where $c_{mix}(t)$, $Area_{ocn}$, and h_{mix} are the perturbed carbon amount in the mixed layer, the area of the world ocean (= 3.62×10^{14} m² in equation (37) of Hooss et al. (1999)), and the global-mean

depth of the mixed layer, respectively. Under a small perturbation, the atmosphere-mixed layer equilibrium condition leads to

$$\frac{c_{mix}(t)}{c_{atm}(t)} = \frac{A_{ocn,0}}{1 - A_{ocn,0}}. \quad (2.1.18)$$

Based on equations (2.1.16), (2.1.17), and (2.1.18), the following relationship can be derived:

$$h_{mix} = \frac{\xi \cdot \bar{c}_{atm}^{pre}}{Area_{ocn} \cdot [DIC]_{mix}^{pre}} \cdot \frac{A_{ocn,0}}{1 - A_{ocn,0}}. \quad (2.1.19)$$

With a different expression of the equilibrium condition, $\frac{h_{mix}}{h_1} = A_{ocn,0}$, one can derive the following:

$$h_1 = \frac{\xi \cdot \bar{c}_{atm}^{pre}}{Area_{ocn} \cdot [DIC]_{mix}^{pre}} \cdot \frac{1}{1 - A_{ocn,0}}. \quad (2.1.20)$$

Now h_1 can be directly computed from equation (2.1.20).

Therefore, equations (2.1.14), (2.1.15), and (2.1.20) are used to compute 7 unknowns ($h_1, h_2, h_3, h_4, \eta_{1,2}, \eta_{2,3}, \eta_{3,4}$) in the box model dynamic equation (equation (2.1.4)). Once the 7 unknowns are estimated, λ_j , $r_{\delta,mit,j}$, $g_{1,j}$ can be determined. The solutions are numerically computed by iteration as no explicit analytical relationships between the IRF and box model solutions can be derived (Hooss et al., 1999, Appendix E). The parameter values adopted in ACC2 (corresponding to R01 NA in Table 3.2 of Hooss (2001)) are as follow:

$$\begin{pmatrix} h_1 \\ h_2 \\ h_3 \\ h_4 \end{pmatrix} = \begin{pmatrix} 768 \\ 479 \\ 1,299 \\ 2,723 \end{pmatrix} \text{ in m}, \quad (2.1.21)$$

$$\begin{pmatrix} \eta_1 \\ \eta_2 \\ \eta_3 \end{pmatrix} = \begin{pmatrix} 19.30 \\ 10.33 \\ 7.23 \end{pmatrix} \text{ in year}^{-1}. \quad (2.1.22)$$

h_{mix} is estimated to be 73 m.

The atmosphere-mixed layer equilibrium assumption has been extensively used because the shortest lifetime in the IRF requires the box model to combine the atmosphere and the mixed layer. If the model run time step is further reduced, the atmosphere and the mixed layer have to be separated and the equilibrium assumption would no longer be valid.

- Carbonate Chemistry

In estimating the box model parameters by using the IRF, the Revelle factor is assumed to be constant, implying that the relative abundances of the carbonate species are kept unchanged and ensuring that the atmospheric CO₂ concentration change always affects the ocean CO₂ uptake linearly. However, in reality, the rate of ocean CO₂ uptake is saturated with rising atmospheric CO₂

concentration because the ocean buffers against the pH drop (Figures 2.3 and 2.4). This buffering mechanism is provided by the dissociate carbonate species functioning as weak acids. In the following, we dynamically describe the thermodynamic equilibria for the carbonate species. The addition of the explicit thermodynamic equilibria extends the validity of the model beyond the linear range of the calibration with IRF; the valid upper range has been extended from the doubling to the quadruple of the preindustrial CO₂ concentration (Hooss, 2001).

When a CO₂ molecule in the atmosphere (CO₂(g)) is dissolved in the seawater, H₂O molecules cluster around the CO₂ molecule, a process termed electrostriction, resulting in the production of CO₂(aq). Approximately 0.1% of CO₂(aq) is turned into carbonic acid (H₂CO₃) but both are collectively expressed as CO₂(aq) for convenience below.



CO₂(aq) progressively dissociates to aqueous ions of HCO₃⁻ and CO₃²⁻ as described in the following chemical equations.



DIC is defined as

$$[\text{DIC}] = [\text{CO}_3^{2-}] + [\text{HCO}_3^-] + [\text{CO}_2(\text{aq})]. \quad (2.1.26)$$

The particular CO₂ molecular structure and the resulting affinity to H₂O molecules explain why CO₂ accounts for a disproportionately large fraction of gases dissolved in the seawater relative to the fraction in the atmosphere. These also explain the large capacity of CO₂ storage in the ocean, but the multiple dissociation of CO₂(aq) is another important factor. The CO₂ dissociation allows more than 90% of the carbon in the seawater to be present as aqueous ions, which are not directly bounded by the CO₂ pressure equilibrium at the air-sea surface. However, this ocean's carbon storage capacity is not without limit; increasing CO₂ concentration acidifies the ocean, resulting in less CO₂ dissociation (in other words, the reactions in equation (2.1.24) and (2.1.25) are pushed to backward) (Figure 2.2). The chain of the chemical equations (equations (2.1.23) – (2.1.25)) provides the buffering effect of the ocean pH ($= -\log_{10}[\text{H}^+]$) against the change in the atmospheric CO₂ concentration. Thus, the sensitivity of the ocean CO₂ uptake to the air-sea CO₂ pressure difference becomes low under rising atmospheric CO₂ concentration. Dissolution of calcium carbonate does play a role in the buffering by providing CO₃²⁻ to lock additional H⁺, but this process is not

included in ACC2 and its implication is discussed in the last subsection of this section.

The following reactions also contribute to the buffering against the pH change:



Thus, the Total Alkalinity (TA), essentially expressing the buffering ability of the seawater against the change in pH, can be written as

$$[\text{TA}] = 2[\text{CO}_3^{2-}] + [\text{HCO}_3^-] + [\text{B(OH)}_4^-] + [\text{OH}^-] - [\text{H}^+]. \quad (2.1.29)$$

Weak acids containing phosphate, silicate, ammonia, and others are omitted because of their low concentrations.

Now, the thermodynamic equilibria for the foregoing reactions (equations (2.1.23) – (2.1.25), (2.1.27), and (2.1.28)) can be written as follows:

$$\text{pCO}_2 = \frac{1}{K_0^*} [\text{CO}_2(\text{aq})], \quad (2.1.30)$$

$$[\text{H}^+][\text{HCO}_3^-] = K_1^* [\text{CO}_2(\text{aq})], \quad (2.1.31)$$

$$[\text{H}^+][\text{CO}_3^{2-}] = K_2^* [\text{HCO}_3^-], \quad (2.1.32)$$

$$[\text{H}^+][\text{OH}^-] = K_w^*, \quad (2.1.33)$$

$$[\text{H}^+][\text{B(OH)}_4^-] = K_B^* [\text{B(OH)}_3]. \quad (2.1.34)$$

pCO_2 denotes the partial pressure of atmospheric CO_2 .⁵ The shift in the thermodynamic equilibria for $\text{CO}_2(\text{aq})$, HCO_3^- , and CO_3^{2-} under changing pH is shown in Figure 2.2.

K_0^* is the inverse of the Henry's constant (3.265×10^{-2} mol/kg/atm in Hooss (2001, p.95)). K_1^* , K_2^* , K_w^* , and K_B^* are the associated thermodynamic equilibrium constants (9.709×10^{-7} mol/kg, 6.903×10^{-10} mol/kg, 6.152×10^{-15} mol²/kg², and 1.835×10^{-9} mol/kg,

⁵ Although the partial pressure is a term used interchangeably with the mole fraction here, the mole fraction is a more consistent property with altitude. To be precise, pCO_2 represents the fugacity of atmospheric CO_2 . The relationship between the partial pressure and the fugacity is similar to that between the concentration and the activity (or effective concentration) in aqueous solutions. The fugacity approaches the partial pressure in dilute mixtures as the activity approaches the concentration in dilute solutions. The fugacity of the atmospheric CO_2 at present is smaller than the partial pressure by merely 0.7% (Zeebe and Wolf-Gladrow, 2001, pp. 61–67). Thus, the distinction between the partial pressure and fugacity is not critical in the discussion here.

respectively, in Bacastow (1981, p.101) obtained from Keeling (1973)). The preceding values are used to compute $[\overline{\text{DIC}}]_{\text{mix}}^{\text{pre}}$ and the Revelle factor for the box model parameter estimation ($h_1, h_2, h_3, h_4, \eta_{1,2}, \eta_{2,3}, \eta_{3,4}$) (Hooss et al., 1999, p.19). Note that the actual values implemented in the GAMS code are scaled with different units. The current estimates of the thermodynamic constants are somewhat different. The examples of the estimates today for K_0^* , K_1^* , K_2^* , and K_w^* are 3.746×10^{-2} mol/kg/atm, 1.119×10^{-6} mol/kg, 7.970×10^{-10} mol/kg, and 2.380×10^{-14} mol²/kg², respectively, at 15°C at the salinity of 35 in Mackenzie and Lerman (2006, Table 5.2) calculated based on Zeebe and Wolf-Gladrow (2001, pp.255-258 and 266-267). The current estimate of K_w^* in particular is larger by a factor of 4 than the old estimate. The actual thermodynamic constants used in ACC2 to characterize the carbonate system are temperature dependent and shown in the next subsection.

The asterisks in superscript mean that the effects of electrostatic interactions among charged solutes, which are important in solution with high ion concentrations such as seawater, are taken into account in these constants. The well-hydrated strong electrolytes have only long-range nonspecific electrostatic interactions while the not-well-hydrated weak electrolytes have short-range specific interactions resulting in the formation of ion pairs and complex ions (Millero, 2006, Chapters 4 and 7). The effective concentrations influencing the chemical reactions, called activities, are smaller in seawater than the ideal stoichiometric concentrations. Because the ion species are defined in stoichiometric concentrations in ACC2, the effects of the electrostatic interactions must be reflected in the equilibrium constants.

The total boron concentration is assumed to be constant ($= 4.09 \times 10^{-4}$ mol/liter in Bacastow (1981) and Hoffert et al. (1981))⁶, based on the fact that the rate of main Boron removal due to oceanic mineral-water reactions has been balanced with the rate of Boron input from the continents on our time scale (Harriss, 1969). That is,

$$[\text{B(OH)}_4^-] + [\text{B(OH)}_3] = 4.09 \times 10^{-4} \text{ (mol/liter)}. \quad (2.1.35)$$

So far the carbonate system has a total of ten variables: pCO_2 , [DIC], $[\text{CO}_2(\text{aq})]$, $[\text{HCO}_3^-]$, $[\text{CO}_3^{2-}]$, $[\text{H}^+]$, $[\text{OH}^-]$, $[\text{B(OH)}_3]$, $[\text{B(OH)}_4^-]$, and TA with eight constraints (equations (2.1.26) and (2.1.29) – (2.1.35)).⁷ Additional two constraints to characterize the carbonate system come from the

⁶ The thermodynamic equilibria of the carbonate species in ACC2 are not so sensitive to the total boron concentration when it changes $\pm 10\%$ (results not shown).

⁷ It is commonly known that characterization of the carbonate system requires the estimates of two of the following four measurable quantities: pH, TA, [DIC], and pCO_2 (Park, 1969; Millero, 2006,

specifications for pCO₂ and TA. First, the atmospheric CO₂ concentration is fixed at 277 ppm in 1750 (Etheridge et al., 1996) and iteratively computed in the following years in the model. Second, as a first order assumption, the mean total alkalinity is maintained at a constant value of 2.435×10⁻³ mol-equivalent/liter (Bacastow, 1981; Hoffert et al., 1981)⁸ because a significant amount of carbonate precipitation or dissolution or addition of alkalinity from land did not occur during the historical period of the model run (Mackenzie and Lerman, 2006, p.136) and is assumed negligible for next hundreds of years. An implication of the TA assumption can be seen from the condition of electroneutrality that the electrical charges of the ions susceptible to H⁺ (that is, TA) must be balanced with those not susceptible (that is, major ions) in the following.

$$\begin{aligned}
 & 2[\text{CO}_3^{2-}] + [\text{HCO}_3^-] + [\text{B}(\text{OH})_4^-] + [\text{OH}^-] - [\text{H}^+] \\
 & = [\text{Na}^+] + [\text{K}^+] + 2[\text{Mg}^{2+}] + 2[\text{Ca}^{2+}] - [\text{Cl}^-] - 2[\text{SO}_4^{2-}]
 \end{aligned} \tag{2.1.36}$$

Equation (2.1.36) shows that the constant TA assumption confirms the conservation of the major ions. Conversely it also indicates that the concentration of the total major ions determines TA, in which the composition of the alkalinity species is allowed to change. Thus, the TA assumption greatly simplifies the characterization of the carbonate system (see carbonate pump in subsection on limitation).

With pCO₂ and TA fixed, [DIC] and pH are numerically calculated in ACC2 using equations (2.1.37) and (2.1.38). This approach is essentially the same with the predecessor model ICM, but ACC2 implements the simpler equations (equations (2.1.37) and (2.1.38)). pH is given from the solution of [H⁺] of the following equation:

$$[\text{TA}] = \text{pCO}_2 K_0^* \left(1 + \frac{K_1^*}{[\text{H}^+]} + \frac{K_1^* K_2^*}{[\text{H}^+]^2} \right) + \frac{[\text{B}(\text{OH})_4^-] + [\text{B}(\text{OH})_3]}{1 + \frac{[\text{H}^+]}{K_B^*}} + \frac{K_w^*}{[\text{H}^+]} - [\text{H}^+]. \tag{2.1.37}$$

The solution for [DIC] is then expressed as a function of [H⁺] as follows:

$$[\text{DIC}] = \text{pCO}_2 K_0^* \left(1 + \frac{K_1^*}{[\text{H}^+]} + \frac{K_1^* K_2^*}{[\text{H}^+]^2} \right). \tag{2.1.38}$$

The foregoing results are implemented to the atmosphere-ocean box model in Section 2.1.4.

Chapter 7).

⁸ This value above is consistent with the box model parameter estimation. This value is slightly larger than 2.29 to 2.38×10⁻³ mol-equivalent/liter (Takahashi, 1989) and the global alkalinity distribution as functions of Sea Surface Temperature (SST) and Sea Surface Salinity (SSS) (Lee et al., 2006). However, a separate analysis indicated that the thermodynamic equilibria of the carbonate species in ACC2 are not so sensitive to the assumed representative value of the alkalinity when it is within the literature range (results not shown).

- Temperature Feedback to Ocean CO₂ Uptake

In the section above, the thermodynamic dependence on the ocean buffering effect is introduced. We now implement the temperature dependence by redefining the thermodynamic constants as functions of the mixed layer temperature. The thermodynamic constants are sensitive to in-situ temperature (Figure 2.3) and pressure but the pressure dependence is not important in the mixed layer. ACC2 adopted the following dissociation constants based on a number of laboratory experiments and field measurements (Millero, 1995; Millero et al., 2006; other references therein).

$$\ln K_0^* = \ln K_0^0 + A_0 \cdot S_{mix} \quad (2.1.39)$$

$$\ln K_0^0 = -60.2409 + 93.4517 \cdot \left(\frac{100}{T_{mix}} \right) + 23.3585 \ln \left(\frac{T_{mix}}{100} \right)$$

$$A_0 = 0.023517 - 0.023656 \left(\frac{T_{mix}}{100} \right) + 0.0047036 \left(\frac{T_{mix}}{100} \right)^2$$

$$pK_1^* - pK_1^0 = A_1 + B_1/T_{mix} + C_1 \cdot \ln T_{mix} \quad (2.1.40)$$

$$pK_1^0 = -126.34048 + 6320.813/T_{mix} + 19.568224 \ln T_{mix}$$

$$A_1 = 13.4191 \cdot \sqrt{S_{mix}} + 0.0331 \cdot S_{mix} - 5.33 \times 10^{-5} \cdot S_{mix}^2$$

$$B_1 = -530.123 \cdot \sqrt{S_{mix}} - 6.103 \cdot S_{mix}$$

$$C_1 = -2.06950 \cdot \sqrt{S_{mix}}$$

$$pK_2^* - pK_2^0 = A_2 + B_2/T_{mix} + C_2 \cdot \ln T_{mix} \quad (2.1.41)$$

$$pK_2^0 = -90.18333 + 5143.692/T_{mix} + 14.613358 \ln T_{mix}$$

$$A_2 = 21.0894 \cdot \sqrt{S_{mix}} + 0.1248 \cdot S_{mix} - 3.687 \times 10^{-4} \cdot S_{mix}^2$$

$$B_2 = -772.483 \cdot \sqrt{S_{mix}} - 20.051 \cdot S_{mix}$$

$$C_2 = -3.3336 \cdot \sqrt{S_{mix}}$$

$$\ln K_B^* = A_B \cdot \frac{1}{T_{mix}} + B_B + C_B \cdot \ln T_{mix} + D_B \cdot T_{mix} \quad (2.1.42)$$

$$A_B = 8966.90 - 2890.51 \cdot \sqrt{S_{mix}} - 77.942 \cdot S_{mix} + 1.726 \cdot S_{mix}^{1.5} - 0.0993 \cdot S_{mix}^2$$

$$B_B = 148.0428 + 137.194 \cdot \sqrt{S_{mix}} + 1.62247 \cdot S_{mix}$$

$$C_B = -24.4344 - 25.085 \cdot \sqrt{S_{mix}} + 0.2474 \cdot S_{mix}$$

$$D_B = 0.053105 \cdot \sqrt{S_{mix}}$$

$$\ln K_w^* = \ln K_w^0 + A_w \cdot \sqrt{S_{mix}} + B_w \cdot S_{mix} \quad (2.1.43)$$

$$\ln K_w^0 = 148.9802 - 13847.26/T_{mix} - 23.6521 \ln T_{mix}$$

$$A_w = -5.977 + 118.67/T_{mix} + 1.0495 \ln T_{mix}$$

$$B_w = -1.615 \times 10^{-2}$$

$\ln x$ is a logarithmic function of x having natural base. px is defined as $\text{px} = -\log_{10} x$ (just as pH). S_{mix} denotes the average salinity of the mixed layer, the value of which is fixed at a representative global-mean estimate of 34.76 (Hoffert et al., 1981). The fixed salinity assumption is consistent with the fixed TA assumption discussed previously because TA is equivalent to the charge balance of the conservative ions (equation (2.1.36)) (Zeebe and Wolf-Gladrow, 2001, p.48). Note that the thermodynamic constants are also not so sensitive to the salinity when it is varied between 1.02 and 1.03 (results now shown). T_{mix} is a representative temperature of the ocean mixed layer (in Kelvin), parameterized with the preindustrial temperature of the mixed layer, T_{mix}^{pre} , and a damping factor, γ , to attenuate the change in surface air temperature change over the ocean,

$\delta T_{ocn-air}(t)$, to the mixed layer temperature change as follows:

$$T_{mix}(t) = T_{mix}^{pre} + \gamma \cdot \delta T_{ocn-air}(t) \quad (2.1.44)$$

The value of $\delta T_{ocn-air}(t)$ is computed by the climate component DOECLIM (Section 2.3). If the IRF is rather employed for temperature calculation, the global-mean temperature change computed from IRF is instead used in equation (2.1.44) (First paragraph of Section 2.3). The values of the preindustrial mixed layer temperature T_{mix}^{pre} and the temperature damping factor γ are estimated in the ACC2 inverse calculation.

The concentration quantities in ACC2 are defined with the molar units of mol/L while the thermodynamic constants are preferably defined with the gravimetric units of mol/kg because they are not dependent on the temperature and pressure. Conversions between the units to define

concentrations and thermodynamic constants are made by using the average seawater density of 1.025 kg/L (Hoffert et al., 1981). One should not be confused between molality (or *molal* concentrations; mol/kg-H₂O) and molarity (or *molar* concentration; mol/L) (Zeebe and Wolf-Gladrow, 2001, pp. 251-253; Mackenzie and Lerman, 2006, p.124).

The functions for K_1^* and K_2^* above are taken from Millero et al. (2006) and the others from Millero (1995) and other references therein. The functions for K_1^* and K_2^* in Millero et al. (2006) were obtained from the measurements in real seawater. They are the replacements for the earlier functions in Millero (1995) based on artificial seawater, which would require further corrections on ion pairing to use as thermodynamic constants (F. Millero, personal communication, September 28, 2006). The functions for K_B^* and K_w^* (Millero, 1995) are also obtained from artificial water, but the corrections for ion pairing are not necessary because the reactions of Mg²⁺ and Ca²⁺ with B(OH)₄⁻ and OH⁻ are include in the artificial seawater measurements (F. Millero, personal communication, October 13, 2006). The K_1^* and K_2^* functions appearing in the abstract in Millero et al. (2006) should be used. The same functions in Millero et al. (2006, Table 5) contain some editorial errors (F. Millero, personal communication, October 13, 2006). Although different functions for K_1^* and K_2^* are shown in Millero (2006, Chapter 7.3), the functions in Millero et al. (2006) should be used (F. Millero, personal communication, September 28, 2006). There are various different estimates of the thermodynamic constants available, which are extensively discussed in Zeebe and Wolf-Gladrow (2001, pp.251-270). The largest factor giving rise to the differences in the thermodynamic constant values is the different pH scales⁹ (Zeebe and Wolf-Gladrow, 2001, Table 1.1.4).

- Limitations for Ocean CO₂ Uptake in ACC2

Of the three major mechanisms of the ocean's control on the atmospheric CO₂ content (solubility pump, carbonate pump, and soft tissue pump) (Mackenzie and Lerman, 2006, pp.305-309), the solubility pump is partly modelled and the soft tissue and carbonate pumps are not at all modelled in ACC2. Although it was shown that describing only the thermodynamic equilibria of carbonate species as we modelled is a valid first-order approach (Maier-Reimer et al., 1996), it is worth discussing the implication of neglecting the other mechanisms, in the high time of mounting concern over the thermohaline circulation collapse¹⁰, ocean acidification, and coral bleach¹¹. Care must be

⁹ Note that three different pH scales are in operation in aquatic chemistry, leading to the situation where the absence of the scale specification would give rise to a large uncertainty in [DIC] (Zeebe and Wolf-Gladrow, 2001, pp. 53–61). Here the seawater scale pH is used for consistency with the functions of the thermodynamic constants discussed in the section of temperature feedback (Millero, 1995; Millero et al., 2006). Technically, the seawater scale pH is defined as $-\log_{10}([H^+]_F + [HSO_4^-] + [HF])$. Also note that $[H^+]_F$ represents H₃O⁺ and H₉O₄⁺ (bonded to a water molecule) as virtually no free protons present in aqueous solutions.

¹⁰ A partial or complete paucity of the thermohaline circulation in the future is projected in various

taken when one uses $[H^+]$ for ocean acidification studies – one needs to be aware of the relevant assumptions of the modelling approach of the ocean carbon cycle in the following.

The solubility pump is the ocean CO_2 uptake driven by the partial CO_2 pressure difference between the atmosphere and the ocean. The rate of the solubility pump depends on the atmospheric CO_2 concentration and its rate of change (Stocker and Schmittner, 1998). The solubility pump is more intense over the cold water. ACC2 accounts for the influence of the solubility pump from the temperature change by calculating the thermodynamic equilibria explicitly, but it cannot resolve the influence from the thermohaline circulation and the ocean ventilation (Falkowski et al., 2000). As a significant portion of ocean CO_2 uptake occurs in the North Atlantic and the Southern Ocean, the rate of the large scale circulation, if it were to change abruptly in the future, is an important factor controlling the ocean CO_2 uptake.

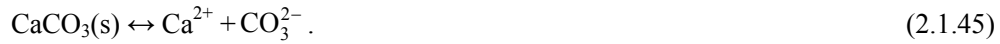
The carbonate pump is the downward transport of calcium minerals, which are formed by calcifying organisms at the surface¹² accompanied with the evasion of atmospheric CO_2 . In ACC2, the dissolution and precipitation of carbonate mineral are neglected, but such an approach is justifiable on our spatial and time scale (Ernst Maier-Reimer, personal communication, November 21, 2006). Over the longer time scale, limestone rocks play a role of stabilizing the pH of the global ocean. When CO_2 is invaded from the atmosphere (equations (2.1.23) and (2.1.24)), H^+ is generated. Then H^+ is locked up with CO_3^{2-} (equation (2.1.25)), resulting in a production of HCO_3^-

modelling studies although the level of the threshold is not well-known. The simplified thermohaline circulation model (Zickfeld and Bruckner, 2003) can be readily coupled with ACC2 although the change in the thermohaline circulation needs to be reflected to the ocean CO_2 uptake.

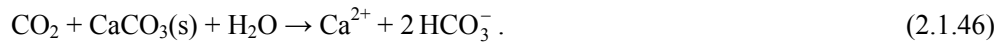
¹¹ The atmospheric CO_2 increase leads to more CO_2 invasion to the ocean, resulting in the ocean acidification. The intensification of the ocean acidification is reported for low latitude regions (Kleypas et al., 1999) and high latitude regions (Orr et al., 2005) by modelling approaches. It has also been shown by laboratorial studies that elevated atmospheric CO_2 concentration results in decreased calcification of coccolithophorids (Riebesell et al., 2000). The acidification is projected to penetrate substantially below the mixed layer beyond 2150 (Caldeira and Wickett, 2003). The impacts of the ocean acidification to coral reef and calcifying organisms are reported in Ruttimann (2006).

¹² In actuality, the thermodynamic equilibrium, $[Ca^{2+}][CO_3^{2-}] = K_{sp}^*$, is far from attained by the biogenical formation of calcium carbonate occurring in two different crystalline forms: ‘calcite’ produced by coccolithophorids and foraminifera and ‘aragonite’ produced by pterpods. As a result, the surface ocean is substantially supersaturated with respect to both calcite and aragonite. The state of supersaturation is maintained down to a depth of some hundreds meter with respect to aragonite and some thousands meter with respect to calcite (Mackenzie and Lerman, 2006, Figure 5.5D). Coccolithophorid blooms affect the surface pCO_2 as suggested by observations (Denman and Pena, 2000) although the mechanism leading to the onset and collapse of the blooms is not well-known from modelling studies (Tyrrell and Taylor, 1996). Their responses to climate change are different across calcifying species and their global implication is uncertain (Ridgwell et al., 2006).

(backward reaction of equation (2.1.25)). CO_3^{2-} is supplemented from the dissolution of limestone as follows:



The net reaction is summarized in the following buffering reaction (Holland, 1978):



Therefore, upon CO_2 invasion from the atmosphere, calcium carbonate is dissolved because of the drop in pH; calcium carbonate provides an additional buffering mechanism against the pH change. However, the provision of such a negative feedback would lead to merely a few percent change in the carbon flux (Maier-Reimer et al., 1996) and would not be consistent with the constant alkalinity assumption in ACC2.

Furthermore, the precipitation of calcium carbonate (equation (2.1.46)) competes with the primary production (equation (2.1.47)) because both of the processes consume CO_2 .



The soft tissue pump is the downward transport of Particulate Organic Matter (POC), which is originally formed by photosynthesis in the euphotic zone accompanied with the invasion of atmospheric CO_2 .¹³ The soft tissue pump is important on the millennium or longer time scale. It is estimated that, without the soft tissue pump, the atmospheric CO_2 concentration would be 150 to 200 ppm higher at present (Falkowski et al., 2000). The soft tissue pump is implicit in the atmospheric CO_2 concentration calculated in ACC2 although the marine biota itself is not modelled. The metabolism of the marine ecosystem is comparable in size with the terrestrial ecosystem (Field et al., 1998). Thus, the influence of the future climate change to the marine ecosystem metabolism is expected to have a significant implication for the global carbon cycle. In fact, satellite observations between 1997 and 2005 demonstrate that, in the midst of the warming accompanied with the reduction in surface ocean mixing, the ocean biological productivity decreased in the tropics and mid-latitudes because of the nutrient limitation (Bahrenfeld et al., 2006; Doney, 2006). However, on the time scale of ACC2, there is no evidence to suggest the relationship between the climate change and the biological productivity.

The role of the coastal zone (up to a depth of 200 m) is significant for the competition between calcium carbonate dissolution and primary production because 10 to 30% of the marine

¹³ Because of the mineralization all the way to the deep ocean, the bottom waters are supersaturated by approximately 30% with respect to CO_2 . Such a disequilibrium is maintained by vertical stratification of the ocean. The trapped CO_2 in the deep ocean returns back to the surface mainly in the Equatorial Pacific by being conveyed through the thermohaline circulation. The pCO_2 in the upwelling region is higher than other ocean (Maier-Reimer and Hasselmann, 1987)

primary production and 45% of the carbonate accumulation occurs in the coastal zone (Mackenzie et al., 2004).¹⁴ The coastal zone is not treated as a separate entity in ACC2 and even GCMs. The coastal zone together with the river system has been studied more in the biogeochemical approach (e.g. Andersson et al. (2006)). The spatial inhomogeneity of the river system and coastal zone hardly reconciles with the GCM approach.

The arguments above are convoluted as processes involving the ocean carbon cycle are highly interlinked. To summarize, the ocean carbon cycle approach in ACC2 does not describe the change in the large-scale ocean circulation, the dissolution/precipitation of the calcium carbonate, and marine biota. Nevertheless, ACC2 describes the inorganic carbon chemistry in the ocean including its temperature dependence, the most important oceanic mechanism for determining the atmospheric CO₂ concentration. Thus, the characterization of the carbonate system (including pH) in ACC2 serves as first-order estimates.

2.1.3. Land CO₂ Uptake

- Land Box Model

ACC2 uses a box model approach to describe the CO₂ uptake associated with the NPP and the CO₂ release associated with the heterotrophic respiration; i.e. the Net Ecosystem Production (NEP) of the global terrestrial biosphere is modelled here. In ACC2, the NPP is controlled by the atmospheric CO₂ concentration and the heterotrophic respiration controlled by the surface air temperature over land. While only the fertilized carbon was modelled in the predecessor model ICM, both the background (preindustrial) and fertilized carbon is modelled in ACC2 because the temperature dependence of the heterotrophic respiration should apply for both the background and fertilized carbon.

First, we discuss the land box model without considering the temperature dependence. Thus we discuss only the fertilized carbon in this subsection. In the land box model, all the reservoirs are directly connected to the atmosphere. Thus, the governing equations for the land reservoirs are as follows:

$$\dot{c}_{ter,l}(t) = k_{ter,l} \cdot \delta f_{NPP}(t) - \frac{1}{d_{ter,l}} c_{ter,l}(t), \quad (2.1.48)$$

¹⁴ Highly complex carbonate chemistry takes place in the coastal zone, influenced by the deposition of organic carbon and inorganic nutrient from land, calcification in coral reef, pelagic and benthic ecosystem, and the water exchange with the open ocean. The coastal zone is susceptible to the mobilized carbon due to soil erosion and the nutrient discharge from fertilized land. Owing to these activities of mankind, the metabolism of the coastal zone has been shifted from net autotrophy to net heterotrophy. Although the distinct biogeochemistry in the coastal zone has a sizable impact on the ocean carbon cycle, even the state-of-the-art coupled Earth system model has no provision in treating the coastal zone as a separate entity. Dynamical modelling of the marine ecosystem in the coastal zone is a difficult task due to the insufficient data and knowledge on the relevant processes (Tanaka and Mackenzie, 2005).

$$c_{ter}(t) = \sum_l c_{ter,l}(t). \quad (2.1.49)$$

$c_{ter,l}(t)$ is the amount of the fertilized carbon in reservoir l . l is the index of a land reservoir. The first term of the right side of equation (2.1.48) describes the fertilized NPP (due to the increase in the atmospheric CO₂ concentration). $\delta f_{NPP}(t)$ denotes the global fertilized NPP. $k_{ter,l}$ is a coefficient to relate the global fertilized NPP to the fertilized NPP of each reservoir l . The second term of the right side of equation (2.1.48) describes the release of carbon accumulated due to fertilized NPP. $d_{ter,l}$ is a decay time constant of each of the land reservoirs.

The fertilized NPP, $\delta f_{NPP}(t)$, is further defined as:

$$\delta f_{NPP}(t) = \bar{f}_{NPP}^{pre} \beta_{NPP} \ln \left(\frac{pCO_2(t)}{pCO_2^{pre}} \right). \quad (2.1.50)$$

\bar{f}_{NPP}^{pre} denotes the global preindustrial NPP and is assumed to be 60 GtC/year (Joos et al., 1996) under the quasi-steady state assumption. The CO₂ fertilization effect is parameterized with the beta factor, β_{NPP} , which logarithmically scales the fractional change in the atmospheric CO₂ concentration relative to its preindustrial level (277 ppm). The parameterization above is one of the standard practices in simple terrestrial biosphere models (Gifford, 1980; Friedlingstein et al., 1995). The value of the beta factor is highly uncertain (Table 3.2 for existing estimates) and is estimated in the inverse calculation. The actual response of plants to the atmospheric CO₂ concentration change varies with species and other environmental conditions (see subsection on the limitation on for land CO₂ uptake in ACC2).¹⁵

Equation (2.1.48) has a Green's function solution as follows:

$$c_{ter}(t) = \int_{-\infty}^t \delta f_{NPP}(t') \sum_l k_{ter,l} \exp \left(-\frac{t-t'}{d_{ter,l}} \right) dt'. \quad (2.1.51)$$

Under a special circumstance where a pulse change in the atmospheric CO₂ concentration is imposed at the time 0, equations (2.1.48) and (2.1.49) have the following simpler solution:

$$c_{ter}(t) = \left[\sum_l k_{ter,l} \exp \left(-\frac{t}{d_{ter,l}} \right) \right] \cdot \delta f_{NPP}(0). \quad (2.1.52)$$

The parameters $k_{ter,l}$ and $d_{ter,l}$ are determined based on the IRF explained below.

¹⁵ The CO₂ fertilization effect is demonstrated both theoretically and experimentally (Free-Air CO₂ Enrichment (FACE)), but the plant response to the CO₂ concentration change depends on the functional group (trees > legumes > C₃ grasses in Ainsworth and Long (2004)), photosynthetic pathway (C₃ > C₄ in Ainsworth and Long (2004)), growth conditions (Körner, 2006), other limiting factors (water, temperature, light, and nutrients), and the experimental setup (Long et al., 2004).

- IRF for Land CO₂ Uptake

The temporal trajectory of the respiratory release of the fertilized biomass is expressed in the following IRF based on the Bern-CC model (Joos et al., 1996) (Figure 2.5):

$$\delta f_{NPP}(0) \cdot IRF_{ter}(t) = \delta f_{NPP}(0) \cdot \sum_{j=1}^4 A_{ter,j} \exp\left(-\frac{t}{\tau_{ter,j}}\right), \quad (2.1.53)$$

where the values for the coefficients in the IRF (equation (2.1.53)) are given as

$$\begin{bmatrix} A_{ter,1} \\ A_{ter,2} \\ A_{ter,3} \\ A_{ter,4} \end{bmatrix} = \begin{bmatrix} -0.71846 \\ 0.70211 \\ 0.013414 \\ 0.0029323 \end{bmatrix} \quad \text{and} \quad \begin{bmatrix} \tau_{ter,1} \\ \tau_{ter,2} \\ \tau_{ter,3} \\ \tau_{ter,4} \end{bmatrix} = \begin{bmatrix} 2.18 \\ 2.86 \\ 20 \\ 100 \end{bmatrix}. \quad (2.1.54)$$

The values of the coefficients, $A_{ter,j}$, in equation (2.1.54) are normalized such that the evaluation of the integral of the IRF (equation (2.1.53)) between 0 and ∞ is unity. Note that the maximum release of CO₂ from the terrestrial biosphere is delayed by approximately 2.7 years from the point of perturbation (Figure 2.5).

The time constants, $\tau_{ter,j}$, are chosen to be the equivalent to the overturning time constants of the reservoirs in the parent model (Bern-CC model), which are detritus, ground vegetation, wood, and soil organic carbon, respectively (Joos et al., 1996). However, each of the terms in the IRF can no longer be *physically* interpreted as a biospheric reservoir. In the IRF expression, all the reservoirs can be interpreted to be directly connected to the atmosphere. On the contrary, in the original Bern-CC model, only the vegetation and wood reservoirs are directly connected to the atmosphere; the detritus and soil reservoirs are connected to the vegetation and wood reservoirs. The reservoirs of the land box model are configured to be the same as the IRF, avoiding cumbersome matrix conversion that was necessary for the ocean counterpart. Mathematically, in the IRF expression, the matrix is made diagonal whereas, in the parent model, it would not be so. The difference in the reservoir configuration explains why a negative coefficient $A_{ter,1}$ appears in the IRF (Fortunat Joos, personal communication, January 25, 2007). The same can be seen in the High-Resolution Terrestrial Biosphere Model as implemented in the Community Terrestrial Biosphere Model (HRBM/CTBM) (Meyer et al, 1999, Figure 3).

- Parameter Estimation of Land Box Model

Equation (2.1.53) is equivalent to the *time derivative* of the box model solution (equation (2.1.52)) except for the sign being opposite because equation (2.1.52) describes the carbon contents (not fluxes) of the terrestrial reservoirs. Then, by comparison, the following relationships are derived:

$$d_{ter,l} = \tau_{ter,l}, \quad (2.1.55)$$

$$k_{ter,l} = A_{ter,l} \tau_{ter,l}. \quad (2.1.56)$$

The number of the reservoirs in the box model is now chosen to be four. Therefore, the box model governing equation is

$$\dot{c}_{ter,l}(t) = A_{ter,l} \tau_{ter,l} \delta f_{NPP}(t) - \frac{1}{\tau_{ter,l}} c_{ter,l}(t), \quad l = 1, 2, 3, 4. \quad (2.1.57)$$

One can confirm that $\sum_{l=1}^4 A_{ter,l} \tau_{ter,l}$ is approximately equal to one (compare with equation (2.1.48)). The temperature dependence of the heterotrophic respiration is implemented to equation (2.1.57) in the next subsection.

The land box model can also be expressed as

$$\dot{c}_{ter}(t) = \delta f_{NPP}(t) - \int_{-\infty}^t \delta f_{NPP}(t') \sum_{j=1}^4 A_{ter,j} \exp\left(-\frac{t-t'}{\tau_{ter,j}}\right) dt', \quad (2.1.58)$$

where the second term of the right side of the equation has the Joos' IRF within the integral. However, because the IRF convolution in equation (2.1.58) cannot be directly implemented to the GAMS code, the box model expression of equation (2.1.57) has been derived.

Note that the predecessor models NICCS and ICM make a further equilibrium assumption for the two short-term land reservoirs because their model time steps (5 years) are longer than the lifetimes of these short-term reservoirs (τ_1 and τ_2) (Hooss et al., 1999). The equilibrium assumption is needed to ensure numerical stability in NICCS and ICM. However, the trouble is that the assumption requires an additional term $\frac{dc_{atm}}{dc_1}$ (Hooss et al., 1999, equation (88)), leading to complication in the model implementation. Such an equilibrium treatment is not necessary for ACC2 because of the finer time step of 1 year.

- Temperature Feedback to Land CO₂ Uptake

The temperature feedback is applied to both the preindustrial and fertilized carbon. The preindustrial (or background) carbon needs to be modelled here. The following conditions can be derived from equation (2.1.57):

$$A_{ter,l} \tau_{ter,l} \bar{f}_{NPP}^{pre} = \frac{1}{\tau_{ter,l}} \bar{c}_{ter,l}^{pre}, \quad l = 1, 2, 3, 4. \quad (2.1.59)$$

Because the preindustrial NPP, \bar{f}_{NPP}^{pre} , is fixed at 60 GtC/year, the preindustrial carbon storage of each reservoir, $\bar{c}_{ter,l}^{pre}$, can be determined from equation (2.1.59). Then, the addition of equations (2.1.57) and (2.1.59) gives:

$$\dot{c}_{ter,l}(t) = A_{ter,l} \tau_{ter,l} \left(\bar{f}_{NPP}^{pre} + \delta f_{NPP}(t) \right) - \frac{1}{\tau_{ter,l}} \left(\bar{c}_{ter,l}^{pre} + c_{ter,l}(t) \right) q(t), \quad l = 1, 2, 3, 4, \quad (2.1.60)$$

$$q(t) = Q_{10}^{\frac{\delta T_{land-air}(t)}{10}}. \quad (2.1.61)$$

Q_{10} is a factor, by which the rate of terrestrial respiration increases with a temperature increase of 10°C, assumed to be 2 in many modelling studies. The parameterization using Q_{10} is often used in physiological studies. In ACC2, the value of the Q_{10} factor is determined by the inverse calculation.

Further discussion on the Q_{10} parameterization is provided in the next subsection. $\delta T_{land-air}(t)$ is the change in surface air temperature change over land and is computed by the climate component DOECLIM (Section 2.3). If the IRF is employed to calculate the air temperature, the global-mean temperature change calculated from the IRF is used here. Note that, when $\delta T_{land-air}(t)$ is equal to 0, equation (2.1.60) is equivalent to equation (2.1.57).

- Limitations for Land CO₂ Uptake in ACC2

Although NPP is determined solely by the atmospheric CO₂ concentration in ACC2, various other factors such as the Photosynthetically Active Radiation (PAR), temperature, water availability, nutrient availability, and species composition come into play in reality (Melillo et al., 1993; Goldewijk et al., 1994). The stomata conductance (i.e. openness) is adjusted by the surrounding soil moisture to maintain proper water holding in the plants, influencing the rate of CO₂ uptake. Nitrogen supply is an important factor among others controlling NPP. It is demonstrated by observations that NPP is significantly affected by variations in diffuse radiation (Gu et al., 2003). The geometry of radiation is important for plant productivity because of the light saturation of photosynthesis (Farquhar and Roderick, 2003).

The effect of temperature on NPP is not modeled in ACC2. The relationship between NPP and surface temperature is highly uncertain as indicated by the results of recent coupled GCMs and Earth system Models of Intermediate Complexity (EMIC) intercomparison experiments (Coupled Climate-Carbon Cycle Model Intercomparison project (C⁴MIP)) (Friedlingstein et al., 2006).¹⁶ If the highly uncertain temperature dependence on NPP would be included in the inverse calculation, other

¹⁶ A recent ECHAM5/MPIOM simulation indicates a negative correlation between surface temperature and NPP in the tropics (between 0 and 30 degree in latitude). In the tropics, an increase in temperature leads to higher autotrophic respiration, resulting in a reduction of NPP. In the mid latitudes, on the contrary, the correlation is positive but not strong enough to offset the negative correlation in the tropics. Thus, on a global scale, there is a negative correlation between NPP and surface temperature (Raddatz et al., in press). On the contrary, Meyer et al. (1999) estimate an increase in NPP by 1.6% per 1°C increase in surface temperature. However, both of the results are well within the range of different coupled GCM/EMIC projections (Friedlingstein et al., 2006).

factors controlling NPP discussed above would be explained wrongly by temperature. Therefore, we describe only the CO₂ concentration control on NPP.

Although the heterotrophic respiration in ACC2 is controlled only by the temperature, the actual heterotrophic respiration also depends on the property of the organic matter, the substrate availability, and the soil moisture. Modelling of the temperature sensitivity to soil carbon decomposition is currently under debate (Davidson and Janssens, 2006). Both observations (Tjoelker et al., 2001; Chen and Tian, 2005) and theories (Davidson and Janssens, 2006) indicate that the value of Q10 decreases with increasing soil temperature. Process-based models such as the Lund-Potsdam-Jena Dynamic Global Vegetation Model (LPJ-DGVM) introduce the temperature dependency of Q10 for the soil respiration and the autotrophic respiration (Sitch et al., 2003). However, the temperature-dependency of Q10 is not so important in the global-mean studies such as ACC2 because the large temperature gradient between the tropics and the high latitudes is not modelled.

Note that the importance of the carbon cycle interaction with other element cycles of nitrogen, sulfur, phosphorus, and oxygen are addressed in Ver et al. (1999), demonstrating that an omission of the interactions among element cycles on land leads to a significant underestimate in the future projection of atmospheric CO₂ concentration. However, multi-element cycles are beyond the scope of ACC2 and have not so far been incorporated in the state-of-the-art coupled GCMs.

2.1.4. Coupling of the Atmosphere-Ocean and Land Box Models

The atmosphere-ocean box model and the land box model have been derived above. Now they are coupled in such a way that the four-reservoirs of the land box model are connected to the composite layer of the atmosphere-ocean box model as follows:

$$\dot{c}_{cmp,1}(t) = e(t) - \frac{\eta_2}{h_{mix}} c_{mix}(t) + \frac{\eta_2}{h_2} c_{ocn,2}(t) - \sum_{l=1}^4 \dot{c}_{ter,l}(t), \quad (2.1.62)$$

$$\dot{c}_{ocn,2}(t) = \frac{\eta_2}{h_{mix}} c_{mix}(t) - \frac{\eta_2 + \eta_3}{h_2} c_{ocn,2}(t) + \frac{\eta_3}{h_3} c_{ocn,3}(t), \quad (2.1.63)$$

$$c_{ocn,3}(t) = \frac{\eta_3}{h_2} c_{ocn,2}(t) - \frac{\eta_3 + \eta_4}{h_3} c_{ocn,3}(t) + \frac{\eta_4}{h_4} c_{ocn,4}(t), \quad (2.1.64)$$

$$c_{ocn,4}(t) = \frac{\eta_4}{h_3} c_{ocn,3}(t) - \frac{\eta_4}{h_4} c_{ocn,4}(t), \quad (2.1.65)$$

$$\dot{c}_{ter,l}(t) = A_{ter,l} \tau_{ter,l} \bar{f}_{NPP}^{pre} (1 + \beta_{NPP}) \ln \left(\frac{pCO_2(t)}{\bar{p}CO_2^{pre}} \right) - \frac{1}{\tau_{ter,l}} (c_{ter,l}^{pre} + c_{ter,l}(t)) \cdot Q_{10} \frac{\delta T_{land-air}(t)}{10}. \quad (2.1.66)$$

We elaborate the expression of the anthropogenic carbon content in the mixed layer, c_{mix} , as a function of the anthropogenic carbon content in the composite layer, $c_{cmp,1}$.

Under a small perturbation, fixed thermodynamic equilibria (in other words, a constant Revelle factor) can be assumed. Thus, by using the equilibrated fraction in the mixed layer, $A_{ocn,0}$, indicated from the IRF (equation (2.1.12)), the following expression can be derived.

$$c_{mix} = A_{ocn,0} \cdot c_{cmp,1} \quad (2.1.67)$$

c_{mix} can be described as a function of [DIC] as follows:

$$\bar{c}_{mix}^{pre} + c_{mix} = Area_{ocn} \cdot h_{mix} \cdot [DIC]. \quad (2.1.68)$$

Recall that [DIC] represents the background as well as perturbed carbon concentration. With equations (2.1.38), [DIC] in equation (2.1.68) is replaced with $[H^+]$ and pCO_2 as follows:

$$\bar{c}_{mix}^{pre} + c_{mix} = Area_{ocn} \cdot h_{mix} \cdot pCO_2 \cdot K_0^* \cdot \left(1 + \frac{K_1^*}{[H^+]} + \frac{K_1^* K_2^*}{[H^+]^2} \right). \quad (2.1.69)$$

Similar to equation (2.1.68), c_{atm} can be described as a function of pCO_2 by using equation (2.1.30) as follows:

$$\bar{c}_{atm}^{pre} + c_{atm} = Area_{ocn} \cdot h_{atm} \cdot pCO_2 \cdot K_0^*. \quad (2.1.70)$$

The conservation in the amount of carbon in the atmosphere-mixed layer subsystem is trivially

$$\bar{c}_{cmp,1}^{pre} + c_{cmp,1} = (\bar{c}_{atm}^{pre} + c_{atm}) + (\bar{c}_{mix}^{pre} + c_{mix}). \quad (2.1.71)$$

Finally, from equations (2.1.69) – (2.1.71), the expression for c_{mix} can be derived as follows:

$$\bar{c}_{mix}^{pre} + c_{mix} = \frac{f([H^+])}{1 + f([H^+])} (\bar{c}_{cmp,1}^{pre} + c_{cmp,1}), \quad (2.1.72)$$

where $f([H^+]) = \left(1 + \frac{K_1^*}{[H^+]} + \frac{K_1^* K_2^*}{[H^+]^2} \right) \cdot \frac{h_{mix}}{h_{atm}}$. Equation (2.1.72) can be substituted into c_{mix} in

equation (2.1.62). The estimate of $[H^+]$ is provided by solving equation (2.1.37) with respect to

$[H^+]$. Equation (2.1.37) together with equation (2.1.38) are key equations to compute the carbonate system variables in ACC2.

2.1.5. CO₂ Radiative Forcing

The atmospheric CO₂ abundance is sufficiently high in our time scale such that the saturation of the absorption bands with increasing CO₂ concentration needs to be taken into account. In ACC2, the

CO₂ radiative forcing is estimated using the following logarithmic parameterization (IPCC, 2001, Table 6.2):

$$RF(\text{CO}_2)_t = RF_{2 \times c(\text{CO}_2)_{pre}} \cdot \frac{\ln(c(\text{CO}_2)_t / c(\text{CO}_2)_{pre})}{\ln 2}. \quad (2.1.73)$$

$RF_{2 \times c(\text{CO}_2)_{pre}}$ denotes the 2×CO₂ forcing, that is, the change in the forcing by doubling the atmospheric CO₂ concentration from the preindustrial level, $c(\text{CO}_2)_{pre}$ (= 277 ppm in ACC2). In ACC2, the 2×CO₂ forcing is fixed at 3.7 W/m² (IPCC, 2001, p.357). The parameterization used here is derived from radiative transfer calculation with three-dimensional climatological meteorological input data (Myhre et al., 1998).

2.2. ATMOSPHERIC CHEMISTRY COMPONENT

2.2.1. Overview

A fairly comprehensive set of forcing agents and the parameterization of their atmospheric chemistry (IPCC, 2001; Joos et al., 2001; WMO, 2003; IPCC, 2005) are implemented in ACC2 as summarized in Table 2.1. Importance of implementing atmospheric chemistry is suggested by the strong feedback of the CH₄ concentration on the CH₄ lifetime associated with OH oxidation (IPCC, 2001, p.250) and also by the photochemical production of tropospheric O₃ from CH₄ oxidation (Brasseur et al., 1999, pp.527-528; IPCC, 2001, p.365). The direct CH₄ radiative forcing is 0.33 W/m², with an indirect forcings of 0.11 W/m² due to OH feedback and an additional indirect forcing of 0.11 W/m² due to tropospheric O₃ production (Lelieveld et al., 1998). The parameterization of CH₄ (lifetime of 8.4 years (IPCC, 2001, p.248)) is better reproduced in ACC2 than in the predecessor model ICM because of the finer temporal resolution of ACC2.

In ACC2, each of the emissions of GHGs, aerosol precursors, and pollutants is separated into the anthropogenic and natural emissions. The historical anthropogenic emissions of CH₄ and N₂O are estimated in the inverse calculation (Section 3.4). The anthropogenic emissions are fixed at zero in 1750 in accordance with the preindustrial quasi-steady state assumption (Section 2.1). The historical natural emissions of CH₄ and N₂O are assumed to be constant over time and estimated in the inverse calculation. Such estimates are also used as the natural emissions of CH₄ and N₂O for future projections. For halocarbons and SF₆, the historical emission in the literatures is not used in ACC2 – respective concentrations are directly prescribed to the model. The historical anthropogenic emissions of CO, NO_x (NO and NO₂), VOC, and SO₂ are based on EDGAR-HYDE 1.3 (van

Aardenne et al., 2001). The future anthropogenic emissions of all of these gases (further separated into energy-related and non-energy-related emissions) use SRES (Nakićenović et al., 2000). The new future emission estimates of IPCC (2005, Chapter 11) is not so far utilized here.

In both the past and future modes of ACC2, the concentrations of CH₄ and N₂O are dynamically calculated by single-reservoir box models. The change in the concentration of each of these gases is generally described as

$$\dot{c} = \frac{e}{\nu} - \frac{c}{\tau}, \quad (2.2.1)$$

where c , e , ν , and τ are the global-annual-mean atmospheric concentration, the sum of the anthropogenic and natural emissions, the unit conversion factor between mass and concentration, and the lifetime of a gas, respectively. The concentrations of SF₆ and halocarbons are also dynamically calculated using equation (2.2.1) in the future mode but they are simply prescribed in the past mode (references in Sections 2.2.5 and 2.2.6). The unit conversion factors ν for these gases are estimated from a linear function of their molecular weights¹⁷ and such estimates are shown in Table 2.2.

The expression for the lifetime τ in equation (2.2.1) is different among the gases. For SF₆ and halocarbons without containing any H atom, their lifetimes are simply expressed as constants (Table 2.2) because their removal processes are virtually independent of OH. On the contrary, for halocarbons containing at least one H atom, their lifetimes are scaled with the OH concentration because they are predominantly depleted by OH (equation (2.2.11)) (IPCC, 2005, p.167). For CH₄ and N₂O, which influence the background chemical processes in complex manners, their lifetimes¹⁸ are given as functional forms (equations (2.2.3) and (2.2.6)). Note that, when a gas has multiple sinks, its lifetime with respect to each of the sinks τ_k ($k=1,2,\dots,n$) holds an inverse relationship with the total lifetime τ_{total} as follows:

$$\frac{1}{\tau_{total}} = \frac{1}{\tau_1} + \frac{1}{\tau_2} + \dots + \frac{1}{\tau_n}. \quad (2.2.2)$$

Equation (2.2.2) is used to define the lifetime of CH₄ in equation (2.2.3).

In both the past and future modes of ACC2, the concentration of OH is directly related to the CH₄ concentration and the pollutant emissions without using dynamic relationships (IPCC, 2001, Table 4.11). Such a treatment is owing to the fact that the OH consumption by oxidizing CH₄ and

¹⁷ The estimates of ν in equation (2.2.1) for various GHGs are compiled in Fuglestvedt and Berntsen (1999, Table 2), most of which are taken from IPCC (1996). These estimates were not updated in IPCC (2001). Fuglestvedt and Berntsen's estimates suggest that the unit conversion factors have a linear relationship with the respective molecular weights as follows: $\nu(A) = 0.1716 \times mw(A)$. $mw(A)$ denotes the molecular weight for gas A.

¹⁸ More precisely, it is the perturbation time (IPCC, 2001, Tables 4.3 and 4.5) and the adjustment time (Seinfeld and Pandis, 2006, p.1048), which is the lifetime taking account of the chemical feedbacks.

CO and the OH formation from NO_x (via O₃ production) are very fast reactions. In the future mode, the concentration of the tropospheric O₃ is similarly treated because of the fast O₃ production from NO_x and the O₃ consumption to yield OH (IPCC, 2001, Table 4.11). The lifetimes of OH and tropospheric O₃ are in the order of minutes and weeks, respectively (Brasseur et al., 1999, Table 13.3; IPCC, 2001, Table 4.1(a) and p.361). In the past mode, the concentration of the tropospheric O₃ is not explicitly provided – the radiative forcing of the total O₃ (Hansen and Sato, 2004) is prescribed.

The relationships between the concentrations and the radiative forcings of the GHGs are parameterized differently depending on their atmospheric concentrations and radiative interferences. The radiative forcings of SF₆ and halocarbons are linearly related to their atmospheric concentrations by scaling with their radiative efficiencies¹⁹ (equations (2.2.12) and (2.2.13)) (IPCC, 2005, p.158 and 163). On the other hand, because CH₄ and N₂O take substantial fractions of the atmospheric gas composition and significantly perturb the Earth's radiation budget, the saturation and overlap effects of the absorption bands for CH₄ and N₂O have to be taken into account to describe their radiative forcings.²⁰ The saturation effects for CH₄ and N₂O are parameterized as square root functions of the associated concentrations (equations (2.2.4) and (2.2.7)) (IPCC, 2001, Table 6.2).²¹ The overlap effects for CH₄ and N₂O are parameterized in an elaborated function shown in equation 2.2.5 (IPCC, 2001, Table 6.2). Although the overlap effects with the other GHGs (IPCC, 2005, Figure 2.6) are not parameterized, the overlap effect with HFC-134a may become important in the future as the concentration of HFC-134a is projected to rise in SRES. Both the past and future modes of ACC2 use the same parameterizations consistently for the radiative forcings of CH₄, N₂O, SF₆, and halocarbons.

In ACC2, the total aerosol forcings are represented by three types of aerosol forcings: 1) direct forcing due to sulfate aerosols of anthropogenic origin, 2) direct forcing due to Organic Carbon (OC) and Black Carbon (BC) emitted from biomass burning and fossil fuel burning, and 3) indirect forcing due to all the anthropogenic aerosols. In both the past and future modes of ACC2, these aerosol forcings are parameterized as functions of the emissions of SO₂ and pollutants (equations (2.2.30) – (2.2.32)).

The radiative forcing is separated further into the radiative forcing over land and the ocean. They are used in the climate component DOECLIM. The land-ocean separations of the radiative forcing involve different assumptions depending on the spatial distributions of the individual

¹⁹ A radiative efficiency is a radiative forcing per concentration unit, typically W/m²/ppb.

²⁰ O₃ and H₂O also play a pivotal role in the saturation and overlap effects of absorption bands in particular when one looks at the natural greenhouse effects. However, such effects for O₃ have not been parameterized (Sections 2.2.8 and 2.2.9). H₂O is not taken as a radiative forcing agent (IPCC, 2001, Appendix 6.1) and rather considered as a feedback (Section 2.2.11).

²¹ CO₂ also plays a substantial role in the atmospheric radiative interference. The radiative forcing for CO₂ is parameterized as a logarithmic function of the CO₂ concentration (Section 2.1.5).

radiative forcings. The details and assumptions for such land-ocean separations are discussed in Section 2.3.5, together with the description of DOECLIM.

In the following, the non-CO₂ GHGs and other radiative agents are discussed in detail. Below, IPCC (2001) and WMO (2003) are mainly referred, where further references are found.

2.2.2. CH₄

CH₄ has been the second most important GHGs after CO₂ during the Anthropocene in terms of the radiative forcing. The IPCC estimate of the CH₄ radiative forcing is 0.48 W/m² in the year 2005 (IPCC, 2007, Figure SPM-2). The atmospheric observation indicates that the CH₄ concentration has stabilized for the past several years. Although the exact reason is unknown, this can be caused by the decrease in the natural emission and/or the increase in the atmospheric OH concentration offsetting the persisting rise in the anthropogenic CH₄ emission. The recently debated CH₄ emission from plants (Keppeler et al., 2006) influences the budgetary calculation. SRES showing the future increase in the CH₄ emission indicates that CH₄ will continue to be an important radiative agent for the next one hundred years. If a proper mitigation strategy is put into place, the atmospheric CH₄ concentration in principle decreases quickly because of its atmospheric lifetime time (8.4 years (IPCC, 2001, p.248)). However, a growing concern lies in a possible large-scale CH₄ emission from the permafrost and ocean sediments depositions.²²

CH₄ has various emission sources such as waste treatment, energy use, biomass burning, termites²³, landfills, rice paddies, CH₄ hydrate, ruminants²⁴, natural wetlands, and ocean (IPCC, 2001, Table 4.2; Lowe, 2006). The literature estimates of the natural CH₄ emission encompass a substantial range.²⁵

²² CH₄ hydrate is stored in the Siberia permafrost and in the ocean sediments. The CH₄ hydrate deposit in the ocean sediments is estimated to be as enormous as 10⁷ TgC (Suess et al., 1999). The current emission from CH₄ hydrate is merely 10 Tg/year (Lelieveld et al., 1998) because most of the methane is oxidized before reaching the surface (Dickens, 2001). However, there are carbon isotopic records suggesting the occurrence of a gigantic CH₄ release from marine hydrate, resulting in 5 to 10°C warming in the surface temperature during the initial Eocene thermal maximum, approximately 55 million years ago (Dickens, 2004). This CH₄ release is triggered by submarine volcanoes indicated by seismic observations (Svensen et al., 2004). A gigantic CH₄ release can also be triggered by large-scale submarine landslides (Nisbet, 1998). The CH₄ emission from the permafrost hydrate is expected to rise as the global warming affects the polar region in an amplified manner.

²³ Termites are white ants relying on bacteria in their stomachs for digestion and producing CH₄ as a by-product of their digestive processes.

²⁴ Ruminants are hooved animals such as cows, goats, sheep, camels, and antelope that digest their foods in two steps, first by eating the raw material and regurgitating a semi-digested form known as cud, then eating the cud.

²⁵ The estimate of the CH₄ emission from natural wetlands has a large uncertainty (IPCC, 2001, Table 4.2; Lowe, 2006). The global distribution of natural wetlands is still not well-known although efforts have been made by various workers initiated by Matthews and Fung (1987) performing an

Such diversified sources are collectively represented as anthropogenic and natural emissions in ACC2. The time series of the historical anthropogenic CH₄ emission is obtained from the inverse calculation. SRES is used as the anthropogenic CH₄ emission in the future mode. In ACC2, the magnitude of the natural CH₄ emission is assumed to be constant over time and is estimated by the inverse calculation. Such an estimate is transferred from the past mode to the future mode and used as the future natural emission of CH₄.

Much simpler are the CH₄ sinks, which are reaction with OH, lost to the stratosphere, and soil uptake (diffusion and microbial oxidation (Ridgwell et al., 1999)). The lifetime of CH₄ is estimated to be 9.58 years with respect to OH depletion²⁶, 120 years with respect to stratospheric loss, and 160 years with respect to soil uptake (IPCC, 2001, p.248).

In the ACC2 past and future modes, the CH₄ lifetime is described as follows (compare equation (2.2.2)):

$$\frac{1}{\tau(\text{CH}_4)_t} = \frac{r(\text{OH})_t}{\tau(\text{CH}_4)^{\text{OH}}} + \frac{1}{\tau(\text{CH}_4)^{\text{stratosphere}}} + \frac{1}{\tau(\text{CH}_4)^{\text{soil}}}. \quad (2.2.3)$$

$\tau(\text{CH}_4)^{\text{stratosphere}}$ and $\tau(\text{CH}_4)^{\text{soil}}$ in equation (2.2.3) correspond to the last two CH₄ sinks and have the values of 120 and 160 years, respectively. The first term on the right side of equation (2.2.3) is the parameterization of the dominant CH₄ sink due to reaction with OH, having an inverse relationship with the *relative* concentration of OH, $r(\text{OH})_t$, that is, the ratio of OH concentration in year t to that in year 2000. The CH₄ lifetime with respect to OH depletion, $\tau(\text{CH}_4)^{\text{OH}}$, is estimated in the inverse calculation (Table 3.2).

The expression of the CH₄ lifetime (equation (2.2.3)) is put into the dynamic equation (equation (2.2.1)) to calculate the CH₄ concentration in both the ACC2 past and future modes. The unit conversion factor between mass in Tg(CH₄) and concentration in ppb, $\nu(\text{CH}_4)$ in equation

extensive observational campaign. Soil moisture data such as the output of the BIOME4 model (Kaplan, 2001; Kaplan, 2002) can be in principle combined with digital terrain models such as Global DTM5 by GETECH and GTOPO30 by US Geological Survey to infer the global wetland distribution. Kaplan formulates the following criteria for a grid cell to be ‘qualified’ as a wetland: 1) Grid cell slope is less than 15%, 2) Soil moisture is more than 65%. However, this approach is criticized by the ignorance of the soil texture (Stefan Hagemann, personal communication). There are substantial discrepancies among model simulations in soil moisture. Furthermore, there are no general patterns in the temporal changes in soil moisture, according to the Global Soil Wetness Project (Dirmeyer et al., 1999, Figure 13), and no long-term reliable observation-based global soil moisture dataset (Zhao and Dirmeyer, 2003, p.1). The estimate of wetland area by using passive microwave techniques has yet to be available. At present, the Global Soil Wetness Project II does not show a global compilation of remotely sensing wetland area.

²⁶ This lifetime estimate with respect to OH depletion refers to the CH₄ concentration of 1745 ppb in the year 1998 (IPCC, 2001, p.248, Figure 4.1, and Table 4.3), based on contemporary CTMs in OxComp showing the range from 6.5 to 13.8 years (IPCC, 2001, p.250 and Table 4.3).

(2.2.1), is 2.746 Tg(CH₄)/ppb.

The first term in equation (2.2.3) and equation (2.2.10) (OH concentration defined as a function of the CH₄ concentration) are combined to express the feedback of the CH₄ concentration on its own lifetime as follows. An increase in the CH₄ concentration is quashed by its oxidation reaction with OH, leading to the formation of CO. Both CO and CH₄ suppress OH, which is the major sink of CH₄. As a result, the CH₄ lifetime lengthens when the CH₄ concentration increases (e.g. Seinfeld and Pandis, 2006, pp.1048-1049). The adjustment time is 12 years in contrast to the lifetime with respect to OH depletion being 9.58 years (IPCC, 2001, pp.251-252; Seinfeld and Pandis, 2006, p.1048). This CH₄ feedback adds 25% to 35% more to the direct CH₄ forcing (IPCC, 2001, p.365). The additional CH₄ feedback to the production of tropospheric O₃ (Section 2.2.1) is accounted for directly in the parameterization of the tropospheric O₃ radiative forcing (equation (2.2.21)).

The radiative forcing for CH₄ is parameterized as follows:

$$RF(\text{CH}_4)_t = 0.036 \cdot \left(\sqrt{c(\text{CH}_4)_t} - \sqrt{c(\text{CH}_4)_{pre}} \right) - \text{Overlap}(c(\text{CH}_4)_t, c(\text{N}_2\text{O})_{pre}) - \text{Overlap}(c(\text{CH}_4)_{pre}, c(\text{N}_2\text{O})_{pre}). \quad (2.2.4)$$

Note that 0.036 in equation (2.2.4) is a coefficient for the parameterization and different from the radiative efficiency of CH₄. The overlap function, $\text{Overlap}(M, N)$, in equation (2.2.4) is defined in the following:

$$\text{Overlap}(M, N) = 0.47 \cdot \ln \left(1 + 2.01 \times 10^{-5} (M \cdot N)^{0.75} + 5.31 \times 10^{-15} M (M \cdot N)^{1.52} \right). \quad (2.2.5)$$

$c(\text{CH}_4)_{pre}$ and $c(\text{N}_2\text{O})_{pre}$ are the respective concentrations in 1750 (710 ppb and 273 ppb, respectively) (Table 3.1). The square roots of the right side of equation (2.2.4) take into account the saturation effect of the CH₄ absorption bands with increasing atmospheric CH₄ concentration. The overlap function parameterizes the radiative effects of the absorption bands that are shared by CH₄ and N₂O between wavelengths of about 10 μm and 7.5 μm.²⁷ The above parameterization of the CH₄ radiative forcing is taken from IPCC (2001, Table 6.2) based on radiative transfer calculations of Myhre et al. (1998).

²⁷ It should be noted that the overlaps of the absorption bands for HFC-134a, CFC-12, HCFC-22, CH₄, and N₂O can significantly affect the associated radiative forcings in future projections; however, they are not parameterized in ACC2, or in any simple model that exists at present. Computation of such effects of absorption band overlaps on the radiative forcing require a sensitivity analysis using a radiative transfer model such as MODTRAN.

2.2.3. N₂O

N₂O is currently the fourth important GHG after CO₂, CH₄, and CFC-12 in terms of the radiative forcing. The IPCC estimate of the radiative forcing due to N₂O in the year 2005 is 0.16 W/m² (IPCC, 2007, Figure SPM-2). N₂O plays a role in the stratospheric O₃ chemistry as a source of NO_x.

The sources of N₂O are cattle and feedlots, industrial sources, biomass burning, agricultural soils, natural soils, ocean (denitrification performed by some specific heterotrophic bacteria in the anoxic environment respiring large amounts of organic matter with the use of nitrate as the electron acceptor), and NH₃ oxidation (IPCC, 2001, Table 4.4). The literature estimates of natural N₂O emission are in a better agreement than those of the anthropogenic N₂O emission – in particular, the emission from agricultural soil due to nitrogen fertilizer applications are quite uncertain.²⁸

In ACC2, similar to the treatment for CH₄, the past anthropogenic N₂O emission is obtained from the inverse calculation. The future anthropogenic N₂O emission adopts SRES. The magnitude of the natural N₂O emission is assumed to be constant and is estimated by the inverse calculation. Such an estimate is transferred from the past mode to the future mode and used as the future natural emission of N₂O.

The sink of N₂O is known to be lost to the stratosphere and photodissociation. The N₂O concentration has a negative feedback on its own lifetime (IPCC, 2001, Table 4.5) although it is weaker than the similar feedback for CH₄. An increase in the N₂O concentration leading to an increase in the production of stratospheric NO_y²⁹ results in a catalytic destruction of O₃, letting more ultraviolet radiation reach the troposphere, which eventually destroys N₂O (Prather, 1998; Seinfeld

²⁸ The agricultural N₂O emission occurs from microbial nitrification and denitrification in the soil (Conrad, 1996) and in the ocean sediments (Shaffer and Rönner, 1984). High N₂O production is associated with denitrification. Denitrification rates are spatially and temporally highly variable across ecosystem types, whereas nitrification is a relatively constant process in many ecosystems. The importance of the agricultural emission suggested from the isotopic N data in Arctic ice cores (Bernard et al., 2006). The future N₂O emission from agricultural sources is expected to increase drastically particularly from the tropics where the terrestrial ecosystem is often phosphorus-limited (Hall and Matson, 1999). A first-order emission model is developed by Bouwman (1996): $E = 1 + 0.0125 \times F$, which relate the nitrous oxide emission (E) from fertilized fields to the N fertilizer applied (F) with E and F in kg(N)/ha/yr. This equation consists of background emission of 1 kg(N)/ha/yr with a range from -0.6 to +3.2 kg(N)/ha/yr and fertilizer-induced emission of 1.25% of fertilizer application rate with a range from 0.25 to 2.25%. This equation was statistically derived from observational dataset and is adequate for global analysis. Note that the sample database excludes data on leguminous crops because these crops usually do not receive N fertilizer but take up N through symbiotic N fixation. The equation above is independent of fertilizer types. Bouwman's equation does not account of the factors controlling the rate of denitrification: soil moisture and temperature, the amount of mineralizable organic carbon, soil oxygen availability, concentrations of nitrate and ammonium, and soil pH. The rate of denitrification is also affected by the availability of O₂, NO₃, and organic-C.

²⁹ Odd-nitrogen gases (NO, NO₂, NO₃, N₂O₅, HONO, HO₂NO₂, and HNO₃) in the stratosphere (e.g. Prather, 1998)

and Pandis, 2006, p.1048). The N₂O negative feedback in the N₂O-NO_y-O₃ system is assessed by using 2-D stratospheric chemical models and parameterized in the expression of the N₂O lifetime used in ACC2:

$$\tau(\text{N}_2\text{O})_t = \tau(\text{N}_2\text{O})_{2000} \cdot \left(\frac{c(\text{N}_2\text{O})_t}{c(\text{N}_2\text{O})_{2000}} \right)^{-0.046} \quad (2.2.6)$$

$\tau(\text{N}_2\text{O})_{2000}$ is estimated in the inverse calculation (110 years in IPCC (2001, Table 4.5, Prather's estimate)) (Table 3.2). The sensitivity coefficient of -0.046 (IPCC, 2001, Table 4.5, Prather's estimate) implies that the N₂O lifetime systematically decreases by about 0.5% with increasing N₂O concentration by 10%. $c(\text{N}_2\text{O})_{2000}$ is fixed at 330 ppb as equation (2.2.6) is calibrated in the sensitivity experiment (IPCC, 2001, Table 4.5). Note that the expression above is different from that of Joos et al. (2001) using emission rather than concentration and with a different lifetime and sensitivity coefficient.

The expression of the N₂O lifetime (equation (2.2.6)) is substituted into the dynamic equation (equation (2.2.1)) for both the past and future modes. The unit conversion factor $\nu(\text{N}_2\text{O})$ is 4.8 Tg(N)/ppb in the dynamic equation.

The radiative forcing for N₂O is described in ACC2 as follows:

$$RF(\text{N}_2\text{O})_t = 0.12 \cdot \left(\sqrt{c(\text{N}_2\text{O})_t} - \sqrt{c(\text{N}_2\text{O})_{pre}} \right) - \text{Overlap}(c(\text{CH}_4)_{pre}, c(\text{N}_2\text{O})_t) - \text{Overlap}(c(\text{CH}_4)_{pre}, c(\text{N}_2\text{O})_{pre}). \quad (2.2.7)$$

Note that 0.12 in equation (2.2.7) is a coefficient for the parameterization and different from the radiative efficiency of N₂O. $c(\text{CH}_4)_{pre}$ and $c(\text{N}_2\text{O})_{pre}$ are the respective concentrations in 1750 (710 ppb and 273 ppb, respectively). Similar to the formulation of CH₄ forcing, the square roots of the right side of equation (2.2.7) express the saturation effect of the N₂O absorption bands with increasing N₂O concentration. The parameterization of the N₂O forcing above is based on IPCC (2001, Table 6.2).

2.2.4. OH

OH is the main cleansing agent in the atmosphere; it oxidizes many kinds of GHGs and pollutants *radically* in an order of seconds. Although OH is not a radiatively active agent, its role of oxidizing CH₄ has a substantial impact on the CH₄ radiative forcing, thus termed “an indirect radiative agent.”

The primary source of OH is the photodissociation of O₃ by solar UV in the troposphere.



O(¹D) is an oxygen atom that is electronically excited while O(³P) is an oxygen atom at ground state (e.g. Seinfeld and Pandis, 2006, pp.84-85). OH is also produced from NO_x (equation (2.2.16)). The sink of OH is the depletion by the oxidation reactions mostly with CH₄ and CO and also with HFCs, HCFCs, and VOCs in the troposphere. The above mentioned nature of the OH sources and sinks leads to the high spatial and temporal variability of OH concentration and the short atmospheric lifetime in the order of minutes.³⁰

There is a large uncertainty in the temporal evolution of the OH concentration. Although the decrease in the OH concentration for the past decade was shown based on the CH₃CCl₃ concentration (Prinn et al., 2001), other modelling studies currently indicate that the global-mean OH concentration has varied little since the preindustrial time because the anthropogenic emissions led to two opposite effects that inadvertently compensated each other (higher CO and CH₄ emissions leading to OH depletion vs. higher NO emission leading to OH formation) (Lelieveld et al., 2004). As for the future projection, the evidences point to a decrease in the OH concentration, but the uncertainty ranges in the projections are too large to reach anything conclusive (IPCC, 2001, p.263; Penkett et al., 2003, p.98). Recent relevant debates are summarized in IPCC (2005, Section 2.2.2).

In ACC2 the relative concentration of OH, $r(\text{OH})$, rather than the absolute concentration, is defined as follows: $r(\text{OH})_t = \frac{c(\text{OH})_t}{c(\text{OH})_{2000}}$, where $c(\text{OH})_t$ and $c(\text{OH})_{2000}$ are the absolute OH concentrations in the year t and 2000, respectively.

In earlier models (e.g. ICM and the model of Harvey (1997)), the OH concentration is not explicitly defined and rather implicit in the definition of CH₄ lifetime as a positive feedback to its own. In ACC2, the relative concentration of OH is explicitly defined as a function of the concentration of CH₄ and the emissions of pollutants NO_x, CO, and VOC in the following.

$$\begin{aligned} \ln(r(\text{OH})_t) &= \ln(c(\text{OH})_t) - \ln(c(\text{OH})_{2000}) \\ &= -0.32\{\ln(c(\text{CH}_4)_t) - \ln(c(\text{CH}_4)_{2000})\} + 0.0042(e(\text{NO}_x)_t - e(\text{NO}_x)_{2000}) \\ &\quad - 0.000105(e(\text{CO})_t - e(\text{CO})_{2000}) - 0.000315(e(\text{VOC})_t - e(\text{VOC})_{2000}) \end{aligned} \quad (2.2.10)$$

As discussed in Section 2.2.1, the concentration of OH is not dynamically described as equation (2.2.1) because of the extremely fast turnover time. $c(\text{CH}_4)_{2000}$ in equation (2.2.10) is the posterior estimate of the atmospheric CH₄ concentration obtained from the ACC2 inverse calculation. This estimate is transferred from the past mode to the future mode and used in the future mode. The

³⁰ The OH concentration is estimated based on the burden and the trend of CH₃CCl₃ (lifetime: 4.8 years (IPCC, 2001, Table 4.1a)), which reacts only with OH. The accuracy of the OH concentration estimates depends on the measurements calibration and proxy emission figures. The recent decline in the CH₃CCl₃ emission under the Montreal Protocol provided an opportunity to better constrain the OH concentration (Penkett et al., 2003, pp.96-97), but the illegal and unaccounted emissions preclude an accurate determination of the OH concentration (Lelieveld et al., 2004).

estimates of the pollutant emissions are provided as scenarios in both the past and future modes.³¹ The role of O₃ in the OH production is implicitly expressed in the terms for pollutants. Equation (2.2.10) is derived from the OxComp workshop where 11 state-of-the-art chemistry transport models ran using a set of emission scenarios between 2000 and 2100 (Joos et al., 2001, p.893; IPCC, 2001, pp. 267-268). The coefficients in equation (2.2.10) are obtained by applying various linear assumptions to the results of the OxComp workshop.³² In ACC2, the relationship in equation (2.2.10) is also assumed to be valid during the historical period.

2.2.5. Halocarbons

Halocarbons are atmospheric halogen- (such as fluorine, chlorine, bromine, and iodine) containing carbon compounds. Halocarbons modelled in ACC2 (Table 2.2) are classified according to their molecular structures into the following categories: perfluorocarbons (PFCs), hydrofluorocarbons (HFCs), chlorofluorocarbons (CFCs), chlorocarbons (carbon tetrachloride (CCl₄) and methyl chloroform (CH₃CCl₃)), halons, hydrochlorofluorocarbons (HCFCs), and monomethyl halides (methyl chloride (CH₃Cl) and methyl bromide (CH₃Br)). CFCs, chlorocarbons, halons, HCFCs, and monomethyl halides are Ozone-Depleting Substances (ODSs), which release chlorine and bromine³³ photochemically in the stratosphere, destroying the stratospheric O₃ in effect. The latest IPCC estimate of the radiative forcing of all the halocarbons is 0.34 W/m² in the year 2005 (IPCC, 2007, Figure SPM-2). CFC-12 is the third strongest GHG after CO₂ and CH₄ in terms of the radiative forcing. Although the radiative interference of each of the halocarbons is currently weak, several halocarbons have extremely long lifetimes on the order of thousands of years, suggesting a need for stringent emission measures. ACC2 describes a total of 29 halocarbon species (all the 27 halocarbons³⁴ in SRES, CH₃Cl, and CH₃Br), in contrast to the predecessor ICM describing only four

³¹ The estimates of pollutant emissions and SO₂ emission in the year 2000 are not consistent in EDGAR-HYDE 1.3 (van Aardenne et al., 2001) and SRES (Nakićenović et al., 2000). However, the literature values are directly adopted to ACC2 without modification.

³² The coefficient of -0.32 in the first term of the right side of the equation was derived from the fact that a 10% increase in the CH₄ concentration in the year 2000 leads to a decrease in the tropospheric OH concentration by 3.0% in 2100 relative to the OH concentration in 2000 (IPCC, 2001, Table 4.11). The coefficient of 0.0042 in the second term of the right side of the equation was obtained from the fact that maintaining the NO_x emission level in the year 2000 throughout the model run leads to a decrease in the OH concentration by 40% in 2100 relative to that in 2000. The rates of the NO_x emission in 2000 and 2100 are 32.5 Tg(N)/yr and 110.0 Tg(N)/yr, respectively. Similarly, the coefficients of -0.000105 and -0.000315 in the third term of the right hand of the equation are obtained (see IPCC (2001, Table 4.11)).

³³ Fluorine is not released in the stratosphere because of its strong bond with carbon. Iodine is a more powerful O₃ depletion agent than chlorine and bromine, but iodine-containing gases are largely removed in the troposphere (WMO, 2003, Q.12).

³⁴ The emission scenarios of halocarbons in SRES (Nakićenović, 2000, Section 5.4.3.) are based on Fenhann (2000). The particular set of 27 species are chosen from over 100 species discussed in WMO (2003) based on the contribution to climate forcing (Jörgen Fenhann, personal

halocarbon species (CFC-11, CFC-12, HCFC-22, and HFC-134a).

Most of the halocarbons are predominantly of industrial origin. The main source of PFCs is the anode effect during aluminum production (Fenhann, 2000). CFCs, HCFCs, and HFCs are emitted from various industrial usages such as semiconductor device fabrication, refrigerants, foam blowing agents, solvents, aerosol spray propellants, fire extinguishing agents, and chemical reagents (Haloalkane in Wikipedia, November 27, 2006). Halons are primarily used in fire extinction (WMO, 2003, 1.21). The principal source of CCl₄ is the CFC production (WMO, 2003, 1.21). CH₃CCl₃ is predominantly used as a solvent and cleansing agent (WMO, 2003, 1.62). CH₃Cl is predominantly of natural origin (ocean and biomass burning) and its main anthropogenic source is coal combustion (WMO, 2003, Table 1-10). CH₃Br is also mainly of natural origin (ocean, fumigation, and biomass burning) and its anthropogenic source is the combustion of leaded gasoline (WMO, 2003, Table 1-9).

The reductions in the emissions of PFCs and HFCs are addressed in the Kyoto Protocol. The emissions of ODSs are regulated by the Montreal Protocol.³⁵ The concentrations of CFCs have dropped abruptly since they are effectively controlled by the Montreal Protocol. The declines in the CFC concentrations are accompanied by rising HCFC concentrations. Under the Montreal Protocol, HCFCs are temporal replacements of CFCs. The Montreal Protocol requires the production and consumption of HCFCs to end in developed nations by 2030 and developing nations by 2040 (WMO, 2003, questions, p.29). HCFCs are 1 to 15% as effective as CFC-12 in depleting stratospheric O₃ because they are removed primarily by tropospheric OH. All HCFC emissions are eventually replaced with HFC emissions. The concentrations of HFCs are rising (WMO, 2003, Figure 1-20). Exceptionally, the concentration of HFC-23, by-product of HCFC-22, has already risen substantially (Oram et al., 1998). In all the six SRES cases, HFC-134a is expected to be the most radiatively important halocarbon in 2100 (0.129 W/m² under SRES A1b: IPCC, 2001, Table 6.14). The concentrations of halons are still increasing because of the substantial reserves in fire extinguishing equipment in spite of the cessation of their production in developed nations (WMO, 2003, questions, p.31). The concentrations of PFCs are rising (WMO, 2003, Figure 1-21).

The past mode of ACC2 uses the concentrations of the SRES 27 halocarbon species

communication, November 27, 2006). Among the halocarbon species that should be included for future projection is trifluoromethyl sulphur pentafluoride (SF₃CF₃) (Sturges et al., 2000), a hybrid of SF₆ and halocarbon, which is still a minor forcing agent at present but has the largest radiative efficiency (W/m²/ppt) ever found in the atmosphere (IPCC, 2001, p.254). Hydrofluoroethers (HFEs) are recently considered as replacements for CFCs (IPCC, 2005, p.151).

³⁵ The Montreal Protocol has been virtually ratified globally (191 countries as of November 14, 2006). The Protocol has been progressively strengthened with Adjustments and Amendments in London in 1990, Copenhagen in 1992, Vienna in 1995, Montreal in 1997, and Beijing in 1999. Substances banned in the Protocol are practically of purely anthropogenic origin except for monomethyl halides. Ultimately, the use of the major human-produced O₃-depleting gases will be phased out and effective stratospheric chlorine will slowly decay, reaching pre-ozone-hole values in the mid-21st century (WMO, 2002, Questions. p.28). The Montreal Protocol proves a resounding success with most of the states being compliant to it so far.

obtained from various station measurements and ice core records: CFCs, chlorocarbons, halons (except for halon2402), and HCFCs (except for HCFC-123) (Sturrock et al., 2002; WMO, 2003); Halon2402 (Fraser et al., 1999); CF₄ (Oram, 1998; Harnisch et al., 1999); C₂F₆ (Oram, unpublished); HFC-23 (Oram, 2000; WMO, 2003, Table 1-12); HFC-125 (WMO, 2003, Table 1-12); HFC-134a (Montzka et al. 1999; WMO, 2003, Table 1-12), and HFC-152a (IPCC, 2001, Figure 4.3; WMO, 2003, Table 1-12). The concentrations of the remaining halocarbon species (C₄F₁₀, HFC-32, HFC-43-10mee, HFC-143a, HFC-227a, HFC-236a, HFC-245a, and HCFC-123) are negligible. To validate the halocarbon concentration data, we extensively used the Carbon Dioxide Information Analysis Center (CDIAC) Data Set DB-1001 ALE (Prinn et al., 2000; <http://cdiac.ornl.gov/>).

For the future mode of ACC2, the concentrations of the 27 halocarbon species are dynamically calculated by using equation (2.2.1). The emission scenario (SRES)³⁶ and the unit conversion factors ν (Table 2.2) are prescribed to equation (2.2.1). The expression of the lifetime of a halocarbon τ depends on its molecular composition as explained below.

Generally, halocarbons containing one or more H atoms (HCFCs, HFCs, and monomethyl halides) are effectively removed by the reaction with OH in the troposphere (IPCC, 2001, p.245; Seinfeld and Pandis, 2006, p.48). Halocarbons not containing any H atom (PFCs, CFCs, and halons) do not react with OH and tend to be long-lived. They can only be destroyed in the stratosphere and above photochemically. Such a ‘rule of thumb’ is manifested (but not without exception) by the Arrhenius A-factors for the reactions of halocarbons with OH (Jet Propulsion Laboratory (JPL), 2003) expressing the reaction rates, showing that halocarbons with at least one H atom tend to react with OH slower than halocarbons without a H atom.

In ACC2 the lifetime of a halocarbon k containing at least one H molecule is defined as

$$\tau(\text{halo}_k)_t = \frac{\tau(\text{halo}_k)_{2000}}{r(\text{OH})_t}. \quad (2.2.11)$$

For a fully halogenated halocarbon, its lifetime is not scaled with the OH concentration and is simply given as a constant (IPCC, 2005, p.167). Estimates for the halocarbon lifetimes are obtained from WMO (2003, Table 1.6), many of which have been updated from IPCC (2001, Table 6.7). In contrast, Joos et al. (2001) assume that the lifetimes of the fully fluorinated species (SF₆, CF₄, C₂F₆, and C₄F₁₀) are independent of the OH concentration whereas the lifetimes of other halocarbons are scaled with the OH concentration. In ICM, all the four halocarbons are independent of the OH concentration.

³⁶ Noted that WMO (2003) discusses the projections of the mixing ratios for 16 species of halocarbon up to the year 2100 (Table 1-16 in p.1.66). However, these mixing ratios are only for the Ab baseline scenario defined in WMO (2003). These projections do not refer to Fenhann (2000). Projections of WMO (2003) and those of IPCC (2001) are not directly comparable; the emission scenarios to calculate the WMO concentration paths are not found. The new future emission estimates in IPCC (2005, Chapter 11) have not been considered in ACC2.

In the future mode of ACC2, the expression for the lifetime (equation (2.2.11)) or a constant lifetime is prescribed in equation (2.2.1) to calculate the halocarbon concentration. The value of the unit conversion factor ν in equation (2.2.1) for each of the halocarbons is shown in Table 2.2. In the past mode of ACC2, the concentration estimates for halocarbons are simply adopted to the model without dynamical calculations.

The radiative forcing of a halocarbon l is simply given as a linear function of its concentration as follows (IPCC, 2005, p.158 and 163):

$$RF(\text{halo}_l)_t = RE(\text{halo}_l) \cdot c(\text{halo}_l)_t. \quad (2.2.12)$$

$RE(\text{halo})$ denotes the radiative efficiency of a particular halocarbon l (Table 2.2). The preindustrial concentration for each of the SRES 27 halocarbons is ignored in equation (2.2.12) as these halocarbons are practically of natural origins.

In addition to the 27 species, the concentrations of CH_3Cl and CH_3Br , primarily of natural origins, are calculated in the future mode of ACC2. The initial CH_3Cl and CH_3Br concentrations in 2000 are given as 536 ppt and 8.1 ppt, respectively (WMO, 2003, Table 1-1). The fixed natural emissions (3684.7 Gg for CH_3Cl ; 192 Gg for CH_3Br) are optimized to explain the Ab mixing ratio scenario (WMO, 2003, Table 1-16) with the respective lifetimes (1.3 year for CH_3Cl ; 0.7 year for CH_3Br (WMO, 2003, Table 1-6)). Inclusion of these two species is required to estimate the Effective Equivalent Stratospheric Chlorine (EESC), which is used to calculate the stratospheric O_3 forcing. CH_3Cl and CH_3Br are rather weak radiative forcing agents with a low radiative efficiency of 0.01 $\text{W/m}^2/\text{ppb}$ (WMO, 2003, Tables 1-6) and thus are not included for the calculation of radiative forcing.

2.2.6. SF_6

SF_6 is a potent GHG characterized by its long atmospheric lifetime, the emission of which is controlled by the Kyoto Protocol. SF_6 does not react with OH and its only sink is photolysis or ion reactions in the mesosphere (IPCC, 2001, p.254). The source of SF_6 is predominantly industrial: the use for insulation of high-voltage electrical equipment and oxidation prevention of molten magnesium (Maiss et al., 1996; Fenhann, 2000). A small amount of SF_6 is emitted naturally from the outgassing from fluorites (CaF_2), giving rise to the background concentration of 0.01 ppt (Harnisch and Eisenhauer, 1998). The anthropogenic emission of SF_6 began to increase in the 1950s. The rising emission trend has been reversed in 1996 in response to the rise in the market price (Maiss and Brenninkmeijer, 1999). The SF_6 concentration in 2000 was 4.7 ppt (WMO, 2003, p.1.61). A global emission reduction by up to 90% is feasible if appropriate measures are taken for replacement and maintenance of relevant equipment (Maiss and Brenninkmeijer, 1998).

In the ACC2 past mode, we use the SF_6 concentration records based on Harnisch and Eisenhauer (1998) between the year 1750 and 1940, Maiss and Brenninkmeijer (1998) between 1953

and 1996, and CDML flask measurements between 1997 and 2000 (<http://www.cmdl.noaa.gov/infodata/ftpdata.html>). In the future mode of ACC2, the SF₆ concentration is dynamically calculated (equation (2.1.1)) on the basis of a SF₆ emission scenario in SRES. The SF₆ lifetime $\tau(\text{SF}_6)$ is fixed at 3200 years (WMO, 2003, Table 1-6)). The unit conversion factor $\nu(\text{SF}_6)$ is 25.1 (Table 2.2).

The radiative forcing of SF₆ is linearly related to its concentration as follows:

$$RF(\text{SF}_6)_t = RE(\text{SF}_6) \cdot c(\text{SF}_6)_t, \quad (2.2.13)$$

where the SF₆ radiative efficiency $RE(\text{SF}_6)$ is 0.52 W/m²/ppb (WMO, 2003, Table 1-6). The effect of the natural background SF₆ concentration is sufficiently small to be neglected in calculating the SF₆ radiative forcing.

2.2.7. Pollutants NO_x, CO, and VOC

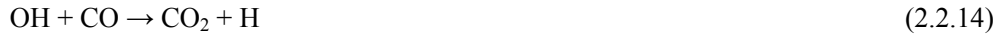
Pollutants do not directly incur discernable changes in the atmospheric radiation budget but indirectly do so by in situ chemical reactions with GHGs, thus called “indirect GHGs.” The direct forcings of CO and VOC are estimated to be merely 0.024 W/m² and 0.015 W/m², respectively (IPCC, 2001, pp.365-366). The emissions of pollutants cause climate and environmental problems (e.g. air quality degradation).

The major sources of NO_x are fossil fuel combustion, biomass burning, soil emission, and lightning (IPCC, 2001, Table 4.8). The sink of NO_x is the atmospheric oxidation of NO₂ by OH. NO is oxidized to NO₂ accompanied by OH production (equation (2.2.16)). NO_x catalyzes the O₃ formation in the troposphere (equations (2.2.14) – (2.2.18)). The sources of CO are CH₄ oxidation, biomass burning, fossil fuel combustion, Non-Methane HydroCarbons (NMHC) oxidation, vegetation, and ocean (IPCC, 2001, Table 4.6). The sinks of CO are predominantly the photochemical depletion involving OH (leading to O₃ formation) and the soil uptake (IPCC, 2001, Table 4.6). The sources of VOC are vegetation, fossil fuel combustion, and biomass burning (IPCC, 2001, Table 4.7(a)). The sink of VOC is the oxidation by OH. NMHC, a class of VOC, include ethane (C₂H₄), propene (C₃H₆), isoprene (C₅H₈), and terpene (C₁₀H₁₆).

The emissions of pollutants are used to parameterize the OH concentration and the O₃ concentration in ACC2. The past pollutant emissions in ACC2 are based on EDGAR-HYDE 1.3 (van Aardenne et al., 2001). The emissions prior to 1890 are extrapolated on the basis of Bairoch (1995, pp.142-144), Klein Goldewijk (2001), United Nations (UN) Population Division (2002), and Houghton (2003). The future pollutant emissions in ACC2 are provided by SRES. The concentrations of the pollutants are not explicitly described because of their heterogeneous emission patterns and short lifetimes. Their direct radiative forcings are relatively small in magnitude and they are thus not included in the radiative forcing calculation in ACC2.

2.2.8. Tropospheric O₃

Tropospheric O₃ positively interferes the Earth's radiation and is a toxic agent in urban smog while stratospheric O₃ negatively interferes the radiation and plays a pivotal role in protecting human health against UV exposure. The IPCC estimate of the tropospheric O₃ radiative forcing in 2005 is 0.35 W/m² (IPCC, 2007, Figure SPM-2). Tropospheric O₃ is formed by the oxidation of CO with O₂ catalyzed by HO_x (H, OH, and HO₂) and NO_x (equations (2.2.14) – (2.2.18)).



In most instances, M is N₂ or O₂. The net reaction for the tropospheric O₃ formation pathway from CO oxidation is in the following.



Tropospheric O₃ is also formed by the oxidation of CH₄ in the presence of NO_x. CH₄ is oxidized to CO and then the reactions (equations (2.2.14) – (2.2.18)) proceed to produce O₃ (e.g. Jacob, 1999, pp. 207-212). The net reaction the tropospheric O₃ formation pathway from CH₄ oxidation is the following.



The foregoing two mechanisms are the dominant mode of tropospheric O₃ formation in the free troposphere. On the other hand, tropospheric O₃ formation near the surface is mainly occurred by the oxidation of NMHC (e.g. Brasseur et al., 2003, pp. 472-473). O₃ is also transported from the stratosphere.

The sinks of O₃ are the photochemical depletion, vegetation uptake, and polar marine boundary layer (IPCC, 2001, p.262). The nature of these sources and sinks and its turnover time of an order of weeks (IPCC, 2001, p.361) lead to so large spatial variability in the tropospheric O₃ concentration that no general trend can be extracted (IPCC, 2001, p.263). On the basis of the surface measurements, satellite measurements, and models, IPCC (2001, Table 4.9) recommends that the O₃ concentration increased from 25 DU in preindustrial time to 34 DU in 2000.

Similar to the OH concentration, the tropospheric O₃ concentration is parameterized based on the OxComp Workshop results (IPCC, 2001, Table 4.11).

$$\begin{aligned} & c(\text{trp_O}_3)_t - c(\text{trp_O}_3)_{2000} \\ & = 5.0 \{ \ln(c(\text{CH}_4)_t) - \ln(c(\text{CH}_4)_{2000}) \} + 0.125(e(\text{NO}_x)_t - e(\text{NO}_x)_{2000}) \\ & + 0.0011(e(\text{CO})_t - e(\text{CO})_{2000}) + 0.0033(e(\text{VOC})_t - e(\text{VOC})_{2000}) \end{aligned} \quad (2.2.21)$$

The parameterization of the tropospheric O₃ concentration is similar to that of OH and related explanations are found in Section 2.2.4.

In the ACC2 past mode, the tropospheric O₃ radiative forcing uses the forcing of Hansen and Sato (2004). In the future mode, the radiative forcing due to tropospheric O₃ is parameterized as follows:

$$RF(\text{trp_O}_3)_t = RE(\text{trp_O}_3) \cdot (c(\text{trp_O}_3)_t - c(\text{trp_O}_3)_{pre}). \quad (2.2.22)$$

The radiative efficiency of tropospheric O₃ is 0.042 W/m²/DU in ACC2 (Joos et al., 2001, p.904) based on the estimates in various models (IPCC, 2001, Table 6.3) ranges from 0.033 to 0.056 W/m²/DU. $c(\text{trp_O}_3)_{pre}$ is assumed to be 25 DU (IPCC, 2001, Table 4.9).

2.2.9. Stratospheric O₃

The stratospheric O₃ concentration had been substantially decreased mainly due to the industrial emissions of halogen-containing gases (Solomon, 1999).



The net reaction is the following.



There are some signs of recovery in the stratospheric O₃ concentration due to the global adherence to the Montreal Protocol (Weatherhead and Andersen, 2006), which imposes the progressive reductions in halogen-containing gas emissions (Section 2.2.5).³⁷ Aside from the primary function of stratospheric O₃ shielding UV from the Earth's surface, stratospheric O₃ is a negative radiative agent, in contrast to tropospheric O₃ being a positive radiative agent. The decrease in the stratospheric O₃ concentration allows more short-wave radiation to penetrate into the surface-troposphere system and less long-wave radiation to be absorbed. These two competing factors result in cooling for the surface-troposphere system (Brasseur et al., 1999, p.527; IPCC, 2001, p.359).

In ACC2, the concentration of stratospheric O₃ is not explicitly described. In the past mode, the stratospheric O₃ radiative forcing uses the forcing of Hansen and Sato (2004). In the future mode, the stratospheric O₃ radiative forcing is given as a function of EESC (Section 2.2.10) as follows (Joos et al., 2001):

$$RF(\text{str_O}_3)_t = -0.07317(c(\text{EESC})_t - c(\text{EESC})_{1970}). \quad (2.2.27)$$

The coefficient of -0.07317 was adopted from Joos et al. (2001) that assumes the present stratospheric O₃ forcing of -0.15 W/m² based on the estimate for the period between 1979 and 1997

³⁷ Note that the stratospheric O₃ concentration is also influenced by the NO emission, volcanic eruptions, solar cycle, and other meteorological conditions (Weatherhead and Andersen, 2006).

(IPCC, 2001, p.360). The IPCC estimate of the stratospheric O₃ forcing is -0.05 W/m^2 in the year 2005 with a range between -0.15 W/m^2 and 0.05 W/m^2 (IPCC, 2007, Figure SPM-2). $c(\text{EESC})_{1970}$ is 1250 ppt (IPCC, 2001, Table II.2.10).

2.2.10. EESC

EESC is the chlorine-equivalent concentration of halogens in the lower stratosphere in terms of the O₃ destruction potential. The estimate of EESC is required to calculate the stratospheric O₃ radiative forcing. EESC is defined in the following (Daniel et al., 1995).

$$\begin{aligned} \text{EESC}_t = & \left\{ \sum_i n_i \cdot c(\text{halo_Cl}_i)_{t-3} \cdot \frac{FC_{\text{halo_Cl}_i}}{FC_{\text{CFC-11}}} \right\} \cdot FC_{\text{CFC-11}} \\ & + \left\{ \sum_j n_j \cdot c(\text{halo_Br}_j)_{t-3} \cdot \frac{FC_{\text{halo_Br}_j}}{FC_{\text{CFC-11}}} \cdot \alpha \right\} \cdot FC_{\text{CFC-11}} \end{aligned} \quad (2.2.28)$$

halo_Cl_i and halo_Br_j denote a halocarbon containing chlorine and bromine, respectively (Table 2.2). n_i and n_j denote the number of chlorine and bromine contained in halo_Cl_i and halo_Br_j , respectively. $FC_{\text{halo_Cl}_i}$ is the fractional release of chlorine from halo_Cl_i relative to CFC-11 (WMO, 2003, Table 1-4). Corresponding definitions hold for $FC_{\text{halo_Br}_j}$. α denotes the enhanced chemical ability of a bromine atom to destroy O₃ relative to a chlorine atom. A constant value of 45 obtained from the work on mid-latitudes (WMO, 2003, p.1-29 and 30) is used for EESC calculations in ACC2. The time lag of three years (Pollock et al., 1992) expresses an average travel time for halogens to reach the lower stratosphere from the emission source.³⁸ Note that the period of three years is generally used for EESC calculations although the travel time differs from a few months to 6 years depending on the source locations (WMO, 2003, p.1-19). The three-year travel time is not a valid assumption for the short-lived substances such as CH₃Br, the lifetime of which is merely 0.7 years.

EESC is calculated only in the future mode because the stratospheric O₃ radiative forcing is calculated only in the future mode. The estimates of the ODS concentrations between 1997 and 2000 (Section 2.2.5) are transferred from the past mode to the future mode in ACC2. The concentrations of CH₃Cl and CH₃Br are computed because of their significant contributions to EESC

³⁸ Note that Equivalent Effective Chlorine (EECl) is identical with EESC except for the fact that EECl does not account for the 3-year time lag of halogen transportation (WMO, 2003, p.1-19).

and do not enter the radiative forcing calculations. Among all the halocarbons described in ACC2, CFC-115 does not take part in the EESC calculation because the estimate of relative fractional release factor of CFC-115 was not found, but a significant change is not expected due to its omission.

The EESC estimate calculated in ACC2 is smaller than in IPCC (2001, Table II.2.10 in Appendix). The lifetimes and fractional release rates in ACC2 are updated with WMO (2003) and IPCC (2005). The EESC estimates in IPCC (2001) are actually taken from WMO (1999) based on the model of Daniel et al. (1995).

2.2.11. Stratospheric H₂O

Although water vapor is one of the two most important GHGs with CO₂, climate change due to water vapor is treated as a feedback rather than a forcing, in accordance with the definition of radiative forcing (IPCC, 2001, pp.405-406). Thus, changes in the H₂O concentration as a result of temperature change are considered as feedbacks. In fact, the representation of water vapor in climate models is a recurring theme of debate (e.g. Soden et al., 2002). The only exception is the stratospheric H₂O produced as a result of CH₄ oxidation. The direct anthropogenic H₂O emission in the troposphere and the H₂O emission from the high-flying aircrafts in the stratosphere³⁹ are insignificant in terms of climate forcing.

The radiative forcing of stratospheric H₂O is parameterized as a function of CH₄ concentration.

$$RF(\text{Stratospheric_H}_2\text{O})_t = 0.035 \left\{ 0.036 \left(\sqrt{c(\text{CH}_4)_t} - \sqrt{c(\text{CH}_4)_{pre}} \right) \right\} \quad (2.2.29)$$

The coefficient of 0.036 is the coefficient used in the CH₄ radiative forcing equation. 0.035 in equation (2.2.29) is based on the fact that the forcing contribution of stratospheric H₂O is 2 to 5% of the total CH₄ forcing (IPCC, 2001, p.366). Joos et al., (2001) uses a similar formulation but their coefficient is 0.05 rather than 0.035. The preindustrial CH₄ concentration in equation (2.2.29) is assumed to be 700 ppb (IPCC, 2001, Table 6.1).

The concentration of stratospheric H₂O is not explicitly specified in ACC2. Observational records for almost half a century indicate a rising trend of stratospheric H₂O concentration of about 1% per year (Rosenlof et al., 2001). The forcing due to stratospheric H₂O is 0.2 W/m² since 1980 (IPCC, 2001, p.367). The estimate of the stratospheric H₂O forcing in the year 2005 is 0.07 W/m² with a range between 0.02 W/m² and 0.12 W/m² (IPCC, 2007, Figure SPM-2).

³⁹ The radiative forcing due to contrails (with respect to only the formation of cirrus clouds) in 2005 is estimated to be 0.01 W/m² (IPCC, 2007, Figure SPM-2) with a large uncertainty.

2.2.12. Aerosols

Aerosols are minute substances present in the atmosphere in a solid or liquid phase. Current scientific knowledge indicates that aerosols are strong negative radiative agents. However, the quantification of the aerosol forcing involves a large uncertainty due to the associated complex interactions with cloud formation and the resulting precipitation efficiency. The elucidation of the magnitude of the aerosol forcing is important to narrow down the uncertainties in climate projections.

Aerosols affect the Earth's radiation budget in the following three ways. First, aerosols generally scatter and absorb radiation, resulting in cooling and warming, respectively (direct effect of the aerosol forcing). Second, relevant to the warm (liquid-water) cloud formation is a role of aerosols in creating water droplets by functioning as cloud condensation nuclei, which leads to an increase in the droplet concentration and a decrease in the cloud albedo, resulting in cooling (first indirect effect). Third, the increase in the droplet concentration further leads to a reduction in the precipitation efficiency, resulting also in cooling (second indirect effect) (IPCC, 2001, p.375). The second indirect effect is regarded as a feedback rather than a forcing because it incurs changes in the tropospheric water vapor (IPCC, 2001, pp.405-406). The second indirect effect was not considered in the Second Assessment Report of IPCC (1996). Aerosols act also as ice nuclei for the formation of ice clouds. However, premature knowledge of the aerosol forcing in terms of ice cloud formation does not allow it to be taken into account in the aerosol forcing in ACC2 although the associated effect to the radiative forcing is estimated to be significant (IPCC, 2001, p.311).

Many species of aerosols are acting on the Earth's radiation budget differently. The representation of the aerosol forcing in the simple model framework requires coarse assumptions. In ACC2, aerosol forcings are divided into three types of forcings: 1) direct effect due to sulfate aerosols of anthropogenic origin, 2) direct effect due to OC and BC emitted from biomass burning and fossil fuel burning, and 3) indirect effect due to all the anthropogenic aerosols. This simplified scheme is used both in the ACC2 past and future mode and based on the following assumptions:

First, the direct effect of the sulfate aerosols is parameterized in the following way as described in Joos et al. (2001):

$$RF(\text{Sulfate_Aerosols}^{direct})_t = RF(\text{Sulfate_Aerosols}^{direct})_{2000} \cdot \frac{e(\text{SO}_2^{anthro})_t}{e(\text{SO}_2^{anthro})_{2000}}, \quad (2.2.30)$$

where $e(\text{SO}_2^{anthro})_t$ denotes anthropogenic SO_2 emission due to fossil fuel combustion at year t . The value of $e(\text{SO}_2^{anthro})_{2000}$ is given in each of the emission scenarios used in the past and future modes (EDGAR-HYDE 1.3 (van Aardenne et al., 2001) and SRES (Nakićenović et al., 2000)) (Footnote No.31). The emission prior to 1890 is extrapolated on the basis of Bairoch (1995,

pp.142-144), Klein Goldewijk (2001), UN Population Division (2002), and Houghton (2003). The future anthropogenic SO₂ emission uses SRES. The estimate of the present sulfate aerosol forcing (direct effect only) $RF(\text{Sulfate_Aerosols}^{direct})_{2000}$ is -0.4 W/m^2 with a range of -0.2 and -0.8 W/m^2 (IPCC, 2001, p.369 and Table 6.4). The central estimate has not been changed since the Second Assessment Report of IPCC (1996). Sulfate aerosols are formed through chemical reactions from sulfate precursors, which are mainly SO₂ originating from fossil fuel combustion, volcanic eruptions, and DMS from marine plankton (e.g. Takemura et al., 2000; IPCC, 2001, Table 5.2). The sulfate forcing formulation above includes only the contribution from anthropogenic SO₂ emission.

Second, the direct effect of carbonaceous aerosols is represented in the following way (Joos et al., 2001):

$$RF(\text{Carbonaceous_Aerosols}^{direct})_t = RF(\text{Carbonaceous_Aerosols}^{direct})_{2000} \cdot \frac{e(\text{CO})_t}{e(\text{CO})_{2000}}. \quad (2.2.31)$$

The value of $e(\text{CO})_{2000}$ is provided from each of the emission scenarios in the past and future modes. Carbonaceous aerosols comprise OC and BC. OC is formed by atmospheric oxidation of biogenic hydrocarbons mainly with OH and takes a large fraction of carbonaceous aerosols. BC is soot and tarry substances originating from fossil fuel combustion and biomass burning. BC has a light absorbing character, which is of particular importance for the direct effect of the carbonaceous aerosols. The parameterization above uses CO emission to approximate various emissions leading to the formation of carbonaceous aerosols (Section 2.2.7 for emission data source). The radiative forcing of biomass burning carbonaceous aerosols is estimated to be -0.2 W/m^2 with an uncertainty range of -0.07 to -0.6 W/m^2 (IPCC, 2001, p.372). The radiative forcing of fossil fuel OC and BC aerosols is -0.1 W/m^2 with an uncertainty of a factor of 3 and 0.2 W/m^2 with an uncertainty of a factor of 2, respectively. The sum of the medians gives the estimate of -0.1 W/m^2 used for $RF(\text{Carbonaceous_Aerosols}^{direct})_{2000}$. Note that the geographical distribution of carbonaceous aerosols is quite different from that of sulfate aerosols (IPCC, 2001, Figure 6.7 (d) and (e)).

Third, the indirect effect due to all the aerosols is parameterized as follows:

$$RF(\text{All_Aerosols}^{indirect})_t = RF(\text{All_Aerosols}^{indirect})_{2000} \times \ln \left[\frac{e(\text{SO}_2^{natur})_{const} + e(\text{SO}_2^{anthro})_t}{e(\text{SO}_2^{natur})_{const}} \right] \div \ln \left[\frac{e(\text{SO}_2^{natur})_{const} + e(\text{SO}_2^{anthro})_{2000}}{e(\text{SO}_2^{natur})_{const}} \right]. \quad (2.2.32)$$

The indirect forcing due to all the aerosols is assumed to be linearly linked to sulfate aerosol load of natural and anthropogenic origin. The logarithmic expression was taken from Harvey et al. (1997).

The value of $e(\text{SO}_2^{anthro})_{2000}$ is provided from each of the emission scenarios in the past and future

modes. The natural SO₂ emission is assumed to be 42 Tg(S)/year (Harvey et al., 1997; Joos et al., 2001). $RF(\text{All_Aerosols}^{\text{indirect}})_{2000}$ is set to -0.8 W/m^2 based on the following estimates. Shine and Forster (1999) estimate that the indirect effect of all aerosols is -1.0 W/m^2 with an uncertainty of at least a factor of two. Joos' formulation similar to equation (2.2.32), the scaling coefficient is set to -0.8 W/m^2 is used for the year 1990 in the IS92a scenario. The GCM estimate of the indirect effect of aerosols has a large uncertainty because of considerable differences in the treatment of microphysical details (IPCC, 2001, p.377). The estimate of the indirect effect of all the aerosols in the year 2005 is -0.7 W/m^2 with an uncertainty range of -1.8 to -0.3 W/m^2 (IPCC, 2007, Figure SPM-2).

Aerosols that are not described in ACC2 are mineral dust, sea salt aerosols, industrial dust, primary biogenic aerosols, and nitrate aerosols. Mineral dust originates mainly from deserts but also from anthropogenic activities. Mineral dust scatters the incoming short-wave solar radiation while it also absorbs radiation over high albedo surface. The IPCC estimate of the radiative forcing of mineral dust is the range between -0.6 and 0.4 W/m^2 (IPCC, 2001, p.373). The mineral dust forcing (at present -0.6 to 0.4 W/m^2 (IPCC, 2001, p.373)) is not described in ACC2 because of the large uncertainty even in the present forcing estimate and also because of the lack of past and future forcing estimates. Sea salt aerosols are physically formed by bursting entrained air bubbles during whitecap formation on the ocean surface. Sea salt aerosols serve as both light scattering and cloud nuclei, which is important in particular over the ocean where wind speeds exceed a certain level (IPCC, 2001, p.297). No explicit estimate for the sea salt aerosol forcing is given in IPCC (2001) (see model-based estimate of Takemura et al., (2003)). Industrial dust is primary particles emitted from transportation, coal combustion, cement manufacturing, metallurgy, and waste incineration. Because of the direct relevance to environmental air quality, this type of aerosols have been well monitored and regulated, whose emissions have already been significantly reduced in developed countries (IPCC, 2001, p.299). On the other hand, the emission of industrial dust is rising in the advancement of emerging economy. Primary biogenic aerosols consist of plant debris, humic matter, and microbial particles and acts as both cloud nuclei and ice nuclei (IPCC, 2001, p.300). The abundance of nitrate aerosols is related to the relative abundances of ammonium and sulfate. The nitrate aerosol forcing is estimated to be merely -0.024 W/m^2 (IPCC, 2001, p.303). Finally, the interactions with aerosols with gases are not taken into account here.

2.3. CLIMATE COMPONENT – DOECLIM

In contrast to the earlier approach in NICCS where an IRF is used for calculating the temperature

response to the radiative forcing (Hooss et al., 2001),⁴⁰ two different energy balance models (EBMs) are available for the temperature calculation in ACC2. The first option is a global-mean EBM, which can be obtained by interpreting the Hooss' IRF as a physical box model (Kriegler, unpublished). Such a box-model representation overcomes a problem of the original IRF which was tied to the value of the climate sensitivity of the parent model used for the IRF calibration (2.39K in Hooss (2001, p.33)). The climate sensitivity is a measure of the asymptotic temperature change after doubling the preindustrial CO₂ concentration in AOGCM. The temperature pathway to reach the new equilibrium largely depends on the nonlinear thermal inertia of the ocean. Thus, the original IRF approach can be erroneous when the value of the climate sensitivity used in ACC2 departs largely from the reference value, and simply scaling the entire temperature response linearly with climate sensitivity would violate the energy conservation between heat flux into the earth system and net energy imbalance at the top of the atmosphere (Figure 2.6). Kriegler's global-mean EBM produces a temperature change projection that conforms to the energy conservation. The use of such an EBM is necessary for the inverse calculation where the climate sensitivity constitutes a tuning parameter to obtain a good fit of the 20th century temperature record. The second option for the temperature calculation in ACC2 is the Diffusion Ocean Energy balance CLIMate model (Acronym: DOECLIM), which is a land-ocean EBM used 'by default' in ACC2. Practically, DOECLIM should be used in all cases except for comparative analyses or solution checks. In this section (2.3), we will present the details of DOECLIM. Note that the sea level component in ACC2 is not actively used at this point,⁴¹ and therefore not discussed further here.

DOECLIM is used to calculate surface temperature change in response to radiative forcing of the earth system as computed by the carbon cycle and atmospheric chemistry components of

⁴⁰ A strength of Hooss' approach is that a fixed spatial pattern of temperature anomalies (relative to the global mean) has been extracted *together* with annual-global-mean time characteristics of the temperature response to radiative forcing. The time-dependent part is computed separately in NICCS; however, the extraction procedure allows to approximate the spatially resolved temperature response by scaling the pattern with the global mean response. DOECLIM or the physical EBM interpretation of the IRF used for temperature calculations in ACC2 does not guarantee the validity of this approximation. Therefore, Hooss' spatial pattern is not actively used by the authors.

⁴¹ The sea level component in ACC2 has been fully upgraded from ICM1.1 by implementing the parameterization of the sea level change summarized in IPCC (2001, Appendix 11.1). The IPCC approach takes account of the sea level rise due to thermal expansion, loss of mass of glaciers and ice caps, loss of mass of the Greenland ice sheet, loss of mass of the Antarctic ice sheet, loss of mass of the Greenland and Antarctic ice sheets due to the ongoing adjustment to past climate change, runoff from thawing of permafrost, and deposition of sediment on the ocean floor. The sea level change component in ACC2 produces a comparable projection to the corresponding IPCC projection up to 2100; however, some erroneous behavior was reported for the projection on a longer time scale. Hitherto, the sea level calculation 'by default' uses the global-annual-mean surface air temperature calculated from DOECLIM. However, since DOECLIM provides the temperature anomaly profile for the entire interior ocean water column, the estimation of sea level rise due to thermal expansion can be considerably improved. The extension of DOECLIM to the calculation of sea level rise is under way.

ACC2. EBMs have found renewed interest in the 1980s for estimating the response of global surface temperature to a human-induced increase in atmospheric GHG concentrations (e.g., Hoffert et al. 1980; Harvey and Schneider, 1985; Schlesinger, 1985; Wigley and Schlesinger, 1985; Hansen et al. 1985; Wigley and Raper, 1992), and since then have been used as emulators for global mean response characteristics of AOGCM (e.g., Murphy, 1995; Raper and Cubasch, 1996; Raper et al., 2001) and as reduced-form climate models in integrated assessments of climate impacts and policies (e.g., Wigley et al. 1996, Nordhaus and Boyer, 2000). These EBMs are based on a linearised treatment of the climate response to small perturbations of the earth's energy balance. A discussion of the basic assumptions that underlie such a linearised treatment and their validity is beyond the scope of this section, but can be found elsewhere (e.g., Kriegler, 2005, Appendix A).

The model DOECLIM was originally constructed in a separate project (Kriegler, 2005) to estimate the joint uncertainty about climate sensitivity, vertical ocean heat diffusivity and sulphate aerosol forcing from a comparison of model response and 20th century surface temperature record. It was coupled to the carbon cycle and atmospheric chemistry components of ACC2 after that analysis was completed. The model structure and model parameter values are unchanged from Kriegler (2005), but the numerical implementation has been upgraded (Section 2.3.4) to eliminate artificial damped oscillations in the temperature response following volcanic spikes in the radiative forcing time series.

Section 2.3.1 motivates the particular model representation that was chosen for the specific purpose of comparing model response to the 20th century surface temperature record. Section 2.3.2 outlines the treatment of the interior ocean which dominates the transient model response. In Section 2.3.3, the model parameters are calibrated so that the set of free parameters is narrowed to climate sensitivity T_{2x} and effective vertical diffusivity κ_v of heat in the ocean. Section 2.3.4 describes the numerical implementation of DOECLIM. In Section 2.3.5, we discuss the coupling of the EBM to the upstream components of ACC2. Due to page constraints, we have tried to keep the model description as concise as possible. A more detailed description, particular of the model calibration and the analytical solution of the 1D-ocean model, can be found in Kriegler (2005, Section 2.1 and Appendices A and B).

2.3.1. Atmosphere – Land – Surface Ocean Model

EBMs of climate change try to assess the response of surface temperature to a perturbation of the (annual average) energy balance at the surface, i.e.,

$$\sigma T_{S,eq}^4 = F_{Sol} + G, \tag{2.3.1}$$

where $T_{S,eq}$ is the surface temperature in equilibrium, $\sigma = 5.67 \times 10^{-8}$ W/(m²K⁴) the

Stefan-Boltzmann constant, F_{Sol} the portion of solar radiation that is absorbed by the earth system and G the additional net energy incident at the surface due to the natural greenhouse effect. If the incident energy $E = F_{Sol} + G$ is perturbed by a small amount ΔE , the first order Taylor approximation of the resulting heat flux into or out of the surface is given by

$$\dot{H}(t) = \Delta E(t) - rT_S(t), \text{ with } r := 4\sigma(T_{S,eq})^3, \quad (2.3.2)$$

where T_S is the surface temperature anomaly with respect to the original equilibrium temperature. The main assumption underlying EBMs of climate change is that the perturbation of the incident energy can be approximated by the sum of a radiative forcing term (Q) capturing alterations of the energy balance due to changes in solar insolation, atmospheric aerosol load and GHG concentrations, and a temperature feedback term which scales with surface temperature anomaly T_S , i.e., $\Delta E := Q + rT_S$. Under this assumption, the simplest EBM of temperature response to a radiative forcing Q is described by

$$\dot{H}(t) = Q(t) - \lambda T_S(t), \quad (2.3.3)$$

where the climate feedback parameter $\lambda = r(1 - f)$ amalgamates the effect of radiative damping and temperature feedback on the incident energy perturbation.

Equation (2.3.3) refers to annual average global mean quantities. Since the heat flux is dominated by the world's ocean, a more realistic model has to consider ocean and land masses separately. Most EBMs of climate change go a step further, and also separate Southern and Northern hemisphere (e.g., Wigley and Raper, 1992; Schlesinger et al., 1997). Two-hemisphere models are useful to capture the spatially inhomogeneous forcing from anthropogenic aerosols and tropospheric ozone, which are concentrated over the Northern hemisphere land masses. However, they come at the costs of additional uncertain parameters, because the inter-hemispheric heat fluxes need to be parameterized. Since the carbon cycle and atmospheric chemistry components of ACC2 provide only global mean quantities, we have decided to restrict ourselves to a separation of ocean and land masses only.

In its initial form, our EBM is constituted by four stylized boxes: land L , troposphere over land AL , troposphere over the ocean AS , and ocean mixed layer S . The model does not include the stratosphere, as it adjusts to a radiative perturbation within months, and these adjustment processes can be accounted for in the choice of radiative forcing (Harvey, 1999). The radiative heating is distributed among the boxes, before it diffuses into the interior ocean. Such a four box EBM is described by (compare Murphy, 1995):

$$\text{Troposphere (land)} \quad C_A \dot{T}_{AL} = Q_{AL}^* - \lambda_{AL}^* T_{AL} - \frac{k^*}{f_L} (T_{AL} - T_{AS}) - k_L^* (T_{AL} - T_L) \quad (2.3.4)$$

$$\text{Land} \quad C_L \dot{T}_L = Q_L^* - \lambda_L^* T_L - k_L^* (T_L - T_{AL}) \quad (2.3.5)$$

$$\text{Troposphere (ocean)} C_A \dot{T}_{AS} = Q_{AS}^* - \lambda_{AS}^* T_{AS} - \frac{k^*}{1-f_L} (T_{AS} - T_{AL}) - k_S^* (T_{AS} - T_S) \quad (2.3.6)$$

$$\text{Ocean mixed layer} c_V z_S \dot{T}_S = Q_S^* - \lambda_S^* T_S - k_S^* (T_S - T_{AS}) - F_O \quad (2.3.7)$$

where $\lambda_{AL}^*, \lambda_L^*, \lambda_{AS}^*, \lambda_S^*$ are the climate feedback parameters in the respective boxes in $W/(m^2K)$,

k^* atmospheric land-sea heat exchange coefficient in $W/(m^2K)$, k_L^* and k_S^* atmosphere-land and atmosphere-sea heat exchange coefficients in $W/(m^2K)$, C_A and C_L heat capacity of atmosphere and land in $W \cdot yr/(m^2K)$, respectively, c_V specific heat capacity of a cubic meter of seawater in $W \cdot yr/(m^3 K)$, z_S depth of ocean mixed layer in m, F_O heat flux into the interior ocean in W/m^2 , and f_L land fraction of earth surface.

Obviously, the differential equations (equations (2.3.4) – (2.3.7)) reflect the basic structure of equation (2.3.3), with temperature separated into T_{AL}, T_L, T_{AS}, T_S the effective temperature anomalies in the respective boxes, and global mean radiative forcing replaced by radiative forcings Q_{AL}^* and Q_{AS}^* of the troposphere over land and ocean, respectively (after stratospheric adjustments), and radiative forcings Q_L^* and Q_S^* at the troposphere-land/ocean interface. In addition, the model includes the anomalous heat transfer to the neighbouring boxes (no direct heat transfer is assumed between land and ocean box), which are assumed to scale with the temperature anomaly gradient between the boxes. Since we express the heat flux per unit area, we need to weigh the heat transfer coefficient between troposphere over land and sea by the land fraction of the earth surface.

The 4-Box model exhibits a variety of parameters, of which in particular the climate feedback parameters of the individual boxes will be difficult to estimate. Moreover, the partitioning of the radiative forcing onto the four boxes will depend on the forcing agent. To eliminate these complications, we take advantage of the fact that there exists a strong coupling between surface and troposphere due to large physical heat fluxes of latent and sensible heat. A perturbation of the radiation balance at the surface-troposphere interface equilibrates much faster due to readjustments of the surface-troposphere temperature gradient than a perturbation at the top of the atmosphere (TOA) due to a change of the effective radiating temperature of the entire earth system (Harvey, 1999). Hence, for the sake of modelling the secular climate response to a radiative perturbation, we can assume that the tightly coupled surface air temperatures (SAT) and troposphere temperatures increase in step ($dT_{AL}/dt = a_L dT_L^{SAT}/dt$, $dT_{AS}/dt = a_S dT_S^{SAT}/dt$). It is generally expected that the

troposphere warms faster than the surface (on a global average; $a_L > 1$, $a_S > 1$) due to the decrease in lapse rate in moister air. The enhancement of effective troposphere warming relative to surface warming has been investigated in several AOGCM experiments, suggesting a globally averaged value of $a = 1.2$ (Hansen 2002). Radiosonde and satellite-borne measurements have shown the opposite trend with surface warming outpacing troposphere warming (Mears et al., 2003). Recently, these measurements have been corrected for residual errors which reconciled model projections with observations (Santer et al., 2005).

The proportionality between surface and troposphere warming allows us to simplify the 4-box model by expressing the increase in effective atmospheric temperatures T_{AL} and T_{AS} in terms of the corresponding increase in near surface air temperature. Over land, the increase in SAT is taken to be equal to the increase in land surface temperature itself. Over the ocean, the situation is more complex. The marine air warms faster than the sea surface due to a reduction in sea ice cover, hence we postulate $dT_S^{SAT}/dt = b_{SI} dT_S/dt$, where b_{SI} captures the air warming enhancement from retreating sea ice (compare Raper and Cubasch, 1996). In summary, we make the assumptions $dT_{AL}/dt = a dT_L/dt$ and $dT_{AS}/dt = ab_{SI} dT_S/dt$, where we have neglected any difference between troposphere warming enhancement over land and ocean ($a_L = a_S = a$). Under these assumptions, the model simplifies to a 2-box representation with a land-troposphere and ocean-troposphere box:

$$\text{Land + Troposphere} \quad C_{AL} \dot{T}_L = Q_L - \lambda_L T_L - \frac{k}{f_L} (T_L - b_{SI} T_S), \quad (2.3.8)$$

$$\text{Ocean + Troposphere} \quad C_{AS} \dot{T}_S = Q_S - \lambda_S T_S - \frac{k}{1-f_L} (b_{SI} T_S - T_L) - F_O. \quad (2.3.9)$$

The effective heat capacities of the two boxes are given by $C_{AL} := aC_A + C_L$ and $C_{AS} := ab_{SI}C_A + c_V z_S$, respectively. $\lambda_L := a\lambda_{AL}^* + \lambda_L^*$ and $\lambda_S := ab_{SI}\lambda_{AS}^* + \lambda_S^*$ denote the climate feedback parameters of the surface-troposphere system over land (relative to SAT) and ocean (relative to SST), respectively, and $k := ak^*$ the effective land-sea heat exchange coefficient relative to the surface air temperature gradient. Finally, the radiative forcing terms are summed to radiative forcings $Q_L := Q_{AL}^* + Q_L^*$ and $Q_S := Q_{AS}^* + Q_S^*$ at the TOA after stratospheric adjustments.

2.3.2. Interior Ocean Model

The transient behavior of the EBM is dominated by the heat uptake of the ocean. Therefore, we need a reasonable model to calculate the heat flux F_O into the interior ocean. Most EBMs for the assessment of anthropogenic climate change utilize a 1-D upwelling-diffusion ocean model that

describes the transfer of heat in the water column (e.g., Hoffert et al., 1980; Dickinson and Schaudt, 1998), i.e.,

$$\frac{\partial}{\partial t} T_O(z,t) = \frac{\partial}{\partial z} \left(\kappa_v(z) \frac{\partial}{\partial z} T_O(z,t) \right) + w \frac{\partial}{\partial z} T_O(z,t), \quad (2.3.10)$$

where $z > 0$ denotes the depth of the interior ocean below the mixed layer, $T_O(z,t)$ the ocean temperature at depth z and time t , κ_v the *effective vertical diffusivity* of heat in cm^2/s and w the upwelling velocity in the water column, which transports heat in the opposite direction of diffusion. The 1-D upwelling-diffusion model gained interest as a model of the globally averaged ocean column, because its equilibrium solution provides a good match to the observed global mean temperature profile in the ocean under reasonable values of upwelling velocity $w = 4$ m/yr and uniform vertical diffusivity $\kappa_v = 1$ cm^2/s (Munk, 1966).

Studies of climate change are interested in the penetration of a heat anomaly into the ocean due to rising sea surface temperatures (boundary condition: $T_O(0,t) = T_S(t)$). Since the upwelling-diffusion equation is linear, the anomalous heat fluxes are governed by equation (2.3.10) with initial condition $T_O(z,0) = 0$, where $T_O(z,t)$ represents now the temperature anomaly at depth z and time t relative to its equilibrium value at depth z and time $t = 0$. An analytical solution of this problem on the half line (case of an infinitely deep ocean) for constant vertical heat diffusivity can be found in Kriegler (2005, Appendix B). More realistic upwelling-diffusion ocean models with finite ocean depth include a heat source at the ocean floor which is hypothesized to represent downwelling polar water entering the main ocean column at the bottom. It was shown in Kriegler (2005, Appendix B) that a 'bucket' ocean with depth $z_B = 4000$ m, and a uniform cross-section and vertical diffusivity throughout the water column yields a good approximation of upwelling-diffusion models with realistic depth-dependent cross-section and diffusivity profiles. This is due to the fact that the heat accumulation arising from the decrease of ocean cross-section with depth is counteracted by the increase of vertical diffusivity with depth (Simmons et al. 2004).

It is also discussed in Kriegler (2005, Appendix B) that a model with infinitely deep upwelling-diffusion ocean has difficulties to reproduce the temperature anomaly profiles from climate change experiments with AOGCMs, particularly at depths. The assumption of bottom heating from downwelling polar water seems to be an important prerequisite for upwelling-diffusion models to emulate the deep ocean warming in AOGCM simulations. However, a heat source at the bottom gives rise to "U-shaped" temperature anomaly profiles with greatest warming in the upper ocean and (to a lesser degree) at the bottom, leading to instability of the global mean ocean column. Some EBMs with upwelling-diffusion oceans try to resolve this instability by redistributing the warming with a simple convection algorithm (Raper et al. 2001). In our opinion, the physical interpretation of such a model of anomalous heat fluxes in the ocean becomes increasingly unclear. This point is reinforced by the finding that such upwelling-diffusion models are not in better

agreement with the temperature anomaly profiles simulated by AOGCMs than pure diffusion models without upwelling (case $w = 0$; see Raper, 2001). Therefore, we restrict ourselves to a physically simpler pure diffusion model described by the following heat diffusion problem:

$$\begin{aligned} \text{for } 0 < z < z_B: \quad & \frac{\partial}{\partial t} T_O(z, t) = \kappa_v \frac{\partial^2}{\partial z^2} T_O(z, t) \\ \text{B.C.:} \quad & T_O(0, t) = T_S(t), \quad \frac{\partial}{\partial z} T_O(z_B, t) = 0 \\ \text{I.C.:} \quad & T_O(z, 0) = 0 \end{aligned} \quad (2.3.11)$$

The boundary conditions ensure that the interior ocean temperature at $z = 0$, i.e., the boundary to the mixed layer, equals the mixed layer temperature T_S , and that the heat flux into the ocean floor at $z = z_B$ vanishes. Kriegler (2005, Appendix B) derives an analytical solution for this problem which consists in an infinite series of solutions for the heat diffusion problem on the half line, i.e.,⁴²

$$\begin{aligned} T_O(z, t) = T_S(t) - \int_0^t \dot{T}_S(t') \text{Erf} \left(\frac{z}{2\sqrt{\kappa_v(t-t')}} \right) dt' \\ + \sum_{n=1}^{+\infty} (-1)^n \int_0^t \dot{T}_S(t') \left(\text{Erf} \left(\frac{2nz_B - z}{2\sqrt{\kappa_v(t-t')}} \right) - \text{Erf} \left(\frac{2nz_B + z}{2\sqrt{\kappa_v(t-t')}} \right) \right) dt' \end{aligned} \quad (2.3.12)$$

The series converges very fast, so that it will be sufficient for our application to just consider the zeroth order term describing the behaviour of an infinitely deep ocean and one to three next order bottom correction terms (depending on ocean heat diffusivity, surface warming and time span of model integration).

Equation (2.3.12) allows us to calculate the heat flux into the interior ocean as a function of the mixed layer temperature T_S , i.e.,

$$\begin{aligned} F_O(t) &= -f_{SO} c_V \kappa_v \frac{\partial}{\partial z} T_O(z, t) \Big|_{z=0} \\ &= f_{SO} c_V \sqrt{\frac{\kappa_v}{\pi}} \int_0^t \frac{\dot{T}_S(t')}{\sqrt{t-t'}} \left(1 + 2 \sum_{n=1}^{+\infty} (-1)^n \exp \left(-\frac{n^2 z_B^2}{\kappa_v(t-t')} \right) \right) dt' \end{aligned} \quad (2.3.13)$$

The heat flux F_O (in W/m^2) has been scaled by a parameter $f_{SO} < 1$, which captures the reduction of ocean area at the bottom of the mixed layer relative to the ocean surface area. This accounts for

⁴² Erf(x) in equation (2.3.12) is the error function defined as $\text{Erf}(x) = \frac{2}{\sqrt{\pi}} \int_0^x e^{-t^2} dt$. The error

function is related to the cumulative normal distribution $\Phi(x) = \frac{1}{\sqrt{2\pi}} \int_{-\infty}^x e^{-\frac{x^2}{2}}$ by

$\Phi(x) = \frac{1}{2} \left(1 + \text{Erf} \left(\frac{x}{\sqrt{2}} \right) \right)$. $\Phi(x)$ is available under the name “errorf” in GAMS that was employed

to implement DOECLIM numerically.

the portion of shallow coastal water, where the heat cannot diffuse into the interior ocean.

Equation (2.3.13) can be inserted into equation (2.3.9) to close the EBM without having to model the entire ocean column explicitly. Such an approach for including a 1-D ocean model in an EBM of anthropogenic climate change was proposed by Wigley and Schlesinger (1985). They approximated the analytical solution of the problem (equation (2.3.11)) for the idealized case of an infinitely deep ocean to derive an ordinary differential equation for the mixed layer temperature T_S . The drawback of their approximation was that they had to introduce an artificial parameter which depended on the particular forcing scenario under consideration. In contrast, we consider the more realistic case of an ocean with finite depth, and do not approximate the resulting integro-differential equation by an ordinary differential equation, since we are seeking a general solution for arbitrary forcing trajectories. Due to the presence of an integro-differential equation for the sea surface temperature T_S , the model integration is complicated, but numerical solutions are still straightforward to obtain as discussed in Section 2.3.4. Once equations (2.3.8) and (2.3.9) are solved, we can recover the development of the entire temperature anomaly profile in the interior ocean by use of equation (2.3.12).

2.3.3. Model Calibration

Equations (2.3.8) and (2.3.9) (with the heat flux F_O into the interior ocean spelled out by equation (2.3.13)) constitute the dynamical core of DOECLIM. The model parameters are summarized in Table 2.3. Our goal is to limit the number of free model parameters to just two: the global climate sensitivity T_{2x} , and the effective vertical diffusivity κ_v of heat in the ocean. The remaining parameter values have to be estimated, at least as a function of climate sensitivity, from comparing the model with empirical data and simulations with more complex climate models, or derived from physical properties of the earth system. The land fraction of the earth surface (f_L) and the fraction of ocean area with depth greater than 60 m (f_{SO}) (relative to surface ocean area) can be derived directly from the topography of the earth system. The interior ocean depth of $z_B = 4000$ m is close to the average ocean depth of 3800 m, and a frequent choice in 1D upwelling-diffusion ocean models (e.g., Schlesinger et al., 1997). As demonstrated in Kriegler (2005, Appendix B) a 'bucket' ocean with that depth and uniform vertical diffusivity yields a good approximation to 1D models with depth-dependent cross-section and diffusivity profiles. The specific heat capacity c_V of a cubic meter of seawater is well known from the literature (e.g., Dickinson, 1981).

We have used seasonal data to estimate the land-sea heat exchange coefficient k and the thermal inertia of the land-troposphere box C_{AL} . Admittedly, this constitutes a difficult choice since our highly aggregated EBM is better suited to simulate secular trends in response to a much smaller forcing modulation than is represented by the seasonal cycle. Nevertheless, simple EBMs have been successfully calibrated with seasonal data (e.g., Schlesinger et al., 1997), or even been used to deduce

estimates for climate sensitivity from seasonal variations (Dutton, 1995). Therefore, we consider it a viable approach to calibrate those model parameters that influence the model response on monthly time scales (k, C_{AL}) with seasonal data.

The calibration procedure is detailed in Krieglner (2005, Appendix A). Here, we only recapitulate the basic approach and the results. In a first step, we have estimated the seasonal forcing on land and ocean boxes by calculating the seasonal cycle of average solar insolation per box, and then using the climatology of monthly mean planetary albedo provided by the NASA Earth Radiation Budget Experiment (ERBE; data available at iridl.ldeo.columbia.edu/SOURCES/.NASA/) to estimate the amount of solar radiation that is absorbed in those boxes.

In a second step, we have constructed a climatology of monthly mean temperature anomalies (relative to the annual average) from the land and sea surface temperature time series provided by the US National Climatic Data Center (NCDC; data available at www.ncdc.noaa.gov/oa/climate/research/anomalies/anomalies.html). Seasonal anomalies showed no significant trend over the last 120 years, so that the mean anomaly averaged over the period 1880-2003 and its standard deviation could be directly estimated for each month. Due to the much smaller thermal inertia of the land-troposphere system, the amplitude of the seasonal cycle of temperature over land is much larger than over the oceans.

We then fitted equation (2.3.8) forced with the seasonal anomalies of absorbed solar radiation over land (Q_L ; derived in Step 1) and sea surface temperature (T_S ; from NCDC data) to the seasonal cycle of observed land surface air temperature anomalies as given in the NCDC data set. The fit estimated the maximum likelihood combination of land-sea heat exchange coefficient k and heat capacity C_{AL} (taking into account correlations between the data points) for fixed values of the climate feedback parameter λ_L . 95% confidence ellipsoids were obtained from the curvature of the likelihood function around the maximum likelihood estimate (k', C'_{AL}).

We found that the data strongly constrains the two parameters k and C_{AL} . The best estimate of the land-sea heat exchange coefficient scales strictly linear with the climate feedback parameter λ_L , i.e.,

$$k = b_k - a_k \lambda_L, \quad \text{with } b_k = 1.59 \pm 0.063 \text{ W/(m}^2\text{K)}, \quad a_k = 0.31. \quad (2.3.14)$$

The relative error on the intercept (from the 95% confidence ellipsoids) is approximately 4%, and will be neglected in the following. The best estimate for the effective heat capacity of the land-troposphere system exhibits only a very small dependence on the climate feedback parameter λ_L . We find an overall value of $C_{AL} = 0.52 \pm 0.05 \text{ W/(m}^2\text{K)}$ (error bounds from the 95% confidence ellipsoids). For the purpose of our study, it suffices to choose the mean value of $C_{AL} = 0.52 \text{ W/(m}^2\text{K)}$. Such a heat capacity corresponds to a land column of approximately 8 m. Since the atmospheric heat capacity equals the heat capacity of a land column of approximately 5 m, the remaining 3 m are the effective depth of the land surface that contributes to the overall heat

capacity of the land-troposphere system.

It would be desirable to estimate the effective heat capacity C_{AS} of the ocean mixed layer-troposphere system in the same manner. However, the seasonal global mean SST anomalies provide a much weaker signal and show a flat maximum during NH summer, when the global mean absorbed solar radiation over the oceans is at its minimum. The anti-correlation results from the difference in land fraction between Northern and Southern hemisphere. Such a behavior can not be explained solely on the basis of heat fluxes between two aggregated land and ocean boxes. Its description would require, as a minimum, the resolution of Northern and Southern hemisphere.

Therefore, we do not try to estimate the effective mixed layer depth from seasonal data, but choose a value of 60 m that has been adopted in the EBM MAGICC for emulating the behavior of several AOGCMs (Raper et al., 2001). The effective mixed layer depth of 60 m includes the thermal inertia of the troposphere (which is equivalent to the inertia of a water column with approximately 2.5 m depth) and amounts to a heat capacity of the ocean mixed layer-troposphere system of $C_{AS} = 7.8 \text{ W}/(\text{m}^2 \text{ K})$. For comparison, Schlesinger et al. (1997) finds an effective depth of 55.9 m (53.9 m ocean mixed layer + 2 m tropospheric contribution) from a fit of their hemisphere resolving EBM to the seasonal cycle of land and sea surface temperatures in both hemispheres. Given the difficulty to constrain the effective heat capacity C_{AS} by seasonal data, it is fortunate that it does not influence markedly the model response to radiative perturbations on decadal to secular time scales. The transient temperature behaviour on these time scales is dominated by the heat flux into the interior ocean.

The remaining three parameters $\lambda_L, \lambda_S, b_{SI}$ refer to climate system properties on decadal to secular time scales and therefore cannot be estimated from seasonal data. We also refrain from utilizing the 20th century temperature record to avoid double counting, since these data will be used later to fit the fully coupled model ACC2 to observations. Instead, we rely on a data set of $2\times\text{CO}_2$ experiments with the model CLIMBER-2 (Schneider von Deimling et al., 2006). CLIMBER-2 is a 2.5-dimensional climate system model with a statistical-dynamical atmosphere module coupled to ocean, sea ice, and terrestrial vegetation modules (Petoukhov et al., 2000). The data set comprised 62 individual model runs with perturbed parameter values covering a wide range of climate sensitivities.

Concerning the marine air warming enhancement b_{SI} , i.e., the ratio between global mean marine surface (2m) air temperature anomaly and global mean SST, we find good agreement between individual model runs despite the heterogeneity of parameter settings relating to radiative transfer processes, heat transport in the ocean, atmospheric lapse rate, cloud cover, and water vapour. At the time of $2\times\text{CO}_2$ (year 70), all experiments showed ratios in the range $b_{SI} = 1.43 \pm 0.05$, which decreased to $b_{SI} = 1.32 \pm 0.05$ after 300 years, and remained constant (with narrowing range) thereafter. On the basis of these experiments, we choose a value of

$b_{SI} = 1.3$. For comparison, Raper and Cubasch (1996) have estimated that retreating sea ice leads to a 20% larger warming of marine surface air than of the sea surface itself ($b_{SI} = 1.2$).

The climate feedback parameters λ_L and λ_S are directly related to the climate sensitivity $T_{L,2\times}$ over land (for 2m air temperature) and $T_{S,2\times}$ at the sea surface (which is lower than the climate sensitivity for 2m marine air temperature by the sea ice enhancement factor b_{SI}). The functional dependence between these quantities can be identified from the equilibrium solution of equations (2.3.8) and (2.3.9), i.e., $dT_S/dt = dT_L/dt = 0$ and $F_O = 0$, for a doubling of the atmospheric CO₂ concentration relative to its preindustrial value (leading to a radiative forcing $Q_{2\times} = 3.7 \text{ W/m}^2$):

$$\lambda_L = \frac{Q_{2\times}}{T_{L,2\times}} - \frac{k}{f_L} \frac{T_{L,2\times} - b_{SI}T_{S,2\times}}{T_{L,2\times}}, \quad \lambda_S = \frac{Q_{2\times}}{T_{S,2\times}} + \frac{k}{1-f_L} \frac{T_{L,2\times} - b_{SI}T_{S,2\times}}{T_{S,2\times}}. \quad (2.3.15)$$

We have investigated the relationship between $T_{L,2\times}$ and $T_{S,2\times}$ with data from the ensemble of CLIMBER-2 2×CO₂ experiments, and found an almost strictly linear relationship $T_{L,2\times} = R_\lambda T_{S,2\times}$ with a land enhancement factor of $R_\lambda = 1.43 \pm 0.02$ (see Kriegler, 2005, Appendix A for details). This value is close to the land-sea ratio of climate sensitivity, $R_\lambda = 1.4$, employed in the EBM MAGICC (Raper et al., 2001). The larger climate sensitivity over land reflects the fact, inter alia, that temperatures at high latitudes will respond more strongly to an increase in atmospheric carbon dioxide concentrations than temperatures at low latitudes. Since the land fraction is highest at mid to high latitudes, this suggests a higher equilibrium temperature increase averaged over land than averaged over the sea (see, e.g., Murphy, 1995; Raper and Cubasch, 1996).

The proportionality between climate sensitivity over land and at the sea surface enables us to express these two parameters in terms of global mean climate sensitivity $T_{2\times} = f_L T_{L,2\times} + (1-f_L) b_{SI} T_{S,2\times}$, i.e.,

$$T_{L,2\times} = \frac{R_\lambda T_{2\times}}{R_\lambda f_L + (1-f_L) b_{SI}}, \quad T_{S,2\times} = \frac{T_{2\times}}{R_\lambda f_L + (1-f_L) b_{SI}}, \quad \text{with } R_\lambda = 1.43. \quad (2.3.16)$$

By means of equation (2.3.14) describing the land-sea heat exchange coefficient k as a function of λ_L , together with equations (2.3.15) and (2.3.16) yielding the climate feedback parameters λ_L and λ_S as a function of $T_{2\times}$ and k , we can express all three parameters λ_L , λ_S , and k as functions of a single uncertain model parameter, global mean climate sensitivity $T_{2\times}$. Figure 2.7 shows the dependence of those parameters on climate sensitivity. In summary, we have calibrated the model DOECLIM described by equations (2.3.8), (2.3.9) and (2.3.13) so that it exhibits only two free parameters dominating the temperature response to anthropogenic forcing on secular time scales: the global mean climate sensitivity $T_{2\times}$ and the effective vertical diffusivity κ_v of heat in the ocean.

Figure 2.8 compares the behaviour of DOECLIM with a CO₂ quadrupling experiment conducted with the coupled AOGCM HadCM3 (Gordon et al., 2000). In this experiment, the Hadley centre model was run for 1040 years with a quadrupling of the atmospheric CO₂ concentration from

280 ppm to 1120 ppm in the first 70 years. The HadCM3 data was kindly provided by Simon Gosling from the UK MetOffice. Since HadCM3 overestimates the magnitude of land warming (compared to HadCM2, other GCMs and CLIMBER-2), we had to adjust the land-warming enhancement factor to $R_\lambda = 1.99$ in order to account for the large land-ocean temperature differential at the end of the HadCM3 simulation. The global mean climate sensitivity in DOECLIM was set to $T_{2\times} = 4.1$ K, which is the effective climate sensitivity of HadCM3 at the end of the simulation period as identified by (Gregory et al., 2004). We have adjusted the vertical ocean heat diffusivity so that DOECLIM reproduces the temperature response of HadCM3 to a CO₂ quadrupling scenario. Figure 2.8 shows that DOECLIM can approximate the HadCM3 behaviour convincingly.

2.3.4. Numerical implementation of DOECLIM

In order to choose an adequate numerical method for the integration of equations (2.3.8) and (2.3.9), we need to assess the range of time scales that are resolved by the model. DOECLIM contains six time scales,

$$\begin{aligned} \tau_L &:= \frac{C_{AL}}{\lambda_L}, \quad \tau_{LS} := f_L \frac{C_{AL}}{k}, \quad \tau_{BO} := \frac{z_B^2}{\kappa_v}, \\ \tau_S &:= \frac{C_{AS}}{\lambda_S}, \quad \tau_{SL} := (1 - f_L) \frac{C_{AS}}{k}, \quad \tau_{FO} := \left(\frac{C_{AS}}{c_V} \right)^2 \frac{\pi}{\kappa_v}, \end{aligned} \quad (2.3.17)$$

which vary from 1-2 months (ocean-to-land heat exchange time scale τ_{LS}) and 3 months (temperature response time scale τ_L over land for low climate sensitivity of 1.5 K) to 2-6 years (ocean mixed layer temperature response time scales τ_S and τ_{SL}) to 10-30 years (average interior ocean heat uptake time scale $\sqrt{\tau_{FO}t}$ for a time horizon of $t = 100$ years and a heat diffusivity of $\kappa_v = 0.5$ to 2 cm²/s). By means of the timescales defined in equation (2.3.17), we can rewrite DOECLIM in compact form:

$$\dot{T}_L = \frac{Q_L}{C_{AL}} - \frac{T_L}{\tau_L} - \frac{T_L - b_{SI}T_S}{\tau_{LS}} \quad (2.3.18)$$

$$\dot{T}_S = \frac{Q_S}{C_{AS}} - \frac{T_S}{\tau_S} - \frac{b_{SI}T_S - T_L}{\tau_{SL}} - \frac{f_{SO}}{\sqrt{\tau_{FO}}} \int_0^t \frac{\dot{T}_S(t')}{\sqrt{t-t'}} \left(1 + 2 \sum_{n=1}^{+\infty} (-1)^n \exp\left(-\frac{n^2 \tau_{BO}}{t-t'}\right) \right) dt'. \quad (2.3.19)$$

Since the time scales range over two orders of magnitude, equations (2.3.18) and (2.3.19) constitute a system of stiff differential equations. Therefore, if we want to choose a time step of the numerical integration (typically, $\Delta t = 1$ year) that is an order of magnitude larger than the fastest time scale in the model ($\tau_{LS} = 1$ -2 months), we need to turn to implicit numerical schemes to integrate the differential equations. To this end, Kriegler (2005) has employed the implicit midpoint rule, which

can be derived as an implicit one-stage Runge-Kutta method with maximum order 2:

$$\dot{T}_i = \frac{T_{i+1} - T_i}{\Delta t} = f\left(t_i + \frac{\Delta t}{2}, \frac{T_i + T_{i+1}}{2}\right), \quad i : \text{time step index}, \quad (2.3.20)$$

where the function symbol f denotes the right-hand side of equations (2.3.18) and (2.3.19). The resulting difference equations are

$$\frac{T_{L,i+1} - T_{L,i}}{\Delta t} = \frac{Q_L\left(t_i + \frac{\Delta t}{2}\right)}{C_{AL}} - \frac{T_{L,i} + T_{L,i+1}}{2\tau_L} - \frac{(T_{L,i} + T_{L,i+1}) - b_{SI}(T_{S,i} + T_{S,i+1})}{2\tau_{LS}}, \quad (2.3.21)$$

$$\begin{aligned} \frac{T_{S,i+1} - T_{S,i}}{\Delta t} = & \frac{Q_S\left(t_i + \frac{\Delta t}{2}\right)}{C_{AS}} - \frac{T_{S,i} + T_{S,i+1}}{2\tau_S} - \frac{b_{SI}(T_{S,i} + T_{S,i+1}) - (T_{L,i} + T_{L,i+1})}{2\tau_{SL}} \\ & - \frac{f_{SO}}{\sqrt{\tau_{SO}\Delta t}} \sum_{j=0}^i (T_{S,j+1} - T_{S,j}) \int_j^{j+1} \frac{1 + 2\sum_{n=1}^{+\infty} (-1)^n \exp\left(-\frac{n^2\tau_{BO}}{\Delta t} \frac{1}{i+1-t'}\right)}{\sqrt{i+1-t'}} dt'. \end{aligned} \quad (2.3.22)$$

The coefficients in the sum on the right-hand side of equation (2.3.22) contain an integral, which can be solved analytically:

$$\begin{aligned} a_{i-j} := & \int_j^{j+1} \frac{1 + 2\sum_{n=1}^{+\infty} (-1)^n \exp\left(-\frac{n^2\tau_{BO}}{\Delta t} \frac{1}{i+1-t'}\right)}{\sqrt{i+1-t'}} dt' \\ = & 2\sqrt{i-j+1} \left(1 + 2\sum_{n=1}^{+\infty} (-1)^n \exp\left(-\frac{n^2\tau_{BO}}{\Delta t} \frac{1}{i-j+1}\right) \right) \\ & - 2\sqrt{i-j} \left(1 + 2\sum_{n=1}^{+\infty} (-1)^n \exp\left(-\frac{n^2\tau_{BO}}{\Delta t} \frac{1}{i-j}\right) \right) \\ & + 4\sum_{n=1}^{+\infty} (-1)^{n+1} n \sqrt{\pi \frac{\tau_{BO}}{\Delta t}} \left(\text{Erf}\left(n\sqrt{\frac{\tau_{BO}}{\Delta t} \frac{1}{i-j}}\right) - \text{Erf}\left(n\sqrt{\frac{\tau_{BO}}{\Delta t} \frac{1}{i-j+1}}\right) \right) \end{aligned} \quad (2.3.23)$$

We note that the coefficient a_0 is well defined, since $\lim_{x \rightarrow 0} e^{-c/x} = 0$ and $\lim_{x \rightarrow 0} \text{Erf}(c/x) = 1$.

The infinite sum in the expression for the a_{i-j} converges very fast, if the time scale of heat penetration to the ocean bottom, τ_{BO} , is on the order of magnitude of the time period $\Delta t(i-j)$ or smaller. For the case of interest here, i.e., the temperature response in the period 1750-2100, and realistic values of ocean heat diffusivity $\kappa_\nu < 5 \text{ cm}^2/\text{s}$, for which $\tau_{BO} > 1000$ years, it is sufficient

to consider just the first order bottom correction term. If the simulation is run longer until, e.g., the year 2500, the inclusion of the second and third order bottom correction terms will be more than sufficient for an accurate approximation of equations (2.3.21) and (2.3.22).

In order to allow a straightforward integration of the model by calculating the land and sea surface temperatures at time step $i+1$ from their predecessors at time step i , we reshuffle the terms in the difference equations (2.3.21) and (2.3.22) to yield the following numerical representation of the time-continuous model described by equations (2.3.18) and (2.3.19):

$$\mathbf{B} \cdot \begin{pmatrix} T_{L,i+1} \\ T_{S,i+1} \end{pmatrix} = \mathbf{Q} + \mathbf{A} \cdot \begin{pmatrix} T_{L,i} \\ T_{S,i} \end{pmatrix}, \quad (2.3.24)$$

$$\text{with } \mathbf{B} := \begin{pmatrix} 1 + \frac{1}{2} \frac{\Delta t}{\tau_L} + \frac{1}{2} \frac{\Delta t}{\tau_{LS}} & -\frac{1}{2} \frac{\Delta t}{\tau_{LS}} b_{SI} \\ -\frac{1}{2} \frac{\Delta t}{\tau_{SL}} & 1 + \frac{1}{2} \frac{\Delta t}{\tau_S} + \frac{1}{2} \frac{\Delta t}{\tau_{SL}} b_{SI} + f_{SO} \sqrt{\frac{\Delta t}{\tau_{FO}}} a_0 \end{pmatrix},$$

$$\mathbf{Q} := \begin{pmatrix} \frac{\Delta t}{2} \frac{Q_L\left(t_i + \frac{\Delta t}{2}\right)}{C_{AL}} \\ \frac{\Delta t}{2} \frac{Q_S\left(t_i + \frac{\Delta t}{2}\right)}{C_{AS}} + f_{SO} \sqrt{\frac{\Delta t}{\tau_{FO}}} \sum_{j=1}^{i-1} (a_{i-j} - a_{i-j+1}) T_{S,j} \end{pmatrix},$$

$$\mathbf{A} := \begin{pmatrix} 1 - \frac{1}{2} \frac{\Delta t}{\tau_L} - \frac{1}{2} \frac{\Delta t}{\tau_{LS}} & \frac{1}{2} \frac{\Delta t}{\tau_{LS}} b_{SI} \\ \frac{1}{2} \frac{\Delta t}{\tau_{SL}} & 1 - \frac{1}{2} \frac{\Delta t}{\tau_S} - \frac{1}{2} \frac{\Delta t}{\tau_{SL}} b_{SI} + f_{SO} \sqrt{\frac{\Delta t}{\tau_{FO}}} (a_0 - a_1) \end{pmatrix}.$$

The weighted sum over the predecessor temperatures $T_{S,j}$ at all earlier times $j < i$ stems from the integral in the integro-differential equation (2.3.19), and reflects the memory of the interior ocean. Due to the presence of this sum, it is not possible to initialize the model at arbitrary times t , as would be the case for a system of ordinary differential equations, but only at a presumed idealised equilibrium state t_0 without radiative forcing ($T_{S,0} = Q_{L,0} = 0$) and temperature anomalies $T_{S,0} = T_{L,0} = 0$. Ocean memory about SST anomalies at earlier times $j < i$ comes into play at time step $i=2$ for the first time, i.e. the sum over predecessor SSTs in the vector \mathbf{Q} is only evaluated for $i \geq 2$. Note that we have omitted the term involving $T_{S,0}$ from this sum, since $T_{S,0} = 0$.

For time steps on the order of $t=1$ year, Equation (2.3.24) yields a stable and accurate integration of the model DOECLIM in most instances of radiative forcing trajectories. However, if distinct forcing spikes due to volcanic aerosols are added to the forcing trajectory, small and quickly (within several years) dampening numerical oscillations occur in the temperature response following

such spikes. In order to remove those artefacts, we have upgraded our numerical scheme to an implicit two-stage Runge-Kutta method with maximum order 4. Such a method was derived by Hammer and Hollingsworth (1955):

$$\begin{aligned} \dot{T}_i &= \frac{T_{i+1} - T_i}{\Delta t} = \frac{p_i + q_i}{2} \quad i : \text{time step index,} \\ \text{with } p_i &= f\left(t_i + \frac{3 - \sqrt{3}}{6}\Delta t, \frac{T_i + T_{i+1}}{2} - \frac{\sqrt{3}}{6}\Delta t q_i\right), \\ q_i &= f\left(t_i + \frac{3 + \sqrt{3}}{6}\Delta t, \frac{T_i + T_{i+1}}{2} + \frac{\sqrt{3}}{6}\Delta t p_i\right), \end{aligned} \quad (2.3.25)$$

To greatly simplify the implementation of the Hammer-Hollingsworth (HH) method, we do not apply it to the integral for the ocean memory, i.e., we retain the integration period ($t_0 = 0$ to $t_i + \Delta t/2$) from the implicit midpoint rule. This amounts to the assumption

$$\begin{aligned} &\int_{t_i + \frac{3 - \sqrt{3}}{6}\Delta t}^{t_i + \frac{3 + \sqrt{3}}{6}\Delta t} \frac{\dot{T}_S(t')}{\sqrt{t - t'}} \left(1 + 2 \sum_{n=1}^{+\infty} (-1)^n \exp\left(-\frac{n^2 \tau_{BO}}{t - t'}\right)\right) dt' \approx \\ &2 \times \int_{t_i + \frac{3 - \sqrt{3}}{6}\Delta t}^{t_i + \frac{\Delta t}{2}} \frac{\dot{T}_S(t')}{\sqrt{t - t'}} \left(1 + 2 \sum_{n=1}^{+\infty} (-1)^n \exp\left(-\frac{n^2 \tau_{BO}}{t - t'}\right)\right) dt', \end{aligned} \quad (2.3.26)$$

which is an excellent approximation as long as the time step Δt (1 year) is an order of magnitude smaller than the time scale of heat uptake by the interior ocean (10-30 years). With this simplification, the HH method yields a numerical representation of DOECLIM that includes the terms from the implicit midterm rule plus additional correction terms:

$$\begin{aligned} (\mathbf{B} + \mathbf{C}) \cdot \begin{pmatrix} T_{L,i+1} \\ T_{S,i+1} \end{pmatrix} &= \mathbf{Q} + \mathbf{Q}_C + (\mathbf{A} + \mathbf{C}) \cdot \begin{pmatrix} T_{L,i} \\ T_{S,i} \end{pmatrix}, \\ \text{with } \mathbf{C} &:= \frac{\Delta t^2}{12} \begin{pmatrix} \frac{1}{\tau_L^2} + \frac{1}{\tau_{LS}^2} + \frac{2}{\tau_L \tau_{LS}} + \frac{b_{SI}}{\tau_{LS} \tau_{SL}} & -\frac{b_{SI}}{\tau_{LS}^2} - \frac{b_{SI}}{\tau_L \tau_{LS}} - \frac{b_{SI}}{\tau_S \tau_{LS}} - \frac{b_{SL}^2}{\tau_{LS} \tau_{SL}} \\ -\frac{b_{SI}}{\tau_{SL}^2} - \frac{1}{\tau_S \tau_{SL}} - \frac{1}{\tau_L \tau_{SL}} - \frac{1}{\tau_{LS} \tau_{SL}} & \frac{1}{\tau_S^2} + \frac{b_{SI}^2}{\tau_{SL}^2} + \frac{2b_{SI}}{\tau_S \tau_{SL}} + \frac{b_{SI}}{\tau_{LS} \tau_{SL}} \end{pmatrix} \\ \mathbf{Q}_C &:= \frac{\sqrt{3}}{12} \Delta t^2 \begin{pmatrix} \frac{\Delta Q_{L,i}}{C_{AL} \tau_L} + \frac{\Delta Q_{L,i}}{C_{AL} \tau_{LS}} - b_{SI} \frac{\Delta Q_{S,i}}{C_{AS} \tau_{LS}} \\ \frac{\Delta Q_{S,i}}{C_{AS} \tau_S} + b_{SI} \frac{\Delta Q_{S,i}}{C_{AS} \tau_{SL}} - \frac{\Delta Q_{L,i}}{C_{AL} \tau_{SL}} \end{pmatrix}, \end{aligned}$$

$$\text{where } \Delta Q_{L/S,i} := Q_{L/S} \left(t_i + \frac{3+\sqrt{3}}{6} \Delta t \right) - Q_{L/S} \left(t_i + \frac{3-\sqrt{3}}{6} \Delta t \right), \quad (2.3.27)$$

where the matrices \mathbf{A} , \mathbf{B} and the vector \mathbf{Q} are the same as in equation (2.3.24). In order to separate the radiative forcing terms into a vector \mathbf{Q} that emerged from the implicit midpoint rule and a correction \mathbf{Q}_C from the two stage approach of the HH method we had to make the additional assumption

$$Q_{L/S} \left(t_i + \frac{\Delta t}{2} \right) \approx \frac{Q_{L/S} \left(t_i + \frac{3-\sqrt{3}}{6} \Delta t \right) + Q_{L/S} \left(t_i + \frac{3+\sqrt{3}}{6} \Delta t \right)}{2} \quad (2.3.28)$$

which is valid for climate change studies concerned with trends in annual mean radiative forcing, as long as the time step Δt is of the order of 1 year.

The numerical representation (equation (2.3.27)) of the time-continuous equations (2.3.18) and (2.3.19) achieves the desired result of an accurate and oscillation-free model integration even for large spikes in the forcing trajectory due to volcanic aerosols. We have implemented equation (2.3.27) with a time step $\Delta t = 1$ year in GAMS (Brooke et al., 1992) (Section 4.1), where it can be used both in forward integrations and as a constraint for optimization problems. It is left to the discretion of the user, whether to activate only the numerical representation (2.3.24) derived from the implicit midpoint rule or to also include the correction terms in equation (2.3.27) derived from the HH method. In addition, the user can choose whether to include 1, 2 or 3 bottom-order correction terms in the calculation of the coefficients a_{i-j} (equation (2.3.23)), depending on the time period under consideration and the magnitude of the vertical ocean heat diffusivity. Final, the climate sensitivity and the vertical ocean heat diffusivity of the model DOECLIM can be adjusted freely, and the resulting values for the time scales and coefficients in equation (2.3.27) will be calculated automatically.

2.3.5. Coupling DOECLIM to the Other Components of ACC2

DOECLIM takes the total radiative forcing from anthropogenic and natural sources calculated by the carbon cycle and atmospheric chemistry modules of ACC2, and computes the response of land, sea surface and interior ocean temperature. The resulting temperature anomalies feed back on the carbon cycle module of ACC2.

ACC2 computes global-annual-mean radiative forcing values which need to be separated into forcing over land and ocean before they can be fed into DOECLIM. The derivation of these two forcings from the global mean radiative forcing proceeds as follows:

- 1) The forcing (in units of W/m^2) from well-mixed GHGs (CO_2 , CH_4 , N_2O , halocarbons, and SF_6)

and from associated stratospheric ozone and water vapour anomalies is assumed to be equal over land and ocean, and thus equal to the global mean forcing from these sources.

- 2) The indirect forcing of anthropogenic aerosols is assumed to be roughly equal over land and ocean. Although the anthropogenic aerosol load over land is significantly larger, aerosol particles are more effective in acting as cloud condensation nuclei over the ocean (Harvey, 1999, Chapter 7.4).
- 3) We also assume that the forcing from volcanic aerosols in the stratosphere is roughly equal over land and ocean. This assumption is not unreasonable, since the volcanic cloud circles the globe rapidly.
- 4) The situation is different for the direct radiative forcing from sulphate and carbonaceous aerosols, which is concentrated over Central Europe, the Eastern United States, and Southeast Asia. We make the rough estimate that the direct sulphate forcing over land exceeds the forcing over the ocean by a factor of 2 (Harvey, 1999, Figure 7.10, Plate 9). Taking into account the ratio of land to ocean surface area, this implies that the direct sulphate forcing per unit area over land is 155% of its global mean value, and over the ocean 78% of its global mean value. In the case of carbonaceous aerosols from fossil fuel and biomass burning, we assume that its direct forcing over land exceeds the forcing over the ocean by a factor 3 (Harvey, 1999, Figure 7.10). This implies that the direct forcing from carbonaceous aerosols over land is 190% of its global mean value, and over the ocean 63% of its global mean value.
- 5) The tropospheric ozone load is concentrated around metropolitan areas. Therefore, its abundance is higher over land than over the ocean, and higher in the Northern hemisphere than in the Southern hemisphere. We assume that the land-ocean ratio of its radiative forcing is of comparable magnitude as the NH:SH ratio, which has been estimated to range between 1.4 and 2 (Harvey, 1999, Table 7.3). Hence, we roughly estimate that the tropospheric ozone forcing over land exceeds the forcing over the ocean by a factor 1.5. This implies that the forcing over land is 131% of its global mean value, and over the ocean 87% of its global mean value.
- 6) The difference of solar forcing over land and ocean depends on the difference of annual mean insolation that the two areas receive, and the difference in annual mean albedo over these two areas. We have calculated these differences from the seasonal and latitudinal distribution of solar insolation and ERBE data (Section 2.3.3). The land surface receives 96% and the ocean 102% of the global mean solar insolation. At the same time, the annual mean albedo over land ($\alpha_L = 0.35$) is larger than over the ocean ($\alpha_O = 0.28$). This implies that the solar forcing over land is 89% of its global mean value, and over the ocean 105% of its global mean value.

The forcing contributions of the individual sources are summed to yield the total radiative forcing over land and the ocean which is then forwarded to DOECLIM. Predominantly due to the larger concentration of cooling aerosols over land, the radiative forcing over the ocean is slightly higher

than over land.

Table 2.1. Summary of model equations in the carbon cycle and atmospheric chemistry components of ACC2

c and e denote the concentration and the emission of a gas, respectively. ν is the conversion factor between the emission unit and the concentration unit of a gas (values given in Table 2.2). τ denotes the atmospheric lifetime of a gas. RE is the radiative efficiency of a gas, that is, a radiative forcing per associated concentration unit. RF is a radiative forcing of a gas. The equations in this table are fully explained in the respective sections. The overlap function is explained in Section 2.2.2.

Forcing agent names	Concentration equations	Radiative forcing equations
CO ₂ (carbon dioxide)	IRF-based ocean four-reservoir box model IRF-based land four-reservoir box model (Section 2.1.4)	$RF(\text{CO}_2)_t = \frac{RF_{2\times c(\text{CO}_2)_{pre}}}{\ln 2} \cdot \left(\ln \frac{c(\text{CO}_2)_t}{c(\text{CO}_2)_{pre}} \right)$
CH ₄ (methane)	$\dot{c}(\text{CH}_4)_t = \frac{e(\text{CH}_4)_t}{\nu(\text{CH}_4)} - \frac{c(\text{CH}_4)_t}{\tau(\text{CH}_4)_t}$ $\frac{1}{\tau(\text{CH}_4)_t} = \frac{c(\text{OH})_t / c(\text{OH})_{2000}}{\tau(\text{CH}_4)^{\text{OH}}} + \frac{1}{\tau(\text{CH}_4)^{\text{stratosphere}}} + \frac{1}{\tau(\text{CH}_4)^{\text{soil}}}$	$RF(\text{CH}_4)_t = 0.036 \cdot \left\{ \sqrt{c(\text{CH}_4)_t} - \sqrt{c(\text{CH}_4)_{pre}} \right\}$ $- \text{Overlap}(c(\text{CH}_4)_t, c(\text{N}_2\text{O})_{pre}) - \text{Overlap}(c(\text{CH}_4)_{pre}, c(\text{N}_2\text{O})_{pre})$ $\text{Overlap}(M, N) = 0.47 \cdot \ln \left\{ 1 + 2.01 \times 10^{-5} (M \cdot N)^{0.75} + 5.31 \times 10^{-15} M (M \cdot N)^{1.52} \right\}$
N ₂ O (nitrous oxide)	$\dot{c}(\text{N}_2\text{O})_t = \frac{e(\text{N}_2\text{O})_t}{\nu(\text{N}_2\text{O})} - \frac{c(\text{N}_2\text{O})_t}{\tau(\text{N}_2\text{O})_t}$ $\tau(\text{N}_2\text{O})_t = \tau(\text{N}_2\text{O})_{2000} \left(\frac{c(\text{N}_2\text{O})_t}{c(\text{N}_2\text{O})_{2000}} \right)^{-0.046}$	$RF(\text{N}_2\text{O})_t = 0.12 \cdot \left\{ \sqrt{c(\text{N}_2\text{O})_t} - \sqrt{c(\text{N}_2\text{O})_{pre}} \right\}$ $- \text{Overlap}(c(\text{CH}_4)_{pre}, c(\text{N}_2\text{O})_t) - \text{Overlap}(c(\text{CH}_4)_{pre}, c(\text{N}_2\text{O})_{pre})$ $\text{Overlap}(M, N) = 0.47 \cdot \ln \left\{ 1 + 2.01 \times 10^{-5} (M \cdot N)^{0.75} + 5.31 \times 10^{-15} M (M \cdot N)^{1.52} \right\}$
OH (hydroxyl radical)	$\ln(c(\text{OH})_t) - \ln(c(\text{OH})_{2000}) = -0.32 \{ \ln(c(\text{CH}_4)_t) - \ln(c(\text{CH}_4)_{2000}) \}$ $+ 0.0042(e(\text{NO}_x)_t - e(\text{NO}_x)_{2000}) - 0.000105(e(\text{CO})_t - e(\text{CO})_{2000})$ $- 0.000315(e(\text{VOC})_t - e(\text{VOC})_{2000})$	Not defined
Halocarbons	Not defined (past mode) $\dot{c}(\text{halo})_t = \frac{e(\text{halo})_t}{\nu(\text{halo})} - \frac{c(\text{halo})_t}{\tau(\text{halo})_t}$ (future mode) ⁴³	$RF(\text{halo})_t = RE(\text{halo}) \cdot c(\text{halo})_t$
SF ₆	Not defined (past mode) $\dot{c}(\text{SF}_6)_t = \frac{e(\text{SF}_6)_t}{\nu(\text{SF}_6)} - \frac{c(\text{SF}_6)_t}{\tau(\text{SF}_6)}$ (future mode)	$RF(\text{SF}_6)_t = RE(\text{SF}_6) \cdot c(\text{SF}_6)_t$
CO, VOC, NOx	Not defined ⁴⁴	Not defined

⁴³ $\tau(\text{halo})$ is a constant for halocarbons containing no hydrogen atom. For halocarbons containing at least one hydrogen atom, $\tau(\text{halo})_t = \frac{\tau(\text{halo})_{2000}}{c(\text{OH})_t / c(\text{OH})_{2000}}$. See

Table 2.2.

⁴⁴ Emissions are used to define the concentrations of tropospheric O₃ and OH (thus, CH₄ and OH-reactive halocarbons) and the radiative forcing of the direct effect of carbonaceous aerosol.

Table 2.1. (Continued) Summary of model equations in the carbon cycle and atmospheric chemistry components of ACC2

Forcing agent names	Concentration equations	Radiative forcing equations
Tropospheric O ₃	Not defined (past mode) $c(\text{trp_O}_3)_t - c(\text{trp_O}_3)_{2000} = 5.0 \{ \ln(c(\text{CH}_4)_t) - \ln(c(\text{CH}_4)_{2000}) \}$ $+ 0.125(e(\text{NO}_x)_t - e(\text{NO}_x)_{2000}) + 0.0011(e(\text{CO})_t - e(\text{CO})_{2000})$ $+ 0.0033(e(\text{VOC})_t - e(\text{VOC})_{2000})$ (future mode)	Radiative forcing scenario (past mode) $RF(\text{trp_O}_3)_t = RE(\text{trp_O}_3) \cdot (c(\text{trp_O}_3)_t - c(\text{trp_O}_3)_{pre})$ (future mode)
Stratospheric O ₃	Not defined	$RF(\text{str_O}_3)_t = -0.07317(c(\text{EESC})_t - c(\text{EESC})_{1970})$
Stratospheric H ₂ O	Not defined	$RF(\text{Stratospheric_H}_2\text{O})_t = 0.035 \left\{ 0.036 \left(\sqrt{c(\text{CH}_4)_t} - \sqrt{c(\text{CH}_4)_{pre}} \right) \right\}$
Sulfate aerosols (direct effect)	Not defined	$RF(\text{Sulfate_Aerosols}^{direct})_t = RF(\text{Sulfate_Aerosols}^{direct})_{2000} \cdot \frac{e(\text{SO}_2^{anthro})_t}{e(\text{SO}_2^{anthro})_{2000}}$
Carbonaceous aerosols (direct effect)	Not defined	$RF(\text{Carbonaceous_Aerosols}^{direct})_t = RF(\text{Carbonaceous_Aerosols}^{direct})_{2000} \cdot \frac{e(\text{CO})_t}{e(\text{CO})_{2000}}$
All aerosols (indirect effect)	Not defined	$RF(\text{All_Aerosols}^{indirect})_t$ $= RF(\text{All_Aerosols}^{indirect})_{2000} \times \ln \frac{e(\text{SO}_2^{natur})_{const} + e(\text{SO}_2^{anthro})_t}{e(\text{SO}_2^{natur})_{const}} \bigg/ \ln \frac{e(\text{SO}_2^{natur})_{const} + e(\text{SO}_2^{anthro})_{2000}}{e(\text{SO}_2^{natur})_{const}}$

Table 2.2. Summary of the information on halocarbons (27 species in SRES, methyl chloride, and methyl bromide) and SF₆

ACC2 adopted the estimates of the unit conversion factors (denoted by ν in Table 2.1) that are linearly scaled with molecular weights (see text). In most of the cases, these estimates used in ACC2 are in good agreements with corresponding estimates in Fuglestvedt and Bernsten (1999, Table 2). The estimates of the lifetimes and the radiative efficiencies were taken from IPCC (2005, Table 2.6). Such estimates are in some cases slightly different from the corresponding earlier estimates in IPCC (2001, Table 6.7) and WMO (2003, Table 1-6). The lifetimes and the unit conversion factors are used in the concentration equations in ACC2 (Table 2.1). The radiative efficiencies are used in the radiative forcing equations in ACC2 (Table 2.1). The estimates of the relative fractional releases were taken from WMO (2003, Table 1-4) and Schauffler et al. (1999). The relative fractional releases are used to calculate EESC (Section 2.2.10).

Groups	Common names	Chemical formula	Molecular weights	Unit conversions	Lifetimes (year)	Radiative efficiencies (W/m ² /ppb)	Relative fractional releases
PFC	FC-14	CF ₄	88	15.1	50000	0.08	
Fully Fluorinated PFC	FC-116	C ₂ F ₆	138	23.7	10000	0.26	
Fully Fluorinated PFC	FC-31-10	C ₄ F ₁₀	238	40.8	2600	0.33	
HFC	HFC-23	CHF ₃	70	12.0	270	0.19	
HFC	HFC-32	CH ₂ F ₂	52	8.9	4.9	0.11	
HFC	HFC-43-10mee	CF ₃ CHFCHFCF ₂ CF ₃	252	43.2	15.9	0.4	
HFC	HFC-125	CHF ₂ CF ₃	120	20.6	29	0.23	
HFC	HFC-134a	CH ₂ FCF ₃	102	17.5	14	0.16	
HFC	HFC-143a	CF ₃ CH ₃	84	14.4	52	0.13	
HFC	HFC-152a	CH ₃ CHF ₂	66	11.3	1.4	0.09	
HFC	HFC-227ea	CF ₃ CHFCF ₃	170	29.2	34.2	0.26	
HFC	HFC-236fa	CF ₃ CH ₂ CF ₃	152	26.1	240	0.28	
HFC	HFC-245ca	CH ₂ FCF ₂ CHF ₂	134	23.0	6.2	0.23	
Fully fluorinated	Sulfur hexafluoride	SF ₆	146	25.1	3200	0.52	
CFC	CFC-11 (Freon-11)	CCl ₃ F	137.35	23.6	45	0.25	1.00
CFC	CFC-12 (Freon-12)	CCl ₂ F ₂	120.9	20.7	100	0.32	0.60
CFC	CFC-113	CCl ₂ FCClF ₂	187.35	32.1	85	0.3	0.75
CFC	CFC-114	CClF ₂ CClF ₂	170.9	29.3	300	0.31	0.28
CFC	CFC-115	CF ₃ CClF ₂	154.45	26.5	1700	0.18	
Chlorocarbon	Carbon tetrachloride	CCl ₄	153.8	26.4	26	0.13	1.06
Chlorocarbon	Methyl chloroform	CH ₃ CCl ₃	133.35	22.9	5	0.06	1.08
Halon	Halon1211	CBrClF ₂	165.35	28.4	16	0.3	1.18
Halon	Halon1301	CBrF ₃	148.9	25.6	65	0.32	0.62
Halon	Halon2402	CBrF ₂ CBrF ₂	259.8	44.6	20	0.33	1.22
HCFC	HCFC-22	CHClF ₂	86.45	14.8	12	0.2	0.35
HCFC	HCFC-141b	CH ₃ CCl ₂ F	116.9	20.1	9.3	0.14	0.72
HCFC	HCFC-142b	CH ₃ CClF ₂	100.45	17.2	17.9	0.2	0.36
HCFC	HCFC-123	CF ₃ CHCl ₂	152.9	26.2	1.3	0.14	1.11
Monomethyl halide	Methyl chloride	CH ₃ Cl	50.45	8.7	1.3	0.01	
Monomethyl halide	Methyl bromide	CH ₃ Br	94.9	16.3	0.7	0.01	

Table 2.3. The parameters of the diffusion ocean energy balance model DOECLIM

The estimate of the global-mean climate sensitivity $T_{2\times}$ is taken from the result of the inverse calculation of ACC2. In the ACC2 inverse calculation, the effective vertical ocean heat diffusivity κ_v is fixed at 0.55 cm²/s because κ_v and $T_{2\times}$ cannot be well-constrained simultaneously (Section 3.3). The value of $T_{2\times}$ influences the estimates of the climate feedback parameter over land $\lambda_L(T_{2\times})$ and over ocean $\lambda_S(T_{2\times})$ (equations (2.3.15) and (2.3.16)) and the land-ocean heat exchange coefficient $k(T_{2\times})$ (equation 2.3.14).

<i>Topographical parameters</i>		
Land fraction of earth surface	f_L	0.29
Ocean fractional area below 60 m depth	f_{SO}	0.95
Interior ocean depth	z_B	4000 m
<i>Heat capacities</i>		
Specific heat capacity of seawater	c_v	0.13 Wyr/(m ³ K)
Effective troposphere-land heat capacity	C_{AL}	0.52 Wyr/(m ² K)
Effective troposphere-ocean mixed layer heat capacity	C_{AS}	7.80 Wyr/(m ² K)
<i>Heat flux and climate feedback parameterisations</i>		
Climate feedback parameter over land	$\lambda_L(T_{2\times})$	0.37 W/(m ² K)
Climate feedback parameter over ocean	$\lambda_S(T_{2\times})$	1.47 W/(m ² K)
Land-ocean heat exchange coefficient	$k(T_{2\times})$	1.48 W/(m ² K)
Marine surface air warming enhancement	b_{SI}	1.3
<i>Free model parameters</i>		
Global mean climate sensitivity	$T_{2\times}$	4.1 K
Effective vertical ocean heat diffusivity	κ_v	0.55 cm ² /s

Figure 2.1. Ocean IRF used to tune the ACC2 atmosphere-ocean box model (after Hooss (2001, Figure 2.1))

In the control run of HAMOCC3i, the atmospheric CO₂ concentration is perturbed at year 0. The three dashed lines from top to bottom show the perturbations in the magnitudes of 300%, 100%, and 1%, respectively. Solid lines are the IRFs fitted to the respective dotted curves. All the perturbation curves and IRFs are normalized. The IRF obtained from the 1% perturbation experiment (bottom) is adopted for ACC2 (equations (2.1.11) and (2.1.12)).

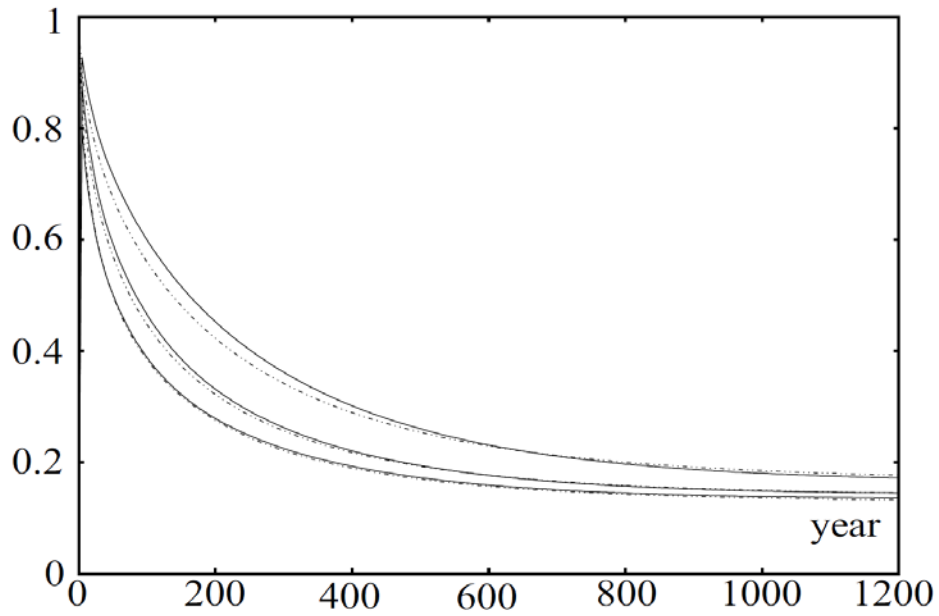


Figure 2.2. Shifts of the thermodynamic equilibria of $\text{CO}_2(\text{aq})$, HCO_3^- , and CO_3^{2-} with the changes in pH and temperature

The equilibrated fractional concentrations are calculated by using the relationships of the equilibrium constants as functions of temperature (Millero, 1995; Millero et al., 2006). In the present day condition, HCO_3^- is the dominant form of DIC in the mixed layer. $\text{CO}_2(\text{aq})$ is the quantity that is directly equilibrated with the atmospheric CO_2 concentration. The fractionation of the carbonate species is thus an important factor determining the carbon storage capacity in the mixed layer.

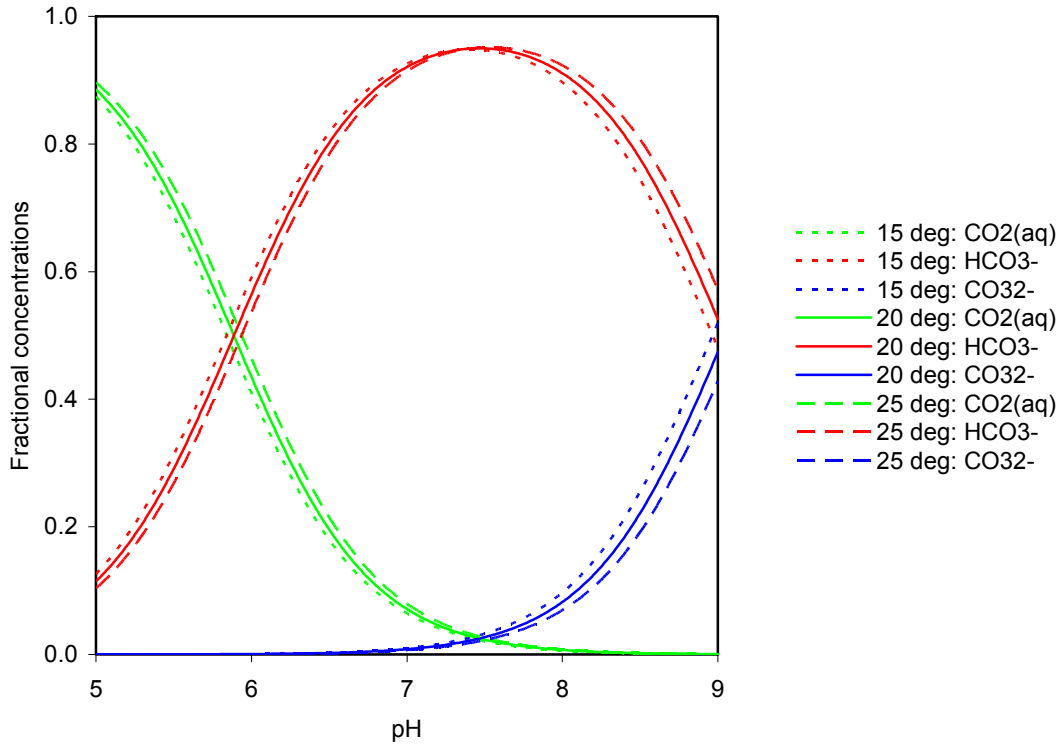


Figure 2.3. The CO₂ equilibrium between the atmosphere and the ocean mixed layer

This figure is aimed at demonstrating the importance of describing the thermodynamic equilibria for the marine carbonate species under a high atmospheric CO₂ concentration. The equilibrium between the atmospheric CO₂ concentration and the mixed layer carbon content computed by four different methods are shown. The first three methods are essentially scalings using the Revelle factor (10, 15, or 20). The last method is based on the explicit calculation of the thermodynamic equilibria of CO₂(aq), HCO₃⁻, and CO₃²⁻ in ACC2. In the last method, a constant alkalinity of 2.435×10⁻³ mol-equivalent/liter and a constant mixed layer temperature of 20°C are assumed.

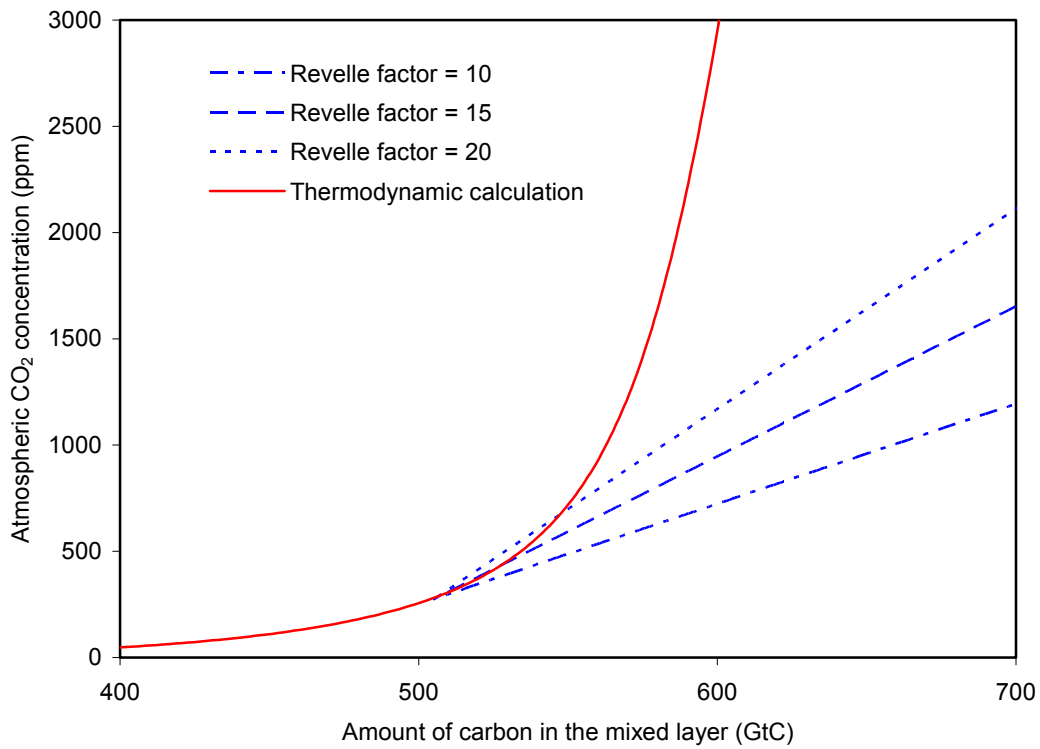


Figure 2.4. pH and the carbon content in the mixed layer under changing atmospheric CO₂ concentration

This figure shows the equilibrium of the CO₂ system in the atmosphere and the mixed layer computed from ACC2. The amount of carbon in the ocean mixed layer is practically saturated even under the present day condition, indicating that there is no significant fast ocean sink. Thus, the remaining ocean sink is primarily in the deep ocean, controlled by the rate of thermohaline circulation.

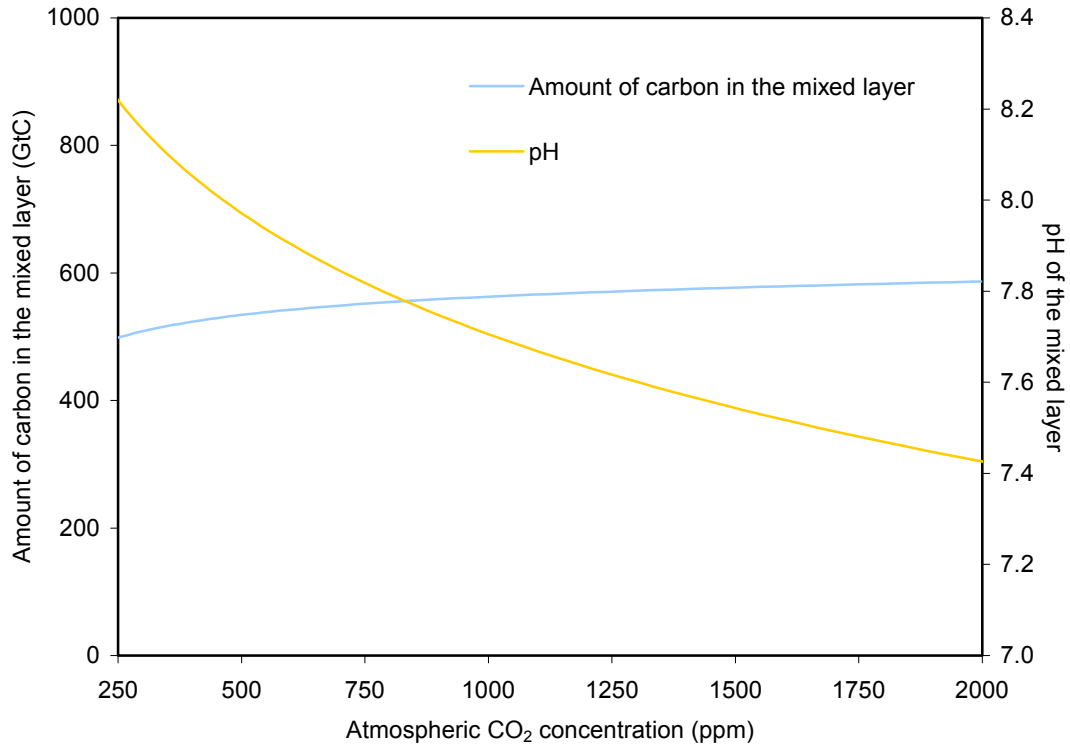


Figure 2.5. Land IRF used to tune the ACC2 land box model

The IRF (heterotrophic respiration flux) is obtained from Bern-CC (Joos et al., 1996).

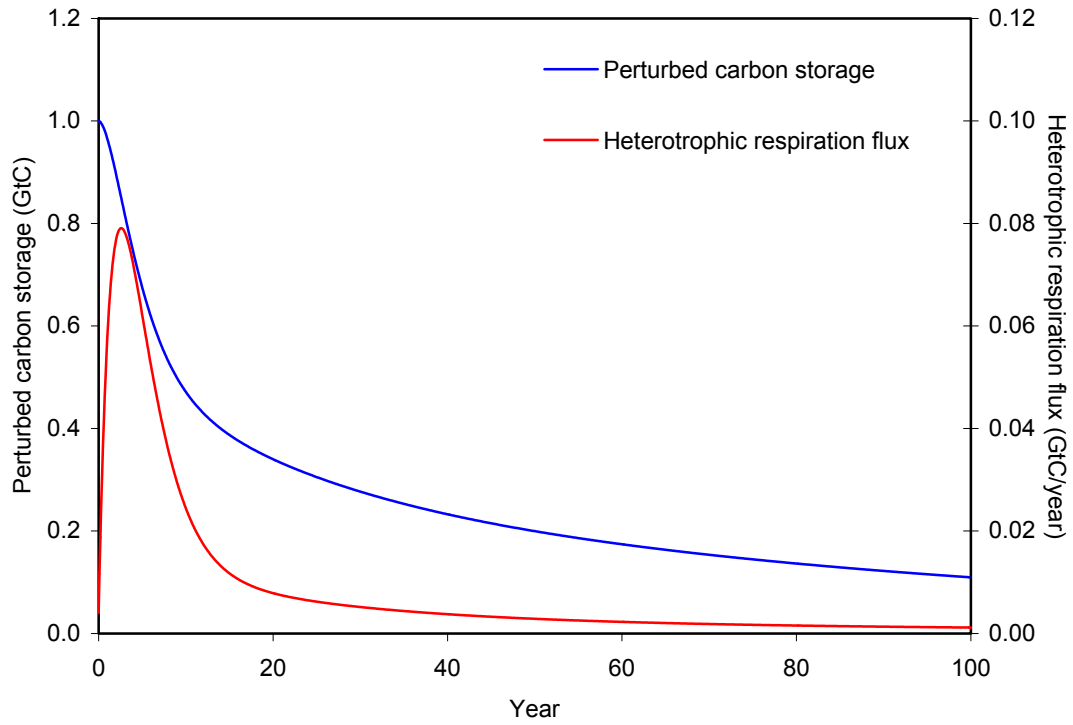


Figure 2.6. Surface air temperature response to the $2\times\text{CO}_2$ forcing

The performances of the IRF (Hooss, 2001) and the global-mean EBM (box-model interpretation of the Hooss' IRF) (Kriegler, unpublished) are evaluated for different climate sensitivity. The Hooss' IRF is linearly scaled with climate sensitivity. Kriegler's EBM accounts for the energy conservation between net radiation imbalance at the top of the atmosphere and heat flux into the earth system. It can be seen that the response of the two models are markedly different. The temperature responses of the two models agree when the climate sensitivity is fixed at the sensitivity of the parent model (2.39°C).

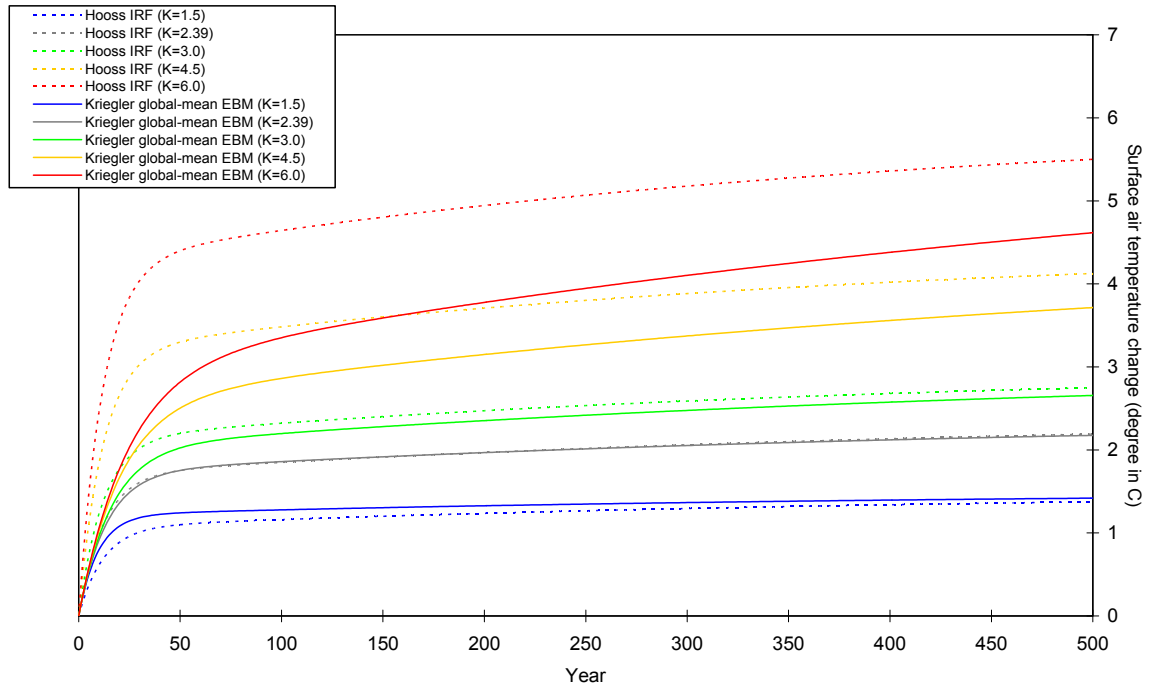


Figure 2.7. Dependence of λ_L and λ_S , and k on global mean climate sensitivity T_{2x}

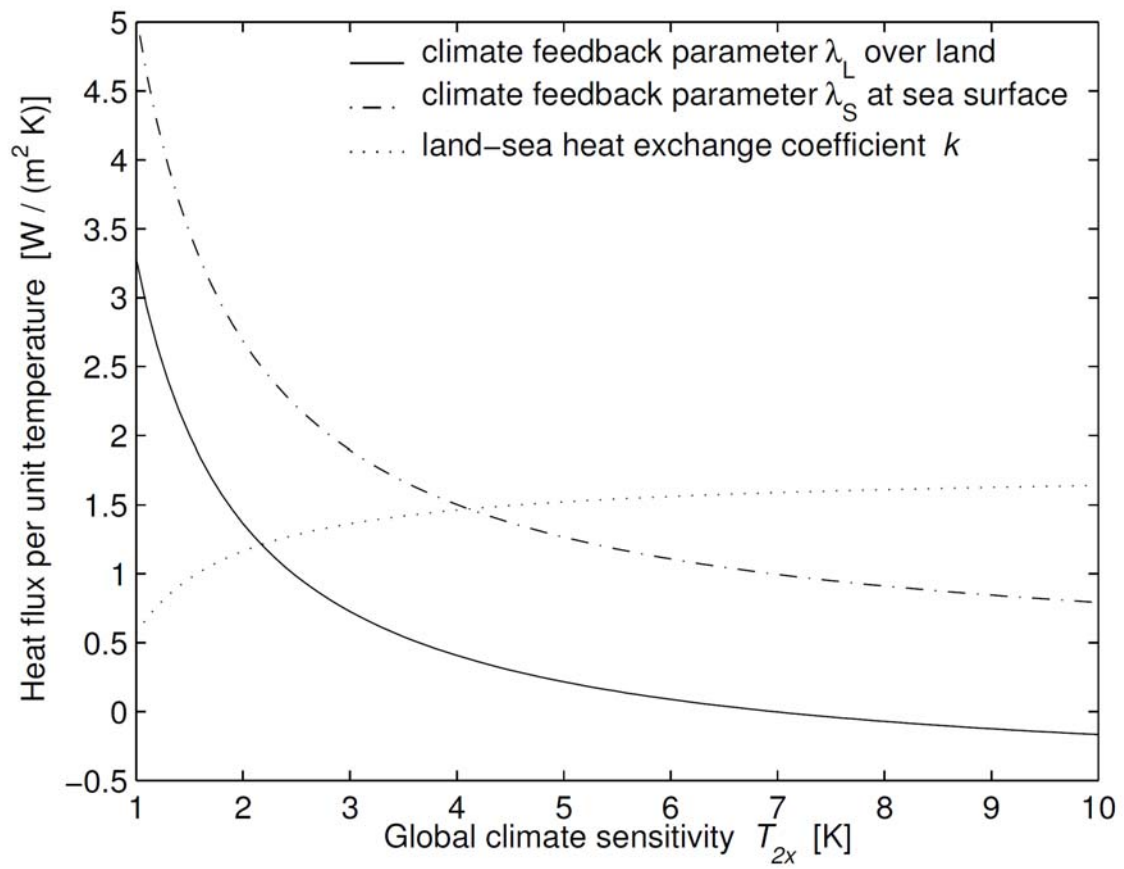
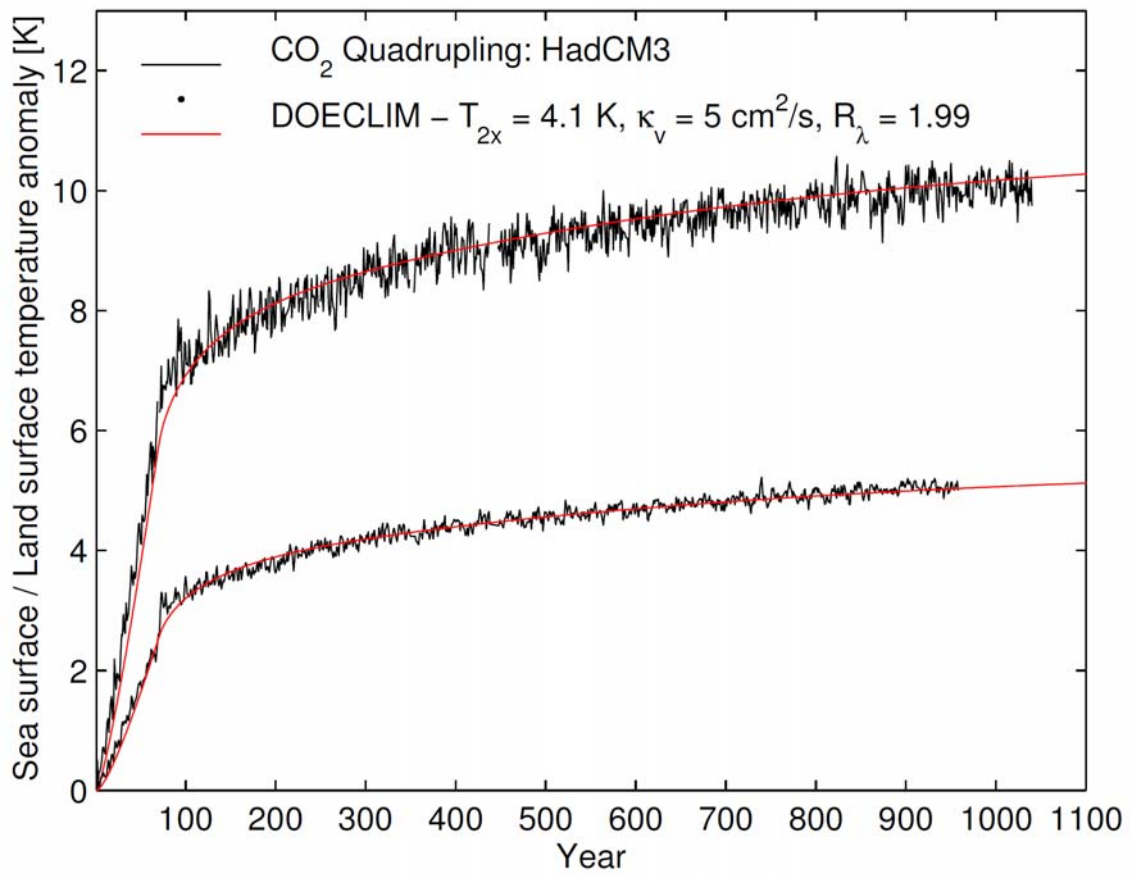


Figure 2.8. Comparison of DOECLIM with results from a CO₂ quadrupling experiment with HadCM3



3 INVERSE MODELLING

3.1 BACKGROUND AND MOTIVATIONS

Uncertainties reside in virtually all the aspects of our knowledge on the Earth system. When one is interested in the uncertainty in a model projection of future climate, uncertainties in the emissions of radiative forcing agents propagate to the uncertainties in the processes associated with the carbon cycle, resulting in a larger combined uncertainty in the future climate projection. The more comprehensive a domain of the Earth system is modeled, the more multiplications and summations of uncertainties sequentially emerge, rendering the uncertainty in the future climate change uncontrollably large, as it is termed “uncertainty explosion” (Schneider, 2002; Schneider and Kuntz-Duriseti, 2002).

Uncertainty analyses of the future climate projections fall into two categories: scenario approach and probabilistic approach. A typical example for the scenario approach is the future GHG emission estimates in SRES (Nakićenović et al., 2000), where various socioeconomic assumptions are made in accordance to the representing storylines for future evolution of globalization, population, economic growth, technological change, and energy system transformation. The scenario approach has an advantage of making underlying assumptions explicit, but the disadvantage is that attaching any probability to scenarios cannot be justified. In other words, one should treat all the projections spanning a wide spectrum equally plausible, posing a difficulty in extracting information for climate policy decision making. An example of the probabilistic approach is the inverse calculation method (e.g. Knutti et al., 2002), where probabilistic model projections are produced by using process descriptions, observations, and parameter estimates including their uncertainties.⁴⁵ A critical problem for the probabilistic approach is that the probabilistic climate projections are sensitive to the subjective choices of assumptions and methods employed (e.g. IPCC Working Group I, 2004b, p.1). In addition, application of the probabilistic approach is limited to the non-human dimensions because future human reflexivity cannot be innately expressed in terms of probability (Dessai and Hulme, 2003). In the human dimensions, the scenario approach is required. The complementary nature of the two approaches calls for the multiplicity of the two approaches. In the past mode of ACC2 (Section 4.1), uncertainties are handled in the context of probabilities. The

⁴⁵ The optimal fingerprint detection method (e.g. Allen et al., 2000) would be another example of the probabilistic approach. The optimal fingerprint approach statistically distinguishes signals from noises in historical climate records and utilizes the maximum signal to noise ratio to estimate a future climate prediction.

outcome of such a probabilistic uncertainty analysis is combined with the future emission scenarios in the future mode of ACC2 (Section 4.2).

The inverse method has been applied to various components of the Earth system; however, none of those studies looked into uncertainties together in the Earth system. With respect to the carbon cycle, research efforts have been put into the uncertainty in the terrestrial biosphere feedback to climate change (e.g. Knorr and Heimann, 2001). As for the atmospheric chemistry, inversion studies have been carried out for CH₄ (e.g. Hein et al., 1997; Mikaloff Fletcher et al., 2004) and CFCs (Hartley and Prinn, 1993). With respect to the climate system, uncertainty analyses have been conducted for the climate sensitivity, the aerosol forcing, and the deep ocean heat uptake (e.g. Forest et al., 2002). However, most of the uncertainty analyses treated one of the three systems in isolation and do not deal with the uncertainties in the Earth system simultaneously.⁴⁶

Thus, a gap can be identified in the uncertainty analyses of the three Earth system components. The state-of-the-art Earth system model in a process of development (e.g. COSMOS project, <http://cosmos.enes.org/>) is, however, not likely to be used for a full-fledged uncertainty analysis in the near future. Prohibitively expensive computational requirement would arise if many uncertain parameters were to be constrained in such a complex model. The *climateprediction.net* project (Allen et al., 2002; Murphy et al., 2004; Stainforth et al., 2005) presented one approach to this technical problem by distributing computational loads to volunteered computers in idle around the globe. Another approach is utilization of a neural network substituting a climate model, which increases the efficiency of ensemble runs by an order of magnitude (Knutti et al., 2003).

Uncertainty analyses often deal with the sources of uncertainties that are hotly debated, leaving the others unaddressed. The estimates of the CH₄ emission from wetlands and N₂O emission from agriculture have substantial uncertainties. The estimate of the *global*-annual-mean CO₂ concentration may actually has a larger uncertainty range than what is currently assumed based on *local* in situ or flask measurements of the monitoring network (e.g. Scripps Institution of Oceanography (SIO) network (Keeling and Whorf, 2005)); the current CO₂ concentration measurement network does not cover the Amazon rainforests and the countries with economy in transition, where the CO₂ concentration is expected to be high (Section 3.3). The estimates of the historical volcanic forcing based on various proxies are not in agreement (e.g. Bertrand et al., 2002;

⁴⁶ Webster et al. (2003) consolidated the two preceding works of (i) Webster et al. (2002) addressing emission uncertainties using a computable general equilibrium model and (ii) Forest et al. (2002) addressing climate system uncertainties using an intermediate complexity climate model. They discussed the relative contributions of uncertainties involving emissions parameters and climate parameters to the climate sensitivity; however, they do not address the uncertainties in the carbon cycle and, more critically, do not analyze the uncertainties simultaneously. Knutti et al. (2003) not only estimated the uncertainties in the aerosol forcing and the climate sensitivity but also the uncertainty in the temperature feedback on the ocean and land CO₂ uptake; however, it does not address the uncertainties in the CO₂ emissions and the CO₂ fertilization effect.

Ammann et al., 2003; Crowley, 2003; Jones and Mann, 2004, Figure 7).

The development of the inverse calculation scheme for ACC2 was inspired by the spinup scheme originally developed in ICM where the beta factor (controlling the CO₂ fertilization effect) is optimized to minimize the deviations from the historical CO₂ emission data and the atmospheric CO₂ concentration measurements. The inverse calculation using ACC2 simultaneously analyzes the chain of uncertainties in the Earth system. Our study is the first attempt to perform an inverse calculation in the coupled carbon cycle, atmospheric chemistry, and climate system. A model like ACC2 is not used in any of the previous inversion studies: simple climate models (e.g. Allen et al., 2000; Andronova and Schlesinger, 2001), intermediate complexity models (e.g. Forest et al., 2002; Knutti et al., 2002; Webster et al., 2002), GCMs (e.g. Murphy et al., 2004; Stainforth et al., 2005), Integrated Assessment models (Mastrandrea and Schneider, 2004), and statistical models (Tol and De Vos, 1998). Our approach deals with only global-annual-mean information. Thus, it can be restated that the novelty of the inversion scheme for ACC2 is the holistic treatment of the uncertainties in the Earth system as a *tradeoff* with the finer spatial and temporal resolutions.

The ACC2 inverse calculation scheme is based on the probabilistic inversion estimation theory of Tarantola (2005). The next section provides the general discussion on the inversion estimation theory. Then, Tarantola's theory is introduced along with assumptions that are made as it is applied to the ACC2 inversion.

3.2 INVERSE ESTIMATION THEORIES

3.2.1 Generalization of Inverse Estimation Theories

Inverse calculations are characterized differently depending on the fields of application. Enting (2002a, p.131) characterizes an inverse calculation as a chain of calculation or inference in the opposite direction to real-world causality where dissipative processes lead to a loss of information about details of causes. Wunsch (1996, p.13) states that an inverse problem is inverse to a corresponding forward or direct problem, interchanging the roles of at least some of the knowns and unknowns. An inverse modelling is also explained as a use of measurements to infer the values of the model parameters (Tarantola, 2005, p.2) and as a mean of interpreting experimental data with uncertainties attached ("inverse problem" in Wikipedia, <http://www.wikipedia.org/>). In this paper, above all, an inversion is characterized as an information synthesis, which we demonstrate by the theoretical derivation in Section 3.2.2.

There are mainly two different theories that underpin inverse calculations: statistical least-square theory and probabilistic inverse estimation theory (including Tarantola's theory adopted for the ACC2 inversion). On the basis of the least-square theory, an inverse problem can be seen as a

minimization of the misfit between the model projections and observations. It is advantageous that the least-square theory provides mathematical insights into the inverse problem for an explicit linear model such as large scale ocean circulation (e.g. Wunsch, 1996, p.12). However, a problem lies in the inherent subjectivity of the definition of the cost function (also termed penalty function or misfit function). If, instead, one rests on the probabilistic inverse estimation theory (Tarantola and Valette, 1982; Mosegaard and Tarantola, 2002; Tarantola, 2005), the form of a cost function is more rigorously defined based on the assumed uncertainty ranges and distributions. In Section 3.2.2 we demonstrate that, under some assumptions, a solution obtained from the least-square approach is a part of the solution obtained from the corresponding probabilistic inverse estimation approach (Tarantola, 2005, Chapter 3). Another advantage of the probabilistic inverse estimation theory is a wide-range of applications including an implicit nonlinear model.

An important issue is that the probabilistic inverse estimation theory presupposes the concept of Bayesian probabilities, which has long been disputed by the camp of the frequentists. For Bayesians a probability can signify a degree of subjective belief while for frequentists the interpretation of a probability is limited to objective and repeatable phenomena. For example, the frequentists would not attach a probability density to the global-annual-mean surface air temperature of a particular time because it cannot be repeatedly measured. Maximum likelihood estimation (discussed in subsection on particularization for ACC2 inverse estimation) falls into the frequentist method. Fundamentally, Tarantola's theory is based on the philosophy that a state of information is generally perceived as a probability density. Shafer (1992) discusses various ways of interpreting probabilities that arrive at different statistical inferences. The dispute is not settled and the jury is still out, but there is a general tendency that the probabilistic inverse estimation approach is increasingly popular across the Earth science disciplines⁴⁷ due to the recent trend of increasing computational power and the relevance to decision makings for climate and environmental policy. In fact, frequentist methods were by far favored twenty years ago due to the subjectivity entering in Bayesian methods (Efron, 1986).

3.2.2 Tarantola's Inverse Estimation Theory

Tarantola's approach to the inverse estimation theory is a probabilistic approach akin to the conventional Bayesian method but is more general. Tarantola (2005) formulates inverse estimation based on the probabilistic notion of conjunction, showing inverse estimation as an information synthesis. Descriptive and technical introductions to Tarantola's theory are given in Tarantola (2006) and Tarantola (2005, Chapter 1), respectively; Tarantola's theory developed for more special settings

⁴⁷ Various applications of inverse estimations are summarized in Enting (2002a, Part B) and Enting (2002b).

is provided in Mosegaard and Tarantola (2002). In this section, we first introduce the most general form of inverse estimation (equation (3.2.1)). This is then transformed to a specific form for the ACC2 application (equation (3.2.14)). Assumptions that are made with the particularization are explicitly discussed at length. Most of the notations are consistent with Tarantola (2005) for the convenience of comparison.

- General Expression of Inverse Estimation

An inverse estimation is a synthesis of information associated with data and parameters. Data and parameters are denoted as \mathbf{d} and \mathbf{m} defined in a finite-dimensional data space \mathcal{D} and a finite-dimensional parameter space \mathcal{M} , respectively.⁴⁸ Data are properties that a model gives projections to; parameters are direct inputs to a model.^{49,50} In the Tarantola's philosophy of the inverse calculation formulation, all the information is expressed as probability densities in the most general settings. All the knowledge on data derived from observations, measurements, reconstructions, other independent modelling studies, and expert elicitation including their uncertainties (or errors) is termed *measurement information on data* (or simply *measurements*), while all the knowledge on parameters including their uncertainties is termed *prior information on parameters* (or simply *prior*).⁵¹ Measurements and prior are collectively called as *prior information*, denoted as a joint *prior* probability density $\rho(\mathbf{d}, \mathbf{m})$ defined in the space $(\mathcal{D}, \mathcal{M})$. A *theoretical relationship of data and parameters* (or simply *theoretical information*), similarly denoted as a joint *theoretical* probability density $\Theta(\mathbf{d}, \mathbf{m})$, consists of functional relationships on the basis of scientific laws and statistical estimations including their modelization uncertainties between data and parameters.⁵² The conjunction (corresponding to logical "and" operation) of prior information and theoretical information is *posterior information*, denoted as a joint *posterior* probability density $\sigma(\mathbf{d}, \mathbf{m})$ defined in the space $(\mathcal{D}, \mathcal{M})$. It is theoretically demonstrated that joint posterior

⁴⁸ The discussion here is limited to the cases with a finite number of parameters and data. Such a discrete approach is sufficient for the inverse calculation for ACC2. For the infinite-dimensional functional approach, see Tarantola (2005, Chapter 5).

⁴⁹ The beta factor for the CO₂ fertilization effect is a *parameter* in ACC2 but a *datum* in complex models such as Lund-Potsdam-Jena Dynamic Global Vegetation Model (LPJ-DGVM) (Sitch et al. 2003), which include process-based phenological descriptions. In non-inversion settings, it would be rather called a *higher order parameter* in LPJ-DGVM.

⁵⁰ We adhere to such definitions of data and parameters in this paper. The meanings of data and parameters used in inversion modelling are different from those used in forward modelling. The definition of a parameter in GAMS is different from an inverse estimation. The terminologies are in some cases even not consistent in inversion studies. Data and parameters are alternatively called observational parameters and model parameters (Tarantola, 2005) and dependent parameters and independent parameters (Tarantola and Mosegaard, 2000).

⁵¹ Note that the terminologies here are not symmetrically defined (Table 3.3).

⁵² Generally, theoretical relationships encompass modelization uncertainties; however, in actual applications, models are often treated as being exact with an implicit assumption that modelization uncertainties are negligible compared to other sources of uncertainties (Figure 3.2).

probability density $\sigma(\mathbf{d}, \mathbf{m})$ can be given as the product of the joint prior probability density $\rho(\mathbf{d}, \mathbf{m})$ and the joint theoretical probability density $\Theta(\mathbf{d}, \mathbf{m})$ in the following (Tarantola and Valette, 1982; Mosegaard and Tarantola, 2002, Section 4.6.2; Tarantola, 2005, Appendix 6.17):⁵³

$$\sigma(\mathbf{d}, \mathbf{m}) = k \frac{\rho(\mathbf{d}, \mathbf{m})\Theta(\mathbf{d}, \mathbf{m})}{\mu(\mathbf{d}, \mathbf{m})}. \quad (3.2.1)$$

$\mu(\mathbf{d}, \mathbf{m})$ is a joint *homogeneous* probability density representing *homogeneous information* defined in the space $(\mathcal{D}, \mathcal{M})$ (Tarantola, 2005, Section 1.2.4 and Appendix 6.2).⁵⁴ k is a normalization

$$\text{constant} \left(\iint_{(\mathcal{D}, \mathcal{M})} \frac{\rho(\mathbf{d}, \mathbf{m})\Theta(\mathbf{d}, \mathbf{m})}{\mu(\mathbf{d}, \mathbf{m})} d\mathbf{d} d\mathbf{m} \right)^{-1}.$$

Equation (3.2.1) is the general expression of inverse estimation (Tarantola, 2005, p.32), where measurement information on data and prior information on parameters are combined with theoretical information, to produce posterior information. Such a concept is illustrated in Figure 3.1. Equation (3.2.1) shows that posterior information depends on prior and theoretical information that is put into an inverse estimation, supporting the general principle that one must include all the relevant information at hand in the right side of equation (3.2.1).⁵⁵ Another point is that a forward calculation (that is, a projection using functional relationships) is embedded in an inverse calculation, in spite of the contrastive terms of “forward” and “inverse.”

Now, the posterior information of parameters is given as a marginal posterior probability density with respect to data

$$\sigma_{\mathcal{M}}(\mathbf{m}) = \int_{\mathcal{D}} \sigma(\mathbf{d}, \mathbf{m}) d\mathbf{d}, \quad (3.2.2)$$

and the posterior information of data as

$$\sigma_{\mathcal{D}}(\mathbf{d}) = \int_{\mathcal{M}} \sigma(\mathbf{d}, \mathbf{m}) d\mathbf{m}. \quad (3.2.3)$$

The solution of an inverse problem is equation (3.2.2). Equation (3.2.2) corresponds to the more restricted Bayesian theorem: $p(\mathbf{m} | \mathbf{d}) = \frac{p(\mathbf{d} | \mathbf{m})p(\mathbf{m})}{p(\mathbf{d})}$, where $p(\cdot)$ denotes a probability

distribution or a probability density. The Bayesian theorem is usually used to explain the probabilistic inverse estimation theory; however, we think that the Tarantola’s derivation is more

⁵³ Although it is easier to derive equation (3.2.1) by assuming the Cartesian product of the data space and the parameter space $\mathcal{D} \times \mathcal{M}$ (equivalent to an independent assumption between data and parameters), the theoretical development here is based on a more general space $(\mathcal{D}, \mathcal{M})$ in order to maintain the description of the inverse estimation at a very general level.

⁵⁴ This term is required except for a linear space represented by a Cartesian coordinate system.

⁵⁵ It is problematic that one can practically ‘pick and choose’ prior information to obtain the posterior information that one wishes (Scales and Tenorio, 2001). Such a procedure is completely odd at the definitions of measurements and prior.

intuitive than the conventional derivation. In the following section, we shall obtain the expression for $\sigma_M(\mathbf{m})$ in more specific settings.

- Particularization for ACC2 Inverse Estimation

The following development tailors the general inversion estimation (equation (3.2.1)) to our needs for ACC2 by making simplifying assumptions. The assumptions that are numbered are discussed extensively in the next subsection.

First of all, we assume that the data and parameter spaces are linear (termed *linear space* or *vector space*), denoted as \mathbb{D} and \mathbb{M} , respectively (Assumption No.1). Under the linear space assumptions, data and parameters can be expressed with components such as $\mathbf{d} = \{d_1, d_2, \dots, d_a\}$ and $\mathbf{m} = \{m_1, m_2, \dots, m_b\}$, respectively. a and b are the total numbers of data and parameters, respectively. Here, for a further simplification, we choose (quasi-)Cartesian coordinates to represent the data space and the parameter space. With Cartesian coordinates, the homogeneous probability density reduces to constants (Tarantola, 2005, Example 1.15). In addition, we restrict ourselves to the circumstances where the relationship between \mathbf{m} and \mathbf{d} is (approximately) linear (Assumption No.2) (Figure 3.2).

A joint probability density can be expressed as the product of a conditional probability density and a marginal probability density. Theoretical information can be broken down as follows:⁵⁶

$$\Theta(\mathbf{d}, \mathbf{m}) = \theta(\mathbf{d} | \mathbf{m}) \theta_M(\mathbf{m}). \quad (3.2.4)$$

$\theta_M(\mathbf{m})$ does not have an information content on parameters themselves. Thus, equation (3.2.4) is simplified to

$$\Theta(\mathbf{d}, \mathbf{m}) = \theta(\mathbf{d} | \mathbf{m}) \mu_M(\mathbf{m}). \quad (3.2.5)$$

$\mu_M(\mathbf{m})$ is a constant in assumed Cartesian coordinates. Then, we further assume that the uncertainty in theoretical information is negligible (in other words, exact theoretical relationships hold) (Figure 3.3) (Assumption No.3). The conditional theoretical probability density can be described with the delta function as follows:⁵⁷

$$\theta(\mathbf{d} | \mathbf{m}) = \delta(\mathbf{d} - \mathbf{g}(\mathbf{m})). \quad (3.2.6)$$

$\mathbf{g}(\cdot)$ is a forward operator representing a model projection.

If we assume that prior information on parameters is independent of measurement information on data (Assumption No.4), a joint prior probability density can be broken down to the product of two marginal prior probability densities as follows:

$$\rho(\mathbf{d}, \mathbf{m}) = \rho_D(\mathbf{d}) \rho_M(\mathbf{m}). \quad (3.2.7)$$

⁵⁶ Note that mathematical complication arises in the expression of the conditional probability if the relationship between \mathbf{m} and \mathbf{d} is strongly nonlinear (Mosegaard and Tarantola, 2002, Sections 2.5, 4.5.2, and B.1; Tarantola, 2005, p.22).

⁵⁷ Note that, without the linear space assumption, the simple delta function above cannot be used here (Tarantola, 2005, p.34 footnote).

The similar relationship holds for the homogeneous probability density as follows:

$$\mu(\mathbf{d}, \mathbf{m}) = \mu_D(\mathbf{d})\mu_M(\mathbf{m}). \quad (3.2.8)$$

Using equations (3.2.1), (3.2.2), (3.2.5) – (3.2.8), the marginal posterior probability density with respect to parameters $\sigma_M(\mathbf{m})$ can be expressed in the following simplified form:

$$\sigma_M(\mathbf{m}) = k' \rho_M(\mathbf{m}) \rho_D(\mathbf{g}(\mathbf{m})), \quad (3.2.9)$$

where k' is the normalization constant. In statistics, $\rho_D(\mathbf{g}(\mathbf{m}))$ in equation (3.2.9) is usually called a likelihood function.⁵⁸ Then, a maximum likelihood point is the maximum of a likelihood function. A likelihood function expresses the ability of a model in explaining data.⁵⁹ Equation (3.2.9) shows a salient point that prior information on parameters plays no part in a likelihood function, indicating that a use of a likelihood function falls into the frequentist approach rather than the Bayesian approach (e.g. Ulrych et al., 2001). In fact, if $\rho_M(\mathbf{m})$ is a uniform probability density, $\sigma_M(\mathbf{m})$ is equal to the likelihood function $\rho_D(\mathbf{g}(\mathbf{m}))$. Thus, with the lowest content in the prior information, a solution obtained from the Bayesian approach is equivalent to a solution obtained from the frequentist approach (Ulrych et al., 2001).

Assuming that measurements \mathbf{d}_{mes} follow Gaussian distributions⁶⁰ characterized by a covariance matrix \mathbf{C}_D (Assumption No. 5), the marginal prior probability density of the data can be written as

$$\rho_D(\mathbf{d}) = \frac{1}{\sqrt{(2\pi)^a \det \mathbf{C}_D}} \exp\left(-\frac{1}{2}(\mathbf{d} - \mathbf{d}_{mes})^T \mathbf{C}_D^{-1}(\mathbf{d} - \mathbf{d}_{mes})\right). \quad (3.2.10)$$

Similarly, by assuming Gaussian uncertainty distributions for prior \mathbf{m}_{prior} characterized by covariance matrix \mathbf{C}_M (Assumption No. 5), the marginal prior probability density of the parameters is

$$\rho_M(\mathbf{m}) = \frac{1}{\sqrt{(2\pi)^b \det \mathbf{C}_M}} \exp\left(-\frac{1}{2}(\mathbf{m} - \mathbf{m}_{prior})^T \mathbf{C}_M^{-1}(\mathbf{m} - \mathbf{m}_{prior})\right). \quad (3.2.11)$$

Then, the marginal posterior probability density of the parameters (equation (3.2.9)) can be expressed in the following form (Tarantola, 2005, Example 1.37):

$$\sigma_M(\mathbf{m}) = k'' \exp(-S(\mathbf{m})). \quad (3.2.12)$$

⁵⁸ A likelihood function is mathematically defined as a probability density divided by the associated homogeneous probability density (not a probability density itself) (Tarantola, 2005, Section 1.6.4).

⁵⁹ $\rho_D(\mathbf{g}(\mathbf{m}))$ is a concise expression of $\rho_D(\mathbf{d}) \cdot \delta(\mathbf{d} - \mathbf{g}(\mathbf{m}))$. Without the assumption on negligible modelization uncertainties, it is $\int_D \frac{\rho_D(\mathbf{d}) \cdot \theta(\mathbf{d} | \mathbf{m})}{\mu_D(\mathbf{d})} d\mathbf{d}$.

⁶⁰ Gaussian distributions can be generalized by using different norms (Tarantola, 2005, Section 6.6) as discussed later. l_2 - norm is assumed here.

k'' is a normalization constant. $S(\mathbf{m})$ is defined as

$$S(\mathbf{m}) = \frac{1}{2} \left((\mathbf{g}(\mathbf{m}) - \mathbf{d}_{mes})^T \mathbf{C}_D^{-1} (\mathbf{g}(\mathbf{m}) - \mathbf{d}_{mes}) + (\mathbf{m} - \mathbf{m}_{prior})^T \mathbf{C}_M^{-1} (\mathbf{m} - \mathbf{m}_{prior}) \right). \quad (3.2.13)$$

When cross-correlations are assumed negligible (in other words, uncertainties are assumed independent) (Assumption No. 6), $S(\mathbf{m})$ reduces to (Tarantola, 2005, Example 1.39) equation (3.2.14) as off-diagonal elements in \mathbf{C}_D and \mathbf{C}_M are zero.

$$S(\mathbf{m}) = \frac{1}{2} \left(\sum_{i=1}^a \left(\frac{g_i(\mathbf{m}) - d_{mes,i}}{\sigma_{d,i}} \right)^2 + \sum_{j=1}^b \left(\frac{m_j - m_{prior,j}}{\sigma_{m,j}} \right)^2 \right) \quad (3.2.14)$$

$\sigma_{d,i}$ and $\sigma_{m,j}$ are one-sigma uncertainty ranges for measurement i and for the prior estimate of parameter j , respectively.

Equation (3.2.14) is the cost function in the ACC2 inverse calculation. Although the residual terms for parameters and data appear symmetrical in the model code, they are fundamentally of different origins as demonstrated above. To summarize, the cost function is the sum of the arguments of the exponential functions representing the marginal posterior probability density of the parameters, which are in essence derived from the conjunction of the joint prior probability density and the joint theoretical probability density. Although the preceding theoretical derivation has taken all the way from a fundamental level, it demonstrates how the parameter term enters in the cost function. This is often questioned and can be intuitively explained only from the foregoing theoretical perspective. Note that frequentists would not, in contrast, include the residual terms associated with parameters in the cost function due to the inherent subjectivity in the prior information on the parameters (discussion on equation (3.2.9)).

The ACC2 inversion scheme determines only a particular solution $\hat{\mathbf{m}}$ that corresponds to the maximum of the marginal posterior probability density of the parameters $\sigma_M(\mathbf{m})$ (equation (3.2.12)); in other words, full posterior probability densities are not produced. Numerically the optimal parameter values that minimize the cost function $S(\mathbf{m})$ (equation (3.2.14)) are the solution for the ACC2 inversion. Our approach is in contrast to several other inversion studies (Forest et al., 2002; Gregory et al., 2002; Knutti et al., 2002; Hegerl et al., 2006) that estimated the probability densities of uncertain climate properties (e.g. climate sensitivity), which provide valuable insights into the extents of unknowns. In fact, it is a technical advantage for us to adhere to the one-point uncertainty estimates because of the use of the state-of-the-art nonlinear optimization solver CONOPT3 provided in the GAMS programming environment. Yet, the one-point estimates obtained from the ACC2 inversion add a distinct value on the basis of the following arguments:

First, our approach estimates the uncertainties in the coupled carbon cycle, atmospheric chemistry, and climate system interactively whereas the other inversion studies treat the individual

systems in isolation. The interactions among different Earth system components have been so far neglected in inversion studies.

Second, our one-point uncertainty estimates allow straightforward interpretation, given the interdependencies in uncertainty estimates. It is important to stress that the maximum value of each of the posterior probability densities of the parameters derived separately is different from each of the associated parameter estimates that correspond to the cost function minimum because the parameter estimates are not independent each other.⁶¹

Third, our optimization approach can exhaustively account for a large number of uncertainties even in each point of time series whereas the probability density approach can consider only a small number of uncertainties because of the computational requirement. For example, in the probability density approach, the uncertainty in the radiative forcing is expressed just by one parameter that scales the fixed time evolution of the radiative forcing (e.g. Knutti et al., 2002). However, in our approach the huge number of interdependencies in the uncertainty estimates associated with time series produces bias in the inversion solution. The cross-correlations cannot be easily quantified because of the complex interactions among the large number of uncertainty estimates. Regional information cannot be used as constraints in our approach at present as we are bound at the current optimization capability.

Based on the arguments above, we contend that our optimization approach is complementary to the probability density approach. The arguments here are crucial when we interpret our inversion results in comparison with the results of the probability density studies (Tanaka et al., 2007).

We have not checked the validity of the particular solution by searching the parameter space or by computing the Hessian matrix to look around the neighborhood of the solution, either of which should be done in principle. The presence of secondary optima cannot be ruled out because of the nonlinearities in the processes and the use of ‘sharp’ information such as the volcanic forcing. However, the ACC2 inversion is beyond the current capability of the global optimization solver BARON available in the GAMS software package (Section A.1). At this point, the evidences to support the validity of the inversion solution are limited to empirical ones. First, the inversion solutions are checked by performing the inversions with different initial points. Second, based on hundreds of inversion calculations along with the inversion scheme development; the sensitivity of the solution to the change in the prior assumptions has not presented any abrupt behavior.

The argument of the exponential function in the posterior parameter estimates (equation (3.2.12)) is equivalent to the cost function typically assumed in the least square approach. Thus, the

⁶¹ A relevant point is that the peaks of the posterior probability densities are different from the corresponding maximum likelihood points, which do not account for the prior information on the parameters.

least square approach with such a cost function can be interpreted as a special case of the probabilistic inversion approach. One should be aware of the fact that the least square method does not provide a priori criteria to decide upon the values of the weighting coefficients. In the probabilistic inversion approach, covariance matrices are theoretically drawn from the assumptions on the prior probability densities. In the least square approach covariance matrices or standard deviations are not necessarily required from the theoretical point of view; they are rather subjectively chosen even for the convenience of the studies. Thus, although the least square method indeed allows a greater freedom in determining the form of the cost function, the results obtained from the least square approach are less rigorous in the absence of theoretical underpinning for the cost function form.

- Assumptions in ACC2 Inverse Estimation

A total of six assumptions have been made to arrive at the formulation of the cost function in ACC2 (equation (3.2.14)) from the general inversion solution (equation (3.2.1)). What follows discusses the implications and issues relevant to such assumptions. Numbering below corresponds to Assumptions No. 1 to 6.

- 1) The assumption of the linearity in the data and parameter spaces requires all the data and parameters to follow the eight axioms associated with addition and scalar multiplication (e.g. Bretscher, 2001, pp.149-150). Positive parameters such as the preindustrial mixed layer temperature (K) and gas lifetime (year) and positive data such as atmospheric gas concentrations (ppb or ppm) do not satisfy the linearity axioms. In theory, they must be expressed in the logarithmic scale (Mosegaard and Tarantola, 2002, pp.8-9; Tarantola, 2005, Examples 1.30 and 1.31): $\ln \frac{x}{x_0}$. x and x_0 are a positive parameter or datum and its arbitrary positive constant, respectively. However, such a logarithmic conversion is practically not needed for the ACC2 inversion because none of the prior information on the parameters and the data is sufficiently close to zero.
- 2) Linearity or mild nonlinearity in the neighborhood of the inversion solution is assumed (equation (3.2.4)). Such an assumption fairly reduces the complexities in the inverse calculation formulation. The natural Earth system as a whole has behaved as a mildly nonlinear system during the Anthropocene. A strong nonlinear response of the Earth system to human perturbation has not been observed for the past hundred years⁶² although process-based model studies give

⁶² This argument is valid only for the processes relevant to the temporal and spatial scale of the ACC2 inversion. Outside of the particular temporal and special time scale, abrupt changes in ecosystem species have been observed, for example (e.g. the widespread amphibian extinction (Boyd and Doney, 2003)). Small scale dynamics in the ocean and the atmosphere are highly nonlinear.

projections of strong nonlinear responses such as ocean circulation reorganization in the next century. The mild nonlinearity as a whole is partly brought about from the offset of nonlinearities; the amplifying nonlinearity due to the reduction in the ocean CO₂ uptake with rising atmospheric CO₂ concentration is nearly cancelled out with the damping nonlinearity due to the decrease in the CO₂ radiative forcing increment (owing to the saturation of CO₂ absorption bands).

- 3) In many applications, modelization (or theoretical) uncertainties are simply overlooked and only parameter and data uncertainties are addressed. Or they assume that modelization uncertainties are sufficiently small to address only parameter and data uncertainties. Note that, as long as Gaussian distributions are assumed for errors, theoretical uncertainties can be viewed as being included in data uncertainties (Tarantola, 2005, Example 1.36).
- 4) It is assumed that the prior information on parameters is independent of the measurement information on data. Such an assumption is justifiable for the ACC2 application because the information used for the prior parameter estimates does not contain the measurements. However, one cannot expect in a strict sense a separation of prior from measurements. An example would be the prior information of the beta factor (parameterization of the CO₂ fertilization effect) obtained from other inversion studies. Such information is derived from the historical carbon budgetary calculation using the atmospheric CO₂ concentration records, which are, however, used as measurements in the ACC2 inverse calculation.
- 5) Gaussian distributions are assumed for errors in the inverse calculation for ACC2. The central limit theorem states that a Gaussian distribution can be used for a phenomenon where one suspects the presence of a large number of small effects acting additively and independently even though each of the small effects is not believed to behave normally. Because the data uncertainties in the ACC2 inversion express all the secondary processes that the model does not explain, it is reasonable to assume that the data uncertainties follow Gaussian distributions. On the other hand, even if the ACC2 inversion stands on the Bayesian probabilistic approach, using Gaussian distributions for the parameter uncertainties should be regarded as a strong assumption. The parameter uncertainties such as the climate sensitivity typically express the imperfectness of our scientific knowledge and are often specified simply as intervals. Applying Gaussian distributions to such intervals can be argued as an overspecification.⁶³

A Gaussian distribution used for the ACC2 inverse calculation and most of the other inverse calculations is a special case of a general Gaussian distribution defined as

⁶³ New approaches of hierarchical Bayes and empirical Bayes are proposed in an attempt to establish a methodology to relax the treatment of prior information that is only poorly known (Malinverno and Briggs, 2004). Another approach is the imprecise probability theory (e.g. Kriegler, 2005), which aims at dealing with prior information that cannot be simply represented by probability distributions.

$\frac{p^{1-1/p}}{2\sigma_p\Gamma(1/p)} \exp\left(-\frac{1}{p} \frac{|x-x_0|^p}{(\sigma_p)^p}\right)$, where $\Gamma(\cdot)$ denotes the gamma function. p corresponds to

l_p – norm that is selected in a particular application (Tarantola, 2005, Sections 6.5 and 6.6).

The cost function is then more generally defined as

$$S(\mathbf{m}) = \frac{1}{p} \left(\sum_i \frac{|g(m_i) - d_{mes,i}|^p}{(\sigma_{d,i})^p} + \sum_j \frac{|m_j - m_{prior,j}|^p}{(\sigma_{m,j})^p} \right). \quad (3.2.15)$$

When $p=2$ (or l_2 – norm), equation (3.2.15) is equivalent to the cost function used in the ACC2 inversion (equation (3.2.14)). With $p=1$ (or l_1 – norm), the assumed probability densities (also called Laplace distributions) have longer tails. Thus, an inverse estimation with a l_1 – norm assumption ensures more robustness to outliers than with a l_2 – norm assumption (Tarantola, 2005, Section 4.4.3). In fact, it is a methodological weakness that the solution for an inverse calculation with l_2 – norm is sensitive to outliers. However, the computation to find out a solution with l_1 – norm norm (or generally l_{odd} – norm) poses a technical problem for the solver CONOPT3 in GAMS caused by the non-smooth absolute functions. In the opposite extreme case of $p = \infty$ (or l_∞ – norm), the assumed probability densities are boxcar functions. Such an assumption would allow strict control on errors, but nonexistence of a solution could result. As a whole, these particular cases of the generalized Gaussian distributions provide the perspective that the least square approach is a special class of the probabilistic inversion estimation approach.

Practically, choices are l_1 – norm, l_2 – norm, or l_∞ – norm. Making use of a l_2 – norm is supported from the fact that the Gaussian distribution (l_2 – norm) has the lowest information content or the highest entropy (Tarantola, 2005, Section 1.2.5 and p.173). The computational easiness and the relevance to the least square methods are also factors favoring the l_2 – norm. The employment of a Gaussian assumption (l_2 – norm) is a common approach in solving inverse estimation problems – the validity of such an assumption is, however, often even not questioned, masked by the popularity.

- 6) The assumption of the independent uncertainties (zero off-diagonal elements in \mathbf{C}_D and \mathbf{C}_M) is introduced in the ACC2 inverse calculation. The independent error assumption is problematic for time series data and parameters such as the atmospheric CO₂ concentration and the CO₂ emission. Such independent assumptions for the time series imply excess weights on time series in the cost function. One approach to tackle this problem is to establish hyperparameters that represent the time series (e.g. parameterized CO₂ emission model). The other approach is to implement an autoregressive process, equivalent to a miniature model to explain correlations

between the neighborhood points in the time series (Kriegler, 2005). These approaches probably alleviate the problem here but they cannot completely solve it because the interdependencies of the large number of uncertainty estimates are extremely complex.

Although making such an assumption is not theoretically correct also in other applications, independent uncertainties are often assumed in part due to the difficulty in estimating off-diagonal elements of the covariant matrices C_D and C_M . Various estimation techniques for off-diagonal elements of the covariant matrices are proposed in the field of data assimilation. Data assimilation, widely applied in short-term weather forecasting and atmospheric retrieval methods, is a variant of inverse estimation, in which the posterior parameter estimates are updated by inversions progressively as new observations are acquired. In data assimilation, statistics for estimating the covariance is made available through successive steps; however, in ACC2 performing an inversion only once, no statistics are available.

A related issue associated with time series is the quality of the data and parameters. For example, the atmospheric CO₂, CH₄, and N₂O concentration records consist of ice core measurements in early periods and station measurements in the last few decades (Section 3.4). Ice core measurements are coarser than the annually-resolved model time step and are interpolated by spline curves with different cutoff lengths. On the other hand, station measurements are the compilations of in-situ measurements, which are continuously sampled, and flask measurements, which are discretely (hourly at Mauna Loa) sampled in glass flasks to be analyzed in respective laboratories. Thus, the information content of the station measurements is denser than that of ice core measurements. To circumvent this problem, it is often proposed to add artificial weights to the residual terms of the ice core data. However, such operations would not possibly be justified under the probabilistic inverse estimation theory (equation (3.2.12)). The problem that the quality of information cannot be entered into an inverse estimation is inherent to the probabilistic inverse estimation theory. In the ACC2 inversion, all the annual measurements are assumed to have equal information content regardless of their quality. Here is where the probability inverse estimation theory hits a limit in dealing with information with a low level of confidence. IPCC recommends that probability densities should be shown only when the level of confidence in the underlying science is high (IPCC Workshop Group I, 2004b, p.2).

The assumptions in the ACC2 inversion have been fundamentally discussed above. Below, the data and parameters used in the ACC2 inverse calculation are discussed.

3.3 DATA IN ACC2 INVERSE CALCULATION

Data in the ACC2 inverse calculation (Table 3.1) are the atmospheric CO₂, CH₄, and N₂O concentration, ocean and land CO₂ uptake, and surface air temperature change, which are all time

series. The relationships between the data and the parameters in the ACC2 inversion are shown in Figure 3.4. The data in the ACC2 inversion are discussed in the following.

In many studies (e.g. Jones and Cox, 2001; Jones et al., 2001), the global-mean atmospheric CO₂ concentration is represented by the station measurements at Mauna Loa, Hawaii. The isolated location of the Mauna Loa station makes the CO₂ concentration measurements less susceptible to local CO₂ fluxes and dampens the seasonal oscillations, making it ideal for interannual or decadal studies. Gammon et al. (1985) suggest, based on the inspection of the CO₂ concentration measured in the SIO air sampling network (Keeling and Whorf, 2005), that the Mauna Loa record or the Mauna Loa record minus 0.2 ppm can be used as a proxy for the global-mean CO₂ concentration for modelling purposes. However, the SIO air sampling stations are distributed mainly over the Pacific and the adjacent land area, without covering the rainforests in Amazon and industrial areas of the countries with economy in transition, where the CO₂ concentration is expected to be significantly higher than the global average. Within the SIO network, the CO₂ concentration difference between Mauna Loa and South Pole measurements had become larger in the second half of the 20th century and has been stabilized around 2.5 ppm for the past 10 years. The increasing parity in the CO₂ concentration measurements can be explained by the trend and locations of the anthropogenic CO₂ emission time series, which, however, poses a question on the representative nature of the Mauna Loa measurements. On an intraannual time scale, the amplitude of the seasonal oscillation in the CO₂ concentration over Alaska is large (approximately 15 ppm at the Point Barrow station in contrast to 5 ppm at the Mauna Loa station), which may corrupt the Mauna Loa measurements that depend on the seasonal atmospheric circulation. The satellite measurements of the atmospheric CO₂ concentration would be an important input for this issue,⁶⁴ but they have not had a global coverage yet. Given the arguments above, Mauna Loa records are still used for the data in the ACC2 inverse calculation, but we apply the uncertainty range larger than the station measurement errors (= 0.2 ppm for all station measurements) by a factor of four. Similar arguments are applicable to the global-mean concentrations of CH₄ and N₂O when station measurements are available. The data uncertainties of the CH₄ concentration are the estimates of the instrumental precision and experimental uncertainty in Table 1 of Masarie et al. (2001). The data uncertainties of the N₂O concentration are larger than the corresponding estimates by a factor of four.

Data for the anthropogenic ocean and land CO₂ uptake are based on the results of C⁴MIP, which includes a total of 11 carbon cycle-climate GCMs and EMIC worldwide (Friedlingstein et al., 2006). The results of two models (CSM-1 and UMD) have been excluded from our analysis as they simulate a global atmospheric CO₂ concentration in the year 2000 different from the observed value

⁶⁴ Chèdin et al. (2003) demonstrate that tropospheric CO₂ concentration measurements between 20°N and 20°S are in a good agreement with the corresponding station measurements and aircraft measurements. The OCO mission (<http://oco.jpl.nasa.gov/>) launching a satellite dedicated to atmospheric CO₂ concentration measurements is underway.

by more than 10 ppm. The average of the remaining model runs in each year between 1861 and 2000 is used as the measurements in the inverse calculation. The largest deviation from the mean is used to form the 2σ Gaussian uncertainty range in each year. The measurements including the uncertainties prior to 1860 are linearly extrapolated from those after 1860. The estimates of the ocean and land CO₂ uptake based on atmospheric $\delta^{13}\text{C}$ and O₂ measurements (IPCC, 2001, Table 3.4) and CFC tracers (e.g. Wetzel, 2004, Table 6.1) are not used here.

Direct instrumental measurements of the surface air temperature (Jones et al., 2006) (<http://www.cru.uea.ac.uk/cru/data/temperature/>) are available from 1856 and are used for the ACC2 inverse calculation. These estimates are frequently updated with new measurements as well as additional past information. Prior to 1855, the temperature reconstruction of Jones et al. (1998) (<http://www.ncdc.noaa.gov/paleo/recons.html>) is used for the ACC2 inversion. Temperature reconstructions are obtained from regression analyses between instrumental temperature records and multi-proxy variables such as tree-rings, ice cores, marine sediments, corals, and historical documents. Proxies are unevenly distributed on the globe. The reconstructions of the southern hemisphere temperature should be regarded with caution because of the scarcity in the proxies (Phil Jones, personal communication, March 14, 2006). Most of the temperature reconstructions represent only the northern hemisphere. Time resolution is another problem: reconstructions such as Mann and Jones (2003) are decadal averaged, where short-term signals from volcanic eruptions are largely smoothed out. The reconstructions of Jones et al. (1998) are the only reconstructions available for both of the hemispheres with an annual resolution. Thus, the average of Jones's reconstructions for the northern and southern hemispheres is used as measurements in the ACC2 inverse calculation. The ranges of the data uncertainties are based on Mann and Jones (2003). It is possible that the uncertainty ranges are larger because of the considerable disagreements among various temperature reconstructions (Jones and Mann, 2004; Moberg et al., 2005).

3.4 PARAMETERS IN ACC2 INVERSE CALCULATION

The parameters in the ACC2 inverse calculation are summarized in Table 3.2. The following time series are parameters in the ACC2 inverse calculation: the emissions of CO₂, CH₄, and N₂O and the missing forcing. The relationships between the parameters and the data in the ACC2 inversion are shown in Figure 3.4. Here we discuss the details of the parameters in the ACC2 inversion.

The CO₂ emission due to fossil fuel combustion is relatively well-known because of the availability of the historical energy statistics, whereas the CO₂ emission due to land use change is subject to a large uncertainty. The literature estimate of the 2σ uncertainty ranges of the fossil fuel CO₂ emission is $\pm 8\%$ of the prior mean (Marland et al., 2006) and that of the land use CO₂ emission is $\pm 50\%$ of the prior mean (Houghton, 2003).

The historical carbon budget is still not well-known because of the uncertainty in the land use CO₂ emission and in the response of the terrestrial biosphere to the atmospheric CO₂ change, climate change, and fertilizer applications. These uncertainties are all linked to balance the historical carbon budget. An additional complexity is speculation on missing carbon cycle processes such as soil erosion (Lal, 2005).

The estimate of the land use CO₂ emission of Houghton (2003) is used as the prior estimates in the ACC2 inverse calculation. Houghton's estimates are available only from 1850 so we extrapolate them linearly to a zero emission in the year 1750 on the basis of the preindustrial quasi-steady state assumption. However, some inversion studies (e.g. Gurney et al., 2002) indicate that Houghton overestimates the amount of land use CO₂ emission, which emerge mostly from deforestation in the tropics (Houghton, 2003, Table 3). The emission estimate due to deforestation is based on FAO's Forest Resource Assessments and their datasets are subject to large uncertainties. Another problem is that Houghton's estimates do not account for wild fire (except for the US) as well as the forest and agricultural management such as changes in species, thinning, and fertilizer application. In inversion results, the land use CO₂ emission may account for missing carbon cycle processes such as soil erosion. Given these arguments, the uncertainty range originally stated by Houghton is doubled for the ACC2 inversion (that is, $\pm 100\%$ of the prior mean).

In models such as ACC2, the CO₂ fertilization effect is parameterized as a logarithmic dependence of NPP on the atmospheric CO₂ concentration. Such a dependency is scaled with the beta factor (equation (2.1.50)). The CO₂ fertilization effect is a major uncertainty in the global carbon cycle, according to the diversity of literature estimates of the beta factor: 0.287 (Meyer et al., 1999; Kicklighter et al., 2001), 0.4 (Gitz and Ciais, 2003), 0.45 (Brovkin et al., 1997), and 0.15 to 0.6 (Kohlmaier et al., 1987). The estimates of the beta factor obtained from inversion studies tend to be higher than those from field experiments (section 2.1.3). Based on the foregoing literature estimates, the prior estimate of the beta factor in the ACC2 inverse calculation is 0.4 with the 2σ uncertainty range between 0.1 and 0.7. When the beta factor is 0.4, doubling atmospheric CO₂ concentration leads to approximately 28% increase in NPP.

The prior mean of Q10 is 2.0 in the ACC2 inversion, which is commonly assumed as a rule of thumb in many biological studies although such a Q10 value is valid under restricted conditions (Davidson and Janssens, 2006). Jones and Cox (2001) estimate that Q10 of the global terrestrial biosphere is 2.1 ± 0.7 by constraining with observations. In this study, the 2σ uncertainty range of Q10 is assumed to be between 1.5 and 2.5. For further discussion on the Q10 parameterization, see subsection on the limitations for the land model in ACC2.

The preindustrial CO₂ degassing from the ocean and the preindustrial land CO₂ uptake are addressed to modify the preindustrial equilibrium assumption (Section 2.1.1).

The prior information of the anthropogenic CH₄ and N₂O emissions is based on van

Aardenne et al. (2001). The data of van Aardenne et al. comprise the mean estimates between 1890 and 2000. On the basis of the curvatures of these emission profiles, the prior mean of the CH₄ emission is nonlinearly extrapolated from 1890 to 1750 by using a quadratic function. The prior mean of the N₂O emission is linearly extrapolated. Both of the CH₄ and N₂O emissions are fixed at zero in 1750 in accordance with the preindustrial quasi-steady state assumption. The associated uncertainty ranges shown in Table 3.2 are based on van Aardenne (personal communication, February 22, 2006). The global emission estimate of CH₄ dating back to 1860 (Stern and Kaufmann, 1998) is not used in this study.

The prior estimates of the natural CH₄ and N₂O emissions are based on Table 4.2 and Table 4.4 in IPCC (2001), respectively. The main source of uncertainty in the natural CH₄ emission is the emission from the wetland because of the lack of knowledge on the global wetland distribution (Section 2.2.2). The main source of uncertainty in the natural N₂O emission is the agricultural emission (Section 2.2.3).

The uncertainties in the atmospheric CH₄ and N₂O lifetimes are derived from the compilations of the corresponding lifetimes in major CTMs (IPCC, 2001, Tables 4.3 and 4.5).

The estimate of the radiative forcing associated with doubling the atmospheric CO₂ concentration is based on various radiative transfer calculations. It is estimated to be 4.37 W/m² in the Second Assessment Report and is revised to be 3.7 W/m² in the Third Assessment Report (IPCC, 2001, pp.356-357). The old estimate does not account for the stratospheric temperature adjustment and the short-wave forcing. IPCC (2001, pp.356-357) shows the range between 3.5 W/m² and 4.1 W/m² for 2×CO₂ forcing uncertainty. However, a sensitivity analysis of the ACC2 inversion indicates that the 2×CO₂ forcing cannot be well constrained with the climate sensitivity. In ACC2, the 2×CO₂ forcing is fixed at 3.7 W/m². The similar problem can be seen in constraining the ocean vertical diffusivity.

The missing forcing is defined as the sum of all the radiative forcings that are not properly accounted for by the other radiative forcings in ACC2. For example, the missing forcing includes the albedo forcing and the remaining aerosol forcings, which are not parameterized in the three classes of the aerosol forcings in ACC2 (Section 2.2.12). Thus, the uncertainty in the missing forcing essentially includes the uncertainty in the total radiative forcing. In the inversion, the missing radiative forcing also in part explains the natural variability of the temperature records (except for the ENSO-induced change after 1930 (Section 3.5.1)). The 2σ prior uncertainty range is assumed to be constantly 0.5 W/m² before 1900 primarily to explain the natural variability in the temperature change. Then the uncertainty range increases linearly to 1.0 W/m² in 2000 to account for the uncertainty in the aerosol forcing, which is consistent with the corresponding range in IPCC (2007, Figure SPM-2).

The rationals for such uncertainty ranges for the missing forcing before 1900 are as

follows. Attribution/detection studies have not so far agreed upon whether the surface temperature rise in the first half of the 20th century is due to natural variability or anthropogenic interference. If the 0.5°C rise in the surface air temperature in that period were to be decadal variability, the missing radiative forcing with a magnitude of about 0.5 W/m² would constantly be required to drive such a temperature rise in ACC2 with an assumed climate sensitivity of 4.5°C (Figure 2.6). The range of 0.5°C is also indicated in the temperature variability in the 1000-year control run of Community Climate System Model (CSM-1.4) (a coupled carbon cycle-climate GCM) (Doney et al., 2006, Figure 4a). Furthermore, the initial state of the system is not well-known and it is not completely equilibrated due to various natural forcings and internal dynamics. The problem of the equilibrium assumption in 1750 can be alleviated by the uncertainty of the missing forcing in such a magnitude.

Here we mention the estimates of solar forcing and volcanic forcing. The associated uncertainties are not addressed individually and are collectively included in the missing forcing uncertainty. The solar forcing in ACC2 is based on the solar irradiance reconstruction of Balmacela et al. (submitted). Solar irradiance reconstructions rely on the statistical analysis of the sunspot numbers recorded by historical documents and isotopic information recorded in tree rings (¹⁴C) and in ice cores (¹⁰Be). Balmacela's solar irradiance reconstruction is estimated to be smaller than the earlier solar irradiance reconstructions such as Lean et al. (1995) and Lean (2000). The scaling of the proxies to the total solar irradiance is subject to a large uncertainty and has recently been revised. In the Balmacela's reconstruction, the statistical analysis is combined with the underlying solar physics of Solanki et al. (2002). The Balmacela's reconstruction shows that the 11-year cycle produces the fluctuations of merely 0.1% of the total solar irradiance, leading to a minor climate response. The volcanic forcing used in ACC2 is adopted from Ammann et al. (2003) and discussed further in Section 3.5.2.

The climate sensitivity is defined as the final equilibrium global-mean surface air temperature change after an instantaneous CO₂ doubling from the preindustrial control state. The climate sensitivity is central to the discussion on the uncertainties in climate projections. The radiative transfer processes involving CO₂ are relatively well-known. However, the climatic feedback such as cloud formation is substantially different across models, resulting in the large uncertainty in the climate sensitivity (<http://www.met.rdg.ac.uk/~radiation/includes/radforc.html>). Throughout the first three IPCC reports, the estimate of the climate sensitivity (between 1.5°C and 4.5°C) has not been changed. The current GCMs around the world indicate the range of the climate sensitivity between 2.5°C and 4.0°C (IPCC Working Group I, 2004a). On the other hand, the inversion studies indicate that the peaks of the probability densities for the climate sensitivity range between 2°C and 3.5°C (Forest et al., 2002; Gregory et al., 2002; Knutti et al., 2002; Hegerl et al., 2006). The most recent summary of the climate sensitivity estimates from inversion approaches is in Räisänen (2007). In the inversion approach, the uncertainty in climate sensitivity depends on the

uncertainties in the aerosol forcing and the vertical ocean diffusivity. Probability densities derived from the inversion approach cover widely from less than 1°C to more than 6°C (e.g. Hegerl et al., 2006). Earlier inversion studies produce a long tail toward high climate sensitivity. GCM ensemble runs also produce a long tail reaching over 10°C (Stainforth et al., 2005). IPCC (2007, SPM) gives the best estimate of about 3°C in the range of 2.0°C to 4.5°C. Based on the literature cited above, the 2σ prior uncertainty range of the climate sensitivity is assumed to be between 0.5°C and 6.5°C (prior mean: 3.5°C) in the ACC2 inversion.

The vertical ocean diffusivity is subject to a large uncertainty. In the framework of the ACC2 inversion, the climate sensitivity and the vertical ocean diffusivity cannot be constrained simultaneously. It would require an explicit process description of the heat diffusion in each layer of the ocean to be constrained by the associated observation (Levitus et al., 2000). The ocean diffusivity is estimated to be $1 \text{ cm}^2 \text{ s}^{-1}$ (Munk, 1966; Simmons et al.; 2004). For the ACC2 inversion, the ocean diffusivity is fixed at $0.55 \text{ cm}^2 \text{ s}^{-1}$ (Elmar Kriegler, personal communication, March 1, 2006).

3.5 FACTORS INFLUENCING THE INTERANNUAL VARIABILITY

Two important factors that influence the interannual variability are the El Niño-Southern Oscillation (ENSO) and volcanic eruptions. The influences of ENSO on the surface air temperature and the atmospheric CO₂ concentration are statistically taken into account in the ACC2 inversion; The Southern Oscillation Index (SOI) and NINO3 index are used to identify ENSO-induced anomalies in the surface air temperature and the atmospheric CO₂ concentration, respectively. The uncertainty ranges of the CO₂, CH₄, and N₂O concentrations, missing forcing, and surface air temperature measurements are assumed to be larger in the ACC2 inversion when the Earth system is under the influence of large volcanic eruptions. Details are discussed in the following.

3.5.1 ENSO

ENSO is the dominant internal oscillation among others (e.g. North Atlantic Oscillation (NAO) and Pacific Decadal Oscillation (PDO)); ENSO is an oscillation in the coupled atmosphere-ocean system in the equatorial Pacific, which has a far reaching effect to the global carbon cycle and climate system through atmospheric teleconnections (McPhaden et al., 2006).

ENSO has a periodicity of three to seven years, with El Niño, a phase of ENSO, persisting usually one to three years. The opposite phase is termed La Niña. During El Niño years, the surface water of the eastern equatorial Pacific is relatively warm. The zonal SST gradient across the equatorial Pacific becomes less pronounced, weakening the tradewind over the equatorial Pacific. The thermocline is suppressed in the eastern Pacific, resulting in the depression or paucity of

upwelling, which would fuel the Peruvian coastal ocean with cold and nutrient-rich water during the normal years. The reduction in the upwelling leads to higher SST in the eastern Pacific, further weakening the tradewind. Such positive feedback is termed Bjerknes feedback (e.g. Neelin et al., 1998; Cane, 2005), which also holds for the La Niña phase. These amplifying loops are counteracted by internal ocean waves such as Kelvin waves and Rossby waves, which are generated in concurrence with the initiation of El Niño. They initially support the growth of El Niño but subsequently counteract it after being reflected at the boundaries (Neelin et al., 1998). The Bjerknes feedback in the atmosphere-surface ocean and the internal wave feedback in the subsurface ocean are combined to control the duration of the ENSO phases (McPhaden et al., 2006).

El Niño usually begins near the end of the year when the SST anomaly becomes largest. During El Niño years, as a result of the complex atmosphere-ocean processes, the global-mean surface air temperature is relatively high (Ropelewski, 1992). The responses of carbon cycle processes to El Niño are two folds (Jones et al., 2001; McPhaden et al., 2006). In the early stage of an El Niño, the CO₂ degassing from the equatorial Pacific, the largest ocean carbon source, decreases because of the depression of the upwelling off the Peruvian coast. In the later stage, the global terrestrial GPP decreases due to the temperature rise in the tropics and the precipitation decrease in tropical Asia and Australia. The plant and soil respiration increases due to the temperature rise in most parts of the globe (Jones et al., 2001). More prominently, the droughts and elevated temperature in the tropics increase the extent of wild fires (e.g. forest fire in Indonesia during the El Niño in 1997 and 1998). Overall, during El Niño the atmospheric CO₂ concentration initially drops due to the suppression of upwelling but subsequently rises due to the terrestrial carbon release. Jones and Cox (2001) demonstrates that the interannual variability in the atmospheric CO₂ concentration is largely controlled by ENSO during the period of 1967-1981, which has been free from large volcanic eruptions.

The intensity and phase of ENSO is captured by the two widely-used atmospheric and oceanic indices: SOI and NINO3. SOI is defined as the difference in the sea level pressure anomalies between Tahiti (17°S, 149°W, French Polynesia) and Darwin (12°S, 131°E, Australia) (<http://www.cru.uea.ac.uk/cru/data/soi.htm>). NINO3 is defined as the average of the mean sea surface temperature anomaly in the area of 150°W-90°W and 5°S-5°N (Kaplan reconstruction between 1856 and 1949; CPC (Reynolds OI SST) from 1950 to present, <http://climexp.knmi.nl/>). These ENSO indices are used to infer the influences of ENSO to the measurements of the surface air temperature and the atmospheric CO₂ concentration in the ACC2 inversion.

With regard to the influence of ENSO to the surface air temperature records, the SOI index is multiplied with the scaling factor (-0.063 for the ocean surface air temperature; -0.148 for the land surface air temperature (Kriegler, 2005, p.32) and then the scaled SOI indices are added to the ocean and land surface air temperature calculated from ACC2 so that the ENSO-related interannual

variability in the temperature measurements is explained. Such an ENSO adjustment for temperature records is applied after 1930. The SOI index exists as early as 1867, but the credibility of the SOI index is thought to be sufficiently high only after 1930. The SOI index requires a three- to six-month lead (Kriegler, 2005, Figure 2.4) or a four- to seven-month lead (Smith et al., 2003) to explain the surface air temperature change. Kriegler (2005) estimates that the optimum lead is four months. The pre-analysis of the ACC2 inversion results also indicate the optimum lead of four months. Thus, the lead of four months is adopted to calculate the annualized SOI index used for the ACC2 inversion.

With regard to the influence of ENSO to the atmospheric CO₂ concentration records, the relationship between NINO3 and the atmospheric CO₂ concentration records is statistically calculated in the model. Our approach is similar to Jones and Cox (2001), which obtained a regression line that explains the natural change in the atmospheric CO₂ concentration as a function of NINO3. In ACC2, the natural change in the atmospheric CO₂ concentration is computed as the total (anthropogenic and natural) change in the atmospheric CO₂ concentration (prior information) subtracted from the anthropogenic CO₂ emission (posterior information) and ocean and land CO₂ uptake (posterior information). The y-intercept and the slope of such a linear regression line are estimated concurrently with the inversion. Our approach uses the posterior information to be consistent with other parts of the model. In the pre-analysis of the ACC2 inversion, it was found that the optimum lead of NINO3 relative to the natural change in the atmospheric CO₂ concentration is seven months. Such a time lead is used to calculate the annualized NINO3 index used for the ACC2 inverse estimation. The ENSO adjustment for the atmospheric CO₂ concentration above is applied from 1960 onward although the NINO3 index exists in as early as 1857. Prior to 1960, the atmospheric CO₂ concentration measurements used in the ACC2 inversion are based on ice core sampling (Etheridge et al., 1996), where the interannual variability due to ENSO is largely smoothed out by spline fitting. The atmospheric CO₂ records are highly perturbed by large volcanic eruptions. Thus, we exclude the period from the line fitting calculation when the absolute magnitudes of the volcanic forcings are less than 0.5 W/m².

Our predictive capability for ENSO cycle is still limited (Cane, 2005; van Oldenborgh et al., 2005). Dynamical models do not produce significantly better forecasts than statistical models (McPhaden et al., 2006). The interaction between the future warming and ENSO is currently under debate (e.g. Neelin et al., 2003; Cane, 2005; van Oldenborgh et al., 2005). The association of volcanic eruptions with ENSO is debated (Robock, 2000; de Silva, 2003; Adams et al., 2003).⁶⁵ Thus, the effect of ENSO is accounted for in the past mode of ACC2.

⁶⁵ The paleoclimate information of ENSO dating back to 130,000 years ago (Tudhope et al., 2001) statistically supports the hypothesis that volcanic eruptions produce a state in the atmosphere-ocean system in the equatorial Pacific that triggers El Niño-like conditions (de Silva, 2003; Adams et al., 2003).

3.5.2 Volcanic Eruptions

The second half of the 20th century saw some major volcanic eruptions (Agung, Indonesia in 1963; El Chichon, Mexico in 1982; Pinatubo, The Philippines in 1991). The largest eruptions for the past 250 years are those of Tambora, Indonesia in 1815 and Krakatau, Indonesia in 1883. The document-based records of past large volcanic eruptions⁶⁶ are given by Siebert and Simkin (2006) (<http://www.volcano.si.edu/world/largeeruptions.cfm>). Several indices of the size of volcanic eruptions are discussed in Zielinski (1995).

Large volcanic eruptions left footprints in global climate records (Robock, 2000). They emit SO₂ to the stratosphere where SO₂ is converted into sulfate aerosols, shading the Earth surface. A recent remarkable example is the Pinatubo eruption, which was followed by the drop in the global-mean temperature and the slowdown in the atmospheric CO₂ concentration rise (Jones and Cox, 2001). The other climatic relevance of volcanic eruptions is their possible association with the ENSO cycle (Section 3.5.1).

Volcanic eruptions add ‘dips’ to past records of the Earth system, influencing the uncertainty estimates derived from the inverse calculation. Wigley et al. (2005) inferred the climate sensitivity using observations during periods influenced by major volcanic eruptions.

Problems and issues associated with the estimate of the past volcanic forcing are discussed in the following. The climatic influence due to large volcanic eruptions typically lasts one to three years. Given the short time scale of the volcanic forcing, the volcanic forcing is coarsely treated in ACC2. Additionally, the temporal evolution of the volcanic forcing depends on the locations of the eruptions (Oman et al., 2005). Such regional features of the volcanic forcing cannot be resolved in ACC2.

The estimate of the past volcanic forcing is based on the sulfate aerosol concentration in ice cores in Greenland (e.g. the GISP2 and Crete ice cores) and Antarctica, instrumental and satellite radiation measurements, and the volcanic eruption catalogue (Siebert and Simkin, 2006). It is generally assumed that, when sulfate signals are found in the ice cores of both poles simultaneously, the corresponding volcanic eruptions are considered markedly influencing the global climate. The estimate of the volcanic forcing (e.g. Bertrand et al., 2002; Ammann et al., 2003; Crowley, 2003) depends on the choice of ice cores (Jones and Mann, 2004, Figure 7). Uncertainties in the volcanic forcing arise from the uncertain relationship between the stratospheric sulfate aerosol load and the sulfate aerosol deposited at the surface and also the uncertain relationship between the stratospheric

⁶⁶ Volcanic Explosivity Index (VEI) is an integrated index for the size of a volcanic eruption based on the compilation of various qualitative data and subjective descriptions of observers in the Smithsonian catalogue. VEI should not be directly taken as the indication for climatic influence from volcanic eruptions, which should also depend on the location, quality of the magma, eruption heights, and other factors. A more climate-relevant index is Ice-core Volcanic Index (IVI), which is based on the amount of sulfate aerosols found in the ice cores in the both pole.

aerosol optical depth and the radiative forcing. The volcanic forcing is affected by the seasonably changing stratospheric transport, which is accounted for only in Ammann et al. (2003). ACC2 uses the volcanic forcing of Ammann et al. (2003).

There are some apparent contradictions between historical temperature reconstructions and volcanic eruption records; temperature does not drop after some large volcanic eruptions (e.g. Tambora and Krakatau eruptions). To explain such puzzling records, the diffuse radiation hypothesis (Robock, 2005) has been put forward. Diffuse radiation is produced from the enhanced forward scattering of the solar radiation due to the stratospheric sulfate aerosols. The photosynthesis of terrestrial plants is more efficient under diffuse radiation than direct radiation because of the reduction in shade area and the saturation level with respect to light intensity (e.g. Farquhar and Roderick, 2003). Thus, the drop in the atmospheric CO₂ buildup after volcanic eruptions (Jones and Cox, 2001) can be attributed to the increase in the land carbon storage due not only to the temperature-driven terrestrial respiration reduction (Lucht et al., 2002) but also to the diffuse radiation-driven photosynthesis enhancement (Gu et al., 2003). As the terrestrial biosphere shows enhanced growth due to high diffuse radiation during volcanic eruptions, temperature reconstructions based on tree rings are possibly biased upward, underestimating the temperature drop after eruptions.

The atmospheric CH₄ concentration growth increased after the Pinatubo eruption (Dlugokencky et al., 1998). This is caused by a reduction in the atmospheric OH concentration, as the reaction with OH is the main sink of CH₄. The production of OH depends on the photodissociation of O₃ by solar UV. Solar UV is scattered by sulfate aerosols after the volcanic eruption (Dlugokencky et al., 1996). The rate of the atmospheric N₂O concentration change decreased after the Pinatubo eruptions due to the enhanced exchange between the troposphere and the stratosphere driven by the heating from the volcanic aerosols (Schauffler and Daniel, 1994). The mechanisms to control the CH₄ and N₂O concentration changes due to volcanic eruptions are not parameterized in ACC2.

Given the foregoing arguments associated with the different volcanic forcing estimates and far reaching effects of volcanic eruptions in the Earth system, the uncertainty ranges of the CO₂, CH₄, and N₂O concentrations, the missing forcing, and the surface air temperature measurements are quadrupled when the absolute magnitude of the volcanic forcing is larger than 0.5 W/m².⁶⁷ Numerically, such modifications of the uncertainty ranges decrease the weights for the associated misfits caused by major volcanic eruptions. This treatment partly alleviates the problems discussed above.

⁶⁷ The treatment of the Earth system influence from volcanic eruptions here is just one approach. Kriegler (2005) halves the magnitudes of the volcanic forcing because of the time scale problem of the fast-conversing volcanic forcing.

Table 3.1. Data defined in the ACC2 inverse calculation

* Four times larger uncertainty range is assumed when the volcanic forcing is stronger than 0.5 W/m².

Names	Periods	Measurement types	Temporal resolutions	2 σ measurement uncertainties	Data sources
Atmospheric CO ₂ concentration	1750-1968	Ice core sampling (Law Dome, Antarctica)	75-year cutoff spline fit with 5-year intervals (1750-1830) 25-year cutoff spline fit with 1-year intervals (1832-1968) Linear interpolations between the data points	*1.2 ppm	Etheridge et al. (1996)
	1969-2000	Station measurements (Mauna Loa, Hawaii)	Annual fit	*0.8 ppm (0.2 ppm in the literature)	Keeling et al. (2005)
Atmospheric CH ₄ concentration	1750-1850	Ice core sampling (Law Dome, Antarctica; Summit, Greenland)	75-year cutoff spline fit with 10-year intervals (1750-1900) 12.5-year cutoff spline fit with 2-year intervals (1900-1984) Linear interpolations between the data points	*5 ppb	Etheridge et al. (1998)
	1851-1983				Etheridge data compiled by Hansen and Sato (2004) Etheridge et al. (1998)
	1984-2000	Station measurements (CMDL global air sampling network)	Annual fit	*12 ppb (3 ppb in the literature)	Dlugokencky data compiled by Hansen and Sato (2004) for mean estimates Masarie et al. (2001, Table 1) for uncertainties
Atmospheric N ₂ O concentration	1750-1961	Ice core sampling (Summit, Greenland)	300-yr cutoff spline fit with 1-year intervals	*Time variant	Flueckiger (personal communication)
	1962-1977			*Interpolation	Hansen and Sato (2004)
	1978-2000	Station measurements (CMDL global air sampling network)	Annual fit	*2.0 ppb (0.5 ppb in the literature)	Hansen and Sato (2004) for mean estimates Masarie et al. (2001, Table 1) for uncertainties
Ocean CO ₂ uptake	1750-1860	N/A	Linear extrapolation to the origin from 1860 to 1750	Average uncertainties between 1865 and 2000	N/A
	1861-2000	C ⁴ MIP GCMs/EMIC	10-year moving average	Maxima and minima of GCMs runs (=1 σ)	Friedlingstein et al. (2006)
Land CO ₂ uptake	1750-1860	N/A	Linear extrapolation to the origin from 1860 to 1750	Average uncertainties between 1865 and 2000	N/A
	1861-2000	C ⁴ MIP GCMs/EMIC	10-year moving average	Maxima and minima of GCMs runs (=1 σ)	Friedlingstein et al. (2006)
Surface air temperature change	1750-1855	Multi-proxy	1-year intervals	*0.36°C	Jones et al. (1998) for mean estimates Mann and Jones (2003) for uncertainties
	1856-2000	Instrumental measurements	Annual fit	*0.20°C (1856-1860) *0.05°C (2000) *Linear interpolation between the periods	Jones et al. (2006)

Table 3.2. Parameters defined in the ACC2 inverse calculation

* Four times larger uncertainty range is assumed when the volcanic forcing is stronger than 0.5 W/m².

Names	Prior estimates	2 σ prior uncertainties	Posterior estimates
Anthropogenic CO ₂ emission due to fossil fuel combustion (time series)	Marland et al. (2006) between 1750 and 2000	±8% of the prior mean (Marland et al., 2006)	Figure 4.1.1
Anthropogenic CO ₂ emission due to land use change (time series)	Houghton (2003) between 1850 and 2000 Linear extrapolation between 1750 and 1849 Zero emission assumed in 1750	±100% of the prior mean (±50% in Houghton (2003))	Figure 4.1.2
Anthropogenic CH ₄ emission (time series)	van Aardenne et al. (2001) between 1890 and 2000 Nonlinear extrapolation between 1750 and 1890 Zero emission assumed in 1750	±50% in 2000, ±100% in 1970 ±150% between 1890 and 1950 Linear interpolations between the periods Absolute uncertainty ranges assumed constant before 1890 (John van Aardenne, personal communication)	Figure 4.1.6
Anthropogenic N ₂ O emission (time series)	van Aardenne et al. (2001) between 1890 and 2000 Linear extrapolation between 1750 and 1890 Zero emission assumed in 1750	±50% in 2000, ±100% in 1970 ±150% between 1890 and 1950 Linear interpolations between the periods Absolute uncertain ranges assumed constant before 1890 (John van Aardenne, personal communication)	Figure 4.1.7
Missing radiative forcing (time series)	Zero forcing assumed between 1750 and 2000	*±0.5 W/m ² between 1750 and 1900 *±1.0 W/m ² in 2000 *Linear interpolation between 1900 and 2000	Figure 4.1.10
Preindustrial ocean CO ₂ uptake (constant)	-0.24 GtC/year (net degassing) (-0.48 GtC/year in Mackenzie and Lerman (2006))	Between -0.48 and 0.0 GtC/year	-0.35 GtC/year
Preindustrial land CO ₂ uptake (constant)	0.30 GtC/year (net uptake) (0.36 - 0.6 GtC/year in Mackenzie and Lerman (2006))	Between 0.0 and 0.60 GtC/year	0.12 GtC/year
Beta factor for CO ₂ fertilization	0.4 (0.287 (Meyer et al., 1999; Kicklighter et al., 2001), 0.4 (Gitz and Ciais, 2003), 0.45 (Brovkin et al., 1997), and 0.15 to 0.6 (Kohlmaier et al., 1987))	Between 0.1 and 0.7 (references in left column)	0.59
Preindustrial mixed layer temperature	19.59°C (Hoffert et al. (1981) pp.290-291; Sundquist and Plummer (1981) p.267)	Between 13.59 and 25.59°C	19.9°C
Atmosphere-mixed layer temperature scaling factor	0.5	Between 0.0 and 1.0	0.352
Q10 for heterotrophic respiration	2.0 (Jones and Cox, 2001; Tjoelker et al., 2001)	Between 1.5 and 2.5 (references in left column)	1.18
Natural CH ₄ emission (constant)	210 Mt(CH ₄)/year (IPCC, 2001, Table 4.2)	Between -30 and 450 Mt(CH ₄)/year (IPCC, 2001, Table 4.2)	320 Mt(CH ₄)/year
Natural N ₂ O emission (constant)	10.2 Mt(N)/year (IPCC, 2001, Table 4.4)	Between 7.8 and 12.6 Mt(N)/year (IPCC, 2001, Table 4.4)	11.3 Mt(N)/year
CH ₄ lifetime with respect to OH depletion	9.6 year (IPCC, 2001, Table 4.3)	Between 5.4 and 13.8 year (IPCC, 2001, Table 4.3)	8.53 year
N ₂ O lifetime	110 year (IPCC, 2001, Table 4.5)	Between 83 and 137 year (IPCC, 2001, Table 4.5)	114 year
Climate sensitivity	3.5°C (Forest et al., 2002; Gregory et al., 2002; Knutti et al., 2002; IPCC Working Group I, 2004a; Kriegler, 2005; Stainforth et al., 2005; Hegerl et al., 2006; IPCC, 2007, SPM; Räisänen, 2007)	Between 0.5 and 6.5°C (references in left column)	4.1°C

Table 3.3. Terminologies used in inverse estimation for ACC2

The terminologies referring to the information on parameters and data before/after an inverse calculation are not symmetrically defined. Nevertheless, such terminologies are commonly used and thus adopted in this study (Section 3.3.2).

	Information on parameters	Information on data	Information on both parameters and data
Before inversion	Prior information (or prior)	Measurement information (or measurements)	Prior information (or prior)
After inversion	Posterior information	Posterior information	Posterior information

Figure 3.1. Two-dimensional illustration of inverse estimations (after Tarantola (2005, Figure 1.12))

This figure illustrates the concept of the Tarantola's inverse estimation theory. The joint probability density, $\rho(\mathbf{d}, \mathbf{m})$, in left panel shows the prior information on parameters and data. Its marginal probability densities with respect to parameters, $\rho_M(\mathbf{m})$, and data, $\rho_D(\mathbf{d})$, are also shown along the respective axes. The probability density, $\Theta(\mathbf{d}, \mathbf{m})$, in middle panel shows the theoretical information between parameters and data. Note that, in the theoretical probability density, there is no information on parameters and data by themselves. The conjunction of the prior information, $\rho(\mathbf{d}, \mathbf{m})$, in left panel and the theoretical information, $\Theta(\mathbf{d}, \mathbf{m})$, in middle panel gives the joint posterior information on parameters and data, $\sigma(\mathbf{d}, \mathbf{m})$. The marginal posterior information with respect to parameters, $\sigma_M(\mathbf{m})$, shown along the horizontal axis is generally the solution of an inverse estimation. See Section 3.2.2.

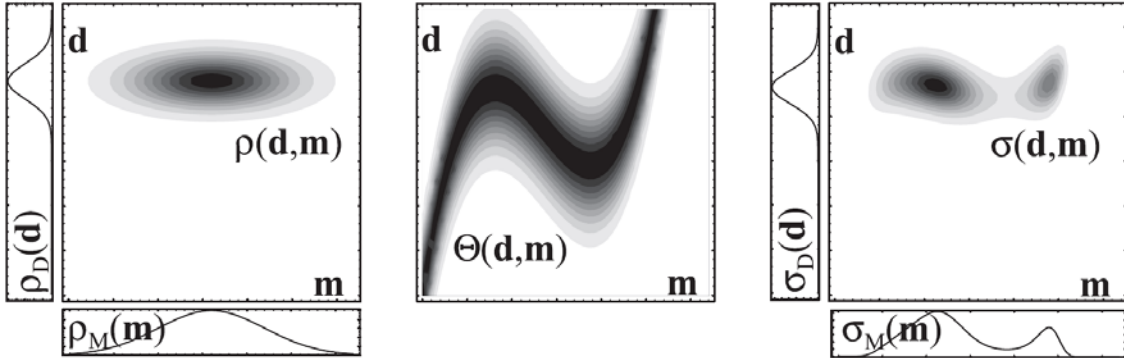


Figure 3.2. Two-dimensional illustration of theoretical information and modelization uncertainties (after Tarantola (2005, Figure 1.4)).

When no modelization uncertainties are assumed (as many practical applications use exact functional relationships), the theoretical information between parameters and data is represented by a line, $\mathbf{d} = \mathbf{g}(\mathbf{m})$, (left panel). In more general settings where modelization uncertainties are explicitly taken into account, the theoretical information is expressed in a form of the probability density, $\theta(\mathbf{d}|\mathbf{m})$, (right panel), which corresponds to the middle panel in Figure 3.1. See Section 3.2.2.

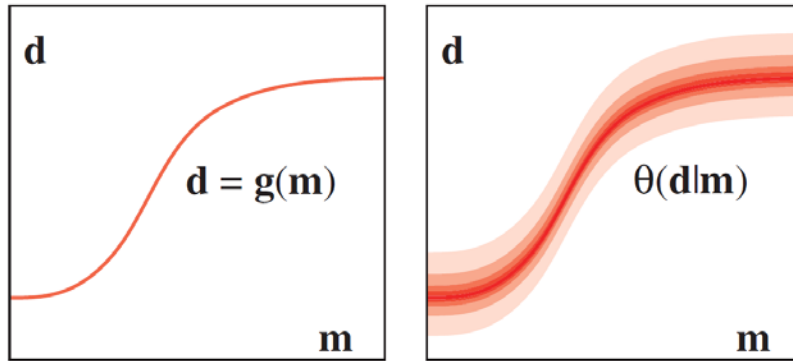


Figure 3.3. Two-dimensional illustration of the nonlinearities in the theoretical relationship between parameters and data (after Tarantola (2005, Figure 3.2)).

Different degrees of nonlinearity are shown in five steps. In top left panel, only the prior information on parameters and data are shown. In top middle panel, the theoretical information (or the functional relationship in a model) is linear and exact. In top right panel, the functional relationship in the model can be linearly approximated around the peak of the prior probability density of parameters. Such an approximation is not valid in bottom left panel as no measurement information would enter. Thus, the functional relationship is linearly approximate linearly around the peak of the measurement probability density (the maximum likelihood estimate). Neither of the linear approximation is possible in bottom middle panel. The bottom right panel shows the most extreme case of nonlinearity where the theory discussed in Section 3.2.2 cannot apply.

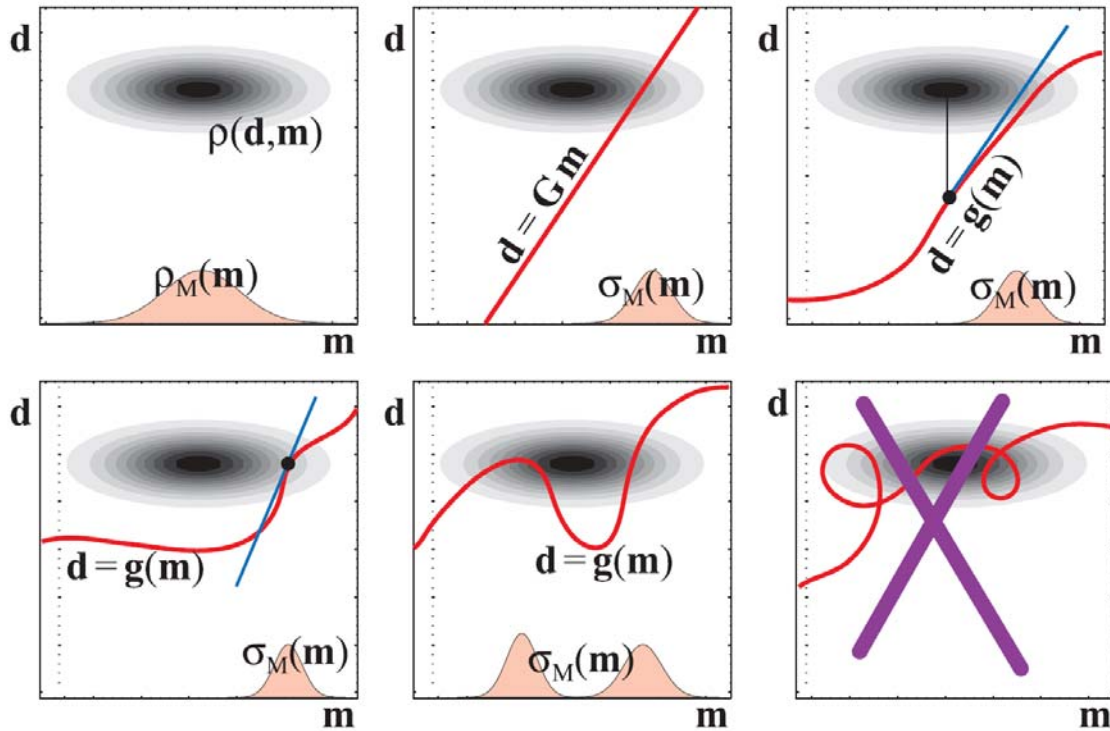
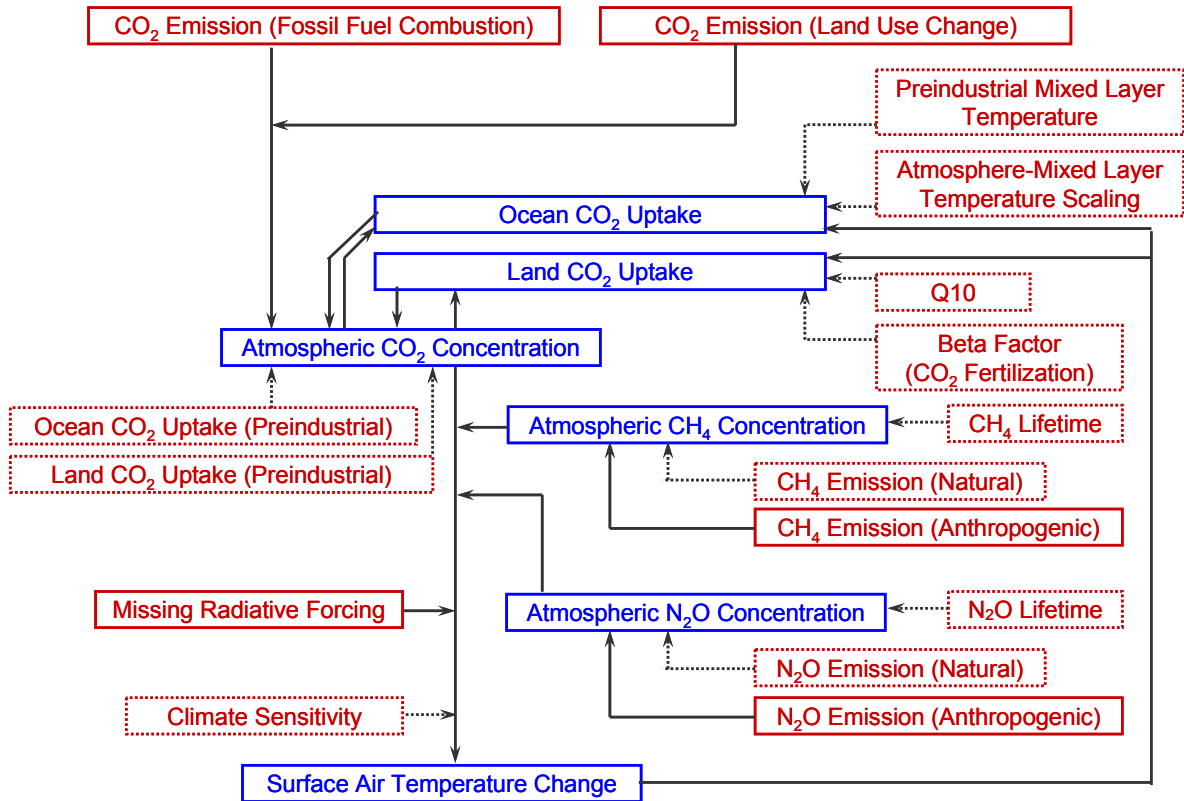


Figure 3.4. The relationships between parameters and data in the ACC2 inverse estimation

Red and blue boxes represent parameters and data, respectively. Solid and dotted boxes represent time series and constants, respectively.



4 RESULTS AND CONCLUSIONS

The results of the ACC2 past mode run are discussed in Section 4.1. The ACC2 inverse calculation results are in comparison with the ACC2 forward calculation results in which all the parameters are fixed at their prior values (Figure 4.1). In Section 4.2, the results of the ACC2 future mode run are discussed by comparing with the corresponding results in IPCC (2001) for six emission scenarios (SRES (Nakićenović et al., 2000)) (Figures 4.2 to 4.5). This section is concluded with future perspectives for the development of ACC2. More details of the inversion results are shown in Appendix B: carbon storage in the ocean and land reservoirs (Figures B.1, B.3, and B.4), the concentrations of marine carbonate species (Figure B.2), historical evolutions of the individual radiative forcings (Figure B.6), the land-ocean separations of the radiative forcing and the surface air temperature (Figure B.7), and the influence of ENSO to the atmospheric CO₂ concentration (Figure B.5) as well as the surface air temperature (Figure B.8). Within the scope of the model description, the results and findings are only highlighted as further discussions are provided in Tanaka et al. (2007).

4.1 RESULTS FOR PAST MODE SIMULATION

The inverse estimation for ACC2 has been set up as it is described in Section 3. Specifically, all the parameters and data in Tables 3.1 and 3.2 are put into the inverse estimation. The inverse calculation takes care of the ENSO-induced changes in the atmospheric CO₂ concentration and the surface air temperature (Section 3.5.1). The prior uncertainty ranges for various time series are adjusted during the periods influenced by large volcanic eruptions (Section 3.5.2). The inverse calculation results are shown in comparison with the forward calculation results by fixing all the parameters at the respective prior values.

Visual inspection of Figure 4.1 shows that most of the posterior estimates are contained within their 2σ prior uncertainty ranges. Comparison between the inverse and forward projections demonstrates how the ACC2 inverse calculation effectively synthesizes various information on the parameter estimates, measurements, and physical-biogeochemical laws.

The posterior estimates of the land use CO₂ emission (Figure 4.1.2) are substantially lower than the corresponding prior estimates for the last 60 years. Similar results can be seen in the posterior estimates of the fossil fuel CO₂ emission (Figure 4.1.1). The reduction in the CO₂ emission is larger for the land use part because the deviations from the prior estimates are penalized less for

the land use CO₂ emission than for the fossil fuel CO₂ emission. The posterior estimates of the ocean and land CO₂ uptake and the atmospheric CO₂ concentration are relatively close to the respective measurements. The posterior value of the beta factor is estimated to be 0.59, which is high in the prior range between 0.1 and 0.7. The results above are in line with Friedlingstein et al. (2006). The estimates of the land use CO₂ emission (Houghton, 2003) are so high that, to explain the observed atmospheric CO₂ concentration, the terrestrial biosphere has to take up excessive carbon by strong CO₂ fertilization. Keep in mind that, in view of the previous inversion studies, the prior uncertainty ranges of the land use CO₂ emission in ACC2 are taken twice as large as the ranges suggested in Houghton (2003). However, the results here should not be regarded just as an indication for lower estimates of the land use CO₂ emission. The knowledge on the response of the global terrestrial biosphere to the changes in the atmospheric CO₂ concentration and climate are not well-established (Friedlingstein et al., 2006). Some missing carbon cycle processes are under debate – it is not known whether soil erosion leads to net carbon release or uptake (Lal, 2005). Therefore, the indication from the inversion results should rather be that the substantially low land use CO₂ emission reflects the overall uncertainties in the historical carbon budget.

The posterior value of Q10 is estimated to be 1.18, which is beyond the 2 σ prior uncertainty range between 1.5 and 2.5 (Sections 2.1.3 and 3.4; Table 3.2). However, such a posterior estimate is not necessarily unrealistic. The prior estimate of Q10 is based on a compilation of field measurements (Tjoelker et al., 2001). The value of Q10 on the global scale can only be speculated although global modelling studies typically assume the value of 2.0. It can be argued that the low Q10 value obtained from the ACC2 inversion reflects the biospheric response to not only the temperature change but also the soil moisture change, which is not described in ACC2. With global warming the contrast between wet and dry regions will increase as virtually all GCMs have demonstrated (Wang, 2005). Precipitation and probably also soil moisture will increase in most of the presently wet regions and decrease in the subtropical regions. More water in presently wet soils will decrease heterotrophic respiration because of the oxygen limitation while less water in presently dry soils will also reduce heterotrophic respiration because of the water limitation. Thus, the temperature effect and the soil moisture effect on the heterotrophic respiration cancel out each other, providing an argument for the low Q10 estimate in the ACC2 inversion results.

The deviations associated with the atmospheric CO₂ concentration (Figure 4.1.3) show decadal variability. There is a plateau in the rise of the atmospheric CO₂ concentration between 1940 and 1960. The temperature rise also stalls during this time and even thereafter. Mechanisms that led to the ‘stagnation’ are in dispute. An inversion study (Trudinger et al., 2002) shows that the slowdown in the atmospheric CO₂ concentration rise is caused by the change in the large-scale ocean circulation. Such a halt does not appear in the prior estimates of the ocean CO₂ uptake based on the C⁴MIP runs (Section 3.3).

The drop in the forward estimates of the atmospheric CO₂ concentration around 1810 is caused by the extremely large terrestrial CO₂ uptake (Figure 4.1.5) when the heterotrophic respiration is drastically reduced by the temperature drop after large volcanic eruptions (Figures B.4 and B.6 for inversion estimates). In the forward run, the heterotrophic respiration is more sensitive to the temperature change since the value of Q10 is fixed at the prior value of 2.0.

The forward projections of the CH₄ and N₂O concentrations (Figures 4.1.8 and 4.1.9) are incorrectly low primarily because the prior estimates of their natural emissions are too low to explain the trend of the concentration measurements. The results here point to a need for better knowledge on the natural CH₄ and N₂O emissions (Table 3.2).

The large downward spikes in the total radiative forcing (Figure 4.1.10) are the signatures of volcanic eruptions (Figure B.6). The inverse calculation shows that some strong volcanic forcing signals between 1750 and 1850 are offset by the positive missing forcing because the reconstructed temperature does not sufficiently drop during the same periods (Figure 4.1.11). It is still a mystery why there are no large temperature drops after the Tambora eruption in 1815. A diffuse radiation hypothesis (Robock, 2005) put forward to explain such seemingly contradicted records is that the tree ring proxies used for the temperature reconstruction are biased by the plant growth enhanced by the diffuse radiation (Section 3.5.1). If this hypothesis is true, the temperature would have actually been lower after the eruption than what the proxies directly suggest. The growth of the atmospheric CO₂ concentration indeed slowed down after the Pinatubo eruption in 1991. The inverse calculation indicates that, because the suppression of the heterotrophic respiration due to the cooling after the eruption was not sufficient to explain the observed CO₂ concentration (Figures 4.1.3 and 4.1.5), the land use CO₂ emission are drastically reduced after the eruption (Figure 4.1.2). The unusually low land use CO₂ emission can be explained by the enhanced plant growth due to diffuse radiation. However, evidences are not yet conclusive as there are large discrepancies among different volcanic forcings and temperature reconstructions (Jones and Mann, 2004, Figures 7 and 8).

The foregoing analysis of the ACC2 inversion results not only reaffirms the existing large uncertainties in the parameters and data but also raises the problem of possible ill-representation of the processes. Acknowledging that, we accept the results of the ACC2 inverse calculation as the synthesis of all the available knowledge and apply such results for future projections.

4.2 RESULTS FOR FUTURE MODE SIMULATION

Results of the ACC2 future mode runs using six different emission scenarios (SRES (Nakićenović et al., 2000)) are shown in Figures 4.2 to 4.5 and Table 4.1. Visual inspection of the figures shows that the projections of the ACC2 future mode run are compatible with the corresponding projections in IPCC (2001, Appendix II) and WMO (2003, Table 1-16). Differences between the ACC2 projections

and the IPCC/WMO projections can be well explained as follows.

The atmospheric CO₂ concentration projections simulated from ACC2 (Figure 4.2) are in the low ranges of the corresponding IPCC projections using IASM and Bern-CC for all the six emission scenarios (Figure 4.2). ACC2 uses a relatively high CO₂ fertilization ($\beta = 0.59$) and a relatively low temperature sensitivity to the heterotrophic respiration ($Q_{10} = 1.18$) as obtained from the inverse calculation (Table 3.2). Such parameter settings in ACC2 are in line with the settings for the low case simulations of IASM and Bern-CC. Thus, the ACC2 projections are compatible with the projections of ISAM and Bern-CC.

The atmospheric CH₄ concentration projections obtained from ACC2 (Figure 4.3.2) are systematically lower than the corresponding IPCC projections, which are based on the OxComp workshop CTMs (IPCC, 2001, Table 4.10). The dynamics between CH₄ and OH are similar because the parameterizations for CH₄ and OH in ACC2 are tuned to the outputs of such CTMs (Section 2.2.2). The relatively low CH₄ concentration projections in ACC2 can be attributed to the combined effect of the lower CH₄ lifetime with respect to OH depletion (= 8.5 years) and the higher natural CH₄ emission (= 320 Mt(CH₄)/year) obtained from the ACC2 inverse calculation (IPCC, 2001, Tables 4.2 and 4.3). As a result of the lower CH₄ concentration projections, the relative OH concentration projections (Figure 4.3.35) are higher in ACC2 than in IPCC (2001).

Conversely, the N₂O concentration projections simulated from ACC2 (Figure 4.3.3) are higher than the corresponding IPCC projections. The feedback of the N₂O concentration to its own lifetime in ACC2 is similar to the feedbacks in the CTMs (Section 2.2.3). The relatively high N₂O concentration projection in ACC2 can be attributed to the combined effect of the higher N₂O lifetime (= 114 years) and the higher natural N₂O emission (= 11.3 Mt(N)/year) obtained from in the inverse calculation (IPCC, 2001, Tables 4.4 and 4.5).

The differences in the projections for the halocarbon concentrations between ACC2 and IPCC/WMO (Figures 4.3.5 to 4.3.33) are mainly due to the differences in the atmospheric lifetimes. The lifetimes in ACC2 are up-to-date with respect to WMO (2003, Table 1-6) and IPCC (2005, Table 2.6).

For non-ODS halocarbons and SF₆ (Figures 4.3.4 to 4.3.17), same emission scenarios are used for the A1B, A1T, and A1FI scenarios (A1 family). However, the differences in the concentration projections for the A1 family scenarios exist because of the differences in the relative OH concentration projections. The lifetimes of halocarbons containing at least one hydrogen atom are defined as functions of the relative OH concentration (Section 2.2.5). For ODS halocarbons (Figures 4.3.18 to 4.3.33), the same emission scenario is used for all the six scenarios. Because ODS halocarbons are not removed by OH, there are no differences in the concentration projections of ODS halocarbons for the six scenarios.

The mismatch in the projections of the tropospheric O₃ concentration (Figure 4.3.36) are

owing to the fact that errors in the IPCC calculation of the tropospheric O₃ concentration projection are not properly corrected even though the modification for error corrections is suggested (IPCC, 2001, Table 4.11).

The basic relationships in the concentration projections between ACC2 and IPCC/WMO hold for the radiative forcing projections (Figure 4.4). The radiative forcings of most of the agents (except for CO₂, CH₄, and N₂O) are defined linearly with the respective concentrations scaled with the individual radiative efficiencies. The radiative efficiencies in ACC2 are up-to-date with respect to WMO (2003, Table 1-6) and IPCC (2005, Table 2.6), which give rise to slight differences for the radiative forcing projections of some halocarbons. As for the solar forcing (Figure 4.4.38), from 2030 onward it is assumed to be equal to the average solar forcing of the 20th century. The solar forcing between 2000 and 2030 is linearly interpolated.

The total radiative forcing projected from ACC2 (Figure 4.5.1) is lower than the corresponding IPCC total radiative forcing for the six scenarios primarily because the CO₂ radiative forcing projected from ACC2 is in the low IPCC ranges as can be inferred from the CO₂ concentration projections (Figure 4.2). On the other hand, the temperature change projections calculated from ACC2 (Figure 4.5.2) are estimated to be higher than the IPCC projections also for the six scenarios. It is not possible to identify exact reasons for the discrepancy because the IPCC results are the averages of the outputs from several simple models with different parameter setups (IPCC 2001, Table 9.A1). Nevertheless, we speculate that the primary reason is the climate sensitivity calculated by ACC2 (= 4.1°C) as the outcome from the inverse calculation, which is substantially higher than the average of the estimates of the climate sensitivity used in the ensemble of simple models.

Clarification of the differences between IPCC projections and the present results is an important requirement for the practical application of ACC2. The differences between the ACC2 projections and the IPCC/WMO projections are all explained above. In particular for the atmospheric CO₂ concentration and temperature change, the differences in the projections emerge directly from the differences in the approaches. While the IPCC projections are based on some representative parameter values, the ACC2 projections consistently uses the parameter values obtained from the inverse calculation.

4.3 CONCLUDING REMARKS AND FUTURE PERSPECTIVES

ACC2 is the third generation of the simple models developed in Germany with various international collaborations. ACC2 is fully up-to-date with respect to the current literature and refined with detailed processes compared to the two predecessor models (NICCS (Hooss, 2001); ICM (Bruckner et al., 2003)). ACC2 could serve as a prototype for complex Earth system models, in particular as a

tool to explore uncertainties in the Earth system.

The most remarkable achievement for the development of ACC2 is the implementation of the inversion scheme. Our inversion approach is the first attempt to perform an inversion for the Earth system. The ACC2 inversion approach limits itself to the global-annual-mean information and produces one-point estimates for the parameters and data (corresponding to the cost function minimum). Our approach is complementary to the approach computing probability densities (e.g. Forest et al., 2002; Gregory et al., 2002; Knutti et al., 2002; Hegerl et al., 2006). Although the probability densities show the extent of the knowledge on uncertainties, the number of uncertainties considered in the probability density approach is limited to several due to the computational requirement. On the other hand, our inversion approach exhaustively accounts for a large number of uncertainties even in each point of time series independently although the associated interdependencies of the large number of uncertainty estimates give bias to the inversion solution and are extremely complex to analyze. Nevertheless, our best guess of the uncertainty estimates provides straightforward interpretation, appealing to further scientific applications (e.g. Tanaka et al., 2006b; Tanaka et al., 2007).

Under the probabilistic inverse estimation theory (Tarantola, 2005; Figure 3.1), we have synthesized the existing scientific evidences comprising various observational databases, parameter estimates, and physical-biogeochemical laws. The ACC2 inverse calculation successfully reproduces a plausible evolution of the Earth system between the year 1750 and 2000 and generates the best guess of parameters (Figure 4.1 and Tables 3.1 and 3.2). The comparison between the inverse calculation and the forward calculation shows how effectively various pieces of information are integrated. Under the Tarantola's theory, assumptions in the ACC2 inverse calculation are thoroughly extracted and discussed (Section 3.2.2).

At the present level of the development and analysis of the inverse estimation, our approach achieves the attainable limits of our knowledge of the Earth system. The estimate of the land use CO₂ emission is not well-known as the bottom-up approach (Houghton, 2003) and the inversion approach (including ours) point to different magnitudes in particular for the past 50 years. Missing carbon cycle processes such as soil erosion (Lal, 2005) need to be investigated further to balance the historical carbon budget. We confirm that the uncertainties in the natural CH₄ and N₂O emissions are substantial. Both the radiative forcing and temperature reconstructions are subject to large uncertainties. Some contradictions between the volcanic forcing and temperature drops may be explained by the diffuse radiation hypothesis (Robock, 2005).

The results of the inverse calculation contain the parameter estimates and model state for the year 2000, on the basis of which the future evolutions of the Earth system are projected up to 2100 (Figures 4.2 to 4.5). On the ground of our consistent treatment of the uncertainties from the past to the future, we contend that our approach is more rigorous than IPCC (2001), where the

ranges of future projections are produced by picking representative parameter values in simple models.

The current stage of the development of ACC2 is sufficient for applications. However, ACC2 encompasses only limited aspects in the Earth system processes even considering at the global-annual-mean level. Further improvements can be done in the inversion methodology. We conclude this document with the following list of future tasks:

- Analyze the interdependencies of the uncertainty estimates including the parameters and data in time series. Cross-correlations can be partly accounted for by auto-regressive models.
- Consider isotopic data to provide additional constraints on carbon budgets.
- Complete the development of the sea level projection component. The thermal expansion calculation by DOECLIM can be combined with the parameterization of the sea level rise (IPCC, 2001, Appendix 11.1).
- Increase the robustness of the inversion against outliers in the misfits (Assumption 5 in Section 3.2.2).
- Enhance the numerical efficiency of the model. Scaling the variables and equations need to be done manually.
- Perform a global solution search. The improvement of the numerical efficiency of the model will enable a global optimum search using solver BARON.

Table 4.1. The results of the ACC2 future mode run

The results of the ACC2 future mode runs for the six emission scenarios (SRES) are shown below. The temperature change refers to the global-mean surface air temperature change relative to the level in 1990.

Year	A1B scenario					A1T scenario				
	CO ₂ concentration (ppm)	CH ₄ concentration (ppb)	N ₂ O concentration (ppb)	Total radiative forcing (W/m ²)	Temperature change (°C)	CO ₂ concentration (ppm)	CH ₄ concentration (ppb)	N ₂ O concentration (ppb)	Total radiative forcing (W/m ²)	Temperature change (°C)
2000	370	1752	317	1.63	0.06	370	1752	317	1.63	0.06
2005	379	1783	322	1.71	0.27	379	1778	322	1.84	0.31
2010	391	1836	327	1.83	0.39	389	1820	326	2.07	0.48
2015	405	1901	332	1.99	0.51	399	1876	330	2.29	0.64
2020	419	1971	337	2.15	0.63	410	1946	334	2.51	0.81
2025	434	2048	341	2.44	0.78	421	2030	337	2.72	0.97
2030	450	2133	345	2.74	0.96	434	2127	340	2.94	1.13
2035	466	2203	350	3.11	1.18	447	2217	344	3.26	1.32
2040	482	2248	354	3.48	1.41	460	2288	347	3.56	1.52
2045	499	2278	358	3.73	1.63	472	2347	350	3.79	1.72
2050	516	2299	361	3.97	1.83	484	2400	353	4.01	1.90
2055	532	2300	365	4.28	2.04	494	2431	355	4.20	2.07
2060	548	2276	368	4.57	2.26	503	2433	358	4.36	2.23
2065	563	2237	371	4.80	2.46	511	2417	360	4.47	2.37
2070	577	2191	374	5.01	2.65	517	2386	362	4.55	2.48
2075	590	2140	377	5.16	2.82	522	2349	364	4.62	2.58
2080	602	2087	380	5.30	2.97	526	2307	365	4.66	2.66
2085	614	2035	382	5.39	3.10	528	2260	367	4.67	2.72
2090	625	1984	385	5.47	3.21	529	2206	368	4.66	2.77
2095	635	1936	387	5.54	3.31	528	2144	370	4.64	2.80
2100	645	1892	389	5.61	3.40	527	2074	371	4.61	2.83

Table 4.1. (Continued) The results of the ACC2 future mode run

Year	A1FI scenario					A2 scenario				
	CO ₂ concentration (ppm)	CH ₄ concentration (ppb)	N ₂ O concentration (ppb)	Total radiative forcing (W/m ²)	Temperature change (°C)	CO ₂ concentration (ppm)	CH ₄ concentration (ppb)	N ₂ O concentration (ppb)	Total radiative forcing (W/m ²)	Temperature change (°C)
2000	370	1752	317	1.63	0.06	370	1752	317	1.63	0.06
2005	379	1777	322	1.74	0.28	379	1780	322	1.78	0.29
2010	389	1814	328	1.87	0.41	389	1825	328	1.95	0.44
2015	401	1866	334	2.06	0.54	401	1880	334	2.02	0.55
2020	415	1933	341	2.27	0.68	414	1941	341	2.11	0.64
2025	432	2013	347	2.49	0.83	429	2011	348	2.28	0.75
2030	450	2106	355	2.74	0.99	445	2091	355	2.47	0.87
2035	471	2210	363	3.10	1.19	463	2176	362	2.77	1.03
2040	495	2324	371	3.49	1.42	481	2266	370	3.06	1.21
2045	521	2441	380	3.97	1.69	499	2358	377	3.36	1.40
2050	549	2557	390	4.46	2.00	518	2451	385	3.65	1.61
2055	579	2657	400	5.00	2.33	537	2548	392	4.01	1.83
2060	608	2736	409	5.52	2.69	558	2650	400	4.39	2.08
2065	638	2804	418	5.96	3.03	579	2756	407	4.77	2.33
2070	668	2870	427	6.38	3.36	601	2864	415	5.15	2.60
2075	698	2935	436	6.70	3.66	624	2973	423	5.50	2.87
2080	728	3001	445	7.02	3.94	649	3083	431	5.86	3.13
2085	757	3063	453	7.27	4.20	675	3192	439	6.18	3.40
2090	786	3120	461	7.50	4.43	703	3299	448	6.51	3.66
2095	813	3171	469	7.72	4.65	732	3407	456	6.85	3.92
2100	840	3212	477	7.93	4.86	763	3513	464	7.19	4.18

Table 4.1. (Continued) The results of the ACC2 future mode run

Year	B1 scenario					B2 scenario				
	CO ₂ concentration (ppm)	CH ₄ concentration (ppb)	N ₂ O concentration (ppb)	Total radiative forcing (W/m ²)	Temperature change (°C)	CO ₂ concentration (ppm)	CH ₄ concentration (ppb)	N ₂ O concentration (ppb)	Total radiative forcing (W/m ²)	Temperature change (°C)
2000	370	1752	317	1.63	0.06	370	1752	317	1.63	0.06
2005	379	1769	322	1.78	0.29	378	1773	322	1.83	0.30
2010	388	1787	328	1.93	0.43	387	1801	326	2.02	0.46
2015	399	1808	333	2.10	0.56	397	1838	330	2.21	0.61
2020	410	1833	338	2.26	0.69	405	1882	334	2.39	0.76
2025	421	1850	344	2.40	0.81	414	1934	337	2.55	0.89
2030	432	1853	349	2.52	0.93	424	1992	341	2.71	1.03
2035	444	1848	354	2.67	1.04	434	2055	344	2.89	1.16
2040	455	1837	359	2.82	1.16	444	2123	347	3.07	1.30
2045	466	1819	363	3.01	1.28	454	2196	350	3.27	1.44
2050	477	1796	368	3.18	1.42	464	2273	353	3.45	1.58
2055	486	1773	372	3.36	1.55	475	2345	356	3.63	1.73
2060	493	1754	375	3.52	1.68	485	2406	359	3.80	1.86
2065	499	1737	379	3.66	1.81	495	2463	361	3.97	2.00
2070	504	1721	381	3.78	1.92	505	2523	364	4.14	2.14
2075	507	1699	384	3.87	2.02	516	2581	367	4.29	2.27
2080	509	1669	386	3.94	2.11	526	2636	369	4.45	2.40
2085	511	1634	388	3.98	2.19	537	2686	372	4.60	2.53
2090	511	1597	390	4.01	2.25	548	2731	374	4.76	2.66
2095	511	1558	391	4.02	2.30	559	2775	377	4.91	2.79
2100	510	1516	392	4.03	2.33	570	2823	379	5.06	2.91

Figure 4.1. The results of the ACC2 past mode run

The series of figures show the results of the ACC2 inverse calculation as explained in Section 3. The posterior estimates of the parameters and data (red lines) are shown in comparison with the respective prior estimates and measurements (black thick lines) including their 2σ prior and measurement uncertainty ranges (black thin lines). The large spikes in the prior and measurement uncertainty ranges are due to their adjustments for large volcanic eruptions (Section 3.5.2). The residuals of the posterior estimates from their corresponding prior estimates (red lines in inserts) are separately shown with their 2σ prior and measurement uncertainty ranges (black lines in inserts). The prior and posterior parameter values are listed in Table 3.2. The blue lines are the results of another past mode run with all the parameter values fixed at the respective prior estimates, which is essentially a forward run.

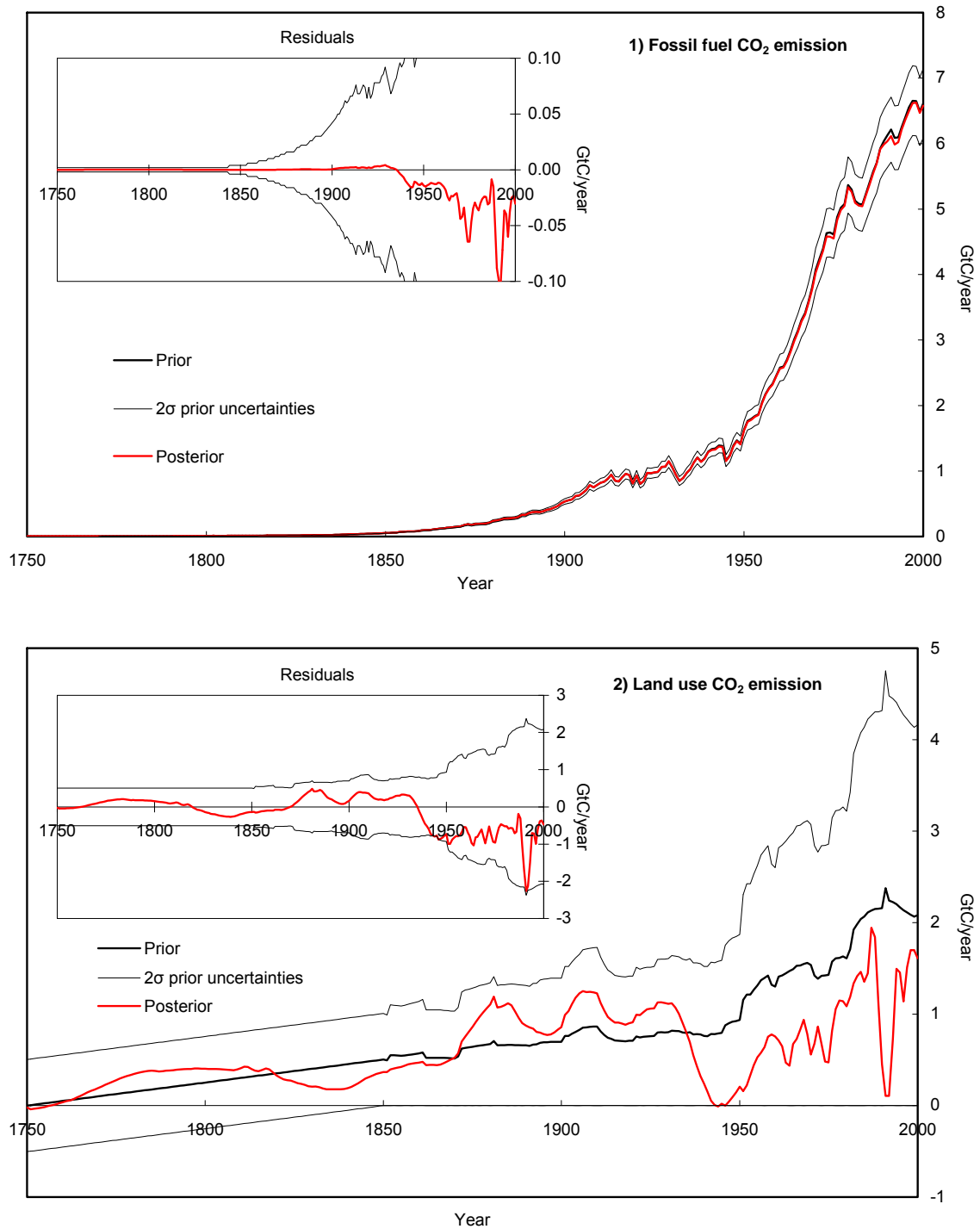


Figure 4.1. (Continued) The results of the ACC2 past mode run

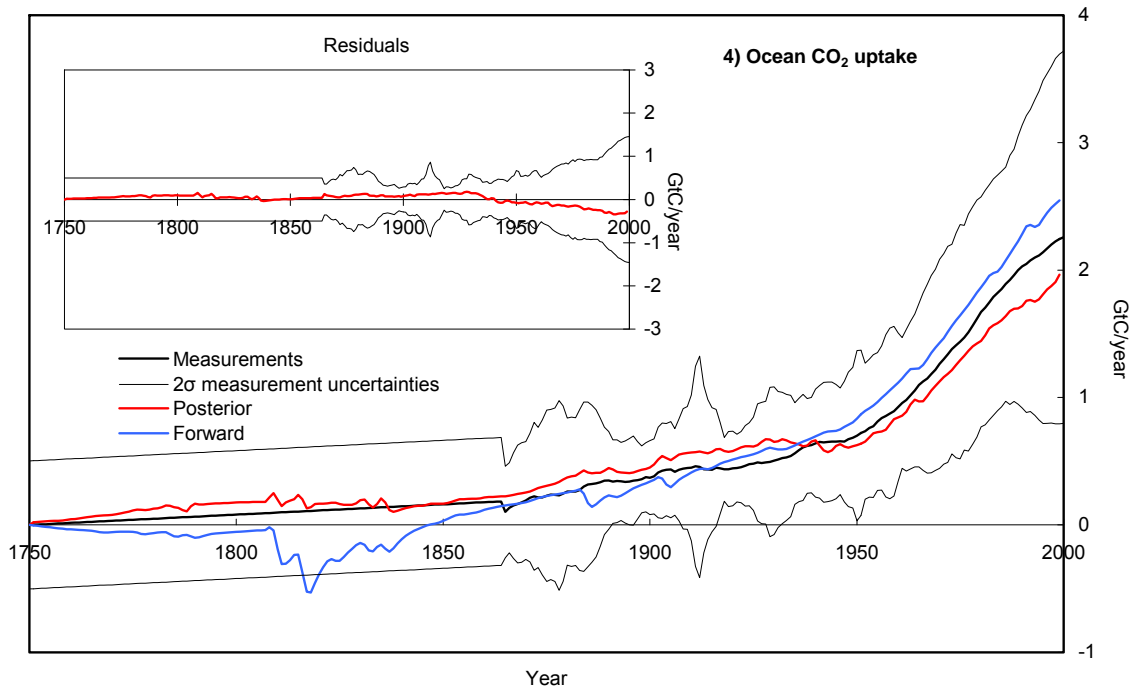
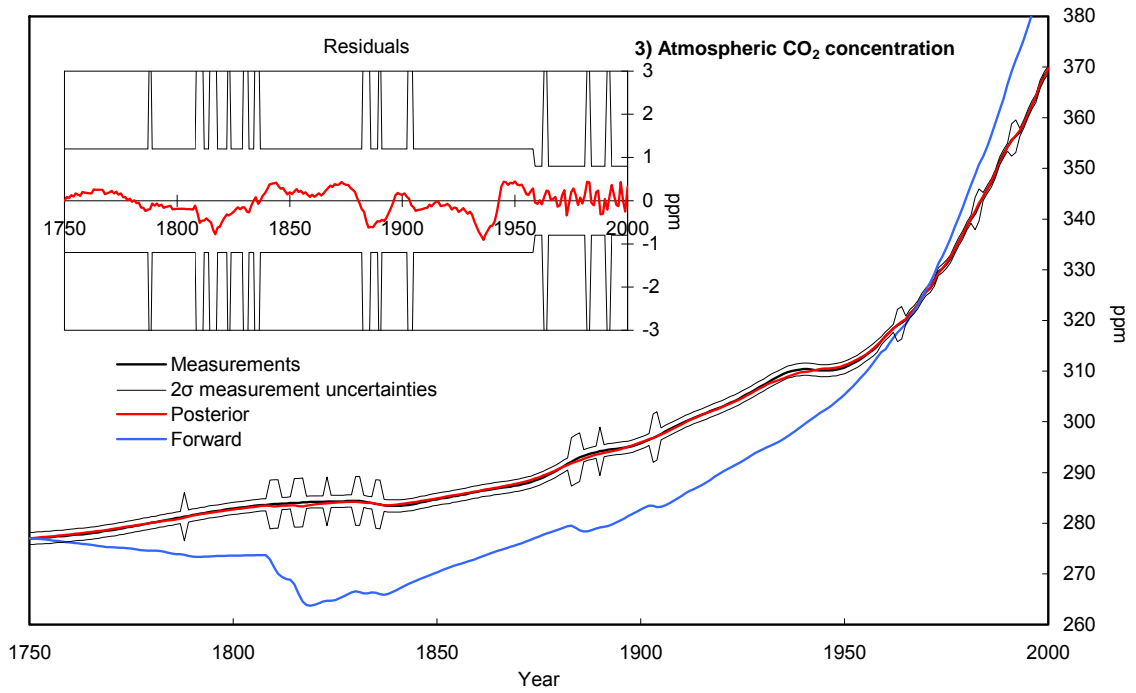


Figure 4.1. (Continued) The results of the ACC2 past mode run

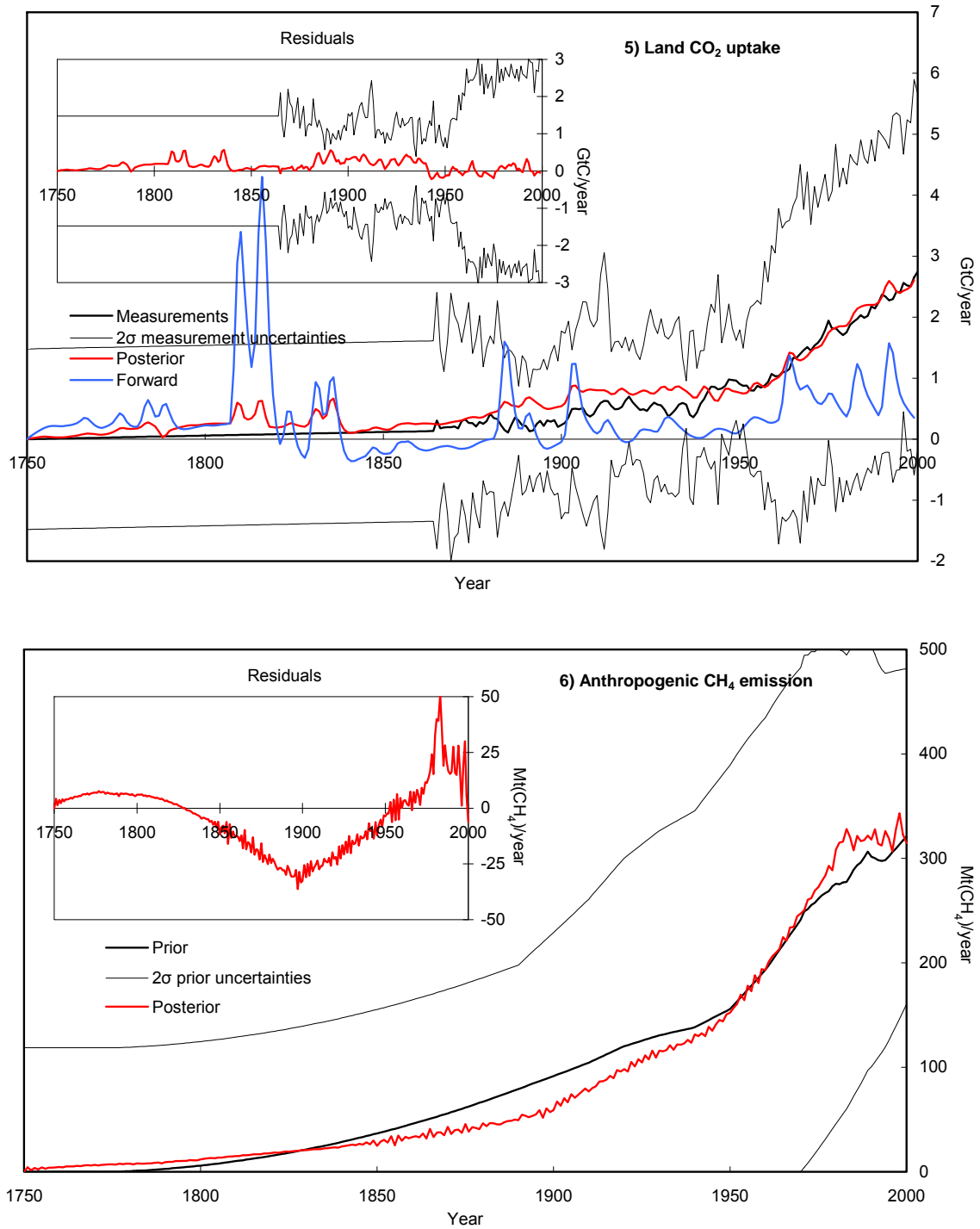


Figure 4.1. (Continued) The results of the ACC2 past mode run

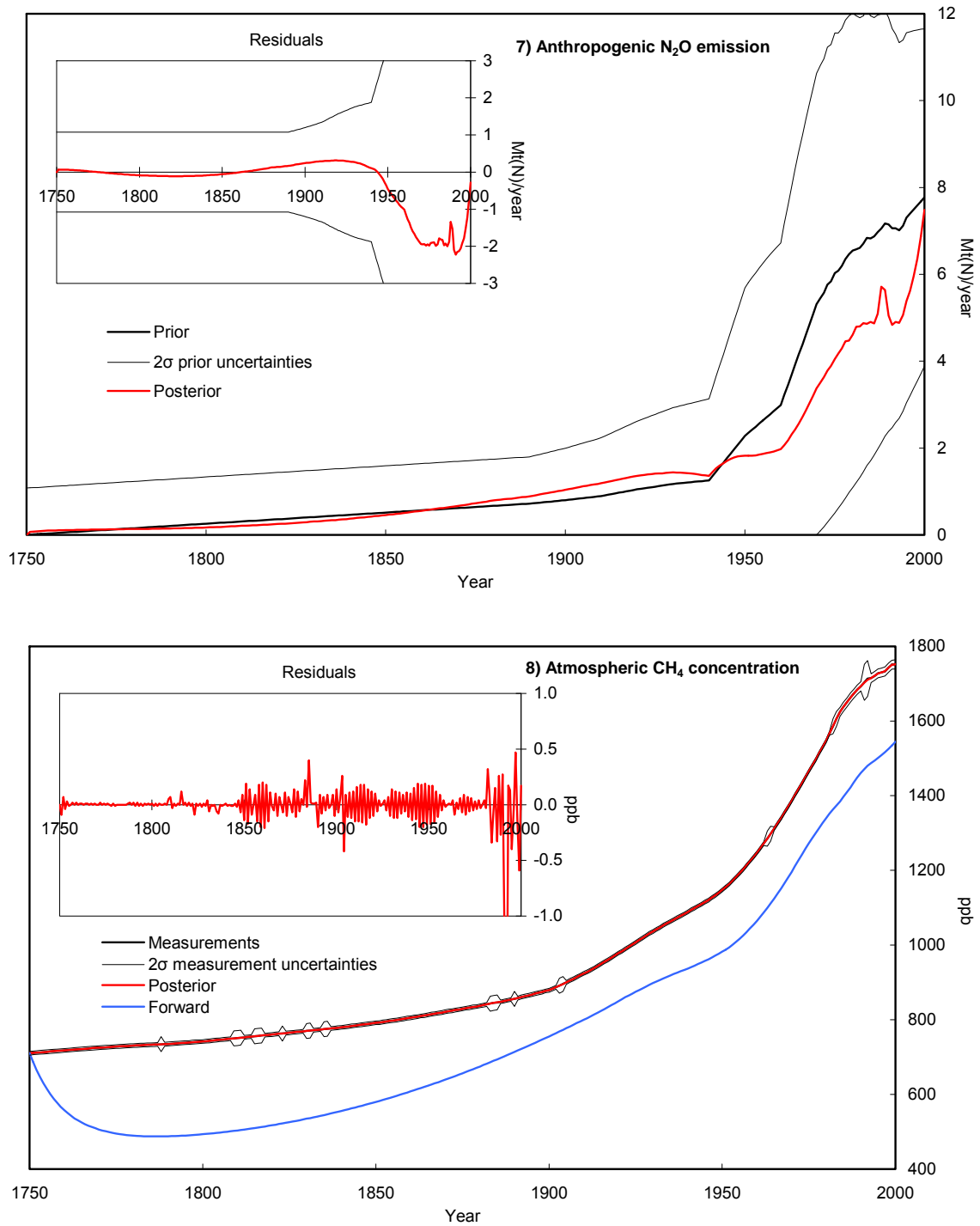


Figure 4.1. (Continued) The results of the ACC2 past mode run

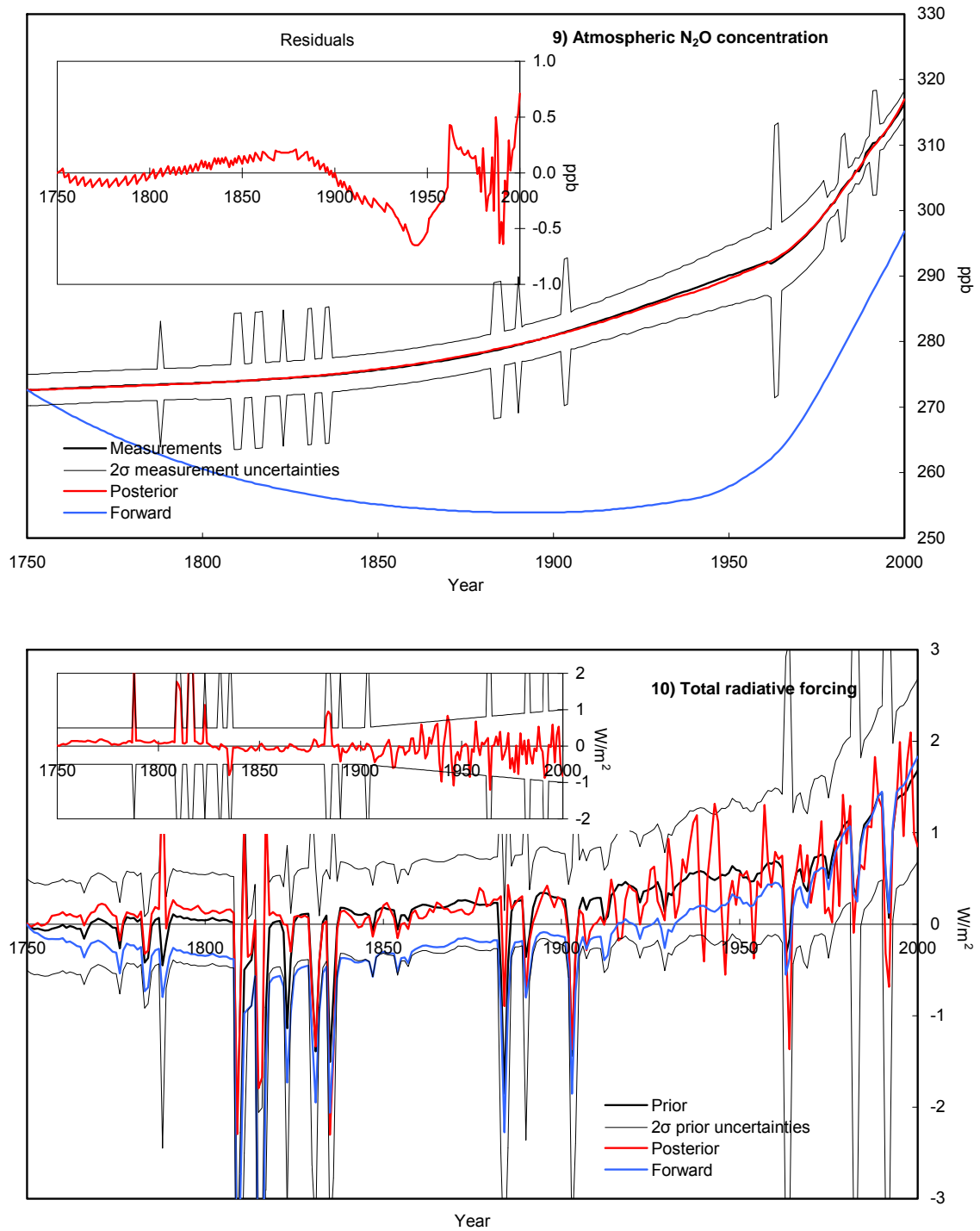


Figure 4.1. (Continued) The results of the ACC2 past mode run

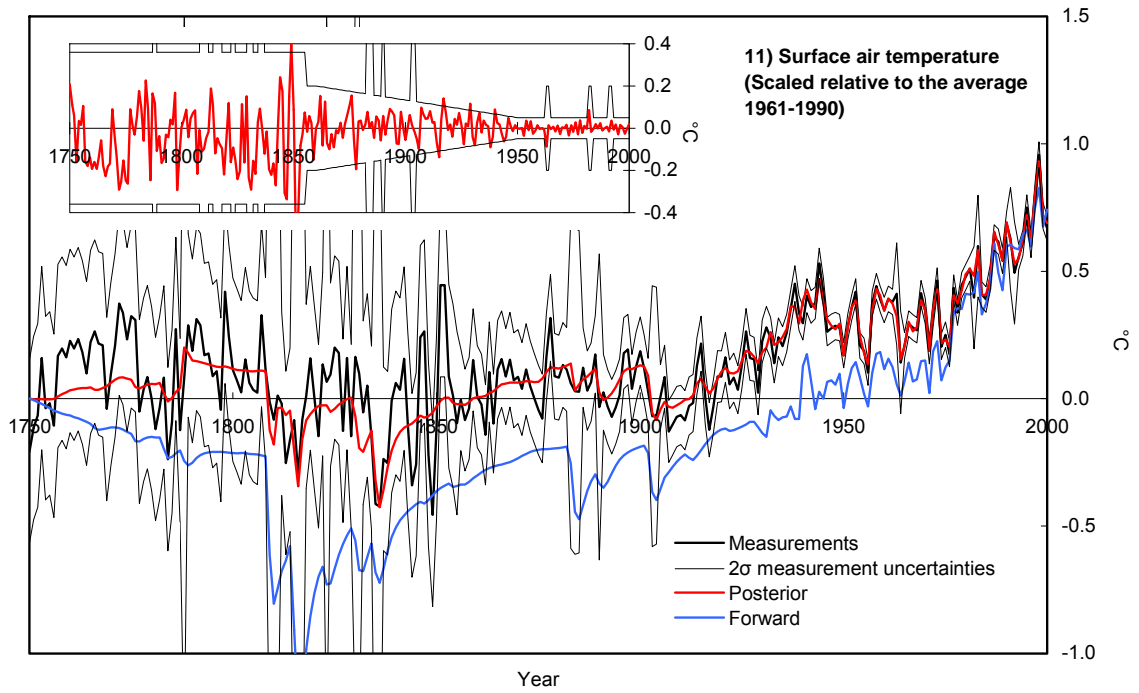


Figure 4.2. The atmospheric CO₂ concentration projections of the ACC2 future run

The CO₂ concentration projections of the ACC2 future runs for the six emission scenarios (SRES) are shown in comparison with the corresponding projections of the Integrated Science Assessment Model (ISAM) and the Bern-CC model (IPCC, 2001, Appendix II). Both ISAM and the Bern-CC model are simple carbon cycle-climate models (IPCC, 2001, Box 3.7). ISAM is tuned to mimic the ranges of projections for the carbon cycle processes shown by several process-based models (IPCC, 2001, Figure 3.10), producing the projections of the “ISAM low, reference, and high” cases. In the “Bern-CC low” case, the transport parameters in the ocean are increased by 50% relative to those in the reference case and no temperature sensitivity is assumed for the heterotrophic respiration. In the “Bern-CC high” case, the ocean transport parameters are decreased by 50% and the CO₂ fertilization effect is capped at the level in 2000.

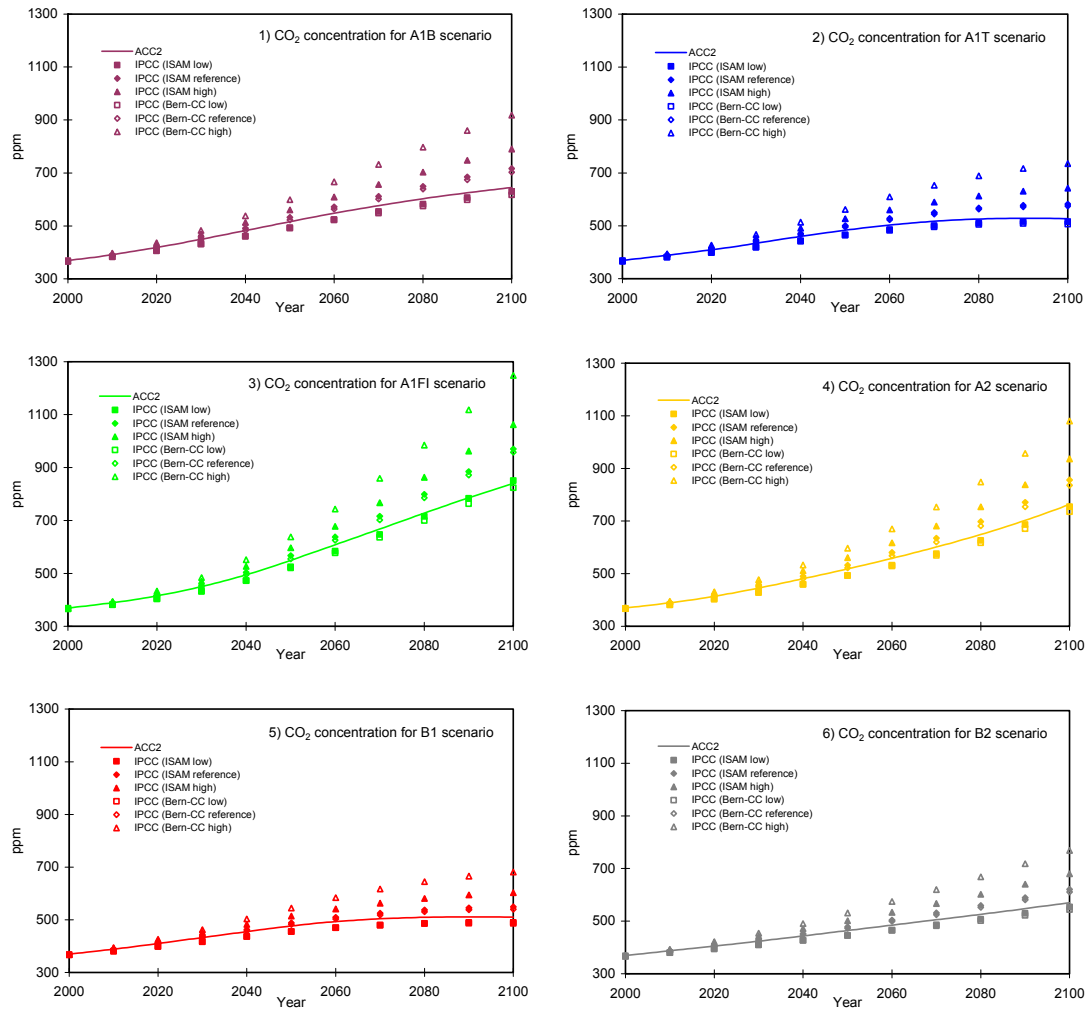


Figure 4.3. The results of the ACC2 future mode run – atmospheric concentrations of radiative agents

The concentration projections of the ACC2 future mode runs for the six emission scenarios (SRES) are shown in comparison with the corresponding projections in IPCC (2001, Appendix II) and WMO (2003, Table 1-16). The emissions of C_4F_{10} , HFC152a, and HFC236fa are kept zero throughout the projection horizon in the six scenarios.

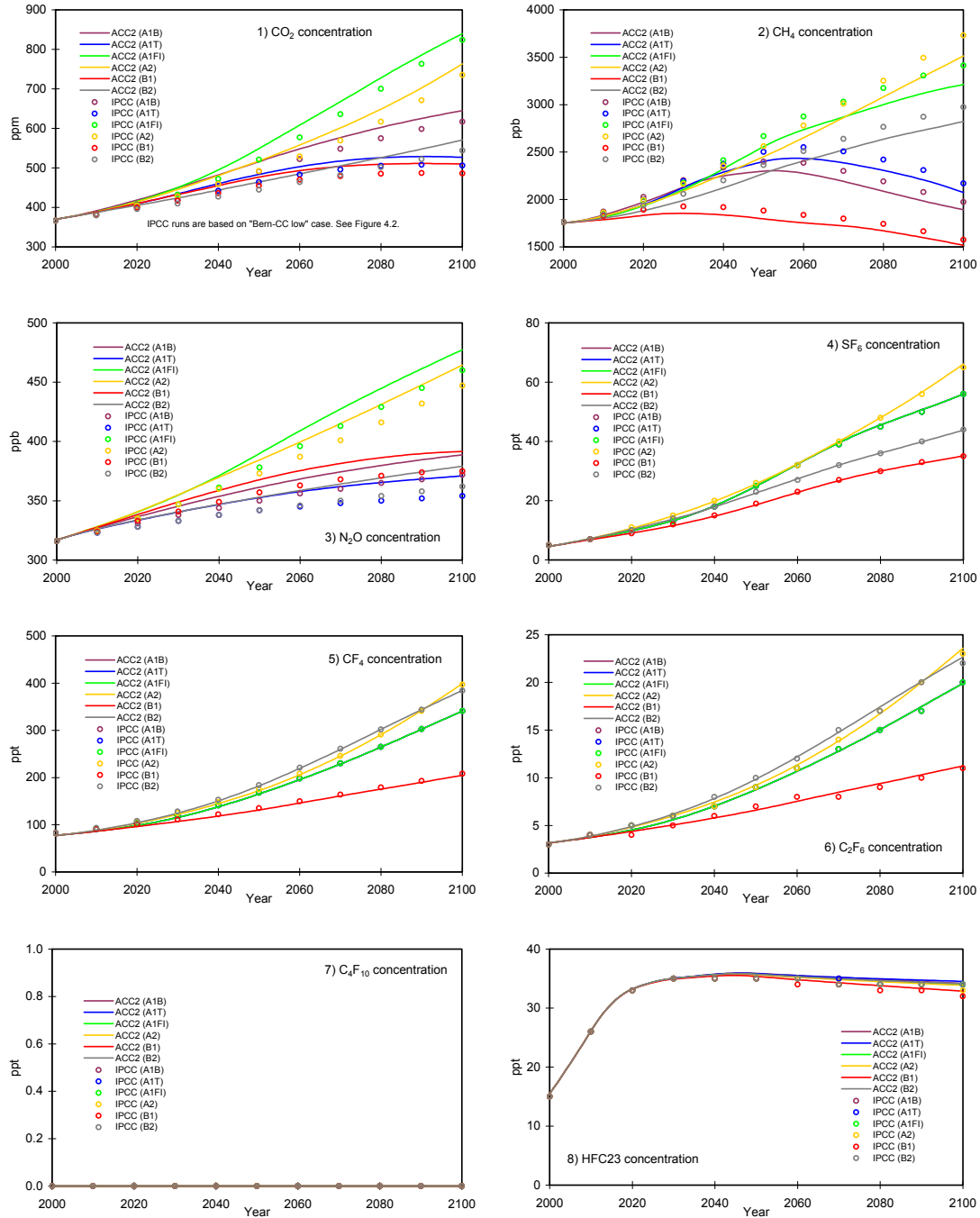


Figure 4.3. (Continued) The results of the ACC2 future mode run – atmospheric concentrations of radiative agents

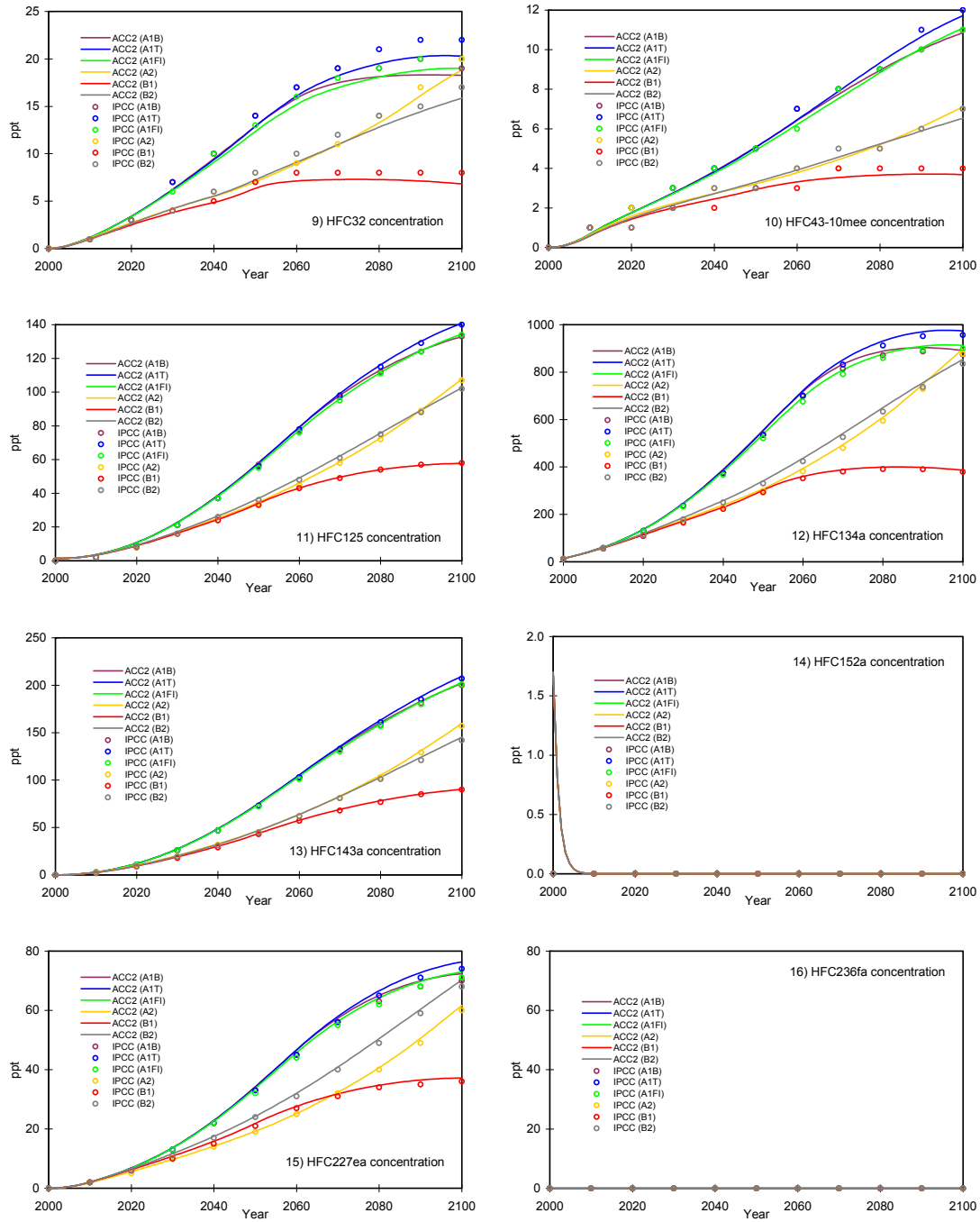


Figure 4.3. (Continued) The results of the ACC2 future mode run – atmospheric concentrations of radiative agents

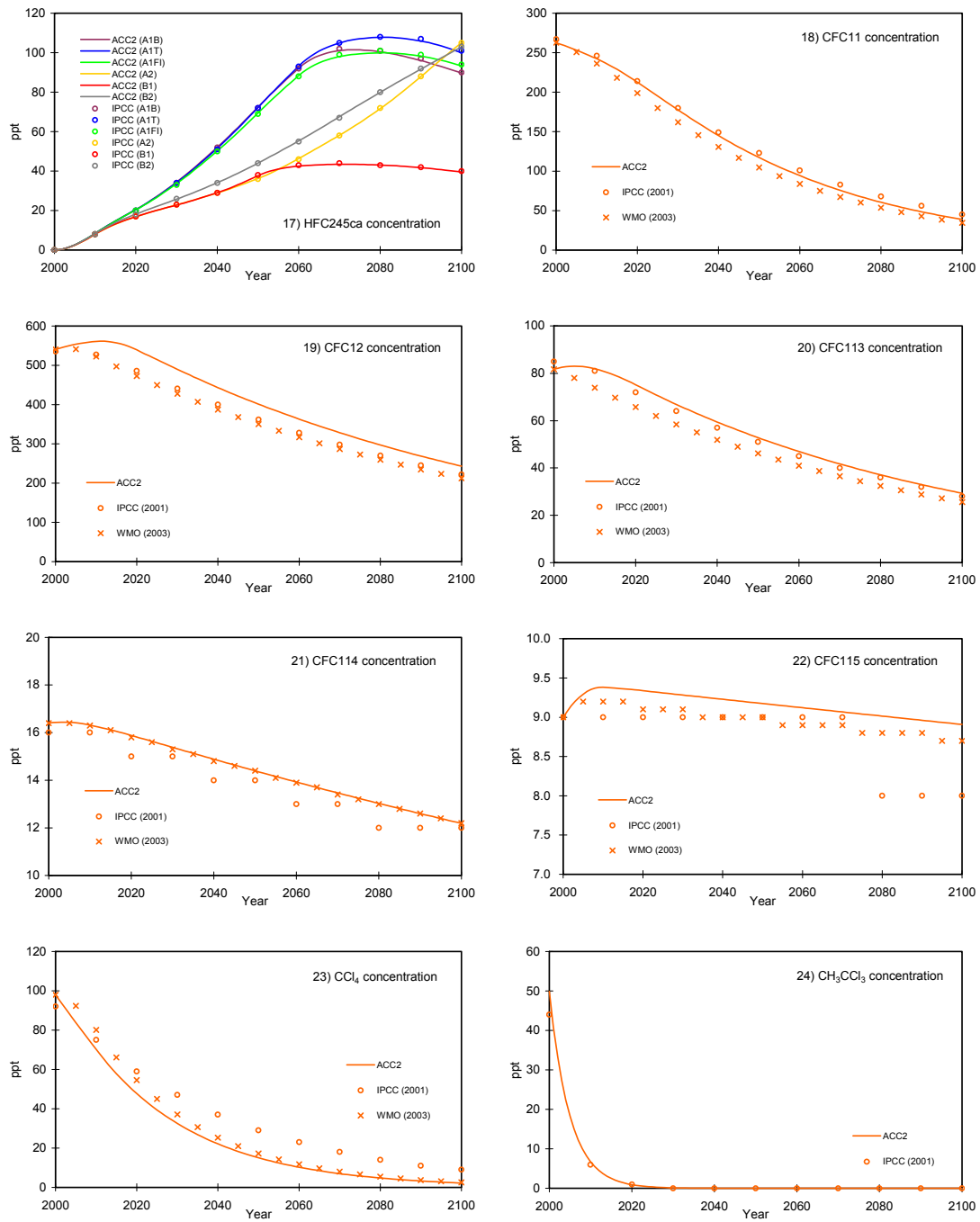


Figure 4.3. (Continued) The results of the ACC2 future mode run – atmospheric concentrations of radiative agents

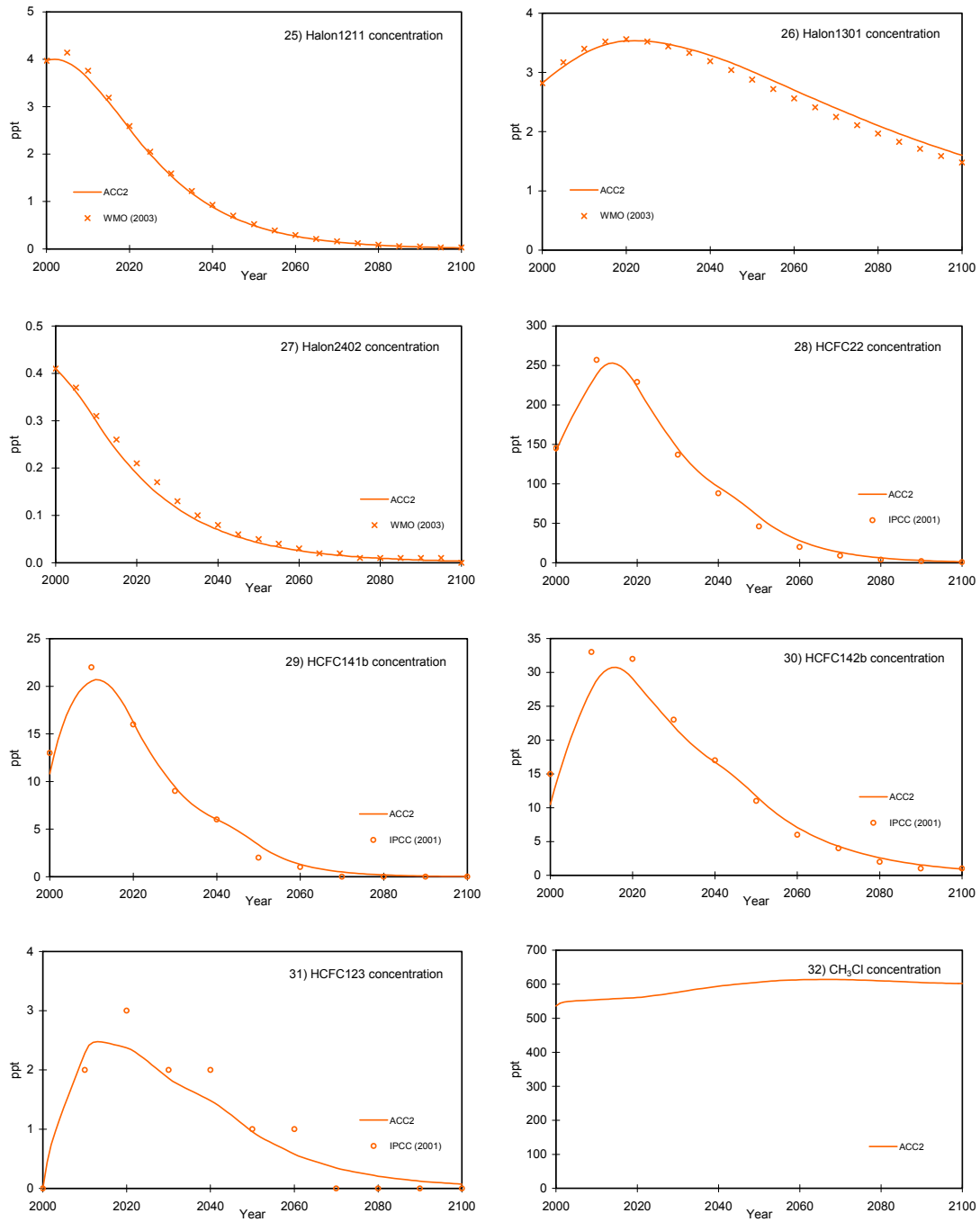


Figure 4.3. (Continued) The results of the ACC2 future mode run – atmospheric concentrations of radiative agents

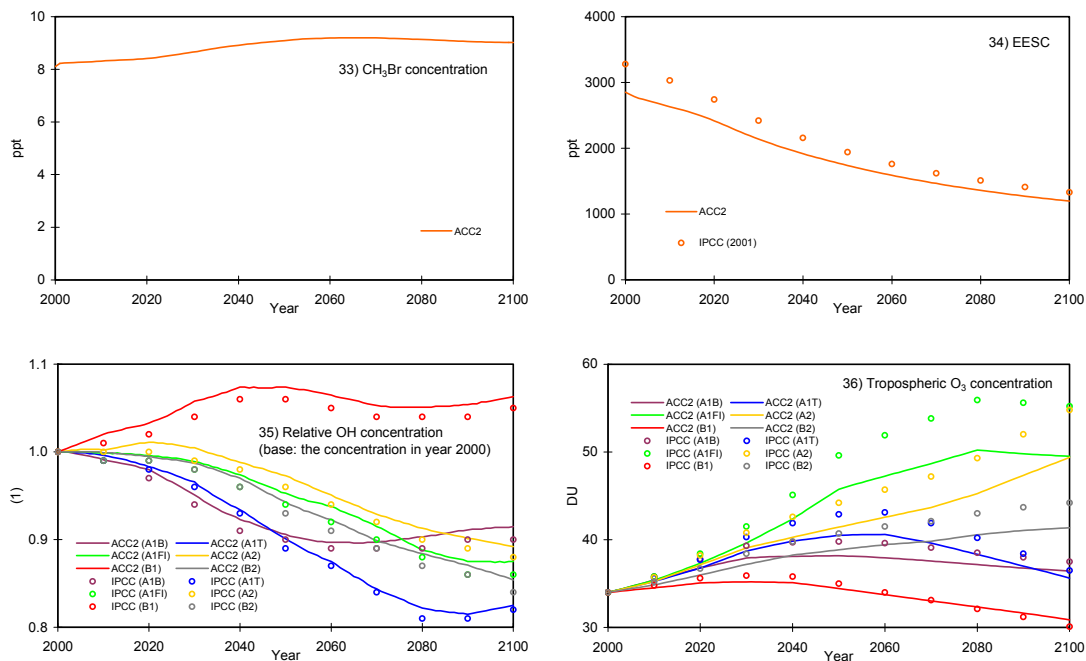


Figure 4.4. The results of the ACC2 future mode run – individual radiative forcings

The radiative forcing projections of the ACC2 future mode runs for the six emission scenarios (SRES) are shown in comparison with the corresponding projections in IPCC (2001, Appendix II). The figures for C_4F_{10} , HFC152a, and HFC236fa are presented here for completeness.

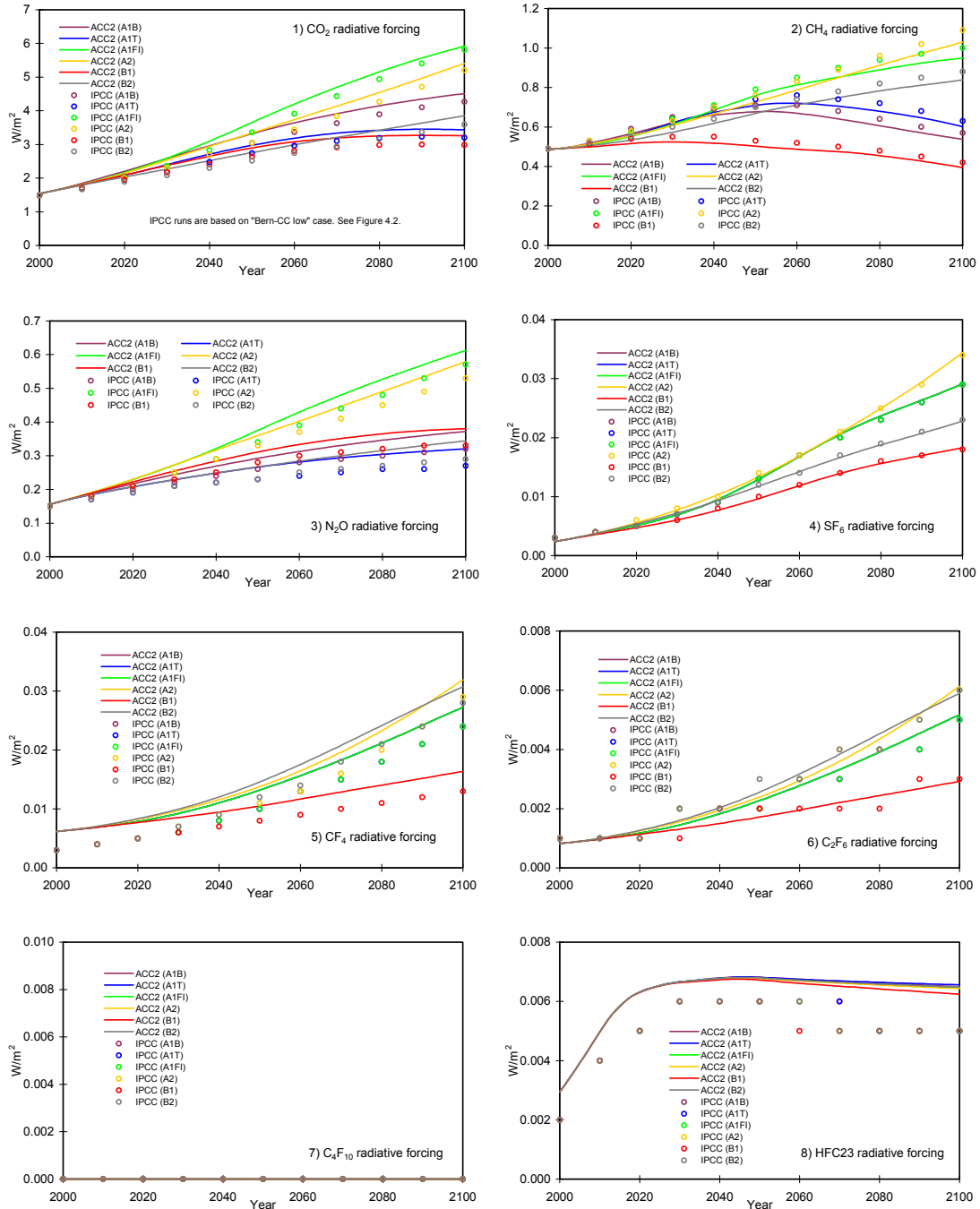


Figure 4.4. (Continued) The results of the ACC2 future mode run – individual radiative forcings

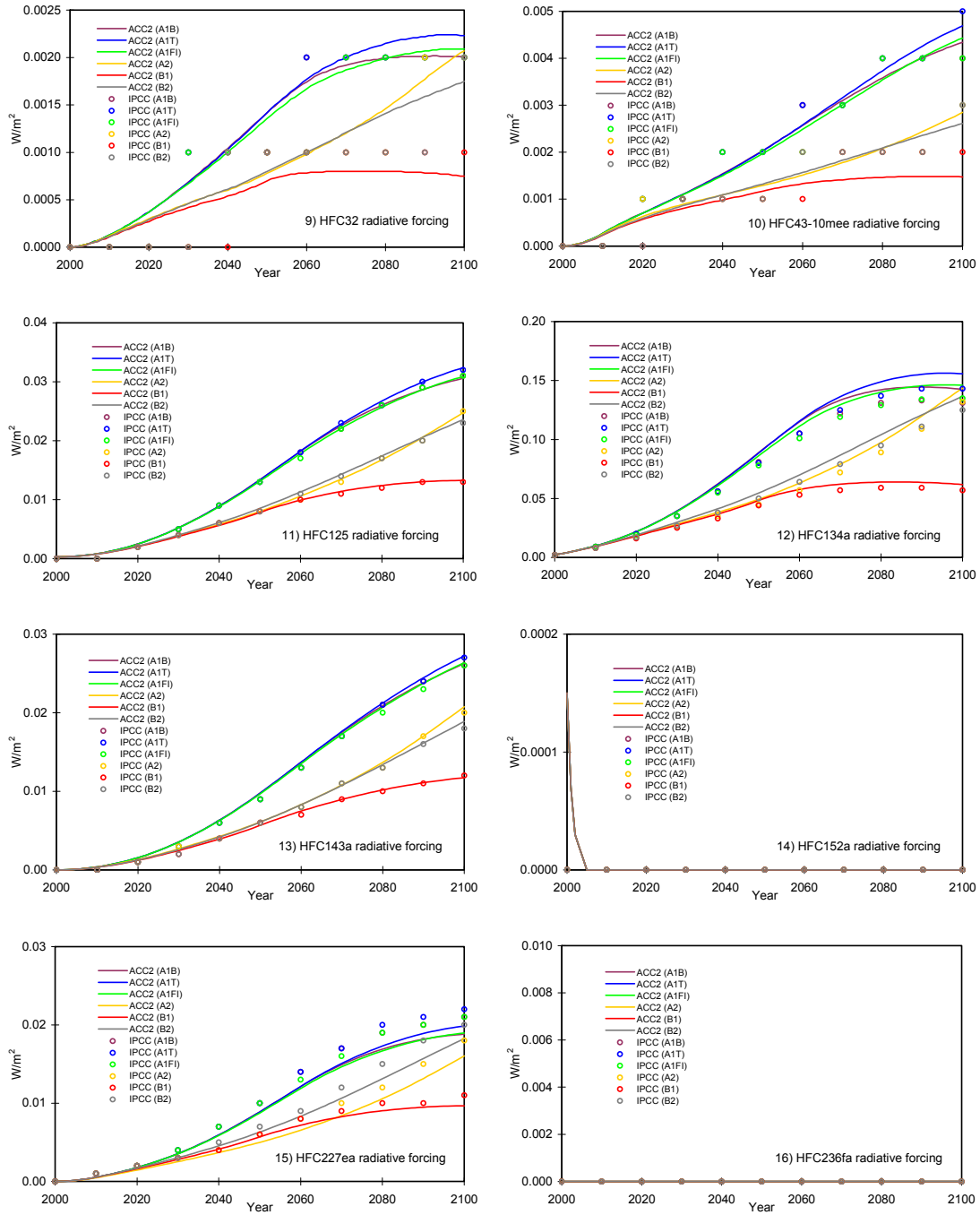


Figure 4.4. (Continued) The results of the ACC2 future mode run – individual radiative forcings

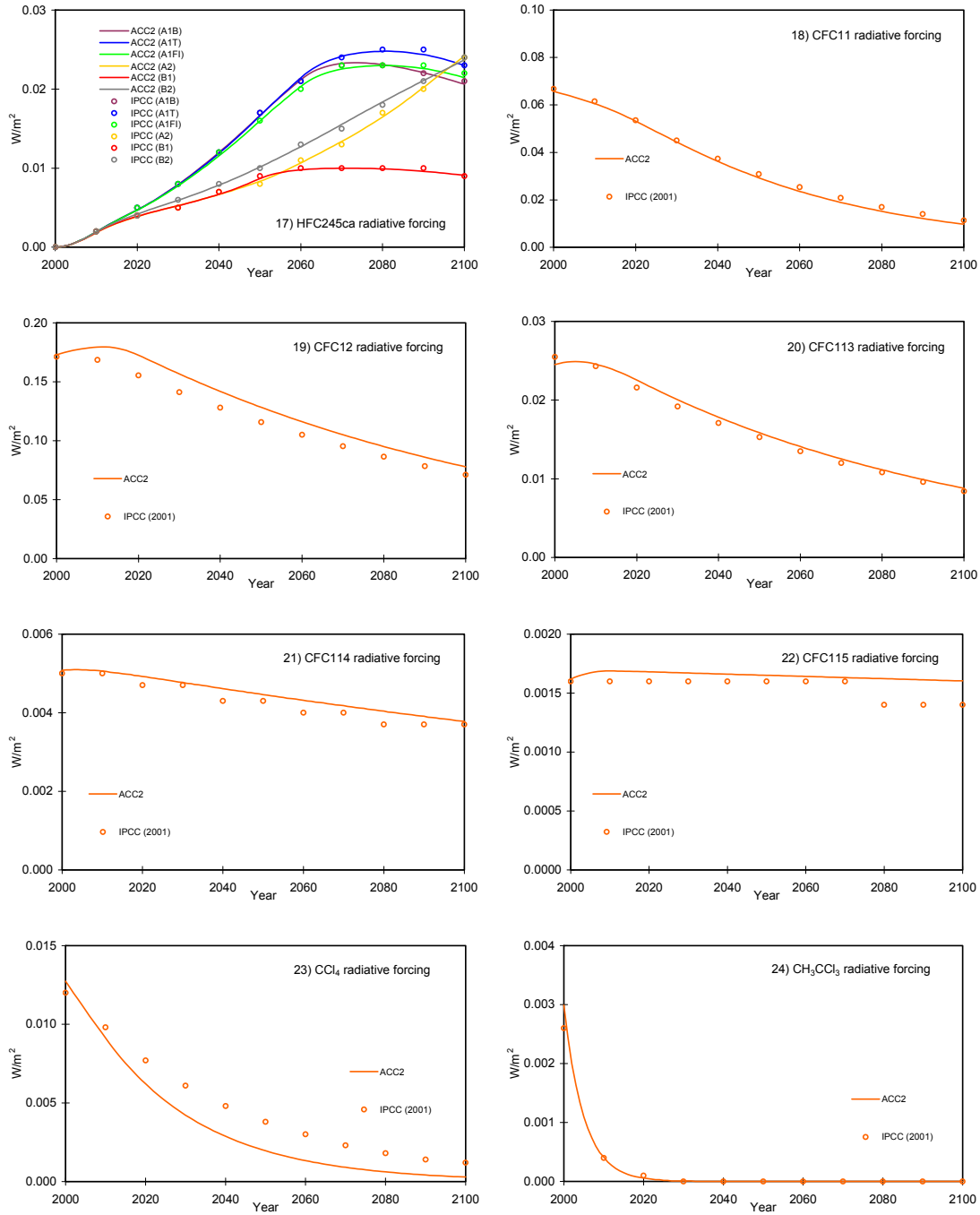


Figure 4.4. (Continued) The results of the ACC2 future mode run – individual radiative forcings

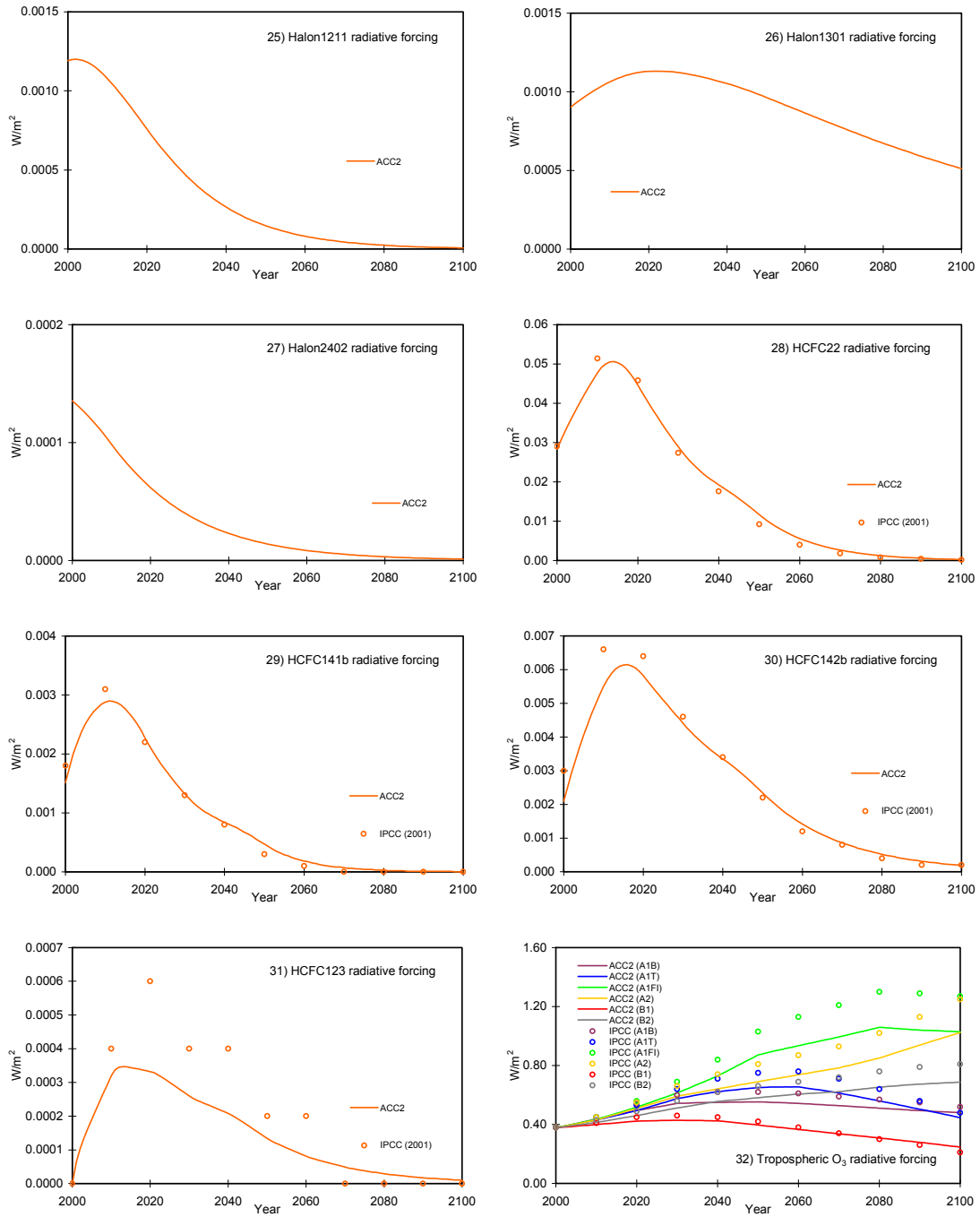


Figure 4.4. (Continued) The results of the ACC2 future mode run – individual radiative forcings

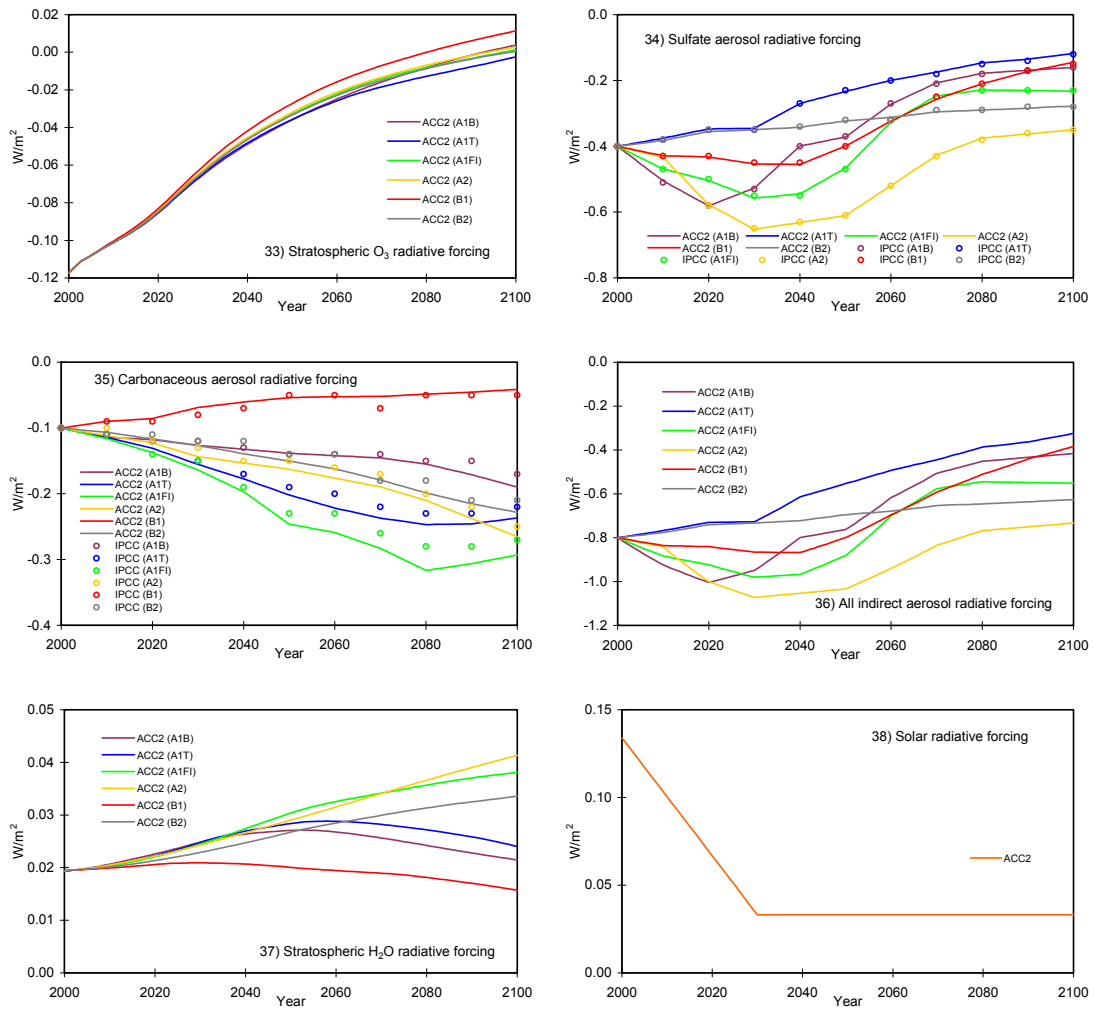
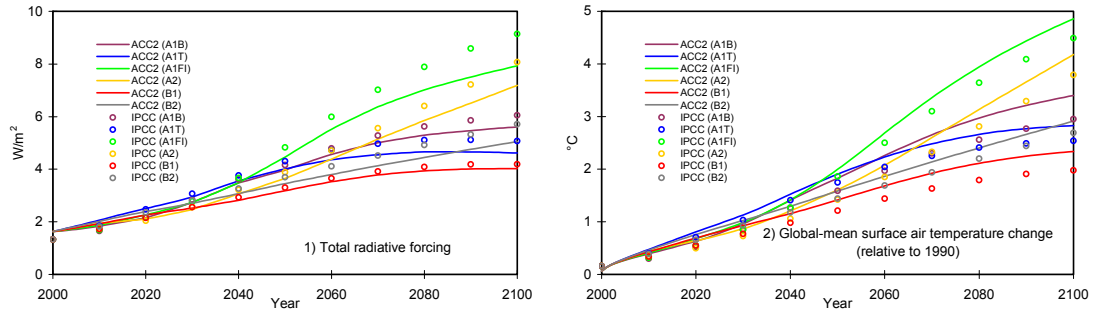


Figure 4.5. The results of the ACC2 future mode run – total radiative forcing and surface air temperature change

The ACC2 projections of the total radiative forcing and global-mean surface air temperature for the six emission scenarios (SRES) are shown in comparison with the corresponding projections in IPCC (2001, Appendix II).



ACKNOWLEDGMENTS

We acknowledge Volkswagen Foundation (ECOBICE project), Max Planck Institute for Biogeochemistry, European Commission (ENSEMBLES project), Max Planck Institute for Meteorology, and International Max Planck Research School on Earth System Modelling for their financial supports for this study. This study has been partly conducted during the first author's stay at the International Institute for Applied Systems Analysis (IIASA) as a participant of the Young Scientists Summer Program in 2005. Katsumasa Tanaka especially thanks the following individuals for their respective contributions and supports in alphabetical order:

John A. van Aardenne	Data provisions	Historical non-CO ₂ GHG emission uncertainties
Arne Stolbjerg Drud	Technical advices	CONOPT3
David M. Etheridge	Data provisions	Historical halocarbon concentrations
Jacqueline Flueckiger	Data provisions	Historical N ₂ O concentration with uncertainties
Klaus Hasselmann	Review	Results and conclusions section
Ernst Maier-Reimer	Scientific advices	Ocean carbon cycle component
Sabastian Rast	Review	Atmospheric chemistry section
Christian Reick	Review	Inversion and numerical intergration sections
Uwe Schneider	Technical advices	GAMS

REFERENCES

- Adams, J. B., M. E. Mann, C. M. Ammann (2003) Proxy evidence for an El Niño-like response to volcanic forcing. *Nature*, **426**, 271-278.
- Ainsworth, E. A., S. P. Long (2004) What have we learned from 15 years of free-air CO₂ enrichment (FACE)? – A meta-analysis review of the responses of photosynthesis, canopy properties and plant production to rising CO₂. *New Phytologist*, **165**, 351-372.
- Akmaev, R. A., V. I. Fomichev, X. Zhu (2006) Impact of middle-atmospheric composition changes on greenhouse cooling in the upper atmosphere. *Journal of Atmospheric and Solar-Terrestrial Physics*, **68**, 1879-1889.
- Allen, M. R., P. A. Stott, J. F. B. Mitchell, R. Schnur, T. L. Delworth (2000) Quantifying the uncertainty in forecasts of anthropogenic climate change. *Nature*, **407**, 617-620.
- Allen, M. R., W. J. Ingram (2002) Constraints on future changes in climate and the hydrologic cycle. *Nature*, **419**, 224-232.
- Ammann C. M., G. A. Meehl, W. M. Washington, C. S. Zender (2003) A monthly and latitudinally varying volcanic forcing dataset in simulations of 20th century climate. *Geophysical Research Letters*, **30** (12), 1657, doi:10.1029/2003GL016875.
- Andersson, A. J., F. T. Mackenzie, A. Lerman (2006) Coastal ocean CO₂–carbonic acid–carbonate sediment system of the Anthropocene. *Global Biogeochemical Cycles*, **20**, doi:10.1029/2005GB002506
- Andronova, N. G., M. E. Schlesinger (2001) Objective estimation of the probability density function for climate sensitivity. *Journal of Geophysical Research*, **106(D9)**, 22605-22611.
- Bacastow, R. (1981) Numerical evaluation of the evasion factor. In (ed.) B. Bolin. *Carbon cycle modelling (SCOPE 16)*. pp. 95-101. John Wiley & Sons. 390 pp.
- Bairoch, P. (1995) *Economics and world history: myths and paradoxes*. University of Chicago Press, Chicago. 200 pp.
- Balmaceda, L., N. A. Krivova, S. K. Solanki (submitted) Reconstruction of solar total irradiance since 1700 from the surface magnetic flux. *Astronomy and Astrophysics*.
- Behrenfeld, M. J., R. T. O'Malley, D. A. Siegel, C. R. McClain, J. L. Sarmiento, G. C. Feldman, A. J. Milligan, P. G. Falkowski, R. M. Letelier, E. S. Boss (2006) Climate-driven trends in contemporary ocean productivity. *Nature*, **444**, 752-755.
- Bernard, S., T. Röckmann, J. Kaiser, J.-M. Barnola, H. Fischer, T. Blunier, J. Chappellaz (2006) Constraints on N₂O budget changes since pre-industrial time from new firn air and ice core isotope measurements. *Atmospheric Chemistry and Physics*, **6**, 493–503.

- Berner, R. A. (1991) A model for atmospheric CO₂ over Phanerozoic Time. *American Journal of Science*, **291**, 339-376.
- Berner, R. A. (1997) The Rise of Plants and Their Effect on Weathering and Atmospheric CO₂. *Science*, **276**, 544-546.
- Bertrand C., M.-F. Loutre, M. Crucifix, A. Berger (2002) Climate of the last millennium: a sensitivity study. *Tellus A*, **54**, 221-244.
- Bouwman, A. F. (1996) Direct emission of nitrous oxide from agricultural soils. *Nutrient Cycling in Agroecosystem*, **46**, 53-70.
- Boyd, P. W., S. C. Doney (2003) The impact of climate change and feedback processes on the ocean carbon cycle. pp. 157-193. In (ed. M. J. R. Fasham) *Ocean Biogeochemistry*. Springer, Berlin, Germany. 297 pp.
- Brasseur, G., J. J. Orlando, G. S. Tyndall (eds.) (1999) Atmospheric chemistry and global change. Oxford University Press, Oxford. 654 pp.
- Brasseur, G. P., P. Artaxo, L. A. Barrie, R. J. Delmas, I. Galbally, W. M. Hao, R. C. Harriss, I. S. A. Isaksen, D. J. Jacob, C. E. Kolb, M. Prather, H. Rodhe, D. Schwela, W. Steffen, D. J. Wuebbles (2003) An integrated view of the causes and impacts of atmospheric changes. pp. 207-271 (eds. G. P. Brasseur, R. G. Prinn, A. A. P. Pszenny) *Atmospheric chemistry in a changing world. The IGBP Series*. Springer, Berlin, Germany. 300 pp.
- Bretscher, O. (2001) Linear algebra with applications. 2nd edition. Prentice Hall, Upper Saddle River, New Jersey, US. 478 pp.
- Brooke, A., D. Kendrick, A. Meeraus (1992) GAMS: A User's Guide, Release 2.25. Scientific Press, San Francisco.
- Brovkin, V., A. Ganopolski, Y. Svirezhev (1997) A continuous climate-vegetation classification for use in climate-biosphere studies. *Ecological Modelling*, **101**, 251-261.
- Bruckner, T., G. Hooss, H.-M. Füssel, K. Hasselmann (2003) Climate system modeling in the framework of the Tolerable Windows Approach: the ICLIPS climate model. *Climatic Change*, **56**, 119-137.
- Bruckner, T. (2004) The ICLIPS Climate Model: Version 1.0, Scientific Reference Manual, Institute for Energy Engineering, Technical University of Berlin, Berlin.
- Burbidge, E. M., G. R. Burbidge, W. A. Fowler, F. Hoyle (1957) Synthesis of the elements in stars. *Reviews of Modern Physics*, **29**, 547-640.
- Caldeira, K., M. E. Wickett (2003) Anthropogenic carbon and ocean pH. *Nature*, **425**, 365.
- Cane, M. A. (2005) The evolution of El Niño, past and future. *Earth and Planetary Science Letters*, **230**, 227-240.
- Chen, H., H.-Q. Tian (2005) Does a general temperature-dependent Q₁₀ model of soil respiration exist at biome and global scale? *Journal of Integrative Plant Biology*, **47**, 1288-1302.

- Chèdin, A., S. Serrar, N. A. Scott, C. Crevoisier, R. Armante (2003) First global measurement of midtropospheric CO₂ from NOAA polar satellites: Tropical zone. *Journal of Geophysical Research*, **108**, D18, 4581, doi:10.1029/2003JD003439.
- Conrad, R. (1996) Soil microorganisms as controllers of atmospheric trace gases (H₂, CO, CH₄, OCS, N₂O, and NO). *Microbiological Review*, **60**, 609-640.
- Cox, P. M., R. A. Betts, C. D. Jones, S. A. Spall, I. J. Totterdell (2000) Acceleration of global warming due to carbon-cycle feedbacks in a coupled climate model. *Nature*, **408**, 184-187.
- Crowley, T. J., S. K. Baum, K.-Y. Kim, G. C. Hegerl, W. T. Hyde (2003) Modeling ocean heat content changes during the last millennium. *Geophysical Research Letters*, **30(18)**, 1932, doi:10.1029/2003GL017801.
- Crutzen, P. J., E. F. Stoermer (2000) The “Anthropocene”. *International Geosphere–Biosphere Programme (IGBP) Newsletter*, **41**, 17-18.
- Daniel, J. S., S. Solomon, D. L. Albritton (1995) On the evaluation of halocarbon radiative forcing and global warming potentials. *Journal of Geophysical Research*, **100**, D1, 1271-1285.
- Davidson, E. A., I. A. Janssens (2006) Temperature sensitivity of soil carbon decomposition and feedbacks to climate change. *Nature*, **440**, 165-173.
- Denman, K. L., M. A. Pena (2000) Beyond JGOFS. In (eds. R. B. Hanson, H. W. Ducklow, J. G. Field) *The changing ocean carbon cycle: a midterm synthesis of the Joint Global Carbon Flux Study*. pp. 469-490. Cambridge University Press. 528 pp.
- de Silva, S. (2003) Eruptions linked to El Niño. *Nature*, **426**, 239-241.
- Dessai S., M. Hulme (2003) Does climate policy need probabilities? Working Paper 34 at Tyndall Centre for Climate Change Research, UK. 42 pp.
- Dickens, G. R. (2001) On the fate of past gas: what happens to methane released from a bacterially mediated gas hydrate capacitor? *Geochemistry, Geophysics, Geosystems (G3)*, **2**, 2000GC000131.
- Dickens, G. R. (2004) Hydrocarbon-driven warming. *Nature*, **429**, 513-515.
- Dickinson, R. E. (1981) Convergence rate and stability of ocean-atmosphere coupling schemes with a zero-dimensional climate model. *Journal of Atmospheric Science*, **38**, 2112-2120.
- Dickinson, R. E., K.J. Schaudt (1998) Analysis of timescales of response of a simple climate model. *Journal of Climate*, **11**, 97-107.
- Dirmeyer, P. A., A. J. Dolman, N. Sato (1999) The pilot phase of the Global Soil Wetness Project. *Bulletin of the American Meteorological Society*, **80**, 851-878.
- Dlugokencky, E. J., E. G. Dutton, P. C. Novelli, P. P. Tans, K. A. Masarie, K. O. Lantz, S. Madronich (1996) Changes in CH₄ and CO growth rates after the eruption of Mt. Pinatubo and their link with changes in tropical tropospheric UV flux. *Geophysical Research Letters*, **23**, 2761–2764.
- Dlugokencky, E. J., K. A. Masarie, P. M. Lang, P. P. Tans (1998) Continuing decline in the growth

- rate of the atmospheric methane burden. *Nature*, **393**, 447-450.
- Doney, S. C. (2006) Plankton in a warmer world. *Nature*, **444**, 695-697.
- Doney, S. C., K. Lindsay, I. Fung, J. John (2006) Natural variability in a stable, 1000-yr global coupled climate–carbon cycle simulation. *Journal of Climate*, **19**, 3033-3054.
- Drud, A. (2006) CONOPT. Available in the GAMS software package. 45 pp.
- Dutton, J. A. (1995) An analytical model of atmospheric feedback and global temperature change. *Journal of Climate*, **8**, 1122-1139.
- Edenhofer, O., N. Bauer, E. Kriegler (2005) The impact of technological change on climate protection and welfare: Insights from the model MIND. *Ecological Economics*, **54**, 277-292.
- Efron, B. (1986) Why isn't everyone a Bayesian? *The American Statistician*, **40**, 1-5.
- Enting, I. G. (2002a) Inverse problems in atmospheric constituent transport. Cambridge University Press, Cambridge, UK. 392 pp.
- Enting, I. G. (2002b) Inverse problems in earth system science: a complex systems perspective. CSIRO Atmospheric Research Technical Paper no. 62. 32 pp.
- Etheridge, D. M., L. P. Steele, R. L. Langenfelds, R. J. Francey (1996) Natural and anthropogenic changes in atmospheric CO₂ over the last 1000 years from air in Antarctic ice and firn. *Journal of Geophysical Research*, **101**, 4115-4128.
- Etheridge, D.M., L.P. Steele, R.J. Francey, and R.L. Langenfelds (1998) Atmospheric methane between 1000 AD and present: Evidence of anthropogenic emissions and climatic variability. *Journal of Geophysical Research*, **103**, D13, 15979-15993.
- Falkowski, P., R. J. Scholes, E. Boyle, J. Canadell, D. Canfield, J. Elser, N. Gruber, K. Hibbard, P. Höglberg, S. Linder, F. T. Mackenzie, B. Moore III, T. Pedersen, Y. Rosenthal, S. Seitzinger, V. Smetacek, W. Steffen (2000) The global carbon cycle: a test of our knowledge of Earth as a system. *Science*, **290**, 291-296.
- Farquhar, G. D., M. L. Roderick (2003) Pinatubo, diffuse light, and the carbon cycle. *Science*, **299**, 1997-1998.
- Fasham, M. J. R. (ed.) (2003) Ocean biogeochemistry: the role of the ocean carbon cycle in global change. Springer, Berlin, Germany. 297 pp.
- Fenhann, J. (2000) Industrial non-energy, non-CO₂ greenhouse gas emissions. *Technological Forecasting and Social Change*, **63**, 313–334.
- Field, C. B., M. J. Behrenfeld, J. T. Randerson, P. Falkowski (1998) Primary production of the biosphere: integrating terrestrial and oceanic components. *Science*, **281**, 237-240.
- Fisher, A. G. (1984) Two Phanerozoic supercycles. In (Eds.) W. A. Berggren, J. A. Van Couvering. *Catastrophes and Earth History*. Princeton University Press, Princeton, New Jersey, US. pp. 129 – 150.
- Forest, C. E., P. H. Stone, A. P. Sokolov, M. R. Allen, M. D. Webster (2002) Quantifying

- uncertainties in climate system properties with the use of recent climate observations. *Nature*, **295**, 113-117.
- Fraser, P. L., D. E. Oram, C. E. Reeves, S. A. Penkett, A. McCulloch (1999) Southern hemispheric halon trends (1978-1998) and global halon emissions. *Journal of Geophysical Research*, **104**, D13, 15985-15999.
- Friedlingstein, P, I. Fung, E. Holland, J. John, G. Brasseur, D. Erickson, D. Schimel (1995) On the contribution of CO₂ fertilization to the missing biospheric sink. *Global Biogeochemical Cycles*, **9**, 541-556.
- Friedlingstein, P., P. Cox, R. Betts, L. Bopp, W. von Bloh, V. Brovkin, P. Cadule, S. Doney, M. Eby, I. Fung, G. Bala, J. John, C. Jones, F. Joos, T. Kato, M. Kawamiya, W. Knorr, K. Lindsay, H. D. Matthews, T. Raddatz, P. Rayner, C. Reick, E. Roeckner, K.-G. Schnitzler, R. Schnur, K. Strassmann, A. J. Weaver, C. Yoshikawa, N. Zeng (2006) Climate–Carbon Cycle Feedback Analysis: Results from the C⁴MIP Model Intercomparison. *Journal of Climate*, **19**, 3337–3353.
- Fuglestedt, J. S., T. Berntsen (1999) A simple model for scenario studies of changes in global climate Version 1.0. CICERO Working Paper 1999:2. University of Oslo.
- Gammon, R., E. Sundquist, P. Fraser (1985) History of carbon dioxide in the atmosphere. In *Atmospheric Carbon Dioxide and the Global Carbon Cycle* (ed. T. Trabalka). Rep. DOE/ER-0239. U. S. Department of Energy, Washington, D.C. pp.25-62.
- Garrels, R. M., F. T. Mackenzie, C. Hunt (1975) Chemical cycles and the global environment: assessing human influences. William Kaufmann, Inc., Los Altos, California. 206 pp.
- Gifford, R. M. (1980) Carbon storage by the biosphere. In *Carbon dioxide and climate* (ed. G. I. Pearman). Australian Academy of Science, Canberra. pp.167-181.
- Gitz, V., P. Ciais (2003) Amplifying effects of land-use change on future atmospheric CO₂ levels. *Global Biogeochemical Cycles*, **17**, 1024, doi:10.1029/2002GB001963.
- Goldewijk, K. K., J. G. van Minnen, G. J. J. Kreileman, M. Vloedveld, R. Leemans (1994) Simulating the carbon flux between the terrestrial environment and the atmosphere. *Water, Air, & Soil Pollution*, **76**, 199-230.
- Gordon, C., C. Cooper, C.A. Senior (2000) The simulation of SST, sea ice extents and ocean heat transports in a version of the Hadley Centre coupled model without flux adjustments. *Climate Dynamics*, **16**, 147-168.
- Greenberg, H. J. (2006) Mathematical Programming Glossary. (ed.) INFORMS Computing Society. <http://glossary.computing.society.informs.org/>
- Gregory, J. M., R. J. Stouffer, S. C. B. Raper, P. A. Stott, N. A. Rayner (2002) An observationally based estimate of the climate sensitivity. *Journal of Climate*, **15**, 3117-3121.
- Gregory, J. M., W.J. Ingram, M.A. Palmer, G.S. Jones, P.A. Stott, R.B. Thorpe, J.A. Lowe, T.C. Johns, K.D. Williams (2004) A new method for diagnosing radiative forcing and climate

- sensitivity. *Geophysical Research Letters*, **31**, doi:10.1029/2003GL018747.
- Gu, L., D. D. Baldocchi, S. C. Wofsy, J. W. Munger, J. J. Michalsky, S. P. Urbanski, T. A. Boden (2003) Response of a deciduous forest to the Mount Pinatubo eruption: enhanced photosynthesis. *Science*, **299**, 2035-2038.
- Gurney, K. R., R. M. Law, A. S. Denning (2002) Towards robust regional estimates of CO₂ sources and sinks using atmospheric transport models. *Nature*, **415**, 626-630.
- Hall, S. J., P. A. Matson (1999) Nitrogen oxide emissions after nitrogen additions in tropical forests. *Nature*, **400**, 152-155.
- Hammer, P. C., J. W. Hollingsworth (1955) Trapezoidal methods of approximating solutions of differential equations. *Mathematical Tables and Other Aids to Computation*, **9**, 92-96.
- Hansen, J., G. Russell, A. Lacis, I. Fung, D. Rind, P. Stone (1985) Climate Response Times: Dependence on Climate Sensitivity and Ocean Mixing. *Science*, **229**, 857-859.
- Hansen J., M. Sato (2004) Data sets used in GISS 2004 GCM. Available at <http://www.giss.nasa.gov/data/simodel/ghgases/GCM.html>
- Harnisch, J., A. Eisenhauer (1998) Natural CF₄ and SF₆ on Earth. *Geophysical Research Letters*, **25**, 2401-2404.
- Harnisch J., R. Borchers, P. Fabian, M. Maiss (1999) CF₄ and the age of mesospheric and polar vortex air. *Geophysical Research Letters*, **26**, 295-298.
- Harriss, R. C. (1969) Boron regulation in the oceans. *Nature*, **223**, 290-291.
- Hartley, D, R. Prinn (1993) Feasibility of determining surface emissions of trace gases using an inverse method in a three-dimensional chemical transport model. *Journal of Geophysical Research*, **98D**, 5183-5197.
- Harvey, L. D. D., S. H. Schneider (1985) Transient climate response to external forcing on 100-104 Year Time Scales. Part 2: Sensitivity experiments with a seasonal, hemispherically averaged, coupled atmosphere, land, and ocean energy balance model. *Journal of Geophysical Research*, **90**, 2207-2222.
- Harvey, L. D. D. (1989) Effect of model structure on the response of terrestrial biosphere models to CO₂ and temperature increases. *Global Biogeochemical Cycles*, **3**, 137-153.
- Harvey, D., J. Gregory, M. Hoffert, A. Jain, M. Lai, R. Leemans, S. Raper, T. Wigley, J. de Wolde (1997) An introduction to simple climate models used in the IPCC Second Assessment Report. IPCC Technical Paper II. 39 pp.
- Harvey, L. D. D. (1999) Global warming: the hard science. Prentice Hall, Harlow. 408 pp.
- Hasselmann, K., S. Hasselmann, R. Giering, V. Ocana, H. V. Storch (1997) Sensitivity Study of Optimal CO₂ Emission Paths Using a Simplified Structural Integrated Assessment Model (SIAM). *Climatic Change*, **37**, 345-386.
- Hegerl, G. C., T. J. Crowley, W. T. Hyde, D. J. Frame (2006) Climate sensitivity constrained by

- temperature reconstructions over the past seven centuries. *Nature*, **440**, 1029-1032.
- Hein, R., P. J. Crutzen, M. Heimann (1997) An inverse modelling approach to investigate the global atmospheric methane cycle. *Global Biogeochemical Cycles*, **11**, 43-76.
- Hoffert, M. I., A.J. Callegari, C. T. Hsieh (1980) The role of deep sea heat storage in the secular response to climate forcing. *Journal of Geophysical Research*, **85**, 6667-6679.
- Hoffert, M. I., A. J. Callegari, C.-T. Hsieh (1981) A box-diffusion carbon cycle model with upwelling, polar bottom water formation and a marine biosphere. In (ed.) B. Bolin. *Carbon cycle modelling (SCOPE 16)*. pp. 287-305. John Wiley & Sons. 390 pp.
- Holland, H. D. (1978) *The chemistry of the atmosphere and oceans*. Wiley, New York. USA. 351 pp.
- Hooss, G, V. Reinhard, K. Hasselmann, E. Maier-Reimer, F. Joos (1999) A nonlinear impulse response model of the coupled carbon cycle-ocean-atmosphere climate system. Max Planck Institute for Meteorology. Report No. 290. 62 pp.
- Hooss, G. (2001) *Aggregate models of climate change: development and applications*. Ph. D. dissertation. Hamburg Universität. <http://www.icbm.de/~hooss/niccs/docum/welcome.html>
- Hooss, G, R. Voss, K. Hasselmann, E. Maier-Reimer, F. Joos (2001) A nonlinear impulse response model of the coupled carbon cycle-climate system (NICCS). *Climate Dynamics*, **18**, 189-202.
- Hooss, K. G. (2004) Modelle der globalen Umwelt und Gesellschaft. *promet*, **30**, 213-224.
- Houghton, R. A., J. L. Hackler (2002) Carbon Flux to the Atmosphere from Land-Use Changes. In *Trends: A Compendium of Data on Global Change*. Carbon Dioxide Information Analysis Center, Oak Ridge National Laboratory, U.S. Department of Energy, Oak Ridge, Tenn., U.S.A. <http://cdiac.ornl.gov/>
- Houghton, R. A. (2003). Revised estimates of the annual net flux of carbon to the atmosphere from changes in land use and land management 1850-2000. *Tellus B*, **55**, 378-390.
- IPCC (1996) *Climate Change 1995: the Science of Climate Change*. [Houghton, J. T., L. G. Meira Filho, B. A. Callander, N. Harris, A. Kattenberg, K. Maskell (eds.)]. Cambridge University Press, Cambridge. 572 pp.
- IPCC (2001) *Climate Change 2001: The Scientific Basis*. Contribution of Working Group I to the Third Assessment Report of the Intergovernmental Panel on Climate Change [Houghton, J.T., Y. Ding, D.J. Griggs, M. Noguer, P.J. van der Linden, X. Dai, K. Maskell, and C.A. Johnson (eds.)]. Cambridge University Press, Cambridge, United Kingdom and New York, NY, USA, 881 pp.
- IPCC Working Group I (2004a) *Workshop report on climate sensitivity*. École Normale Supérieure Paris, France. 26–29 July, 2004. 177 pp.
- IPCC Working Group I (2004b) *IPCC Workshop on describing scientific uncertainties in climate change to support analysis of risk and of options*. 11–13 May, 2004, National University of Ireland, Maynooth, Co. Kildare, Ireland. 138 pp.
- IPCC (2005) *IPCC Special Report on Safeguarding the Ozone Layer and the Global Climate*

- System: Issues related to Hydrofluorocarbons and Perfluorocarbons. Cambridge University Press, Cambridge, United Kingdom and New York, NY, USA, 486 pp.
- IPCC (2007) Climate Change 2007: The Physical Science Basis. Summary for Policymakers. Contribution of Working Group I to the Fourth Assessment Report of the Intergovernmental Panel on Climate Change. [R. Alley, T. Berntsen, N. L. Bindoff, Z. Chen, A. Chidthaisong, P. Friedlingstein, J. Gregory, G. Hegerl, M. Heimann, B. Hewitson, B. Hoskins, F. Joos, J. Jouzel, V. Kattsov, U. Lohmann, M. Manning, T. Matsuno, M. Molina, N. Nicholls, J. Overpeck, D. Qin, G. Raga, V. Ramaswamy, J. Ren, M. Rusticucci, S. Solomon, R. Somerville, T. F. Stocker, P. Stott, R. J. Stouffer, P. Whetton, R. A. Wood, D. Wratt (drafting authors)], 21 pp.
- Jacob, D. (1999) Introduction to atmospheric chemistry. Princeton University Press, Princeton, New Jersey, USA. 264 pp.
- Jet Propulsion Laboratory (JPL) (2003) Chemical kinetics and photochemical data for use in atmospheric studies: evaluation number 14.
- Jones, P. D., K. R. Briffa, T. P. Barnett, S. F. B. Tett (1998) Millennial Temperature Reconstructions. IGBP PAGES/World Data Center-A for Paleoclimatology Data Contribution Series #1998-039. NOAA/NGDC Paleoclimatology Program, Boulder, Colorado, USA.
- Jones, C. D., P. M. Cox (2001) Modeling the volcanic signal in the atmospheric CO₂ record. *Global Biogeochemical Cycles*, **15**, 453-465.
- Jones, C. D., M. Collins, P. M. Cox, S. A. Spall (2001) The carbon cycle response to ENSO: a coupled climate-carbon cycle model study. *Journal of Climate*, **14**, 4113-4129.
- Jones, P. D., M. E. Mann (2004) Climate over past millennia. *Review of Geophysics*, **42**, RG2002.
- Jones, P. D., D. E. Parker, T. J. Osborn, K. R. Briffa (2006) Global and hemispheric temperature anomalies – land and marine instrumental records. In Trends: A Compendium of Data on Global Change. Carbon Dioxide Information Analysis Center, Oak Ridge National Laboratory, U.S. Department of Energy, Oak Ridge, Tenn., U.S.A. <http://cdiac.ornl.gov/>
- Joos, F., M. Bruno, R. Fink, U. Siegenthaler, T. F. Stocker (1996) An efficient and accurate representation of complex oceanic and biospheric models of anthropogenic carbon uptake. *Tellus*, **48B**, 397-417.
- Joos, F., C. Prentice, S. Sitch, R. Meyer, G. Hooss, G.-K. Plattner, S. Gerber, K. Hasselmann (2001) Global warming feedbacks on terrestrial carbon uptake under the Intergovernmental Panel on Climate Change (IPCC) emission scenarios. *Global Biogeochemical Cycles*, **15**, 891–907.
- Kaplan, J. O. (2001) Geophysical applications of vegetation modeling. Ph. D. Dissertation at Lund University.
- Kaplan, J. O. (2002) Wetlands at the Last Glacial Maximum: Distribution and Methane Emissions. *Geophysical Research Letters*, **29-6**, 1079.
- Keeling, C. D. (1973) The carbon dioxide cycle: reservoir models to depict the exchange of

- atmospheric carbon dioxide with the oceans and land plants. In (ed.) S. Rasool. *Chemistry of the lower atmosphere*. Plenum Press, New York, New York, USA. pp. 251-329.
- Keeling, C. D., T. P. Whorf (2005) Atmospheric CO₂ records from sites in the SIO air sampling network. In *Trends: A Compendium of Data on Global Change*. Carbon Dioxide Information Analysis Center, Oak Ridge National Laboratory, U.S. Department of Energy, Oak Ridge, Tenn., U.S.A. <http://cdiac.ornl.gov/>
- Kemfert, C., W. Knorr (2006) Bewertung des Klimawandels anhand von gekoppelten, global vernetzten Ökonomie-Biosphäre-Klima-Modellen ECOBICE (Economy-Biosphere-Climate). 114 pp.
- Keppler, F., J. T. G. Hamilton, M. Brass, T. Röckmann (2006) Methane emissions from terrestrial plants under aerobic conditions. *Nature*, **439**, 187-191.
- Kicklighter, D. W., M. Bruno. S. Dönges, G. Esser, M. Heimann, J. Helfrich, F. Ift, F. Joos, J. Kaduk, G. H. Kohlmaier, A. D. McGuire, J. M. Melillo, R. Meyer, B. Moore III, A. Nadler, I. C. Prentice, W. Sauf, A. L. Schloss, S. Sitch, U. Wittenberg, G. Würth (1999) A first-order analysis of the potential role of CO₂ fertilization to affect the global carbon budget: a comparison of four terrestrial biosphere models. *Tellus*, **51B**, 343–366.
- Klein Goldewijk, K. (2001) Estimating global land use change over the past 300 years: the HYDE database. *Global Biogeochemical Cycles*, **15**, 417-433.
- Kleypas, J. A., R. W. Buddemeier, D. Archer, J.-P. Gattuso, C. Langdon, B. N. Opdyke (1999) Geochemical consequences of increased atmospheric carbon dioxide on coral reefs. *Science*, **284**, 118-120.
- Knorr, W., M. Heimann (2001) Uncertainties in global terrestrial biosphere modeling, Part II: global constraints for a process-based vegetation model. *Global Biogeochemical Cycles*, **15**, 227-246.
- Knutti, R., T. F. Stocker, F. Joos, G.-K. Plattner (2002) Constraints on radiative forcing and future climate change from observations and climate model ensembles. *Nature*, **416**, 719-723.
- Knutti, R., T. F. Stocker, F. Joos, G.-K. Plattner (2003) Probabilistic climate change projections using neural networks. *Climate Dynamics*, **21**, 257–272.
- Kohlmaier, G. H., H. Brohl, E. O. Siré, M. Plöchl, R. Reville (1987) Modelling stimulation of plants and ecosystem response to present levels of excess atmospheric CO₂. *Tellus*, **39B**, 155–179.
- Körner, C. (2006) Plant CO₂ responses: an issue of definition, time and resource supply. *New Phytologist*, **172**, 393-411.
- Kriegler, E. (2005) Imprecise probability analysis for Integrated Assessment of climate change. Ph. D. dissertation. Potsdam Universität. 256 pp. <http://opus.kobv.de/ubp/volltexte/2005/561/>.
- Kriegler, E., O. Edenhofer, K. Lessmann (2006) On the link between mitigation of and damages from climate change. Solicited oral presentation at the EGU General Assembly 2006, Vienna, Austria. 02/04 – 07/04/2006.

- Lal, R. (2005) Soil erosion and carbon dynamics. *Soil and Tillage Research*, **81**, 137-142.
- Laws, E. A., (1997) Mathematical methods for oceanographers: an introduction. Wiley, New York, 343 pp.
- Lean, J. (2000) Evolution of the Sun's spectral irradiance since the Maunder Minimum. *Geophysical Research Letters*, **27**, 16, 2425-2428.
- Lean, J., J. Beer, R. Bradley (1995) Reconstruction of solar irradiance since 1610: implications for climate change. *Geophysical Research Letters*, **22**, 23, 3195-3198.
- Lee, K., L. T. Tong, F. J. Millero, C. L. Sabine, A. G. Dickson, C. Goyet, G.-H. Park, R. Wanninkhof, R. A. Feely, R. M. Key (2006) Global relationships of total alkalinity with salinity and temperature in surface waters of the world's oceans. *Geophysical Research Letters*, **33**, L19605, doi:10.1029/2006GL027207.
- Lelieveld, J., P. J. Crutzen, F. J. Dentener (1998) Changing concentration, lifetime and climate forcing of atmospheric methane. *Tellus B*, **50**, 128-150.
- Lelieveld, J., F. J. Dentener, W. Peters, M. C. Krol (2004) On the role of hydroxyl radicals in the self-cleansing capacity of the troposphere. *Atmospheric Chemistry and Physics*, **4**, 2337-2344.
- Levitus, S., J. I. Antonov, T. P. Boyer, C. Stephens (2000) Warming of the world ocean. *Science*, **287**, 2225-2229.
- Li, Y.-H. (2000) A compendium of geochemistry. Princeton University Press, Princeton, New Jersey, US. 475 pp.
- Libes, S. M. (1992) An introduction to marine biogeochemistry. Wiley, New York, New York, USA. 734 pp.
- Long, S. P., E. A. Ainsworth, A. Rogers, D. R. Ort (2004) Rising atmospheric carbon dioxide: plants FACE the future. *Annual review of plant biology*, **55**, 591-628.
- Lowe, D. C. (2006) A green source of surprise. *Nature*, **439**, 148-149.
- Lucht, W., I. C. Prentice, R. B. Myneni, S. Sitch, P. Friedlingstein, W. Cramer, P. Bousquet, W. Buermann, B. Smith (2002) Climatic Control of the High-Latitude Vegetation Greening Trend and Pinatubo Effect. *Science*, **296**, 1687-1689.
- Mackenzie, F. T. (2002) Our changing plant: an introduction to earth system science and global environmental change. Third edition. Prentice Hall, New Jersey, U.S.A.
- Mackenzie, F. T., A. Lerman, A. Andersson (2004) Past and present of sediment and carbon biogeochemical cycling models. *Biogeosciences*, **1**, 11-32.
- Mackenzie, F. T., A. Lerman (2006) Carbon in the Geobiosphere: Earth's Outer Shell. Springer, Dordrecht, The Netherlands. 402 pp.
- Maier-Reimer, E., K. Hasselmann (1987) Transport and storage of CO₂ in the ocean – an inorganic ocean-circulation carbon cycle model. *Climate Dynamics*, **2**, 63-90.
- Maier-Reimer, E., U. Mikolajewicz, A. Winguth (1996) Future ocean uptake of CO₂: interaction

- between ocean circulation and biology. *Climate Dynamics*, **12**, 711-721.
- Maiss, M., L. P. Steele, R. J. Francey, P. J. Fraser, R. L. Langenfelds, N. B. A. Trivett, I. Levin (1996) Sulfur hexafluoride—A powerful new atmospheric tracer. *Atmospheric Environment*, **30**, 1621-1629.
- Maiss, M., C. A. M. Brenninkmeijer (1998) Atmospheric SF₆: Trends, sources, and prospects. *Environmental Science and Technology*, **32**, 3077-3086.
- Maiss, M., C. A. M. Brenninkmeijer (1999) A reversed trend in emissions of SF₆ to the atmosphere? p.199-204, in (eds. J. Van Ham, A.P.M. Baede, L.A. Meyer, and R. Ybema) *Non-CO₂ Greenhouse Gases: Scientific Understanding, Control and Implementation*, Proceedings of the 2nd International Symposium, Noordwijkerhout, The Netherlands, 8-10 September 1999, Kluwer Academic Publishers, Dordrecht, The Netherlands.
- Malinverno, A., V. A. Briggs (2004) Expanded uncertainty quantification in inverse problems: hierarchical Bayes and empirical Bayes. *Geophysics*, **69**, 1005-1016.
- Mann, M. E., P. D. Jones (2003) Global surface temperatures over the past two millennia. *Geophysical Research Letters*, **30**(15), 1820, doi:10.1029/2003GL017814.
- Marland, G., T. A. Boden, R. J. Andres (2006) Global, regional, and national CO₂ emissions. In Trends: A Compendium of Data on Global Change. Carbon Dioxide Information Analysis Center, Oak Ridge National Laboratory, U.S. Department of Energy, Oak Ridge, Tenn., U.S.A. <http://cdiac.ornl.gov/>
- Masarie, K. A., R. L. Langenfelds, C. E. Allison, T. J. Conway, E. J. Dlugokencky, R. J. Francey, P. C. Novelli, L. P. Steele, P. P. Tans, B. Vaughn, J. W. C. White (2001) NOAA/CSIRO flask intercomparison project: a strategy for directly assessing consistency among atmospheric measurements made by independent laboratories. *Journal of Geophysical Research*, **106**, D17, 20445-20464.
- Mastrandrea, M. D., S. H. Schneider (2004) Probabilistic integrated assessment of “dangerous” climate change. *Science*, **304**, 571-575.
- Matthews, E., I. Fung (1987) Methane emission from natural wetlands: global distribution, area, and environmental characteristics of sources. *Global Biogeochemical Cycles*, **1**, 61-86.
- McCarl, B. (1996) GAMBAS: a program for saving an advanced basis for GAMS. Version 1. Accompanied in the GAMS software package.
- McCarl, B. (2006) McCarl GAMS User Guide. Version 22.2. Accompanied with the GAMS software package.
- McPhaden, M. J., S. E. Zebiak, M. H. Glantz (2006) ENSO as an integrating concept in Earth science. *Science*, **314**, 1740-1745.
- Mears, C. A., M.C. Schabel, F. J. Wentz (2003) A reanalysis of the MSU channel 2 tropospheric temperature record. *Journal of Climate*, **16**, 3650-3664.

- Melillo, J. M., A. D. McGuire, D. W. Kicklichter, B. Moore III, C. J. Vorosmarty, A. L. Schloss (1993) Global climate change and terrestrial net primary production. *Nature*, **363**, 234-240.
- Meyer, R., F. Joos, G. Esser, M. Heimann, G. Hooss, G. Kohlmaier, W. Sauf, R. Voss, U. Wittenberg (1999) The substitution of high-resolution terrestrial biosphere models and carbon sequestration in response to changing CO₂ and climate. *Global Biogeochemical Cycles*, **13**, 785-802.
- Mikaloff Fletcher, S. E., P. P. Tans, L. M. Bruhwiler, J. B. Miller, M. Heimann (2004) CH₄ sources estimated from atmospheric observations of CH₄ and its ¹³C/¹²C isotopic ratios: 1. Inverse modeling of source processes. *Global Biogeochemical Cycles*, **18**, GB4004, doi:10.1029/2004GB002223.
- Millero, F. J. (1995) Thermodynamics of the carbon dioxide system in the oceans. *Geochimica et Cosmochimica Acta*, **59**, 661-677.
- Millero, F. J. (2006) Chemical oceanography. 3rd edition. CRC Press, Taylor & Francis Group. Boca Raton, Florida, US. 496 pp.
- Millero, F. J., T. B. Graham, F. Huang, H. Bustos-Serrano, D. Pierrot (2006) Dissociation constants of carbonic acid in seawater as a function of salinity and temperature. *Marine Chemistry*, **100**, 80-94.
- Moberg, A., D. M. Sonechkin, K. Holmgren, N. M. Datsenko, W. Karlén (2005) Highly variable Northern Hemisphere temperatures reconstructed from low- and high-resolution proxy data. *Nature*, **433**, 613-617.
- Montzka, S. A., J. H. Butler, J. W. Elkins, T. M. Thompson, A. D. Clarke, L. T. Lock (1999) Present and future trends in the atmospheric burden of ozone-depleting halogens. *Nature*, **398**, 690-694.
- Mosegard, K., Tarantola, A. (2002) Probabilistic approach to inverse problems. In *International Handbook of Earthquake & Engineering Seismology, Part A*. (eds. W. H. K. Lee, H. Kanamori, P. Jennings, C. Kisslinger), pp. 237-265, Academic Press, Amsterdam, The Netherlands.
<http://www.ipgp.jussieu.fr/~tarantola/>
- Munk, W. (1966) Abyssal recipes. *Deep Sea Research*, **13**, 707-730.
- Murphy, J. M. (1995) Transient response of the Hadley Centre coupled ocean-atmosphere model to increasing carbon dioxide. Part III: Analysis of global mean response using simple models. *Journal of Climate*, **8**, 496-514.
- Murphy, J. M., D. M. H. Sexton, D. N. Barnett, G. S. Jones, M. J. Webb, M. Collins, D. A. Stainforth (2004) Quantification of modelling uncertainties in a large ensemble of climate change simulation. *Nature*, **430**, 768-772.
- Myhre, G., E. J. Highwood, K. P. Shine, F. Stordal (1998) New estimates of radiative forcing due to well mixed greenhouse gases. *Geophysical Research Letters*, **25**, 14, 2715-2718.
- Nakićenović, N., R. Swart (eds.) (2000) Special Report on Emissions Scenarios. Cambridge University Press, Cambridge, United Kingdom, 612 pp.

- Neelin, J. D., D. S. Battisti, A. C. Hirst, F. -F. Jin, Y. Wakata, T. Yamagata, S. E. Zebiak (1998) ENSO theory. *Journal of Geophysical Research*, **103**, C7, 14261-14290.
- Neelin, J. D., C. Chou, H. Su (2003) Tropical drought regions in global warming and El Niño teleconnections. *Geophysical Research Letters*, **30**, doi:10.1029/2003GL018625.
- Nisbet, E. G., D. J. W. Piper (1998) Giant submarine landslides. *Nature*, **392**, 329-330.
- Nordhaus, W. D., J. Boyer (2000) Warming the world: economic models of global warming.
- Oman, L., A. Robock, G. Stenchikov, G. A. Schmidt, and R. Ruedy (2005) Climatic response to high-latitude volcanic eruptions. *Journal of Geophysical Research*, **110**, D13103, doi:10.1029/2004JD005487.
- Oram, D. E., W. T. Sturges, S. A. Penkett (1998) Growth of fluoroform (CHF₃, HFC-23) in the background atmosphere. *Geophysical Research Letters*, **25**, 35-38.
- Oram, D. E., W. T. Sturges, S. A. Penkett, A. McCulloch, P. J. Fraser (2000) Atmospheric Fluoroform (CHF₃, HFC-23) at Cape Grim, Tasmania. In Trends: A Compendium of Data on Global Change. Carbon Dioxide Information Analysis Center, Oak Ridge National Laboratory, U.S. Department of Energy, Oak Ridge, Tenn., U.S.A. <http://cdiac.ornl.gov/>
- Orr, J. C., V. J. Fabry, O. Aumont, L. Bopp, S. C. Doney, R. A. Feely, A. Gnanadesikan, N. Gruber, A. Ishida, F. Joos, R. M. Key, K. Lindsay, E. Maier-Reimer, R. Matear, P. Monfray, A. Mouchet, R. G. Najjar, G. -K. Plattner, K. B. Rodgers, C. L. Sabine, J. L. Sarmiento, R. Schlitzer, R. D. Slater, I. J. Totterdell, M. -F. Weirig, Y. Yamanaka, A. Yool (2005) Anthropogenic ocean acidification over the twenty-first century and its impact on calcifying organisms. *Nature*, **437**, 681-686.
- Park, K. (1969) Oceanic CO₂ system: an evaluation of ten methods of investigation. *Limnology and Oceanography*, **14**, 179-186.
- Penkett, S. A., K. S. Law, T. Cox, P. Kasibhatla (2003) Atmospheric Photooxidants. pp. 73-124. In (eds. G. P. Brasseur, R. G. Prinn, A. A. P. Pszenny) *Atmospheric chemistry in a changing world. The IGBP Series*. Springer, Berlin, Germany. 300 pp.
- Petit, J. R., J. Jouzel, D. Raynaud, N. I. Barkov, J.-M. Barnola, I. Basile, M. Bender, J. Chappellaz, M. Davisk, G. Delaygue, M. Delmotte, V. M. Kotlyakov, M. Legrand, V. Y. Lipenkov, C. Lorius, L. Pépin, C. Ritz, E. Saltzmank, M. Stievenard (1999) Climate and atmospheric history of the past 420,000 years from the Vostok ice core, Antarctica. *Nature*, **399**, 429-436.
- Petoukhov, V., A. Ganopolski, V. Brovkin, M. Claussen, A. Eliseev, C. Kubatzki, S. Rahmstorf (2000) CLIMBER-2: A climate system model of intermediate complexity. Part I: Model description and performance for present climate. *Climate Dynamics*, **16**, 1-17.
- Plattner, G.-K., F. Joos, T. F. Stocker, O. Marchal (2001) Feedback mechanisms and sensitivities of ocean carbon uptake under global warming. *Tellus*, **53B**, 564-592.
- Pilson, M. E. Q. (1998) An introduction to the chemistry of the sea. Prentice Hall, Upper Saddle River, New Jersey, US, 431 pp.

- Pollock, W. H. L. E. Heidt, R. A. Lueb, J. F. Vedder, M. J. Mills, S. Solomon (1992) On the age of stratospheric air and ozone depletion potential in polar region. *Journal of Geophysical Research*, **97**, 12993-12999.
- Prather, M. J. (1998) Time scales in atmospheric chemistry: coupled perturbations to N₂O, NO_y, and O₃. *Science*, **279**, 1339-1341.
- Press, W. H., S. A. Teukolsky, W. T. Vetterling, B. P. Flannery (2001) Numerical recipes in Fortran: the art of scientific computing. Volume 1. Cambridge University Press, Cambridge, UK. 934 pp. http://www.nr.com/nronline_switcher.php
- Prinn, R.G., R. F. Weiss, P. J. Fraser, P. G. Simmonds, D. M. Cunnold, F. N. Alyea, S. O'Doherty, P. Salameh, B. R. Miller, J. Huang, R. H. J. Wang, D. E. Hartley, C. Harth, L. P. Steele, G. Sturrock, P. M. Midgely, and A. McCulloch (2000) A history of chemically and radiatively important gases in air deduced from ALE/GAGE/AGAGE. *Journal of Geophysical Research* **105**, 17751-17792.
- Prinn, R. G., J. Huang, R. F. Weiss, D. M. Cunnold, P. J. Fraser, P. G. Simmonds, A. McCulloch, C. Harth, P. Salameh, S. O'Doherty, R. H. J. Wang, L. Porter, B. R. Miller (2001) Evidence for substantial variations of atmospheric hydroxyl radicals in the past two decades. *Science*, **292**, 1882-1888.
- Raddatz, T. J., C. H. Reick, W. Knorr, J. Kattge, E. Roeckner, R. Schnur, K.-G. Schnitzler, P. Wetzel, J. Jungclaus (in press) Will the tropical land biosphere dominate the climate - carbon cycle feedback during the 21st century? *Climate Dynamics*.
- Räisänen, J. (2007) How reliable are climate models? *Tellus*, **59A**, 2-29.
- Raper, S. C. B., U. Cubasch (1996) Emulation of the results from a coupled general circulation model using a simple climate model. *Geophysical Research Letters*, **23**, 1107-1110.
- Raper, S. C. B., J.M. Gregory, T.J. Osborn (2001) Use of an upwelling-diffusion balance climate model to simulate and diagnose A/OGCM results. *Climate Dynamics*, **17**, 601-613.
- Revelle, R., W. Munk (1977) The carbon dioxide cycle and the biosphere. In *Energy and Climate*, Studies in geophysics. National Academy Press, Washington, D.C., US. pp. 140-158.
- Ridgwell, A. J., S. J. Marshall, K. Gregson (1999) Consumption of atmospheric methane by soils: a process-based model. *Global Biogeochemical Cycles*, **13-1**, 59-70.
- Ridgwell, A, I. Zondervan, J. C. Hargreaves, J. Bijma, T. M. Lenton (2006) Significant long-term increase of fossil fuel CO₂ uptake from reduced marine calcification. *Biogeosciences Discussion*, **3**, 1763-1780. SRef-ID: 1810-6285/bgd/2006-3-1763.
- Riebesell, U., I. Zondervan, B. Rost, P. D. Tortell, R. E. Zeebe, F. M. M. Morel (2000) Reduced calcification of marine plankton in response to increased atmospheric CO₂. *Nature*, **407**, 364-367.
- Robock, A. (2000) Volcanic eruptions and climate. *Reviews of Geophysics*, **38**, 191-219.

- Robock, A. (2005) Cooling following large volcanic eruptions corrected for the effect of diffuse radiation on tree rings. *Geophysical Research Letters*, 32, L06702, doi: 10.1029/2004GL022116.
- Ropelewski, C. F. (1992) Predicting El Niño events. *Nature*, **356**, 476-477.
- Rosenlof, K., S. J. Oltmans, D. Kley, J. M. Russell III, E. -W. Chiou, W. P. Chu, D. G. Johnson, K. K. Kelly, H. A. Michelsen, G. E. Nedoluha, E. E. Remsberg, G. C. Toon, M. P. McCormick (2001) Stratospheric water vapor increases over the past half-century. *Geophysical Research Letters*, **28**, 1195-1198, 10.1029/2000GL012502, 2001.
- Rosenthal, R. E. (2007) GAMS – a user’s guide. GAMS Development Corporation, Washington, DC, USA. 271 pp.
- Ruddiman, W. F. (2003) The anthropogenic greenhouse era began thousands of years ago. *Climatic Change*, **61**, 261–293.
- Ruttimann, J. (2006) Sick seas. *Nature*, **442**, 978-980.
- Santer, B. D., T. M. L. Wigley, C. Mears, F. J. Wentz, S. A. Klein, D. J. Seidel, K. E. Taylor, P. W. Thorne, M. F. Wehner, P. J. Geckler, J. S. Boyle, W. D. Collins, K. W. Dixon, C. Doutriaux, M. Free, Q. Fu, J. E. Hansen, G. S. Jones, R. Ruedy, T. R. Karl, J. R. Lazarante, G. A. Meehl, V. Ramaswamy, G. Russel, G. A. Schmidt (2005) Amplification of surface temperature trends and variability in the tropical atmosphere. *Science*, **309**, 1551-1556.
- Scales J. A., L. Tenorio (2001) Prior information and uncertainty in inverse problems. *Geophysics*, **66**, 389-397.
- Schauffler, S. M., J. S. Daniel (1994) On the effects of stratospheric circulation changes on trace gas trends. *Journal of Geophysical Research*, **99(D12)**, 25747-25754.
- Schauffler, S. M., E. L. Atlas, D. R. Blake, F. Flocke, R. A. Lueb, J. M. Lee-Taylor, V. Stroud, W. Travnicek (1999) Distributions of brominated organic compounds in the troposphere and lower stratosphere. *Journal of Geophysical Research*, **104, D17**, 21513-21535.
- Schlesinger, M. E. (1985) Appendix A: Analysis of results from energy balance and radiative convective models. In (Eds.) M.C. MacCracken, F. M. Luther. *Projecting the Climate Effects of Increasing Carbon Dioxide*. US Department of Energy, DOE/ER-0237, pp. 281-319.
- Schlesinger, W. H. (1997) *Biogeochemistry: an analysis of global change*. Academic Press, San Diego, California, USA. 588 pp.
- Schlesinger, M. E., N.G. Andronova, B. Entwistle, A. Ghanem, N. Ramankutty, W. Wang, F. Yang (1997) Modeling and simulation of climate and climate change. In *Proceedings of the International School of Physics Enrico Fermi CXXXIII*. IOS Press, Amsterdam, pp. 389-429.
- Schneider (2002) Can we estimate the likelihood of climatic changes at 2100?: an editorial comment, *Climatic Change*, **52**, 441–451.
- Schneider, S. H., K. Kuntz-Duriseti (2002) Uncertainty and climate change policy. pp.53-87. In *Climate change policy: a survey* (eds. S. H. Schneider, A. Rosencranz, J. O. Niles). Island Press,

- Washington, D. C., USA. 563 pp.
- Schneider von Deimling, T., H. Held, A. Ganopolski, S. Rahmstorf (2006) Climate sensitivity estimated from ensemble simulations of glacial climate. *Climate Dynamics*, **27**, 149-163.
- Seinfeld, J. H., S. N. Pandis (2006) Atmospheric chemistry and physics: From air pollution to climate change. 2nd edition. Wiley, New York, USA. 1203 pp.
- Shaffer, G., U. Rönner (1984) Denitrification in the Baltic proper deep water. *Deep Sea Research*, **31**, 197-220.
- Shafer, G. (1992) What is probability? In *Perspectives on Contemporary Statistics* (eds. David C. Hoaglin and David S. Moore). Mathematical Association of America, MAA Notes Number 21, pp. 93-105.
- Shine, K., P. Forster (1999) The effect of human activity on radiative forcing of climate change: a review of recent developments. *Global and Planetary Change*, **20**, 205-225.
- Siebert, L., T. Simkin (2006). Volcanoes of the World: an Illustrated Catalog of Holocene Volcanoes and their Eruptions. Smithsonian Institution, Global Volcanism Program Digital Information Series, GVP-3, (<http://www.volcano.si.edu/world/>).
- Simmons, H. L., S.R. Jayne, L.C.S. Laurent, A. J. Weaver (2004) Tidally driven mixing in a numerical model of the ocean circulation. *Ocean Modelling*, **6**, 245-263.
- Sitch, S., B. Smith, I. C. Prentice, A. Arneth, A. Bondeau, W. Cramer, J. O. Kaplan, S. Levis, W. Lucht, M. T. Sykes, K. Thonicke, S. Venevsky (2003) Evaluation of ecosystem dynamics, plant geography and terrestrial carbon cycling in the LPJ dynamic global vegetation model. *Global Change Biology*, **6**, 161-185.
- Smith, S. V., F. T. Mackenzie (1987) The ocean as a net heterotrophic system: implications from the carbon biogeochemical cycle. *Global Biogeochemical Cycles*, **1**, 187-198.
- Smith, R. L., T. M. L. Wigley, B. D. Santer (2003) A bivariate time series approach to anthropogenic trend detection in hemispheric mean temperatures. *Journal of Climate*, **16**, 1228-1240.
- Soden, B. J., R. T. Wetherald, G. L. Stenchikov, A. Robock (2002) Global cooling after the eruption of Mount Pinatubo: a test of climate feedback by water vapor. *Science*, **296**, 727-730.
- Solanki, S. K., M. Schüssler, M. Fligge (2002) *Astronomy and Astrophysics*, **383**, 706.
- Solomon, S. (1999) Stratospheric ozone depletion: a review of concepts and history. *Reviews of Geophysics*, **37**, 275-316.
- Stainforth, D. A., T. Aina, C. Christensen, M. Collins, N. Faull, D. J. Frame, J. A. Kettleborough, S. Knight, A. Martin, J. M. Murphy, C. Piani, D. Sexton, L. A. Smith, R. A. Spicer, A. J. Thorpe, M. R. Allen (2005) Uncertainty in predictions of the climate response to rising levels of greenhouse gases. *Nature*, **433**, 403-406.
- Stern, D. I., R. K. Kaufmann (1998) Annual estimates of global anthropogenic methane emissions: 1860-1994. Trends Online: A Compendium of Data on Global Change. Carbon Dioxide

- Information Analysis Center, Oak Ridge National Laboratory, U.S. Department of Energy, Oak Ridge, Tenn., U.S.A. <http://cdiac.ornl.gov/>
- Stocker, T. F., A. Schmittner (1998) Influence of CO₂ emission rates on the stability of the thermohaline circulation. *Nature*, **388**, 862-865.
- Sturges, W. T., T. J. Wallington, M. D. Hurley, K. P. Shine, K. Sihra, A. Engel, D. E. Oram, S. A. Penkett, R. Mulvaney, C. A. M. Brenninkmeijer (2000) A potent greenhouse gas identified in the atmosphere: SF₅CF₃. *Science*, **289**, 611-613.
- Sturrock, G. A., D. M. Etheridge, C. M. Trudinger, P. J. Fraser, A. M. Smith (2002) Atmospheric histories of halocarbons from analysis of Antarctic firn air: Major Montreal Protocol species. *Journal of Geophysical Research*, **107**(D24), 4765, doi:10.1029/2002JD002548.
- Suess, E., G. Bohrmann, J. Greinert, E. Lausch (1999) Flammable ice. *Scientific American*, 52-59 and 76-83.
- Sundquist, E. T., L. N. Plummer (1981) Carbon dioxide in the ocean surface layer: some modelling considerations. In (ed.) B. Bolin. *Carbon cycle modelling (SCOPE 16)*. pp. 259-269. John Wiley & Sons. 390 pp.
- Svensen, H., S. Planke, A. Malthes-Sørensen, B. Jamtveit, R. Myklebust, T. R. Eidem, S. S. Rey (2004) Release of methane from a volcanic basin as a mechanism for initial Eocene global warming. *Nature*, **429**, 542-545.
- Takahashi, T. (1989) The carbon dioxide puzzle. *Oceanus*, **32**, 22-29.
- Takemura, T., H. Okamoto, Y. Maruyama, A. Numaguti, A. Higurashi, T. Nakajima (2000) Global three-dimensional simulation of aerosol optical thickness distribution of various origins. *Journal of Geophysical Research*, **105**, D14, 17853-17873.
- Takemura, T., T. Nakajima, A. Higurashi, S. Ohta, N. Sugimoto (2003) Aerosol distributions and radiative forcing over the Asian Pacific region simulated by Spectral Radiation-Transport Model for Aerosol Species (SPRINTARS). *Journal of Geophysical Research*, 108, D23, 8659, doi:10.1029/2002JD003210.
- Tanaka, K., T. Bruckner, W. Knorr, R. Tol, G. Hooss (2005) Uncertainty analysis of carbon cycle and climate parameters using a simple climate model. Poster presentation at EGU General Assembly 2005, Vienna, Austria. 25/04 – 31/04/2005.
- Tanaka, K., F. T. Mackenzie (2005) Ecosystem behavior of southern Kaneohe Bay, Hawaii: a statistical and modelling approach. *Ecological Modelling*, **188**, 296-326.
- Tanaka, K., R. Tol, W. Knorr, T. Bruckner, E. Kriegler, T. Raddatz (2006a) Uncertain Analysis using Aggregated Carbon Cycle, Atmospheric Chemistry, and Climate Model (ACC2). Poster presentation at the EGU General Assembly 2006, Vienna, Austria. 02/04 – 07/04/2006.
- Tanaka, K., R. S. J. Tol, D. Rokityanskiy, B. C. O'Neill, M. Obersteiner (2006b) Evaluating Global Warming Potentials as historical temperature proxies: an application of ACC2 inverse

- calculation. FNU-118, Hamburg University and Centre for Marine and Atmospheric Science, Hamburg, Germany. (Also submitted to *Climatic Change*)
http://www.uni-hamburg.de/Wiss/FB/15/Sustainability/Working_Papers.htm
- Tanaka, K., T. Raddatz, C. Reick (2007) Constraining climate sensitivity in the Earth system: an application of ACC2 inverse calculation. *in preparation*
- Tarantola, A., B. Valette (1982) Inverse problems = quest for information. *Journal of Geophysics*, **50**, 159-170. <http://www.ipgp.jussieu.fr/~tarantola/>
- Tarantola, A., K. Mosegaard (2000) Mathematical basis of physical inference. *Mathematical Physics*, arXiv:math-ph/0009029. <http://arxiv.org/>
- Tarantola, A. (2005) Inverse problem theory and methods for model parameter estimation. Society for Industrial and Applied Mathematics (SIAM), Philadelphia, US. 342 pp.
<http://www.ipgp.jussieu.fr/~tarantola/>
- Tarantola, A. (2006) Popper, Bayes and the inverse problem. *Nature Physics*, **2**, 492-494.
- Tahvonen, O., H. von Storch, J. von Storch (1994) Economic efficiency of CO₂ reduction programs. *Climate Research*, **4**, 127-141.
- Tjoelker, M. G., J. Oleksyn, P. B. Reich (2001) Modelling respiration of vegetation: evidence for a temperature-dependent Q10. *Global Change Biology*, **7**, 223-230.
- Tol, R. S. J., A. F. De Vos (1998) A bayesian statistical analysis of the enhanced greenhouse effect. *Climatic Change*, **38**, 87-112..
- Tomczak, M., J. S. Godfrey (1994) Regional oceanography: an introduction. Pergamon, Elsevier Science, Oxford, England. 422pp.
- Toth, F. (2003) Integrated Assessment of Climate Protection Strategies. *Climatic Change*, **56**, 1-5.
- Trudinger, C. M., I. G. Enting, P. J. Rayner, R. J. Francey (2002) Kalman filter analysis of ice core data 2: double deconvolution of CO₂ and $\delta^{13}\text{C}$ measurements. *Journal of Geophysical Research*, **107(D20)**, 4423-4446, doi:10.1029/2001JD001112.
- Tudhope, A. W., C. P. Chilcott, M. T. McCulloch, E. R. Cook, J. Chappell, R. M. Ellam, D. W. Lea, J. M. Lough, G. B. Shimmield (2001) Variability in the El Niño – Southern Oscillation through a glacial-interglacial cycle. *Science*, **291**, 1511-1517.
- Tyrrell, T., A. H. Taylor (1996) A modelling study of *Emiliania huxleyi* in the NE Atlantic. *Journal of Marine Systems*, **9**, 83-112.
- United Nations (UN) Population Division (2002) World urbanization prospects: the 2001 revision. 182 pp.
- Ulrych, T. J., M. D. Sacchi, A. Woodbury (2001) A Bayes tour of inversion. *Geophysics*, **66**, 55-69.
- van Aardenne, J. A., F. J. Dentener, J. G. J. Olivier, C. G. M. Klein Goldewijk, J. Lelieveld (2001) A 1 x 1 degree resolution dataset of historical anthropogenic trace gas emissions for the period 1890-1990. *Global Biogeochemical Cycles*, **15(4)**, 909-928.

- van Oldenborgh, G. J., S. Y. Philip, M. Collins (2005) El Niño in a changing climate: a multi-model study. *Ocean Science*, **1**, 81-95.
- Ver, L. M. B., F. T. Mackenzie, A. Lerman (1999) Biogeochemical responses of the carbon cycle to natural and human perturbations: past, present, and future. *American Journal of Science*, **299**, 762-801.
- Wang, G. (2005) Agricultural drought in a future climate: results from 15 global climate models participating in the IPCC 4th assessment. *Climate Dynamics*, **25**, 739-753.
- Weatherhead, E. C., S. B. Andersen (2006) The search for signs of recovery of the ozone layer. *Nature*, **441**, 39-45.
- Weber, M., V. Barth, K. Hasselmann (2005) A multi-actor dynamic integrated assessment model (MADIAM) of induced technological change and sustainable economic growth. *Ecological Economics*, **54**, 306-327.
- Webster, M. D., M. Babiker, M. Mayer, J. M. Reilly, J. Harnisch, R. Hyman, M.C. Sarofim, C. Wang (2002) Uncertainty in emissions projections for climate models. *Atmospheric Environment*, **36**, 3659-3670
- Webster, M., C. Forest, J. Reilly, M. Babiker, D. Kicklighter, M. Mayer, R. Prinn, M. Sarofim, A. Sokolov, P. Stone, C. Wang (2003) Uncertainty analysis of climate change and policy response. *Climatic Change*, **61**, 295-320.
- Wetzel, P. (2004) Interannual and decadal variability in the air-sea exchange of CO₂ – a model study. Reports on Earth System Science, 7/2004, Max Planck Institute for Meteorology, Hamburg.
- Wigley, T. M. L., M. E. Schlesinger (1985) Analytical solution for the effect of increasing CO₂ on global mean temperature. *Nature*, **315**, 649-652.
- Wigley, T. M. L., S. C. B. Raper (1992) Implications for climate and sea level of revised IPCC emissions scenarios. *Nature*, **357**, 293-300.
- Wigley, T. M. L., R. Richels, J. A. Edmonds (1996) Alternative emissions pathways for stabilizing concentrations. *Nature*, **379**, 240-243.
- Wigley, T. M. L., C. M. Ammann, B. D. Santer, S. C. B. Raper (2005) Effect of climate sensitivity on the response to volcanic forcing. *Journal of Geophysical Research*, **110**, D09107, doi:10.1029/2004JD005557.
- Winston, W. L. (1994) Operations research: applications and algorithm. Third edition. International Thomson Publishing, Belmont, California, USA. 1318 pp.
- World Meteorological Organization (WMO) (1998) Scientific assessment of ozone depletion: 1998, Global Ozone Research and Monitoring Project—Report No. 44, Geneva. 650 pp.
- World Meteorological Organization (WMO) (2003) Scientific assessment of ozone depletion: 2002, Global Ozone Research and Monitoring Project—Report No. 47, Geneva. 498 pp.
- Wunsch, C. (1996) The ocean circulation inverse problem. Cambridge University Press, Cambridge,

- UK. 442 pp.
- Zeebe, R., D. Wolf-Gladrow (2001) CO₂ in seawater: equilibrium, kinetics, isotopes. Elsevier, Amsterdam, The Netherlands. 346 pp.
- Zhao, M., P. A. Dirmeyer (2003) Production and analysis of GSWP-2 near-surface meteorology data sets. Technical Report No. 159, Center for Land-Ocean-Atmosphere Studies, Calverton, Maryland, USA. 38 pp. <http://www.iges.org/gswp/>
- Zickfeld, R., T. Bruckner (2003) Reducing the risk of abrupt climate change: emissions corridors preserving the Atlantic Thermohaline Circulation. *Integrated Assessment*, **4**, 106-115.
- Zielinski, G. A. (1995) Stratospheric loading and optical depth estimates of explosive volcanism over the last 2100 years derived from the Greenland Ice Sheet Project 2 ice core. *Journal of Geophysical Research*, **100**(D10), 20937-20956.

APPENDIX A TECHNICALITIES

A.1 PROGRAMMING LANGUAGE AND SOLVERS

ACC2 is programmed in GAMS (Distribution 22.4, released on February 14, 2007, <http://www.gams.com>). GAMS is a language designed for mathematical programming and optimization. It is used for various model applications (GAMS Model Library in the GAMS software package) including economic models (e.g. Dynamic Integrated model of Climate and the Economy (DICE) (Nordhaus and Boyer, 2000)). Descriptions on GAMS (including tutorial and some advanced materials) are provided in the GAMS software package.

GAMS falls into the category of fifth-generation programming language, which requires the programmers only to describe the particular problems (e.g. functional relationships and boundary conditions) without building up their algorithms and specifying machine-related matters such as address calculations (“fifth-generation programming languages” in Wikipedia). GAMS is easier for humans to read than the third-generation programming languages such as C and Fortran. GAMS is available for various operation systems – the 32-bit Windows version is used for the development of ACC2. ACC2 has been partly tested on the 64-bit Windows version and has not shown any difference from the 32-bit Windows version in the model calculation results. We have seen small numerical differences between the Windows-based GAMS and the Linux-based GAMS in the model calculation results, but such differences are sufficiently small and can thus be disregarded in practical applications.

One of the strengths of the ACC2 approach is its compactness; the model is small enough to run even on a laptop PC. It typically takes about one day to run the ACC2 past mode on a Windows XP machine (Pentium® M 1300MHz). The future mode needs only some minutes to complete (between 2000 and 2100 for one emission scenario) as it has no nasty optimization. The past mode of ACC2 heavily relies on the optimization capability of GAMS while the future mode of ACC2 uses GAMS just as a simulator. In the future mode, the cost function is set to a trivial constant (zero) because a cost function is formally required in a GAMS-based model. The multivariable equations describing inorganic carbonate chemistry (Section 2.1.2) and the implicit numerical integration method (Sections 2.3.4 and 4.2) are solved by utilizing iterative computation algorithm in GAMS.

The GAMS software package comprises a *compiler* to convert from the high-level language to a low-level machine-readable language and a suite of *solvers* for various mathematical problems such as linear, nonlinear and mixed integer optimization problems (e.g. Winston, 1994)

(for general information on GAMS solvers, <http://www.gams.com/solvers/solvers.htm>). All of the individual solvers are explained in detail in the solver manual contained in the GAMS software package. The GAMS software package offers three local optimization solvers for NonLinear Programming (NLP): CONOPT, MINOS, and SNOPT. The choice of a solver is model-dependent as each of the solvers has strengths and weaknesses. Some guidelines for choosing between CONOPT and MINOS are available at <http://www.gams.com/docs/minosvsconopt.htm>. ACC2 uses only CONOPT for its past and future modes. CONOPT and MINOS are complementary in terms of their algorithms. In fact, ACC2 cannot be solved with MINOS. ACC2 is too large to be dealt with SNOPT.

One could use solvers EXAMINER and GAMSCHK to check the feasibility of the solution. Alternatively, BARON, the *global* optimization solvers for NLP, should be useful to check the solution obtained from the *local* optimization solver CONOPT. However, BARON cannot be used for ACC2 at this point because BARON does not support a model solved with CONOPT (extension in progress (Nick Sahinidis, personal communication, February 14, 2007)) and also because ACC2 is beyond the capacity of BARON. BARON can deal with up to some thousand of variables (Nick Sahinidis, personal communication, February 23, 2007) whereas ACC2 has more than 50,000 variables. The time for BARON to parse and reformulate the model is significant, depending on the nonlinearity and the size of a model. ACC2 needs to increase its numerical efficiency by scaling the variables and equations manually and changing equation structures. Furthermore, BARON does not support the “errorf” functions used in the DOECLIM component in ACC2.

The optimization for the ACC2 inverse estimation is performed by using solver CONOPT3 developed by Arne Stolbjerg Drud, ARKI Consulting and Development (<http://www.conopt.com/>). CONOPT3 is the third version of the CONOPT series and is occasionally updated. Both CONOPT2 and CONOPT3 were required during some development phases of ACC2. We currently use only the latest CONOPT3 (version 3.14q) for ACC2 for all model settings. The performances of different solvers can be compared by utilizing a solver BENCH (better with EXAMINER and PAVER options), which is also included in the GAMS software package. CONOPT3 is said to be the most advanced solver designed for nonlinear programming in the IA community. Switching to different solvers only requires a change in one option statement on the solver assignment.

CONOPT3 is designed for large and sparse models and has been proved to solve models with over 20,000 equations and variables. It is suitable for models with functions depending on a small number of variables (Drud, 2006, p.2). ACC2 has over 50,000 equations and variables, according to model statistics in GAMS. CONOPT3 is designed for the class of models that are declared as “NLP” in GAMS. Such models must contain only smooth functions (or without any discontinuous first derivative). It can still be used with models containing non-smooth functions,

which are declared as “Dynamic NonLinear Programming (DNLP)” in GAMS – however, the DNLP mode is not recommended for CONOPT3 (Drud, 2006, Section 7; Rosenthal, 2007, p.72). CONOPT3 is based on the Generalized Reduced Gradient (GRG) algorithm (Drud, 2006, p.22); that is, CONOPT3 first tries to find a feasible solution (satisfying all the constraints), from which CONOPT3 then tries to look for an optimal solution on the feasible pathways (Drud, 2006, p.30). Scaling of variables and equations are automatically done by default. A major change in CONOPT3 over the previous CONOPT2 is that CONOPT3 uses second derivatives (Hessian matrix if computationally feasible) to determine search directions more efficiently in nonlinear models.

The algorithms in CONOPT3 are technically described in Drud (2006, Appendix A). Here, the flow of the CONOPT3 algorithms is briefly introduced. During the first phase of feasible solution search (Phase 0 in CONOPT3), the Newton’s method and the Linear Programming (LP) techniques are used. During the second phase of feasible solution search and the phase of optimal solution search (Phase 1 to 4 in CONOPT3), if the model is linear or close to linear around the current point, CONOPT3 basically uses a steepest descend algorithm (Press, 2001, Figure 10.6.1; http://www.nr.com/nronline_switcher.php). When the evaluations of nonlinear constraints are costly, the Sequential Linear Programming (SLP) techniques are employed for a linear approximation of the model at a current point by using the first-order Taylor expansion (Greenberg, 2006, “Sequential Linear Programming”) to look for good search directions. CONOPT3 also offers the steepest edge algorithm alternatively. When the model is nonlinear, the Sequential Quadratic Programming (SQP) procedures are adopted for a quadratic approximation of the model at a current point by using the second-order Taylor expansion (Greenberg, 2006, “Sequential Quadratic Programming”). The second-order Taylor expansion requires a Hessian matrix, which can be computed by CONOPT3 (neither CONOPT1 nor CONOPT2). If the whole Hessian matrix cannot be computed due to technical reason, the Broyden-Fletcher-Goldfarb-Shanno (BFGS) algorithm is used to obtain approximately the second order information without computing the Hessian matrix directly. Then the conjugate gradient algorithm is used to determine solution search directions.

Although CONOPT3 is designed to adjust its own performance to the characteristics of a model, it can be ‘fine-tuned’ through the statements in the associated option file. The option files for CONOPT3 used in ACC2 are named “conopt.opt” and “conopt3.opt”. Both of these CONOPT option files are identical. As only one of them is read depending on the version of GAMS, two identical files are prepared. This file is recognized at the beginning of the model run (both the past and future modes). Note that, even if an option file is not successfully recognized, the process goes anyway without prompting the user to check, except for delivering hardly noticeable error lines in the file with an extension “*.lst.” The technical explanation of the option files is provided in pdf files called “Basic Solver Usage” and “CONOPT” in the GAMS software package. Use of the solver options requires specific knowledge and experiences on numerical algorithms. The solver options for

ACC2 are set under a guidance of Arne Stolbjerg Drud. Further explanations on the solver options are provided directly in the option files.

Features of GAMS themselves are also controlled through option statements. The GAMS option statements for ACC2 are directly written in the main files (Section 4.2). The option for automatic scaling is activated. In ACC2, the variables and the equations are not individually scaled by using “scale” suffixes. The BAS option (McCarl, 1996) is activated in the ACC2 past mode. Thus, the basis information such as the equation marginals, variable levels, and variable marginals is used to provide the initial points for the subsequent past mode run. This feature has been highly exploited when the model is solved repeatedly with slightly different initial conditions. Note that the past mode can also be completed without the BAS option. Lastly, GAMS is a commercial software package; a license is required to run ACC2. Demo-version GAMS limits the size of models to be solved and cannot be used for ACC2.

A.2 NUMERICAL INTEGRATION

The time dependent differential equations of the carbon cycle and atmospheric chemistry components in ACC2 are numerically solved by using a variant of Heun’s Predictor-Corrector method. The climate component DOECLIM uses the HH method (Section 2.3.4). The multiplicity of the numerical integration methods in ACC2 is not a problem because suitable numerical methods should be chosen in accordance with the characteristics of dynamic equations and the precisions required. This section begins with the general ideas of numerical integration methods. The discussion of Heun’s Predictor-Corrector method follows.

The Predictor-Corrector method is one of the methods to solve Ordinary Differential Equations (ODEs) numerically. An ODE includes only one dependent variable and should be distinguished from Partial Differential Equations (PDEs), which have more than one dependent variable. When one wishes to advance from t_n to $t_n + \Delta t$ (Δt : a model time step) for an ODE $y'(t) = f(t, y)$, one can use the following calculus theorem:

$$y(t_n + \Delta t) = y(t_n) + \int_{t_n}^{t_n + \Delta t} f(t', y) dt' . \quad (\text{A.2.1})$$

Note that, if function $f(\cdot)$ is independent of y , the problem reduces to a function integration.

ACC2 uses the following numerical integration scheme:

$$y(t_n + \Delta t) = y(t_n) + \Delta t \cdot \left\{ \frac{y'(t_n + \Delta t) + y'(t_n)}{2} \right\} . \quad (\text{A.2.2})$$

The estimate of $y(t_n + \Delta t)$ is obtained by interactive computation algorithms in CONOPT3. The initial value of $y'(t_n + \Delta t)$ is a specific pre-defined value in some cases (specified in the initial value files) or zero by default in other cases.

Equation (A.2.2) corresponds to the predictor step in the standard Heun's Predictor-Corrector method. But it is used differently in ACC2 as explained above. Heun's Predictor-Corrector method is one of the simplest Predictor-Corrector methods. More sophisticated numerical integration methods are exemplified by the Adams-Bashforth-Moulton scheme (Press, 2001, Section 16.7), the Runge-Kutta method (Press, 2001, Sections 16.1 and 16.2)⁶⁸, and the Bulirsch-Stoer method (Press, 2001, Section 16.4). However, these methods are not suitable for GAMS implementation because of the complications in their formulations.

The numerical integration method used in ACC2 is implicit in a sense that there is no explicit analytical expression because of the iterative scheme. An explicit method such as the Euler method is unstable for stiff problems where the scales of variables are not entirely in a same range (Press et al., 2001, Section 16.6). Thus, an implicit method is required for models such as ACC2.

Furthermore, the numerical integration of equation (A.2.2) is suitable for the estimation of the ENSO-driven CO₂ concentration change. In ACC2, the natural change in the atmospheric CO₂ concentration is statistically explained by the NINO3 index (Section 3.5.1). The natural CO₂ change in ACC2 is defined as the average of the slopes for the previous time step and for the following time step, to be compatible to the numerical integration of equation (A.2.2). An explicit Euler method would complicate the treatment for time derivatives. This method would bring in a time lead or time lag because it considers the derivative only for one side.

A.3 MODEL OPERATIONS AND FILE STRUCTURE

ACC2 succeeded to the framework of model operation in the predecessor model ICM. The two modes of operation in ACC2 are

- 1) Past mode: estimation of the uncertain parameters and the projection of the historical evolution of the carbon cycle, atmospheric chemistry, and climate system (year 1750 – 2000)
- 2) Future mode: projection of the future evolution of the carbon cycle, atmospheric chemistry, and

⁶⁸ The fourth-order Runge-Kutta is frequently used in other applications. This method evaluates derivatives four times at each step:

$$y(t_n + \Delta t) = y(t_n) + \frac{k_1}{6} + \frac{k_2}{3} + \frac{k_3}{3} + \frac{k_4}{6}, \quad (\text{A.2.3})$$

$$k_1 = \Delta t \cdot f(t_n, y(t_n)), \quad (\text{A.2.4})$$

$$k_2 = \Delta t \cdot f\left(t_n + \frac{h}{2}, y(t_n) + \frac{k_1}{2}\right), \quad (\text{A.2.5})$$

$$k_3 = \Delta t \cdot f\left(t_n + \frac{h}{2}, y(t_n) + \frac{k_2}{2}\right), \quad (\text{A.2.6})$$

$$k_4 = \Delta t \cdot f(t_n + h, y(t_n) + k_3). \quad (\text{A.2.7})$$

climate system (year 2000 to typically 2100).

The inverse estimation (Section 3) is performed in the ACC2 past mode. The results of the inverse calculation provide the model state for the year 2000 to be used for subsequent future mode runs. The future mode also uses a future emission scenario as a driver (SRES (Nakićenović et al., 2000)). The past and future modes were separated in year 1990 in ICM, but it has been shifted to 2000 in ACC2. An advantage of the separation of the past and future modes is that resource-intensive multi-scenario runs need only one common past mode run.⁶⁹ Notice that, whenever any part of the model (coefficient values and functional relationships) is altered, the past mode has to be performed again to reflect such a change to the estimates of the parameter values and model state for 2000.

The model code is contained separately in several files, the names of which always start with ACC2 (e.g. ACC2_equations_common.inc) (Table A.1). The names of the files used for the past mode are coded as “past” (e.g. ACC2_bounds_spinup.inc). Similarly, those for the future mode are coded as “future.” Those coded as “common” (e.g. ACC2_equations_common.inc) are used for both the past and future modes.

The main program for the past mode is in the file “ACC2_main_past.gms.” Files used for two modes of operation above are called through INCLUDE command lines in the respective main files (ACC2_main_past.gms and ACC2_main_future.gms). The outputs of a past mode run such as emissions, concentrations, radiative forcings, and temperature change are separately exported in several files named with “out” (e.g. “out_past_1.dat”). The past mode also generates the file “ACC2_init_future.inc,” which contains the estimates of uncertain parameters and model state for 2000. This file is then called from the main program for the ACC2 future mode “ACC2_main_future.gms.” Once the initial file for the future mode is generated, the past mode needs not to be performed unless changes are made to the model as discussed above. The outputs of a future mode run are similarly exported in several files named “out” (e.g. “out_future_1.dat”).

After a past mode run, a file “ACC2_past_main.bas” is produced, where the basis information such as the equation marginals, variable levels, and variable marginals is contained. This basis file is read next time the past mode run is performed. This is a feature of GAMS BAS, improving the efficiency for the solution searches for the past model. GAMS BAS is also used for the future mode. “gamsbas.opt” exists only for formality and no options for GAMS BAS are specified there.

“conopt.opt” and “conopt3.opt” provides the options for CONOPT3 in both the past and future modes. These CONOPT option files are identical and only one of them is read depending on the version of GAMS.

⁶⁹ The six emission scenarios (SRES) are stored in GAMS tables ENGSCN and NEGSCN, which contain the energy-related and non-energy-related GHG emissions, respectively. Multi-scenario runs require only the changes in the set assignments for ENGSCN and NEGSCN in file “ACC2_main_future.gms.”

One change in the file structure from ICM to ACC2 is the addition of ‘switchboard’ contained in the file “ACC2_switchboard_common.inc,” where data and parameters used in the inverse estimation can be controlled.⁷⁰ Flags are assigned in each of (or each time series of) the parameters or data for the inverse calculation. ACC2 users can assign “1” to a flag to include a particular parameter or datum in the inverse estimation. Otherwise, “0” should be assigned to the flag. The switchboard also contains flags to control feedbacks and other features in the model. For example, the flags to control the temperature feedback to the ocean and terrestrial carbon cycle allow one to turn on/off the climate-carbon cycle feedback. The complex calculation for the thermodynamic carbonate equilibria can be replaced with a simpler calculation using the Revelle factor by changing the relevant flag assignment. One could look into how the inverse calculation result changes when the ENSO effects on the atmospheric CO₂ concentration and the temperature records are not accounted for just by changing the relevant flag assignments. More switchboard features are directly explained in the switchboard file.

When an ACC2 model run is completed, it is desirable that no variables be stuck at their bounds. After the completion of the ACC2 past and future runs, the model produces files “out_past_alert.dat” and “out_future_alert.dat,” respectively, where variables are listed if they are stuck at their bounds. Users should check the content of an alert file after a model run. When any variables are found to be stuck, the relevant bounds should be changed and/or model equations need to be looked into. Specifics are shown in the SolVAR section in “ACC2_past_main.lst” or “ACC2_future_main.lst.” An alert system such as above is not provided with the GAMS software package, so the codes to generate alerts are explicitly written at the ends of “ACC2_past_main.gms” and “ACC2_future_main.gms”. Any addition or removal in upper or lower bounds in “ACC2_past_bounds.inc” or “ACC2_future_bounds.inc” should be reflected in the associated codes in the ACC2 main files.

ICM has been extensively used for emission corridor calculations (Zickfeld and Bruckner, 2003). An emission corridor is the domain of admissible emissions to achieve a certain climatic goal. The emission corridors are used for studies that seek cost-effective mitigation strategies and admissible emissions corridors that would keep the system within a domain of tolerable climate change. ACC2 can also be used for emission corridor calculations. Limits of tolerability can be specified in the file called ACC2_settings_future.inc, which are taken as additional optimization constraints for GAMS. The separation of the past and future modes is a technical advantage for corridor calculations.

⁷⁰ Theoretically, an inverse estimation should use all the information available on parameters and data in order to provide a best inversion result. Controlling the parameters and data used in an inverse calculation can only be justified when one analyzes the influence of particular information to the result of an inverse calculation.

A.4 PRACTICAL TIPS ON RUNNING ACC2

Running ACC2 requires not only understanding on the model but also some practical experience on GAMS. Here are practical tips that should be emphasized:

- 1) As a general rule, keeping the model simple helps the model debugging on the long-term.
- 2) The pathways to reach a solution are in some cases sensitive to the structures of model equations – in particular, those contain multiplications and divisions of variables and exponential/logarithmic functions. The behavior of the model should be checked when the model equations are altered.
- 3) When a model run is aborted, GAMS does not erase the “225 directory” (within the ACC2 folder) where temporary files are stored. The unerased 225 directories need to be removed periodically as GAMS can hold only up to twenty six 225 directories. When the model no longer runs after many executions and abortions, 225 directories should be erased.
- 4) When two different bounds are set for one variable in GAMS, the bound appearing earlier in the code is ignored. Upon the addition of a new bound, users should check if another bound has already been set elsewhere.
- 5) In the ACC2 model, conditional statements cannot be used for variables as the model is declared as “NLP” in GAMS. The conditional statements in GAMS involve only set elements, coefficients, and scalars.
- 6) There are cases when, even after a feasible solution has been found and the program has stopped, a better solution can still be found with an additional execution of the program. We suggest that the users confirm the solution by executing the program twice.
- 7) The solution finding procedures may run into a phase where very small changes in the cost function are made at every iteration. When this happens for so long, one could try a different starting point by using a *.bas file from another run. One could also try without using GAMSBAS.
- 8) It is generally more difficult to fix an error due to equation infeasibilities than variable infeasibilities. When one encounters an equation infeasibility error, a good starting point to check is “out_past_alert.dat” or “out_future_alert.dat.” showing variables stuck at their bounds.

Table A.1. Lists of files used for the ACC2 past and future modes

The model code for the ACC2 past and future modes are contained in several files. The main files, “ACC2_main_past.gms” and “ACC2_main_future.gms,” call the other subsequent files at the beginnings of the respective model runs. “ACC2_init_future.inc” is generated after a past mode run and used in a subsequent future mode run to provide parameter values and model state for the year 2000. See Section 4.3 for further explanations on the file structure.

Past mode	Future mode
ACC2_main_past.gms	ACC2_main_future.gms
ACC2_set_common.inc	ACC2_set_common.inc
ACC2_coefficients_common.inc	ACC2_coefficients_common.inc
ACC2_variables_common.inc	ACC2_variables_common.inc
ACC2_bounds_past.inc	ACC2_bounds_future.inc
ACC2_scenarios_past.inc	ACC2_scenarios_future.inc
ACC2_switchboard_common.in	ACC2_switchboard_common.inc
ACC2_settings_past.inc	ACC2_settings_future.inc
ACC2_init_past.inc	ACC2_init_future.inc
ACC2_equations_common.inc	ACC2_equations_common.inc
ACC2_main_past.bas	ACC2_main_future.bas
conopt.opt	conopt.opt
conopt3.opt	conopt3.opt
gamsbas.opt	gamsbas.opt
out_past_1.dat	out_future_1.dat
out_past_2.dat	out_future_2.dat
out_past_1a.dat	out_future_3.dat
out_past_1b.dat	out_future_4.dat
out_past_1c.dat	out_future_alert.dat
out_past_2a.dat	
out_past_inv.dat	
out_past_alert.dat	

APPENDIX B DETAILS OF INVERSION RESULTS

In this appendix, the details of the ACC2 inverse calculation results are shown in Figures B.1 to B.8. Explanations for the figures are provided in the respective notes.

Figure B.1. Carbon accumulations in the reservoirs of the ACC2 atmosphere-ocean box model

The two figures below show the cumulative (1) and annual (2) carbon inputs to the reservoirs of the ACC2 atmosphere-ocean box model. In the composite reservoir, the atmosphere and the ocean mixed layer are equilibrated at every time step. The partition of the carbon between the atmosphere and the ocean mixed layer is determined by the atmospheric CO₂ concentration, the chemical state of the ocean mixed layer, the ocean surface air temperature, and the mixed layer temperature. The fluctuations in the annual amount of carbon input are largest in the composite layer, which gradually propagate to the subsequent ocean reservoirs.

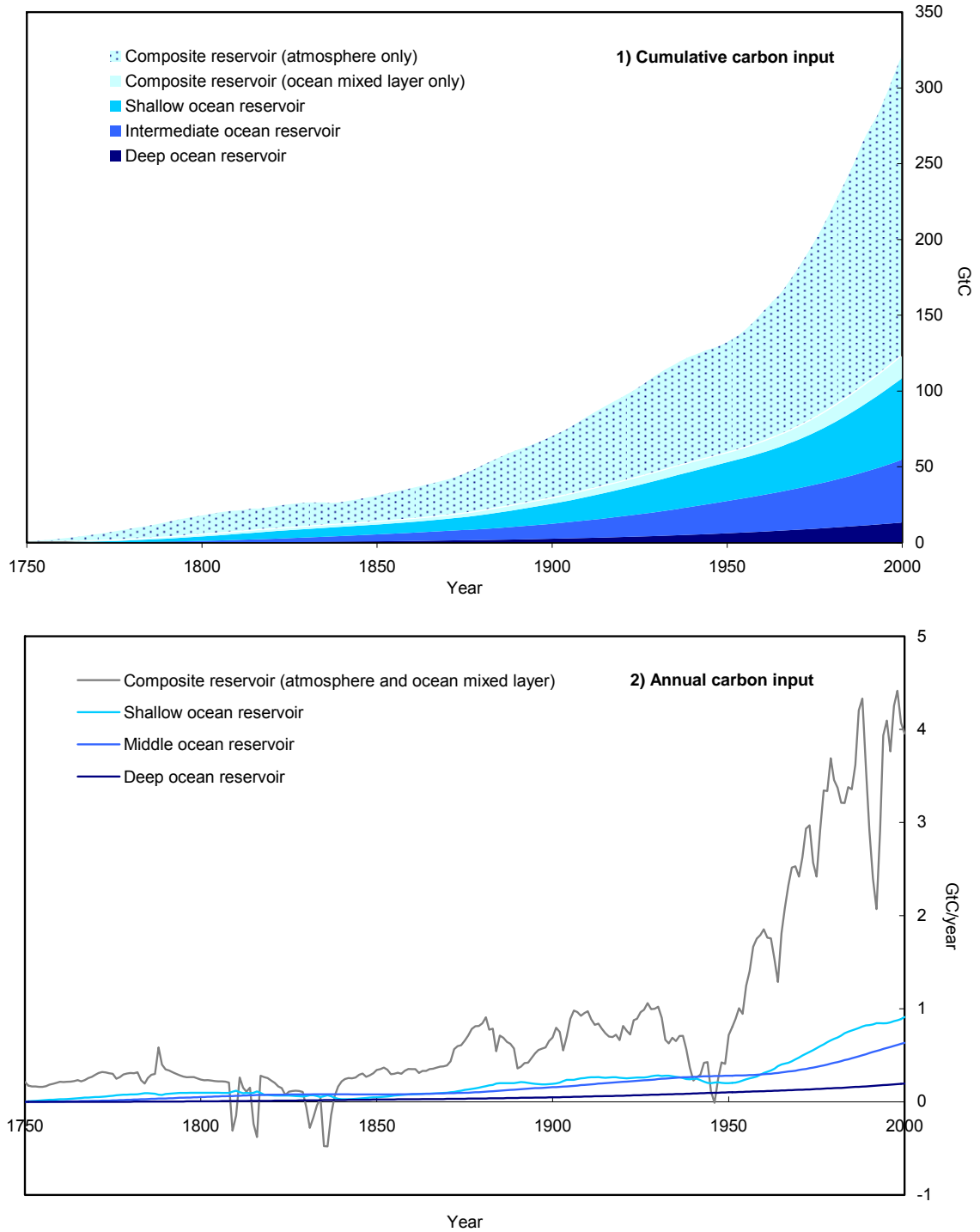


Figure B.2. Changes in the chemistry of the ocean mixed layer over the last 250 years

The ACC2 inverse calculation indicates that pH has dropped by about 0.1 during the last 250 years, accompanied by the changes in the composition of the carbonate species ($\text{CO}_2(\text{aq})$, HCO_3^- , and CO_3^{2-}) (compare Figure 2.2).

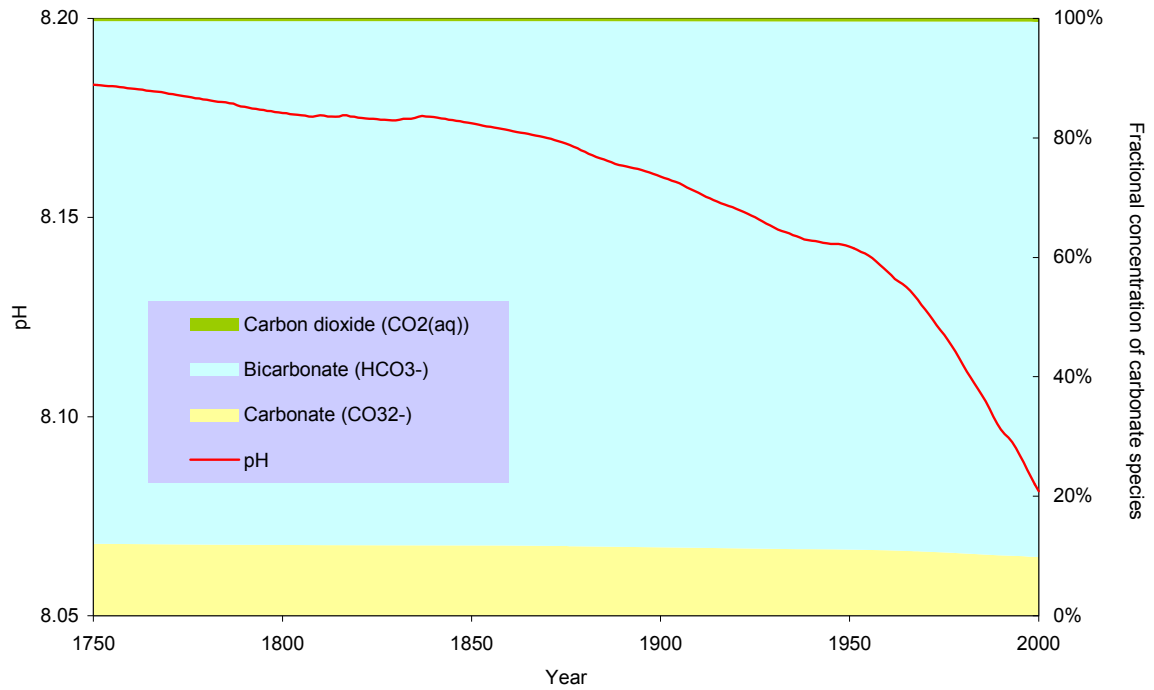


Figure B.3. Carbon accumulations in the reservoirs of the ACC2 land box model

The cumulative (1) and annual (2) carbon inputs to the reservoirs of the ACC2 land box model are shown. The numbers in the brackets correspond to the time constants of the reservoirs ($\tau_{ter,i}$ in equation (2.1.54)). Note that the reservoirs cannot be directly interpreted as physical reservoirs even though the time constants are chosen to be the same with the parent Bern-CC model (Joos et al., 1996). In fact, the land reservoir D *negatively* accumulates carbon ($A_{ter,i}$ in equation (2.1.54)). This counterintuitive phenomenon occurs because all the four reservoirs are directly connected to the atmosphere (more precisely, the composite reservoir) whereas in the parent model, the reservoirs of detritus, ground vegetation, wood, and soil organic carbon are directly connected each other (subsection on IRF for CO₂ Uptake in Section 2.1.3).

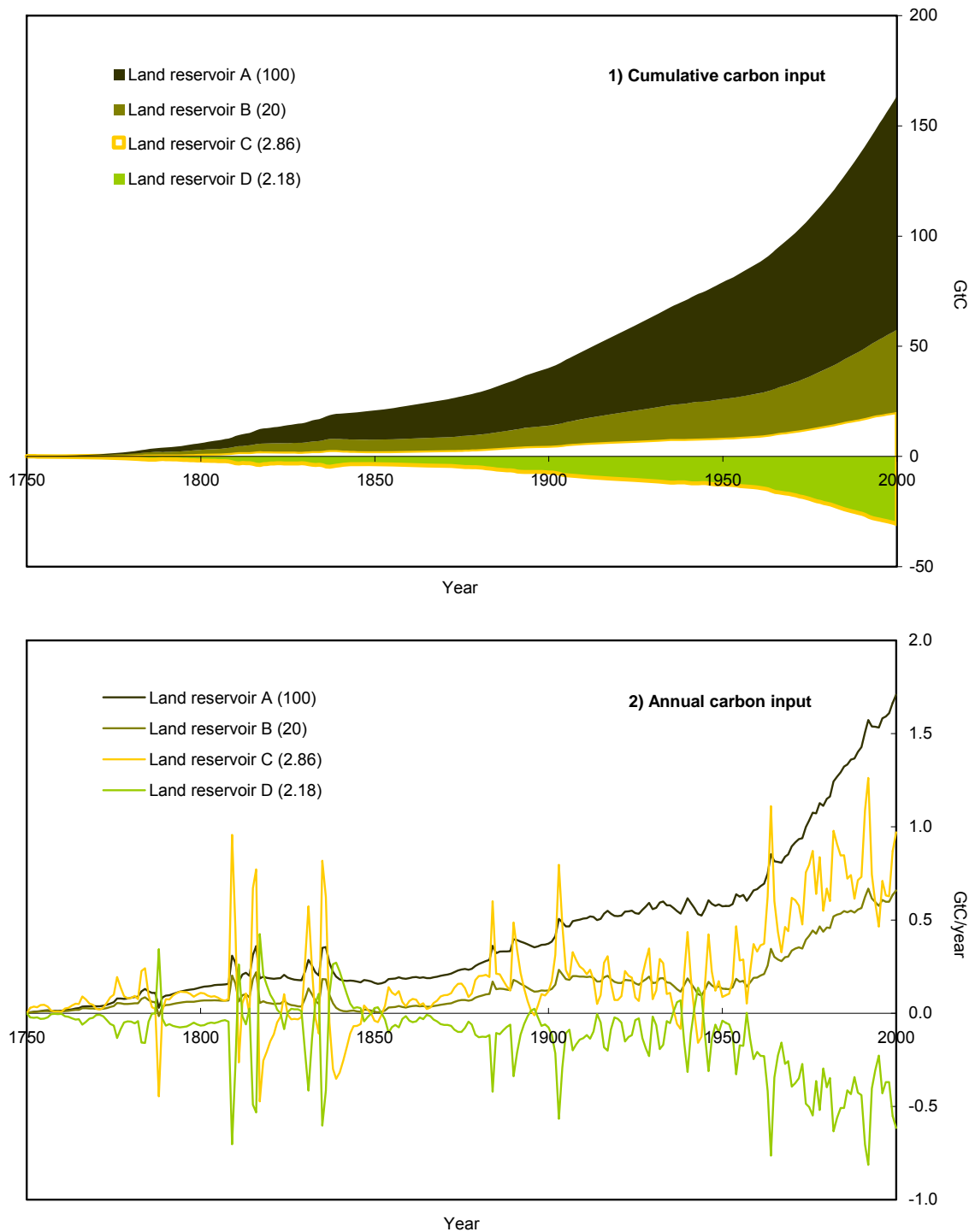


Figure B.4. Temporal changes in NPP and heterotrophic respiration

The total NPP and the heterotrophic respiration for the sum of all the four land reservoirs in ACC2 are shown. The NPP and the heterotrophic respiration are initially balanced under the quasi-steady state assumption (Section 2.1.1) and change thereafter by reflecting the atmospheric CO₂ concentration and the land surface air temperature change, respectively. The difference between the NPP and the heterotrophic respiration is the carbon accumulation in the land reservoirs.

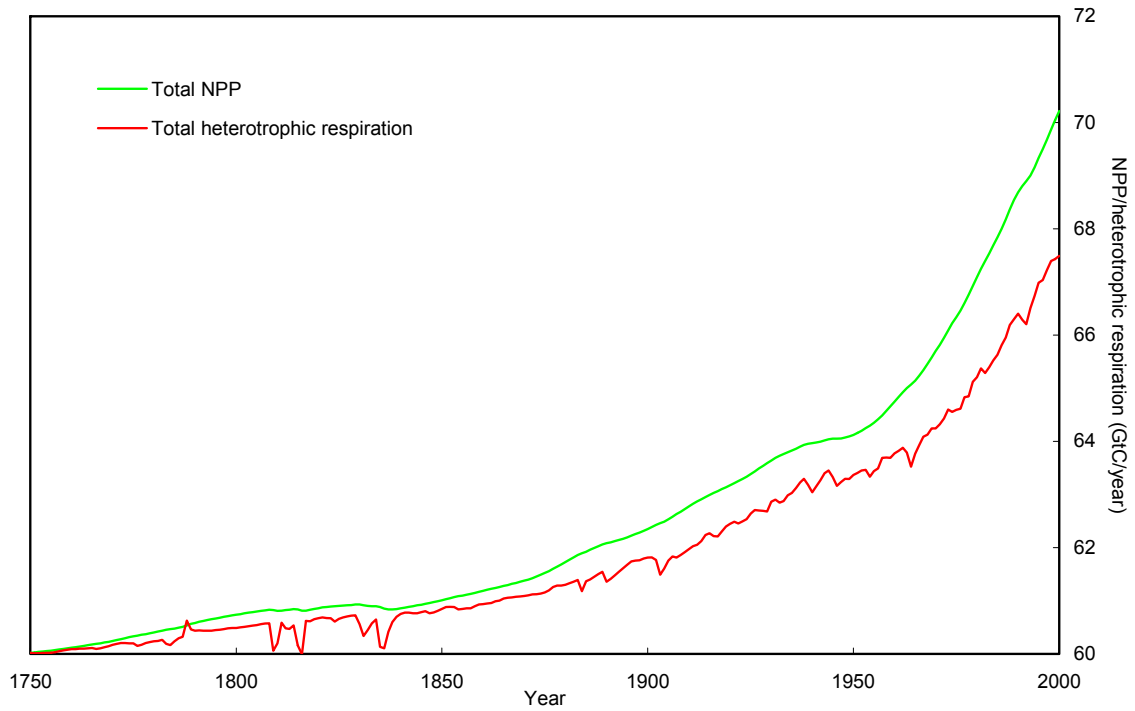


Figure B.5. ENSO-induced anomalies in the atmospheric CO₂ concentration

The ACC2 inverse calculation uses a regression line that explains the natural change in the atmospheric CO₂ concentration as a function of NINO3 index (Section 3.5.1). The result of the statistical inference is the blue line. Although the associated R² value is a merely 0.30, the significance test in correlation still rejects the null hypothesis that the two variables are uncorrelated. The low R² value is due to the fact that the ENSO-induced variation in the atmospheric CO₂ concentration is partly explained by the land use CO₂ emission in the inverse calculation results. The effect of the large volcanic eruptions can be seen in the large discrepancies between the statistically inferred changes and the natural change in 1981 and 1992. The slowdown in the CO₂ concentration rise followed by large volcanic eruptions cannot be described by the model. Related deviations can be seen in insert. These deviations are penalized less as the uncertainty ranges in the atmospheric CO₂ concentration are assumed larger by a factor of four than the ranges in non-volcanic periods.

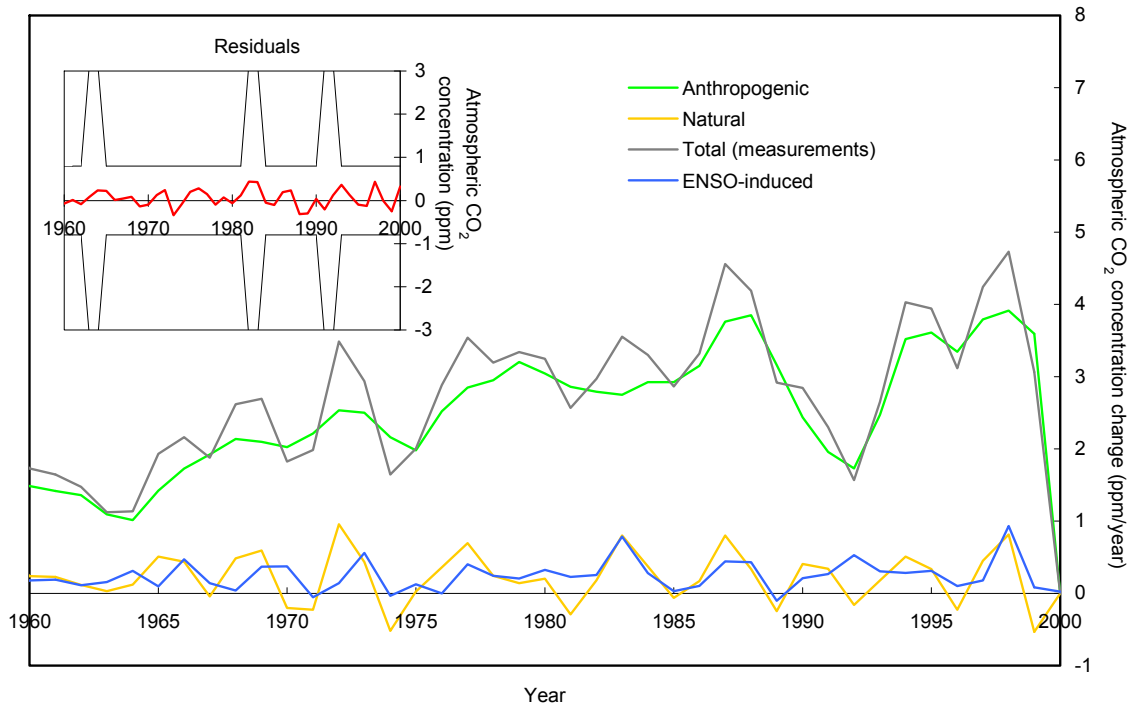


Figure B.6. Evolutions of the individual radiative forcings in the ACC2 inverse calculation

The time series of the missing forcing are parameters estimated from the inverse estimation. The CO₂ radiative forcing is nearly cancelled out by the sum of the three aerosol forcings. The missing forcing tends to be positive for the last 50 years, except for the periods under the influence of large volcanic eruptions. In the earlier period, the large downpeaks of the volcanic forcing are in some cases counteracted by the large positive missing forcing. There is one instance around 1780 when a large positive in the missing forcing occurs not in concurrent to a large volcanic forcing to explain the rise in the temperature records.

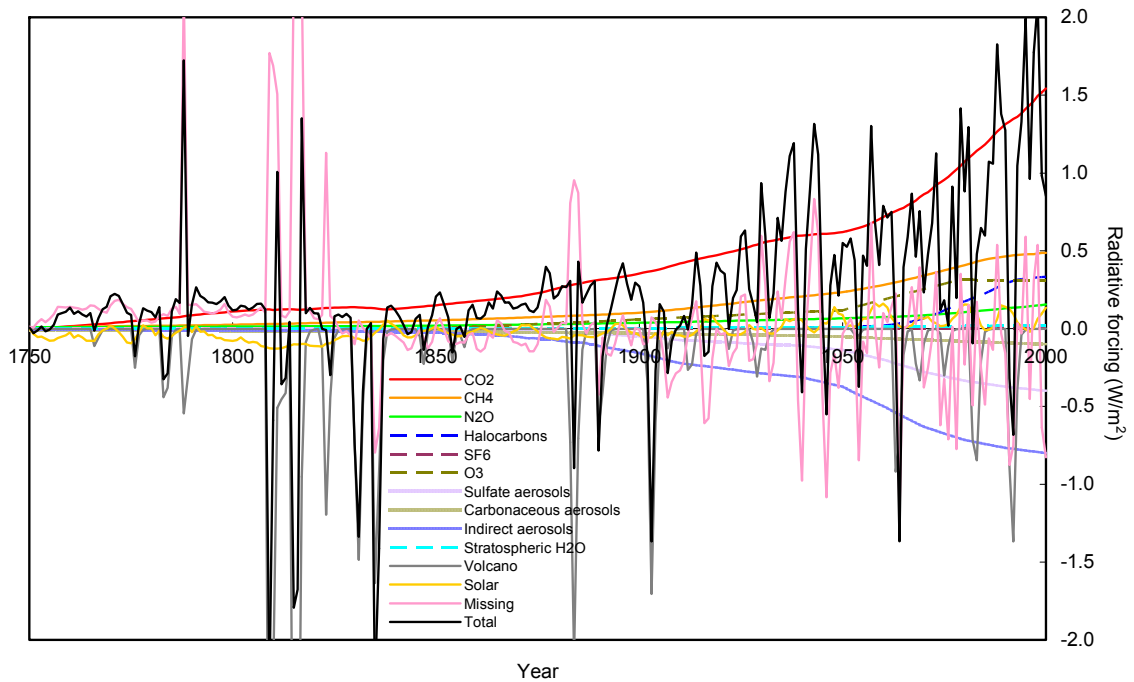


Figure B.7. Land-ocean contributions of the radiative forcing and the surface air temperature

The temperature calculation in DOECLIM is performed by considering the ocean and the land separately. The individual forcings (Figure B.6) are separately scaled for the ocean and the land (Section 2.3.5). The anthropogenic radiative forcing over land is smaller than that over the ocean primarily because the aerosol forcing is overweighted over land. On the contrary, the climate sensitivity over land is larger than the sensitivity over the ocean by 43%. As a result, the trend and the variability in the surface air temperature are amplified over land relative to those over the ocean. Note that the effect of ENSO is excluded in the temperature projections to allow for better comparison between the radiative forcing and the temperature change.

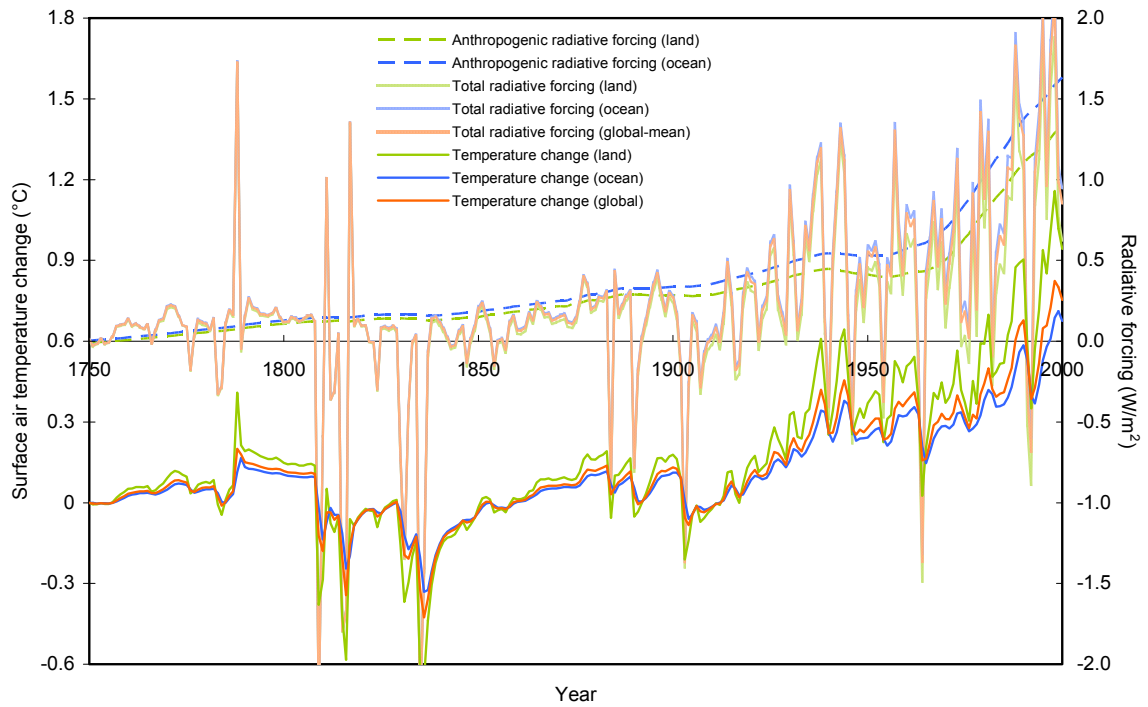
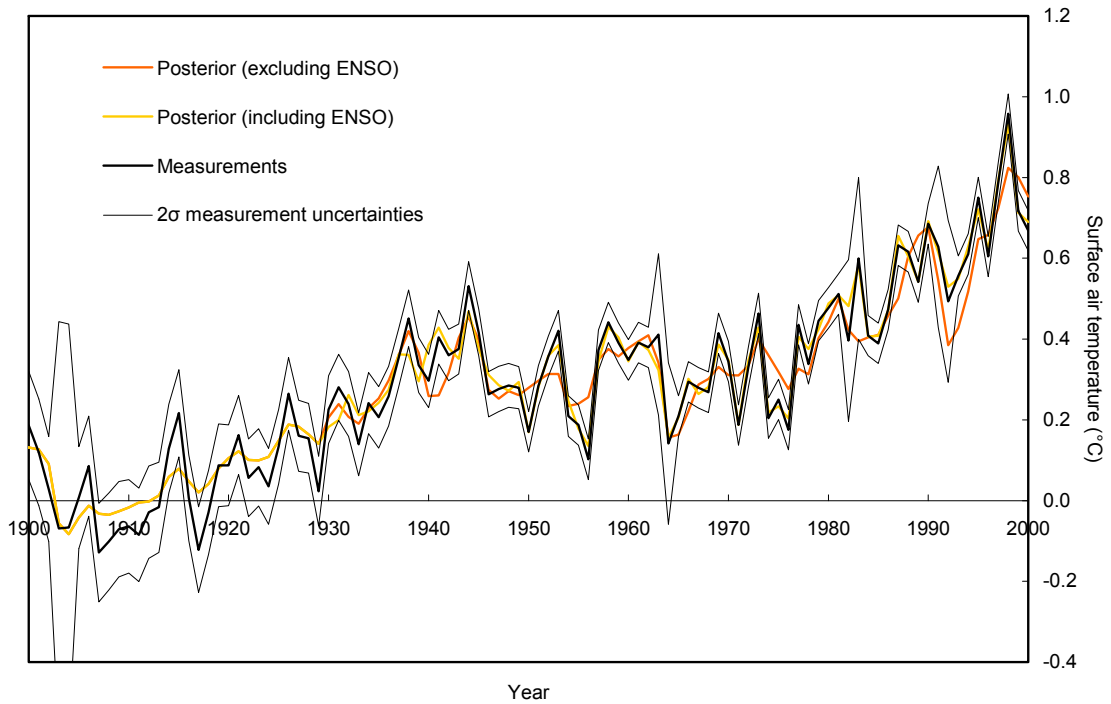


Figure B.8. ENSO-induced anomalies in the surface air temperature

The influence of ENSO on the surface air temperature is taken into account in the ACC2 inverse calculation between 1930 and 2000. A regression line is used to explain the natural variability in the surface air temperature as a function of the SOI index (Section 3.5.1). The variability in the posterior temperature estimates accounting for the ENSO influence is closer to the variability in the temperature records.



APPENDIX C ACRONYMS AND ABBREVIATIONS

Table C.1. List of acronyms and abbreviations

Acronyms and abbreviations	Full names
ACC2	Aggregated Carbon Cycle, Atmospheric Chemistry, and Climate model
AOGCM	Atmosphere-Ocean General Circulation Model
BC	Black Carbon
BFGS	Broyden-Fletcher-Goldfarb-Shanno
CDIAC	Carbon Dioxide Information Analysis Center
CFC	ChloroFluoroCarbons
CMDL	(NOAA) Climate Monitoring and Diagnostics Laboratory
CTM	Chemistry-Transport Model
C ⁴ MIP	Coupled Carbon Cycle Climate Model Intercomparison Project
DIC	Dissolved Inorganic Carbon
DICE	Dynamic Integrated model of Climate and the Economy
DMS	Dimethylsulphide
DNLP	Dynamic NonLinear Programming
EBM	Energy Balance Model
ECHAM	European Centre Hamburg Model
ECOBICE	Economy-Biosphere-Climate project
EECI	Effective Equivalent Chlorine
EESC	Equivalent Effective Stratospheric Chlorine
EMIC	Earth system Models of Intermediate Complexity
ENSO	El Niño-Southern Oscillation
ERBE	Earth Radiation Budget Experiment
EOF	Empirical Orthogonal Function
FACE	Free-Air CO ₂ Enrichment
FC	Fractional release of Chlorine
GAMS	General Algebraic Modeling System
GCM	General Circulation Model
GHG	GreenHouse Gas
GPP	Gross Primary Production
GRG	Generalized Reduced Gradient (algorithm)
HAMOCC	HAMBURG Model of the Ocean Carbon Cycle
HCFC	HydroChloroFluoroCarbons
HFC	HydroFluoroCarbons
HFE	Hydrofluoroether
HH	Hammer-Hollingsworth method
IA	Integrated Assessment
ICLIPS	Integrated Assessment of Climate Protection Strategies
ICM	ICLIPS Climate Model
IPCC	Intergovernmental Panel on Climate Change
IRF	Impulse Response Function
JPL	Jet Propulsion Laboratory
LP	Linear Programming
LPJ	Lund-Potsdam-Jena
LSG	Large-Scale Geostrophic ocean model
MADIAM	Multi-Actor Dynamic Integrated Assessment Model
MIND	Model of INvestment and Technological Development
NAO	North Atlantic Oscillation
NEP	Net Ecosystem Production
NICCS	Nonlinear Impulse-response representation of the coupled Carbon cycle-Climate System model
NLP	NonLinear Programming
NMHC	Non-Methane HydroCarbons
NPP	Net Primary Production
OCO	Orbiting Carbon Observatory
ODE	Ordinary Differential Equations
ODS	Ozone-Depleting Substance
PAR	Photosynthetically Active Radiation
PDE	Partial Differential Equation
PDO	Pacific Decadal Oscillation
PFC	PerFluoroCarbons

Table C.1. (Continued) List of acronyms and abbreviations

Acronyms and abbreviations	Full names
POC	Particulate Organic Carbon
SAT	Surface Air Temperature
SIO	Scripps Institution of Oceanography
SLP	Sequential Linear Programming
SOI	Southern Oscillation Index
SPM	Summary for PolicyMakers
SQP	Sequential Quadratic Programming
SRES	Special Report on Emissions Scenarios
SSS	Sea Surface Salinity
SST	Sea Surface Temperature
TOA	Top Of the Atmosphere
VOC	Volatile Organic Compound
UN	United Nations
UV	UltraViolet (solar radiation)
VEI	Volcanic Explosivity Index

Publikationsreihe des MPI-M

**„Berichte zur Erdsystemforschung“ , „Reports on Earth System Science“, ISSN 1614-1199
Sie enthält wissenschaftliche und technische Beiträge, inklusive Dissertationen.**

Berichte zur Erdsystemforschung Nr.1 Juli 2004	Simulation of Low-Frequency Climate Variability in the North Atlantic Ocean and the Arctic Helmuth Haak
Berichte zur Erdsystemforschung Nr.2 Juli 2004	Satellitenfernerkundung des Emissionsvermögens von Landoberflächen im Mikrowellenbereich Claudia Wunram
Berichte zur Erdsystemforschung Nr.3 Juli 2004	A Multi-Actor Dynamic Integrated Assessment Model (MADIAM) Michael Weber
Berichte zur Erdsystemforschung Nr.4 November 2004	The Impact of International Greenhouse Gas Emissions Reduction on Indonesia Armi Susandi
Berichte zur Erdsystemforschung Nr.5 Januar 2005	Proceedings of the first HyCARE meeting, Hamburg, 16-17 December 2004 Edited by Martin G. Schultz
Berichte zur Erdsystemforschung Nr.6 Januar 2005	Mechanisms and Predictability of North Atlantic - European Climate Holger Pohlmann
Berichte zur Erdsystemforschung Nr.7 November 2004	Interannual and Decadal Variability in the Air-Sea Exchange of CO₂ - a Model Study Patrick Wetzel
Berichte zur Erdsystemforschung Nr.8 Dezember 2004	Interannual Climate Variability in the Tropical Indian Ocean: A Study with a Hierarchy of Coupled General Circulation Models Astrid Baquero Bernal
Berichte zur Erdsystemforschung Nr.9 Februar 2005	Towards the Assessment of the Aerosol Radiative Effects, A Global Modelling Approach Philip Stier
Berichte zur Erdsystemforschung Nr.10 März 2005	Validation of the hydrological cycle of ERA40 Stefan Hagemann, Klaus Arpe and Lennart Bengtsson
Berichte zur Erdsystemforschung Nr.11 Februar 2005	Tropical Pacific/Atlantic Climate Variability and the Subtropical-Tropical Cells Katja Lohmann
Berichte zur Erdsystemforschung Nr.12 Juli 2005	Sea Ice Export through Fram Strait: Variability and Interactions with Climate- Torben Königk
Berichte zur Erdsystemforschung Nr.13 August 2005	Global oceanic heat and fresh water forcing datasets based on ERA-40 and ERA-15 Frank Röske
Berichte zur Erdsystemforschung Nr.14 August 2005	The HAMburg Ocean Carbon Cycle Model HAMOCC5.1 - Technical Description Release 1.1 Ernst Maier-Reimer, Iris Kriest, Joachim Segschneider, Patrick Wetzel
Berichte zur Erdsystemforschung Nr.15 Juli 2005	Long-range Atmospheric Transport and Total Environmental Fate of Persistent Organic Pollutants - A Study using a General Circulation Model Semeena Valiyaveetil Shamsudheen

Publikationsreihe des MPI-M

„Berichte zur Erdsystemforschung“ , „*Reports on Earth System Science*“, ISSN 1614-1199
Sie enthält wissenschaftliche und technische Beiträge, inklusive Dissertationen.

Berichte zur Erdsystemforschung Nr.16 Oktober 2005	Aerosol Indirect Effect in the Thermal Spectral Range as Seen from Satellites Abhay Devasthale
Berichte zur Erdsystemforschung Nr.17 Dezember 2005	Interactions between Climate and Land Cover Changes Xuefeng Cui
Berichte zur Erdsystemforschung Nr.18 Januar 2006	Rauchpartikel in der Atmosphäre: Modellstudien am Beispiel indonesischer Brände Bärbel Langmann
Berichte zur Erdsystemforschung Nr.19 Februar 2006	DMS cycle in the ocean-atmosphere system and its response to anthropogenic perturbations Silvia Kloster
Berichte zur Erdsystemforschung Nr.20 Februar 2006	Held-Suarez Test with ECHAM5 Hui Wan, Marco A. Giorgetta, Luca Bonaventura
Berichte zur Erdsystemforschung Nr.21 Februar 2006	Assessing the Agricultural System and the Carbon Cycle under Climate Change in Europe using a Dynamic Global Vegetation Model Luca Criscuolo
Berichte zur Erdsystemforschung Nr.22 März 2006	More accurate areal precipitation over land and sea, APOLAS Abschlussbericht K. Bumke, M. Clemens, H. Graßl, S. Pang, G. Peters, J.E.E. Seltmann, T. Siebenborn, A. Wagner
Berichte zur Erdsystemforschung Nr.23 März 2006	Modeling cold cloud processes with the regional climate model REMO Susanne Pfeifer
Berichte zur Erdsystemforschung Nr.24 Mai 2006	Regional Modeling of Inorganic and Organic Aerosol Distribution and Climate Impact over Europe Elina Marmer
Berichte zur Erdsystemforschung Nr.25 Mai 2006	Proceedings of the 2nd HyCARE meeting, Laxenburg, Austria, 19-20 Dec 2005 Edited by Martin G. Schultz and Malte Schwoon
Berichte zur Erdsystemforschung Nr.26 Juni 2006	The global agricultural land-use model KLUM – A coupling tool for integrated assessment Kerstin Ellen Ronneberger
Berichte zur Erdsystemforschung Nr.27 Juli 2006	Long-term interactions between vegetation and climate -- Model simulations for past and future Guillaume Schurgers
Berichte zur Erdsystemforschung Nr.28 Juli 2006	Global Wildland Fire Emission Modeling for Atmospheric Chemistry Studies Judith Johanna Hoelzemann
Berichte zur Erdsystemforschung Nr.29 November 2006	CO₂ fluxes and concentration patterns over Euro Siberia: A study using terrestrial biosphere models and the regional atmosphere model REMO Caroline Narayan

Publikationsreihe des MPI-M

**„Berichte zur Erdsystemforschung“ , „Reports on Earth System Science“, ISSN 1614-1199
Sie enthält wissenschaftliche und technische Beiträge, inklusive Dissertationen.**

**Berichte zur
Erdsystemforschung Nr.30**
November 2006

**Long-term interactions between ice sheets and
climate under anthropogenic greenhouse forcing
Simulations with two complex Earth System Models**
Miren Vizcaino

**Berichte zur
Erdsystemforschung Nr.31**
November 2006

**Effect of Daily Surface Flux Anomalies on the
Time-Mean Oceanic Circulation**
Balan Sarojini Beena

**Berichte zur
Erdsystemforschung Nr.32**
November 2006

**Managing the Transition to Hydrogen and Fuel Cell
Vehicles – Insights from Agent-based and
Evolutionary Models –**
Malte Schwoon

**Berichte zur
Erdsystemforschung Nr.33**
November 2006

**Modeling the economic impacts of changes in
thermohaline circulation with an emphasis on the
Barents Sea fisheries**
Peter Michael Link

**Berichte zur
Erdsystemforschung Nr.34**
November 2006

Indirect Aerosol Effects Observed from Space
Olaf Krüger

**Berichte zur
Erdsystemforschung Nr.35**
Dezember 2006

**Climatological analysis of planetary wave
propagation in Northern Hemisphere winter**
Qian Li

**Berichte zur
Erdsystemforschung Nr.36**
Dezember 2006

**Ocean Tides and the Earth's Rotation -
Results of a High-Resolving Ocean Model forced by
the Lunisolar Tidal Potential**
Philipp Weis

**Berichte zur
Erdsystemforschung Nr.37**
Dezember 2006

**Modelling the Global Dynamics of
Rain-fed and Irrigated Croplands**
Maik Heistermann

**Berichte zur
Erdsystemforschung Nr.38**
Dezember 2006

**Monitoring and detecting changes in the meridional
overturning circulation at 26°N in the Atlantic
Ocean- The simulation of an observing array in
numerical models**
Johanna Baehr

**Berichte zur
Erdsystemforschung Nr.39**
Februar 2007

**Low Frequency Variability of the
Meridional Overturning Circulation**
Xiuhua Zhu

